

TECHNISCHE UNIVERSITÄT MÜNCHEN

Lehrstuhl für Funktionelle Materialien E13

Forschungs-Neutronenquelle Heinz Maier-Leibnitz

Irradiation behavior of modified high-performance nuclear fuels

Rainer Jungwirth

Vollständiger Abdruck der von der Fakultät für Physik der Technischen Universität München zur Erlangung des akademischen Grades eines

Doktors der Naturwissenschaften (Dr. rer. nat)

genehmigten Dissertation.

Vorsitzender: Univ.-Prof. Dr. Harald Friedrich

Prüfer der Dissertation: 1. Univ.-Prof. Dr. Winfried Petry
2. Priv.-Doz. Dr. Christoph Morkel

Die Dissertation wurde am 29. September 2011 bei der Technischen Universität München eingereicht und durch die Fakultät für Physik am 3. November 2011 angenommen.

“We choose to go to the moon in this decade, not because it is easy, but because it is hard, because that goal will serve to organize and measure the best of our energies and skills, because that challenge is one that we are willing to accept, one we are unwilling to postpone, and one which we intend to win.”
(J.F. Kennedy, 12. Sept. 1962)

Abstract

There are strong international efforts to reduce the enrichment of the nuclear fuel currently used in high performance research and test reactors. However, these efforts were hindered due to the fact that the most promising candidate for a new fuel - a Uranium-Molybdenum alloy (UMo) dispersed in an aluminium matrix - suffered from unforeseeable and unacceptable swelling during in-pile test irradiations. The main cause for this behaviour is the build-up of an Al rich diffusion layer at the interface between the UMo and the Al matrix during irradiation. To overcome this problem, four different possibilities have been identified: (i) the modification of the Al matrix, e.g. by adding diffusion limiting elements (ii) the insertion of a diffusion barrier at the interface UMo-Al (iii) further alloying the UMo with a third element to stabilize the γ -UMo phase (iv) a combination of means (i)-(iii). In consequence, 20 different UMoX/AlY (X=Si, Ti, Mg, Bi, with and without oxidation layer; Y=Nb, Ti, Pt) samples have been produced and examined before and after irradiation with Iodine at 80MeV from a tandem accelerator. It has been shown before, that heavy ion irradiation causes similar effects than in-pile irradiation inside the samples without the drawback of strong activation of the samples. First it has been shown, that a protective oxidation layer on the UMo grains does not prevent the formation of a destructive interdiffusion layer. In contrast, it could be shown, that additions to the Al matrix and/or additions to the UMo can be reduced to the self-acting formation of a protective layer at the UMo/Al interface. These layers form already during the production process or latest during in-pile irradiation and prevent the undesired UMo/Al diffusion. On the other hand, ternary additions to the UMo in order to stabilize the γ -UMo upon heating are of minor importance since irradiation with heavy ion or in-pile reverses the phase decomposition of UMo.

Zusammenfassung

Die internationale Gemeinschaft betreibt große Anstrengungen, den Anreicherungsgrad des Kernbrennstoffs von Hochfluß-Forschungsreaktoren zu reduzieren. Da die erfolgversprechendste Option auf einen neuen Kernbrennstoff - eine Uran-Molybdän Legierung dispers verteilt in einer Aluminium Matrix - unvorhersehbares und nicht akzeptables Schwellverhalten während Testbestrahlungen in Reaktoren an den Tag legte wurden die Umrüstungsbemühungen stark verzögert. Der Hauptgrund für dieses starke Schwellen ist der Bestrahlungs-getriebene Aufbau einer aluminiumreichen Diffusionsschicht am Übergang zwischen UMo und Al. Um dieses Problem zu lösen wurden vier verschiedene Möglichkeiten untersucht: (i) Veränderung der Al Matrix, z.B. durch Zugabe von Elementen, die die Diffusion verzögern sollen. (ii) Aufbringen einer Diffusionsbarriere am Übergang UMo zu Al. (iii) Legieren des UMo mit einem dritten Element um die γ -Phase des UMo zu stabilisieren. (iv) Jede Kombination von Möglichkeiten (i)-(iii). Es wurden daher 20 verschiedene UMoX/AlY (X=Si, Ti, Mg, Bi, mit und ohne Oxydschicht; Y=Nb, Ti, Pt) Proben hergestellt und vor und nach Bestrahlung mit Jod untersucht. Die Jodionen besaßen dabei eine Energie von 80MeV und stammten aus einem Tandem Beschleuniger. Zuvor war von anderen Autoren bewiesen worden, dass die Bestrahlung mit Schwerionen vergleichbare Effekte in UMo/Al verursacht wie Bestrahlungen im Reaktor - allerdings ohne die Proben stark zu aktivieren. Zusammenfassend lässt sich sagen, dass die Ausbildung einer Oxydschicht die Bildung der Interdiffusionsschicht während Bestrahlung nicht verhindert. Hingegen führen Beimischungen zur Al Matrix und/oder zum UMo zur Bildung einer Schutzschicht während der Herstellung der Proben oder spätestens während der Bestrahlung am Übergang UMo/Al. Diese Schutzschicht verhindert oder verzögert die ungewollte UMo/Al Diffusion. Andererseits stabilisieren Zusätze zum UMo zwar die γ -Phase während der Probenherstellung. Dies ist jedoch von geringer Bedeutung da die Zersetzung dieser Phase während der Bestrahlung mit Schwerionen oder auch im Reaktor rückgängig gemacht wird.

Contents

Abstract	5
Zusammenfassung	7
1 Motivation	11
2 Scientific background	17
2.1 Radiation damage in metals	17
2.2 Uranium and uranium alloys - Phase behavior	32
2.2.1 Pure uranium	32
2.2.2 Uranium alloys	32
2.3 Uranium - Aluminum diffusion	42
3 Experiment	55
3.1 Sample preparation	55
3.2 Heavy ion irradiation	56
3.3 Pre- and Postirradiation examinations - Methods	62
4 Results and discussion	67
4.1 Irradiation conditions - Methodology	67
4.1.1 Experimental method	67
4.1.2 Results	69
4.2 Oxidized particles	75
4.2.1 Pre-irradiation state	76
4.2.2 Post-irradiation state	79
4.2.3 Discussion	82
4.3 UMo/AlSi	84
4.3.1 Sample production	84
4.3.2 Characterization before irradiation	86
4.3.3 Characterization after irradiation	99
4.3.4 Conclusions	102
4.4 UMo/AlBi	103
4.4.1 Characterization before irradiation	103
4.4.2 Characterization after irradiation	104
4.4.3 Conclusions	104
4.5 UMo/AlTi Systems	108
4.5.1 Matrix addition: UMo/Al2wt%Ti	109
4.5.2 Ti as diffusion barrier	109

4.5.3	Discussion	111
4.6	UMo/AlMg	111
4.7	UMo Ground powder	112
4.7.1	Pre-irradiation state of ground UMo fuels	112
4.7.2	Irradiation behavior of ground fuel - IDL formation and phase behavior	127
4.7.3	Conclusions on ground UMo fuels	131
5	Summary and outlook	133
5.1	Summary	133
5.2	Further prospects for heavy ion irradiation	139
A	Sample preparation	141
B	Phase diagrams	143
	Own Publications	157
	Acknowledgment	159
	List of figures	163
	List of tables	165
	Bibliography	182

Chapter 1

Motivation

The new neutron source “Forschungs-Neutronenquelle Heinz Maier-Leibnitz (FRM II)” in Garching provides neutrons for science, industry and medicine since the year 2004 thus continuing the long and successful story of neutron science at the Technische Universität München. A large variety of instruments, suitable for fundamental and applied research, has been installed since then. The energy spectrum of the neutrons at the FRM II covers a region from as low as 10^{-7} eV (“ultra-cold neutrons”) over 0.025 eV (“thermal neutrons”) up to 10^7 eV (“fission neutrons”). The FRM II offers a high thermal neutron flux¹ outside the reactor core. However, its thermal power is as low as 20 MW_{th} and the reactor core is comparatively small which is achieved by using one single, cylindrical shaped, fuel element and a high density, highly enriched (93wt%²³⁵U) nuclear fuel². The outer diameter of the fuel element is 243 mm, the inner diameter is 118 mm and the active height is 700 mm resulting in an active zone of only 17 l. It contains 113 involute shaped fuel plates, separated by cooling channels. The control rod moves inside the central hole of the fuel element (compare figure 1.1). Light water is used for cooling of the fuel element and for a first moderation of the neutrons, whereas heavy water surrounds the fuel element to reflect and further moderate the neutrons [1].

The compact reactor core of the FRM II together with the high neutron flux demand a very high uranium density inside the fuel plates. This goal is achieved by using U₃Si₂ powder dispersed in an aluminum matrix. Hereby U₃Si₂ powder is rolled in aluminum and clad with AlFeNi plates. This guarantees a good removal of the heat from the fuel plates. The thickness of the so called “meat layer”, which contains the U₃Si₂, is 0,6 mm, the thickness of the cladding is 0,38 mm (compare chapter 3.1). The uranium density inside the meat is 3.0 gU/cm³ near the center of the fuel element and 1.5 gU/cm³ near the outer edge, respectively. At the end of the cycle, up to $2.0 \cdot 10^{21}$ fissions per cm³ took place inside the meat [3–5].

Combining metallic, high enriched nuclear fuel (U₃Si₂) with a very small core volume and usage of light water for cooling and moderation and heavy water for reflection of the neutrons results in the world wide best ration $\Phi_{\text{therm,max}} / \text{reactor power}$.

In the course of the program “Reduced Enrichment for Research and Test Reactors” (RERTR) there are great international efforts to convert research and test reactors

¹ $\Phi_{\text{therm,max}} = 8 \cdot 10^{14} \frac{\text{neutrons}}{\text{cm}^2 \cdot \text{s}}$, unperturbed

²HEU = High Enriched uranium



Figure 1.1: Drawing of the FRM II fuel element. The inner diameter is 118 mm, the outer diameter is 243 mm, the active height is 243 mm. The fuel element contains 113 involute shaped fuel plates, separated by cooling channels. The control rod moves inside the central hole [1,2].

world wide to operate with low enriched uranium³. The goal of the RERTR program is to reduce the spread of weapon grade uranium worldwide and so to minimize the risk of proliferation. Up to now, 43 reactors world wide have been converted, among them two in Germany: in the year 1991 the FRG-1 in Geesthacht and in the year 2000 the BER-II in Berlin. Among the reactors preparing their conversion in the USA are the High Flux Isotope reactor (HFIR, Oak Ridge), the Advanced Test Reactor (ATR, Idaho), the MIT nuclear research reactor (MITR, Massachusetts) and the University of Missouri Research Reactor (UMRR, Missouri) [6–8]. In europe, the research reactors Orphee and Institut Laue-Langevin (ILL) in France, the Belgian Reactor 2 BR2 in Belgium and the Forschungsneutronenquelle Heinz Maier-Leibnitz (FRM II) are preparing their conversion.

The third and final operation license of the FRM II, received in the year 2003, contains the obligation to reduce the enrichment of the nuclear fuel used inside the FRM II as fast and as much as possible under the condition of a marginal influence on the scientific quality. A complete reconstruction of the reactor core is unrealistic, which means that the size and geometry of the fuel element must remain unchanged. However, to preserve the high thermal neutron flux of $\Phi_{\text{therm,max}} = 8 \cdot 10^{14} \frac{\text{neutrons}}{\text{cm}^2 \cdot \text{s}}$ (unperturbed) and the cycle length of 60 days the amount of fissionable ^{235}U inside the reactor core has to increase slightly and the total uranium load has to be more than doubled [9,10]. This means that a fuel with a higher uranium density than the one current used has to be found. Calculations showed that the minimum uranium density inside the fuel element meat must be at least 8.0 gU/cm^3 to reach an enrichment reduction from currently 93% ^{235}U to about 50% ^{235}U [11].

To achieve this aim, it is on the one hand necessary to increase the volume fraction of fuel particles inside the meat. However, the technical limit is reached at approximately 55 vol% of fuel particles in the aluminum matrix [12]. On the other hand an uranium compound with an higher uranium density than U_3Si_2 has to be found.

³LEU=Low Enriched uranium, enrichment $^{235}\text{U} < 20\text{wt}\%$

Table 1.1: Some uranium compounds with densities higher than that of U_3Si_2 [13].

Compound	Density [g/cm ³]	U-density [g/cm ³]
U_3Si_2	12.2	11.3
UCo	15.4	12.3
U_2Ti	15.1	13.7
U_2Mo	16.6	13.8
U_2Ru	16.9	13.9
U_6Co	17.7	17.0
U_6Ni	17.6	16.9
U_6Fe	17.7	17.0
U_6Mn	17.8	17.1

Beside pure uranium metal ($\rho(U)=19.05$ g/cm³) there are several uranium compounds and alloys which offer a higher uranium density than U_3Si_2 [13], compare table 1.1 and 1.2. It is well known that the orthorhombic α -phase of uranium, present in pure uranium at room temperature, is not suitable as a reactor fuel [14–17] (see picture 1.2). Regarding the uranium compounds, only intermetallics of the U_6 metal class like U_6Mn , U_6Fe , U_6Ni and U_6Co possess a uranium density high enough to meet the requirements of the FRM II. Test plates containing U_6Mn and U_6Fe powder dispersed in aluminum were tested in the Oakridge Research Reactor (ORR) in the United States of America. Both showed a poor irradiation behavior and exhibited break away swelling at a burn up as low as $3 \cdot 10^{21}$ fissions per cm³ inside the fuel particles. It has been concluded that they do not meet the requirements on stability during operation of a high density, high performance fuel for research and test reactors [18,19]. It is expected that similar compounds like U_6Ni and U_6Co show a similar poor irradiation behavior [13,20].

Alloying the uranium aims to stabilize the cubic γ -phase of uranium at room temperature [21,22]. Only the γ -phase of uranium has adequate properties to be used as a nuclear fuel [14]. Table 1.2 shows the densities and uranium densities of two uranium-molybdenum and uranium-zirconium-niobium alloys. Both alloys retain the γ -phase of uranium at room and have a sufficient uranium density. However, U-Zr-Nb showed a poor performance during both, annealing and in-pile irradiation experiments⁴ under research reactor conditions [13].

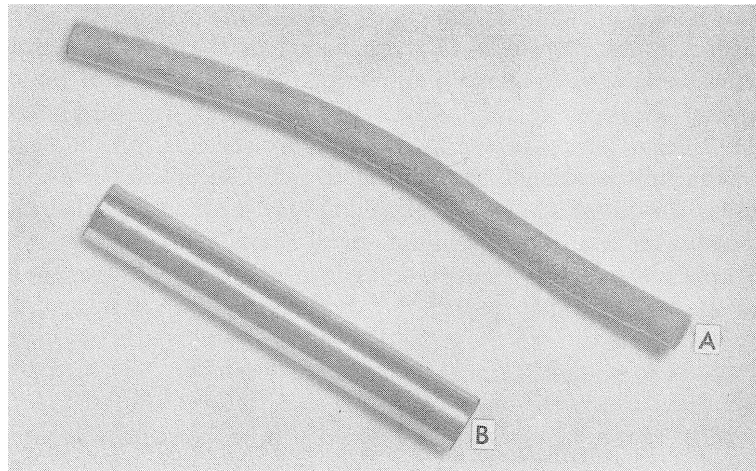
The remaining U-Mo alloy showed a good irradiation behavior in the past and allows uranium densities of around 8.5 gU/cm³ inside the meat at a volume loading of 55vol%. Hence, the U-Mo alloy, well-known since the 50s of the last century, is currently the subject of the renewed interest of the international research-reactor-fuel developing community. The addition of 7wt% to 10wt% of Mo to the U is the best compromise between a high uranium density and a good γ -stability of the UMo (compare section 2.2) [20,23–26].

Up to now many test fuel plates prepared with UMo powder dispersed in an Al matrix failed during in-pile irradiation. The fuel plates are affected by a large swelling

⁴During in-pile irradiation experiments, a fuel plate is irradiated inside a nuclear reactor.

Table 1.2: Some uranium alloys with higher density than that of U_3Si_2 [13].

Compound	Density [g/cm ³]	U-density [g/cm ³]
U_3Si_2	12.2	11.3
U-9wt%Mo (U-19at%Mo)	17.0	15.5
U-5wt%Mo (U-11at%Mo)	17.9	17.0
U-2wt%Zr-9wt%Nb	16.2	14.3
U-4wt%Zr-2wt%Nb	17.3	16.3

Figure 1.2: A. Growth of a highly textured α -uranium rod during irradiation. B. Size of the uranium rod before irradiation [16, 27].

and pillowing which leads to break away swelling and finally a rupture of the cladding. As main reason for the abnormal swelling, the build-up of an interdiffusion layer (IDL) at the interface between the UMo and the surrounding Al matrix has been identified. The IDL consists in general of, depending on the irradiation conditions, an either amorphous [28] or crystalline [29] U-Al compound. The thermal conductivity of the IDL is suspected to be lower than the one of the surrounding Al which increases the fuel temperature [30]. Furthermore, the density of the IDL is lower than the one of Al and UMo which results in a volume expansion [31]. Moreover, since the ability of the IDL to retain fission gases, which are produced during in-pile irradiation, is very limited, the growth of large gas bubbles inside the fuel plates is promoted. With increasing burn-up, the growth of the IDL and of fission gas bubbles pillow the fuel plate which finally can lead to a cladding failure (for more details compare section 2.3) [32–34]. Such a behavior can not be accepted inside the fuel assemblies of research and test reactors.

For this reason, different means have been proposed to reduce the interaction between the UMo and the surrounding Al. There are in principal 3 possibilities, that also can be combined:

1. Addition of a diffusion limiting element to the matrix [35–38].

2. Insertion of a diffusion barrier at the interface between the UMo and the Al [39–42].
3. Alloying of the UMo with a third element [25, 43–45].
4. Any combination of possibility 1, 2 or 3.

A detailed discussion of possible elements will follow in chapter 2.

It has been shown that during irradiation UMo/Al samples with swift heavy ions (e.g. iodine at 80 MeV from a tandem accelerator) an IDL grows at the interface between the UMo and the Al. The physical properties of this IDL are comparable to the properties of the IDL grown during in-pile irradiation [46]. The samples will not be activated during the heavy ion bombardment so that they can be handled with normal laboratory equipment. No complex and costly shielding is necessary during the post-irradiation examinations (PIEs), in contrast to in-pile irradiated samples. Moreover, the equivalent damage of months or even years of in-pile irradiation can be reached within some hours using heavy ions [47, 48]. For these reasons, heavy ion irradiation is an excellent tool to perform an efficient screening of potential fuel candidates prior to an in-pile test.

For this thesis, different measures to avoid the UMo/Al diffusion have been identified. From the options discussed there, the most promising available material combinations have been chosen and in total 20 different sample-fuel-plates have been manufactured. From each plate, a set of samples has been irradiated with heavy ions to simulate the in-pile irradiation. A full set of post irradiation examinations has been performed afterwards. The heavy ion irradiated samples have been compared with the non-irradiated case. The aim of this work was to identify the influence of different material combinations on the behavior of the IDL and finally to find a promising candidate for a future in-pile test.

The whole work was accomplished in close collaboration between the Commissariat à l’Energie Atomique (CEA) and AREVA-CERCA. The samples examined during this thesis have been produced by AREVA-CERCA and have kindly been provided free of charge. Our colleagues from CEA contributed outstanding knowledge on sample irradiation and characterization. Most of the post irradiation examinations took place in the “Laboratoire UO₂” of CEA in Cadarache where I was kindly hosted for several weeks. I have been shown all the methods for proper sample examination and received extraordinary support for my work. Furthermore, our samples have been examined during beam times obtained from CEA groups at the μ -XRD beamlines of the Swiss Light Source (SLS) of the Paul Scherrer Institute (PSI, Villingen, Switzerland) and of the European Synchrotron Radiation Facility (ESRF, Grenoble, France). It shall be pointed out that without the constant support of two special persons - Hervé Palancher and Christophe Jarousse - this work would not have been successful.

Chapter 2

Scientific background

2.1 Radiation damage in metals

The cause for the property changes occurring inside UMo/Al dispersion fuels during in-pile irradiation can be directly ascribed to the high radiation level to which the material is exposed during operation. In this chapter an overview of the physics of radiation damage inside metals will be given. Thereby it will be confined to metals and later especially to Uranium and its alloys.

The physics of radiation damage inside condensed matter and especially metals has been reviewed several times before e.g. by D. Billington and J.H. Crawford jr. in their textbook “Radiation damage in solids” [50], by W. Schilling and H. Ullmaier with a focus on radiation damage inside Uranium [51], by F. Seitz and J.S. Koehler with focus on single particle collisions and displacements [52–54] and by R.S. Averback and T. Diaz de la Rubia with focus on the effects occurring in energetic cascades [55].

Types of radiation and stopping mechanisms. Matter in the solid state frequently alters its properties when exposed to radiation of different kinds. This effect is especially visible inside crystalline materials. With the construction of the first nuclear reactors in the 40s and 50s of the last century, the theory of radiation defects in solids became technological interesting. Inside a nuclear reactor, all materials are exposed to different kinds of energetic radiation:

- High level **γ -radiation** which is produced during fission and the following decay of fission products. About 10 MeV of gamma rays are produced per fission [54].
- **β -particles** from the decay of the neutron-rich fission products. The β -particles carry in total about 7 MeV [54].
- **Anti-Neutrinos** from the β -decay of the fission fragments. They carry in total about 13MeV [54].
- In average 2.4 **neutrons** are produced per fission which have in total about 5 MeV kinetic energy [54].
- The two **fission fragments** produced during fission have an energy of about 165 MeV which splits on the two particles according to the distribution depicted in

figure 2.1. These particles have by far the greatest amount of energy available to produce radiation damage. However, their mean free path is limited to some μm inside most materials.

Normally, the influence of the fission fragments and the high-energetic neutrons greatly outweighs the effects of other types of radiation on the materials inside a nuclear reactor. The nuclear fuel itself is hereby especially affected by the fission products whereas the cladding materials are rather affected by the neutron radiation [54].

In general, the energy loss dE of an energetic particle traversing a distance dx can be described by the following mechanism [51, 55]:

$$\frac{dE}{dx} = \frac{\partial E}{\partial x}|_d + \frac{\partial E}{\partial x}|_e + \frac{\partial E}{\partial x}|_n \quad (2.1)$$

where:

1. $\frac{\partial E}{\partial x}|_e$ describes inelastic interactions between the bombarding particle and the electrons in the solid, the index e stands for electronic losses. Electronic losses occur only in case of charged moving particles which can be charged initial particles like heavy ions or fission fragments but also knock-on atoms. The electronic energy loss is the predominant stopping mechanism in case the ion energy exceeds some hundred of keV/u [56]. The electronic losses can cause permanent property changes inside insulators, metallic glasses and also metals. During irradiations with very high energetic heavy ions in the GeV regime the electronic excitations may result in so called ‘‘Coulomb explosions’’ [57].
2. $\frac{\partial E}{\partial x}|_d$ describes energy loss due to elastic collisions between the moving particle and the lattice atoms. It is the predominant stopping mechanism in case the ion energy is below $\approx 100 \text{ keV/u}$ [56]. The moving particle thereby transfers an amount of energy T to a lattice atom. If the transferred energy exceeds a material-dependent threshold energy for displacement, T_d , the hit atom leaves its original site, thereby creating a interstitial-vacancy pair that is also called ‘‘Frenkel-pair’’ or ‘‘Frenkel-defect’’. The index d stands for displacement. High energetic neutrons and fission fragments transfer recoil energies which are many times higher than T_d . In this case, the primary knock-on atom (PKA) is by itself able to displace neighboring atoms. If the energy is high enough, the secondaries may displace ternaries and so on which results in a displacement cascade¹.
3. $\frac{\partial E}{\partial x}|_n$ refers to inelastic collisions between the projectile and the nuclei of the solid. An example are nuclear reactions with thermal or fast neutrons or interactions of heavy ions with target atoms at energies above the Coulomb barrier. Inelastic collisions typically result in excitation of the target. This effect is important in nuclear reactors because it enables neutron radiation to activate the structure materials. However, the energy of the fission products is normally below the Coulomb barrier.

¹PKA is normally defined as the first atom that is displaced from its original lattice site after interaction with the radiation, e.g. a neutron. However swift heavy ions or fission fragments are often regarded to be the primary knock-ons oneself.

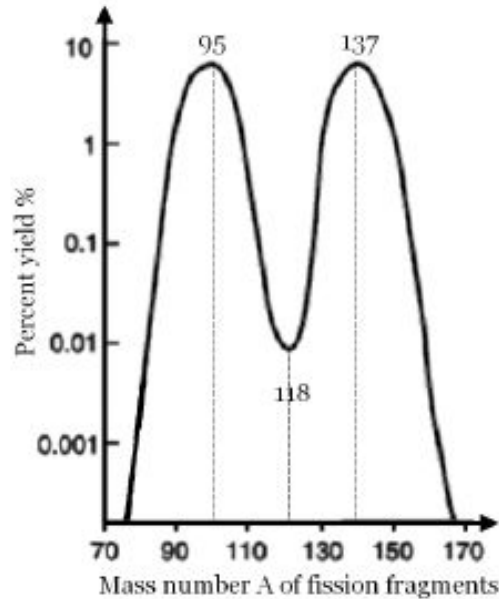


Figure 2.1: Fission fragment distribution after the fission of ^{235}U with thermal neutrons [58].

If the PKA or incoming heavy ion has got an energy bigger than $T \approx 1\text{keV}$, which means $T \gg T_d$, the PKA will slow down over a distance much bigger than the interatomic distances. This process occurs in a very short time in the order of picoseconds. Thereby it creates a so called displacement cascade (DC). [50]. The displacement cascade can be divided into two different stages: First a collision cascade occurs followed by a thermal spike.

In the collision cascade the PKA generates secondary, tertiary and so on recoils inside the lattice. It lasts about 0.1 ps which is less than a typical atomic vibration time. The collisions between the PKA and the target atoms occur rarely, i.e. the trail of the respective secondaries are well separated from each other (compare Fig. 2.2(a)). This stage is also called the ballistic phase and mostly two body collisions occur. At the end of the collision cascade all recoils have slowed down to energies below T_d , so they can not knock on further atoms. The results of a collision cascade are atoms displaced more than one atomic distance from their original lattice site, leaving behind vacancies, i.e. the collision cascade results in the production of Frenkel-pairs.

When the PKA loses energy the cross section for collisions with lattice atoms rises. Below a certain threshold, the trails of the respective secondaries are no longer well separated but the disturbed regions will overlap. Here, the majority of the atoms are displaced and are in violent motion, i.e. the region is heated up and a thermal spike is created. This motion decays in times of order of 10 ps. It has been shown that in the center of a thermal spike temperatures over $2000\text{ }^\circ\text{C}$ are easily reached for about 1-10 ps [52, 55, 59]. Therefore a liquid-like, overheated droplet forms that rapidly solidifies again. The droplet normally recrystallizes according to the surrounding lattice.

This picture is somewhat different from the theory Brinkman suggested 1954 [59], although it uses a similar terminology. Brinkman's theory must be regarded out-dated

today, nevertheless it will be described shortly. According to his model [59] the path of a high-energetic PKA consists of a trail of vacancies and interstitial atoms caused by elastic collisions. As the PKA further loses energy the distance between the single collisions with the lattice atoms decreases. Below a certain energy, the mean free path between displacement collisions is the order of one atomic distance. The disturbed region may now be pictured as a large hole surrounded by a shell of lattice atoms which are surrounded by the interstitials atoms created by the knock-on collisions. The interstitials increase the pressure on the hole and cause the displacement spike to collapse and to recrystallize. This theory provides a model in which atoms may be moved large distances and may be intermixed [60]. Brinkmans displacement spike differs from the thermal spike in the fact, that inside the thermal spike $T < T_d$, so no displacements are possible whereas the displacement spike contains Frenkel pairs [52].

Long cylindrical ion tracks have been observed inside ceramics, polymers, amorphous materials and also some metals after irradiation with ions at an energy bigger than $\approx 1\text{MeV/u}$. These ion tracks start at the sample surface and reach the penetration depth of the ion in the respective material. The ion tracks are caused by the incoming ions that penetrate the target material [61,62]. To explain this effect another model has been developed: In case the incoming ion possesses an energy bigger than $\approx 1\text{MeV/u}$ less than 10% of this energy is dissipated by direct knock-on collisions, mainly at the end of the ion track [63]. Before, the ion is slowed down by “Coulomb-explosions” [57] and electronic stopping due to the interaction with the target atoms electrons. The later effect leads to the formation of a “thermal spike”² along the ion track. Bringa et.al. [64] describe the process as follows: When a high energetic ion enters the target material it interacts with the target atoms electrons. In case the interaction is strong enough, the atoms will be ionized and reject each other due to the Coulomb force. This force produces atomic motion and pushes atoms away from their original lattice site. As the incoming ion has lost some energy the interaction with the target atoms electrons becomes less violently. The electron lattice is set into vibration. The deposited energy is thermalized via electron-electron interactions and transferred to the atomic lattice via electron-atom interactions. It has been shown that this interaction leads to a cylindrical region of $\approx 1\mu\text{m}$ diameter around the path of the incoming ion in which the temperatures rises far above the melting temperature of most materials. Within some ps, this liquid cylinder cools down and a highly disordered track region is quenched in [56,61]. When the ion has lost $\approx 90\%$ of its initial energy, the rest is dissipated by direct knock-on collisions. Here it must be pointed out that so far there is no agreement among different authors concerning the importance of the “Coulomb-explosion” and the thermal spike mechanism on the formation of quenched-in ion tracks [56,64,65]

Mean free path The mean free path for elastic collisions between the PKA and the lattice atoms decreases with decreasing energy. The mean free path depends on the type of interaction potential. In case of charged particle irradiation, fission fragments or PKAs the interaction potential between the moving particle and the lattice atoms

²Although the notation is the same, the “thermal spike” mechanism described here differs somewhat from the one described above

is a screened Coulomb interaction potential [55]:

$$V(r) = \frac{Z_1 Z_2 e^2}{r} \chi(r/a) \quad (2.2)$$

Where $\chi(r/a)$ is a screening function and a is the screening length. In case of the screening function equal to one, i.e. no screening the Coulomb potential is given by:

$$V(r) = \frac{Z_1 Z_2 e^2}{r} \quad (2.3)$$

In this case the scattering cross section is given by

$$\frac{d\sigma}{dT} = \frac{\pi m_1 Z_1^2 Z_2^2 e^4}{m_2} \frac{1}{E_1 T^2} \quad (2.4)$$

Where E_1 stands for the energy of the charged moving particle and T stands for the energy transferred to the recoil. The average recoil energy $\langle T \rangle$ increases only logarithmically with projectile energy:

$$\langle T \rangle = T_{min} \ln \frac{T_{max}}{T_{min}} \quad (2.5)$$

Where T_{min} is the minimal energy needed to create recoils ($\approx 200\text{eV}$) and T_{max} is the maximum possible energy transfer which depends essentially on the mass of the particles.

In case of non-charged particles or very high energetic charged particles the interaction potential is a hard-sphere potential. The scattering cross section in this case is given by

$$\frac{d\sigma}{dT} = \pi \rho_0^2 \frac{1}{T_{max}} \quad (2.6)$$

where ρ_0 is the hard sphere radius and T_{max} is again the maximal possible energy transfer defined by the masses of the colliding partners. The average recoil energy in case of equal masses of the two collision partners is $\langle T \rangle = T_{max}/2$.

The mean free path $l(T)$ between collisions of energy greater than T can be calculated using

$$l(T) = \left[N_0 \int_T^{T_{max}} dT \frac{d\sigma(E, T)}{dT} \right]^{-1} \quad (2.7)$$

The mean free path of fission fragments, swift heavy ions or PKAs with energies bigger than several tens of keV is long compared to interatomic distances. However, most secondary recoils have energies much below the energy of the PKA. They will undergo subsequent collisions close to their original recoil site. The structure of a cascade originating from a high energetic PKA will therefore consist of a string of localized regions containing high defect densities, separated by regions of relatively few defects.

Simulation of radiation damage It has been shown that different kinds of radiation produce in principal the same initial effect inside an atomic lattice, a PKA, even though the initial collision happens at different energies. This being said the question

arises to which extent it is possible to simulate radiation damage of one kind by using radiation of another kind, especially radiation from particle accelerators. This topic is of special technological interest for material science dealing with fast neutron and fission fragment damage since in these cases the materials will be radioactive after the respective irradiation. In case of simulation of fission fragment damage the choice is easy and can be made according to Fig. 2.1: one just has to choose an isotope with a mass and energy typical for fission products. It has been shown before, that it is possible to simulate the damage due to fission fragments using e.g. Iodine at 80MeV from a Tandem accelerator [46].

In case of fast neutron radiation the choice is more complicated. The first intention, replacing 1 MeV neutron radiation by 1 MeV protons, must be wrong since neutrons interact over a hard-sphere potential with the lattice atoms while protons interact over the Coulomb potential. Moreover, the protons are affected by electronic energy loss. It can be shown that it is possible to simulate fast neutron irradiation using heavy ions like e.g. Ni or Au at energies between 1-10 MeV [55].

Irradiation effects Beside the creation of Frenkel-pairs which lead e.g. to creep and embrittlement of irradiated materials two other effects occur upon irradiation: atomic mixing and phase transition [51].

Inside a displacement cascade or thermal spike considerable atomic motion occurs. In consequence, atoms involved will often end up at positions different from their original lattice site. Under the assumption that the displacement cascade or thermal spike occurs at or sufficiently near to the interface of two different materials a phenomenon called cascade mixing or ion-beam mixing is observed. The idea of ion-beam mixing can be easily understood according to the idea of S.T. Konobevsky [66] which will be discussed in more detail on page 32 in section 2.2.2 using Fig. 2.13. The contribution of the ballistic mixing during the collision cascade phase and of the mixing by melting and recrystallization during the thermal spike phase of the displacement cascade can be calculated. It has been found, that mixing occurs primarily during the hot melt phase of the thermal spike. The ballistic effects are much smaller and can be regarded unimportant for the ion-beam mixing. The ion beam mixing increases with mass of the bombarding ion and decreasing melting temperature of the target [51].

Two different types of phase changes can occur during irradiation: Radiation induced amorphization (RIA) and radiation induced disordering (RID). There are two different routes to RID and RIA. The first route is realized with fast ion or fast neutron irradiations. Here, RID and RIA are the result of the very rapid cooling of the liquid spike cores, whereby disorder or amorphous zones are locally quenched. With increasing dose the sample volume fills gradually with these zones until the whole sample becomes amorphous. The second route is realized by irradiation with fast electrons. It is characterized by the continuous accumulation of point defects. This route leads firstly to disordering and, after a critical amount of disorder has been reached, to amorphization of the complete sample. However, at higher temperatures, which is the case for most of the experiments, the irradiation induced point defects start to migrate thermally. Thereby they can restore the original equilibrium phase and so compete with the process of disordering and amorphization.

Under ion irradiation at low temperatures there are two classes of ordered compounds:

one class shows RID, the other class shows RIA. All RID type compounds are ordered solid solutions which disorder thermally at a temperature T_{disord} below their respective melting temperature T_m . The RIA type, on the other hand, is typically represented by intermetallic compounds which remain order up to T_m [51]. For example U_3Si_2 or U_3Si show a RIA behavior when exposed to heavy ion irradiation or fission fragments [67–69]. It has also been observed that the interaction layer that builds up at the interface UMo-Al upon pile irradiation at lower temperatures around 100-150 °C is amorphous [70].

UMo/Al affected by Iodine at 80 MeV In the following paragraph the irradiation of UMo and UMo/Al samples with Iodine127 at 80 MeV (0.63MeV/u) will be discussed. Iodine at 80 MeV is used to simulate the fission product damage. All data presented in this paragraph have been calculated using J.F. Ziegler's SRIM Code [63, 71]. The SRIM code is a Monte Carlo code that “shoots” single ions into a bulk material and follows their trail plus, if needed, the trail of the knock-on atoms until the energy falls below a certain limit - most of the time the energy required to displace further atoms. The SRIM code is therefore a statistical code which means that many ions must be simulated to get accurate average values for e.g. the penetration depth of the ions. It offers two different options for damage calculation:

1. **Ion Distribution and Quick Calculation of Damage:** This option should be used if one does not care about target damage or sputtering. The damage calculated with this option will be quick statistical estimates based on the Kinchin-Pease formalism. The following data will be calculated correctly: Final distribution of ions in the target, ionization energy loss by the ion into the target, energy transferred to recoil atoms, backscattered ions and transmitted ions [63].
2. **Detailed Calculation with full Damage Cascades:** This option follows every recoil until its energy drops below the lowest displacement energy of any target atom. Hence all collisional damage to the target is analyzed. [63].

Thus, most questions can be answered using option one. For the user of the SRIM code it seems to be advised to use option one whenever no detailed knowledge about the final position of the recoils is needed. The processor time required to calculate damage in this case is reduced considerably compared to option two. Thus, option one allows calculations involving more ions which gives better statistical results. For example, it is no problem to calculate the path of 100 000 Iodine ions at 80 MeV inside U8Mo using option one within reasonable time (about 24h) on a normal PC (3GHz Intel CPU). On the other hand, when option two is used, the path of every ion and every recoil is followed and can be stored. The calculation time is much longer and the amount of data stored can become very high. For example calculation of only 1000 Iodine ions at 80 MeV in U8Mo takes more than 24 hours on a normal PC (3GHz Intel CPU). Thereby, some 10 GB of data are produced and stored.

In the calculations presented in the following, most of the time option one has been used. In case option two has been used, it will be indicated. The incoming heavy ion will be considered as the PKA.

Fig. 2.2(a) and 2.2(c) show the path of a single Iodine ion in U8Mo and Al, respectively. A full damage cascade has been calculated. Red indicates the path of the incoming ion while green and blue indicate the path of the recoils. It can be seen that, in agreement with the theory presented above, the incoming ion creates several knock-on zones which are initially separated. The distance of the zone decreases with increasing penetration depth, i.e. with decreasing ion energy. Since the U-atoms are much heavier than the Al atoms and UMo has got a higher density than Al, the range of the knock-on atoms is higher inside Al. For many incoming ions, the recoil of the single events start to superpose each other, compare Fig. 2.2(b) and 2.2(d). Note that the x-axis scale is different in Figs. 2.2. The mean penetration depth inside UMo and Al has been calculated to be $4.96 \mu m$ and $12.8 \mu m$, respectively.

Inside UMo, 89.58% of the incoming particles energy are dissipated by electronic interactions leading to the formation of a recrystallized ion track due to a thermal spike. 10.41% of the initial particle energy are dissipated by the creation of knock-ons. However, only 0.34% of the total energy is used to create permanent interstitial-vacancy pairs while 6.65% of the energy is dissipated by phonons. 6.63% of the total energy loss is due to phonons created by the knock-ons while only 0.02% is due to the phonons created by the incoming particle. 3.45% of the energy are dissipated by the knock-on during electronic interactions (compare Tab. 2.1). The phononic and the electronic energy loss of the knock-ons create a second thermal spike at the end of the ion track during the ballistic phase of the ion stopping. Displacements due to the two different thermal spike mechanism outweigh therefore greatly displacements by direct knock-on collisions.

Inside Al, 92.61% of the total ions energy are directly dissipated by electronic interactions leading to a thermal spike along the ion track. Only 7.35% of the total energy are dissipated by the creation of knock-ons. Here, only 0.16% of the energy are used to create Frenkel pairs. 3.09% of the total energy is dissipated by phononic losses from which 3.06% is due to phononic losses created by knock-ons. Furthermore 4.14% of the energy loss is due to electronic energy loss of the knock-ons. The phononic and electronic losses of the knock-ons lead to a thermal spike at the end of the ion track (compare Tab. 2.1). It can be concluded that also in Aluminum the main mechanism for atomic rearrangement is the thermal spike.

Figure 2.3 shows the penetration depth (a,b), the energy transferred to recoils(c,d) and the electronic stopping power (e,f) inside U8Mo and Al, respectively. It can be seen, that the energy transferred to recoils has got a peak at the penetration depth of the respective material. The energy transferred by electronic interactions decreases with increasing penetration depth in both cases. The maximum stopping power due to ionization is almost a factor of ten higher than the stopping power due to direct collisions: $2800 eV/\text{\AA}$ vs. $300 eV/\text{\AA}$ in case of U8Mo and $1100 eV/\text{\AA}$ vs. $120 eV/\text{\AA}$ in case of Al.

Ion beam mixing occurs at interfaces of type UMo/Al and Al/UMo inside dispersed samples irradiated with heavy ions. However, the first case is by far predominant during in-pile irradiation because the fission fragments are only generated inside the UMo. In this case, Al/UMo mixing only occurs when a second UMo particle is within the range of a fission fragment created in a first UMo particle. To examine the influence of UMo/Al and Al/UMo interfaces on the energy loss behavior of an Iodine ion at 80MeV different double layers have been simulated using SRIM [63]. UMo layers ranging from

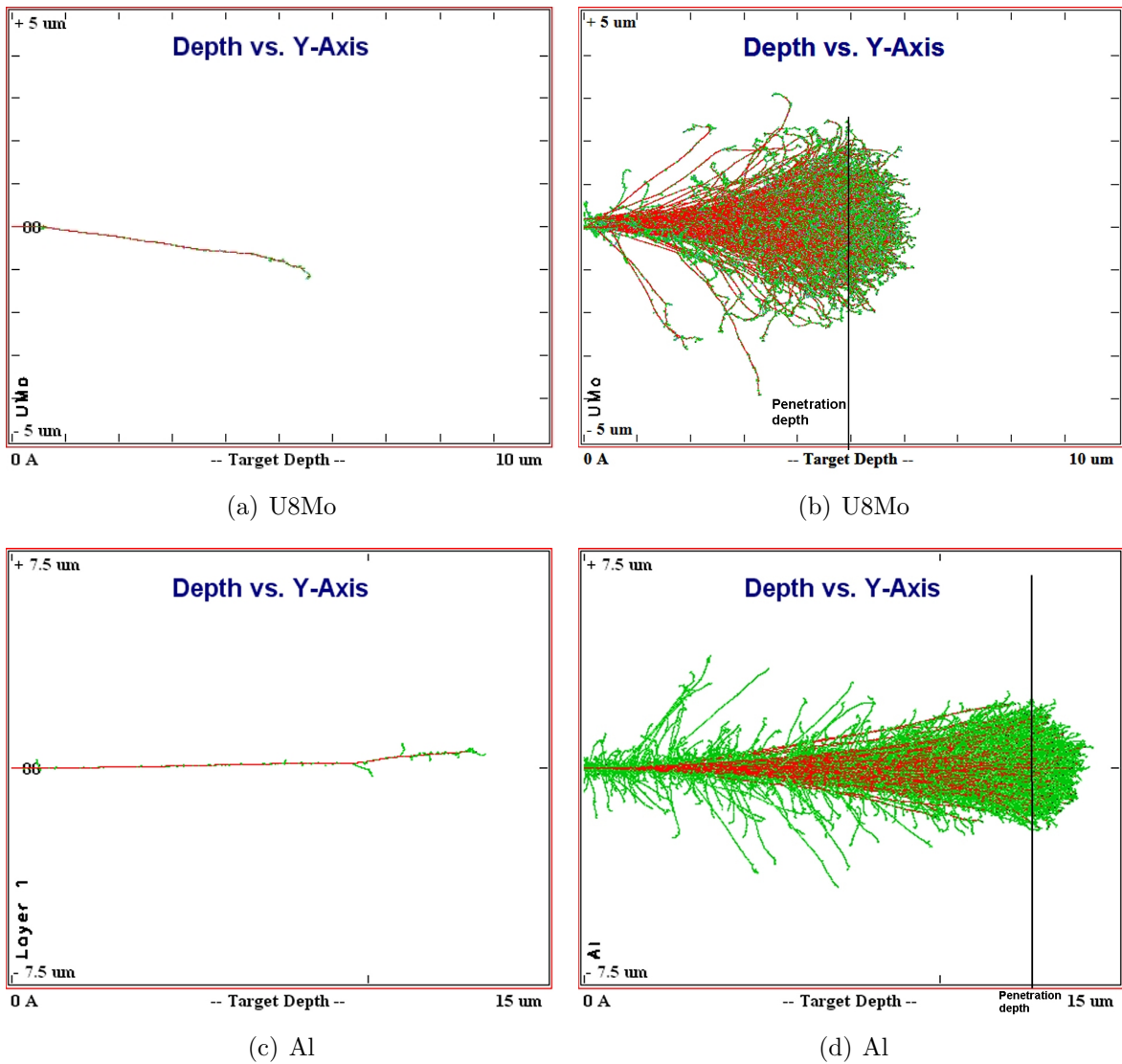


Figure 2.2: Path of one single (a,c) or many (b,d) Iodine atoms at 80MeV through bulk UMo or Al. Red indicates the path of the heavy ion while green and blue indicates the path of the recoiled atoms (Al or U and Mo, respectively). Calculation performed using full damage cascades. The penetration depths for Iodine at 80MeV of 4.96 μm inside UMo and of 12.8 μm inside Al are indicated in the pictures [63].

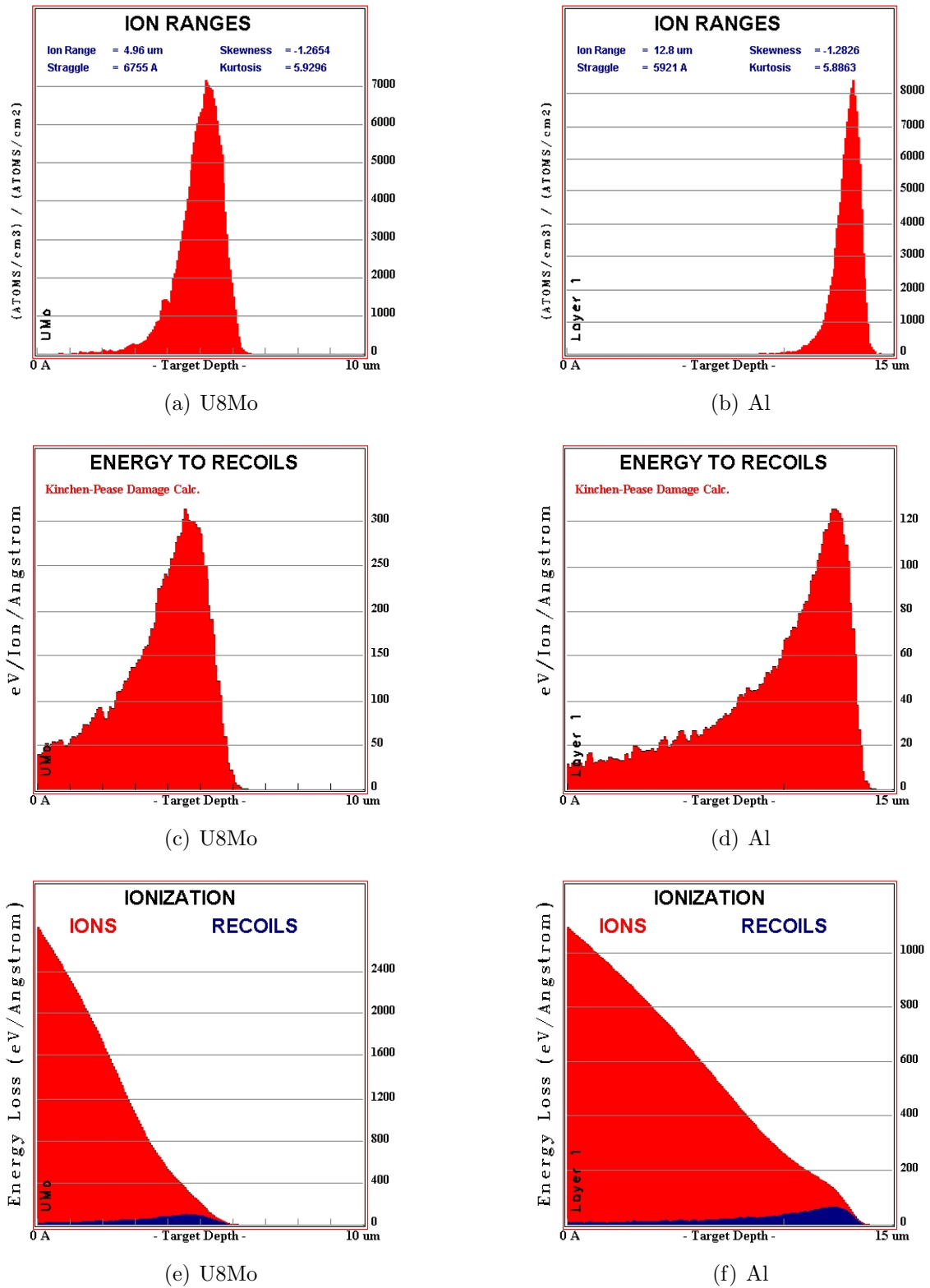


Figure 2.3: Ion range (a,b) energy loss to recoils (c,d) and electronic energy loss (e,f) inside U8Mo and Al [63].

0.5 μm to 6 μm on Al and Al layers ranging from 6 μm to 13 μm have been examined. The energy loss behavior for both cases together with pure UMo and pure Al is shown in Tab. 2.1. In both cases the values of the energy loss behavior with increasing layer thickness lie between the values of the two pure materials, respectively. Figure 2.5 and 2.6 shows the energy transferred to recoils and the phononic energy loss in UMo/Al layer systems of 3 μm , 4 μm and 5 μm thickness(a-c) and of Al/Umo layer systems of 6 μm , 11 μm and 13 μm thickness (d-f). In case of UMo/Al layers the energy transferred to recoils and the phononic energy loss shows always a peak at the interface UMo/Al on the UMo side and drops of on the Al side. In the case of Al/UMo layers the phononic energy loss is rather low at the interface on the Al side but there is a peak short after the interface on the UMo side. It can therefore be concluded that a considerable amount of energy is deposited at or near the UMo/Al and Al/UMo interface, respectively. Over 95% of the energy transferred to recoils is dissipated by electronic interactions or by phonon creation. This leads to the formation of thermal spikes which in turn lead to diffusion between UMo and Al at the interface.

Figure 2.4 shows the direct electronic energy loss of the incoming ion for the respective layer system. Over 90% of the total ions energy are dissipated by this mechanism. It can therefore be expected that a long thermal spike along the track of the incoming ion will occur. The energy deposited in this spike will further drive the UMo/Al diffusion. As a conclusion the thermal spike process will lead to diffusion between UMo/Al or Al/UMo interfaces affected by fission fragments or swift heavy ions. The phononic and electronic energy loss outweighs by far the energy loss due to displacements. However, it must be noted that SRIM does not calculate atomic rearrangement due to thermal spikes. Only single atomic displacements due to knock-on collisions can be calculated and stored. However, these rearranged atoms are not regarded in the further simulation which means that each simulated ion enters a "fresh" target. It is therefore not possible to calculate the build-up of a diffusion layer at material interfaces without further knowledge of the dose dependent diffusion constants. These constants must be determined experimentally.

Table 2.1: Results of the calculation of Iodine at 80MeV into U8Mo, Al and different U8Mo/Al layer systems [63].

System	Penetration Depth [μm]	Percentage of energy loss [%]									
		Ions			Recoils			Total			
		Ionization	Frenkel Pairs	Phonons	Ionization	Frenkel Pairs	Phonons	Frenkel Pairs	Phonons	Recoils	Total
U8Mo	4.96	89.58	0.01	0.02	3.45	0.33	6.63	0.34	6.65	10.41	
Al	12.8	92.61	0.01	0.03	4.14	0.15	3.06	0.16	3.09	7.35	
0.5 μm U8Mo15 μm Al	12.0	92.53	0.01	0.03	4.13	0.15	3.15	0.16	3.18	7.43	
1 μm U8Mo14 μm Al	11.1	92.43	0.01	0.03	4.12	0.16	3.25	0.17	3.28	7.53	
2 μm U8Mo13 μm Al	9.53	92.19	0.01	0.03	4.07	0.17	3.54	0.18	3.57	7.78	
3 μm U8Mo12 μm Al	7.95	91.77	0.01	0.03	4.03	0.19	3.98	0.20	4.01	8.20	
4 μm U8Mo11 μm Al	6.54	91.08	0.01	0.02	3.86	0.23	4.79	0.24	4.81	8.88	
5 μm U8Mo10 μm Al	5.36	90.00	0.01	0.02	3.61	0.30	6.07	0.31	6.09	9.98	
6 μm U8Mo9 μm Al	4.97	89.60	0.01	0.02	3.44	0.33	6.61	0.34	6.63	10.38	
6 μm Al9 μm U8Mo	8.69	90.08	0.01	0.02	3.53	0.30	6.06	0.31	6.08	9.89	
8 μm Al7 μm U8Mo	9.91	90.48	0.01	0.02	3.57	0.28	5.64	0.29	5.66	9.49	
10 μm Al5 μm U8Mo	11.1	91.10	0.01	0.03	3.71	0.24	4.92	0.25	4.95	8.87	
11 μm Al4 μm U8Mo	11.7	91.67	0.01	0.03	3.69	0.21	4.39	0.22	4.42	8.29	
12 μm Al3 μm U8Mo	12.2	92.16	0.01	0.03	3.86	0.18	3.76	0.19	3.80	7.80	
13 μm Al2 μm U8Mo	12.7	92.57	0.01	0.03	4.06	0.15	3.17	0.16	3.20	7.38	

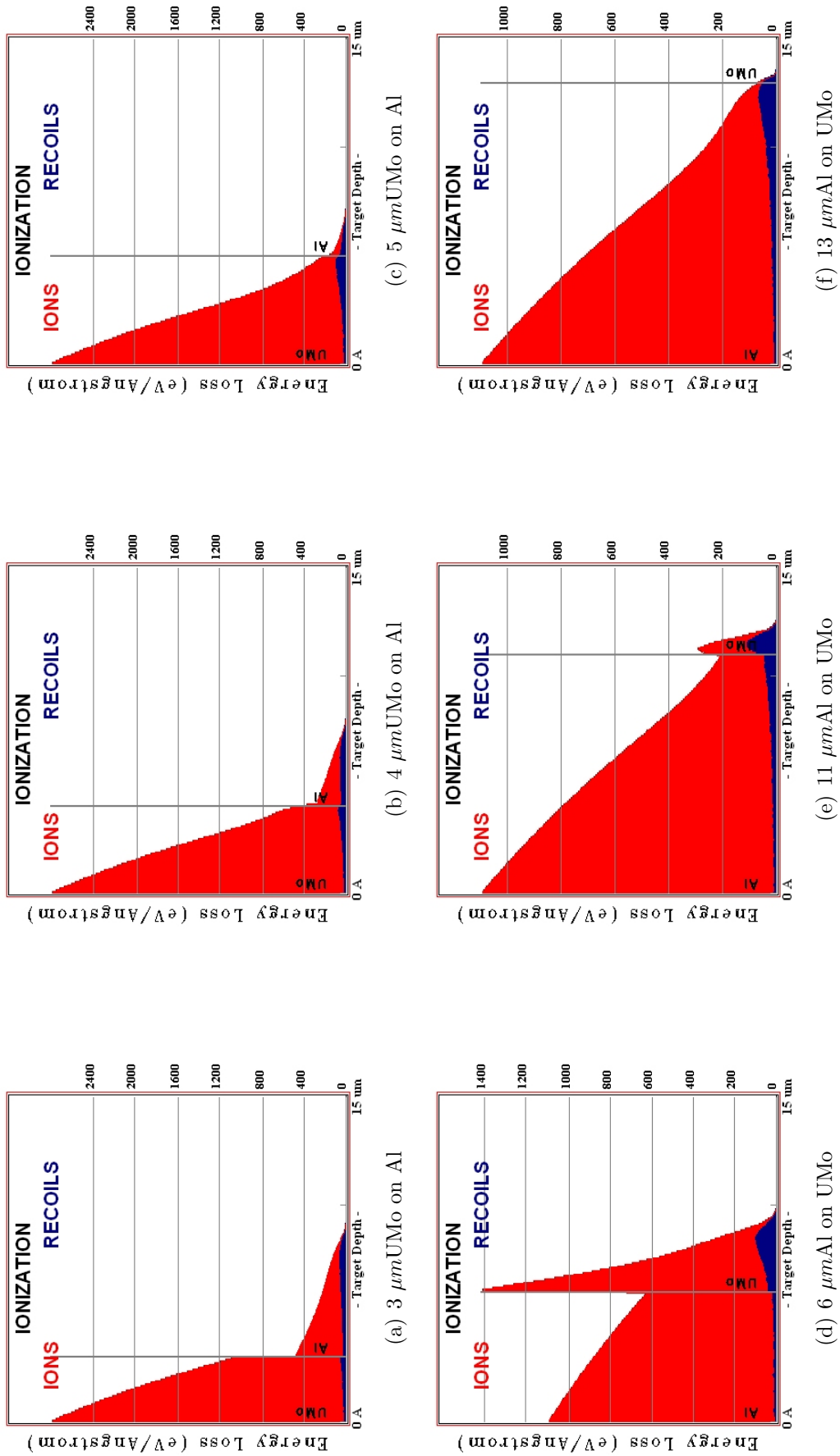
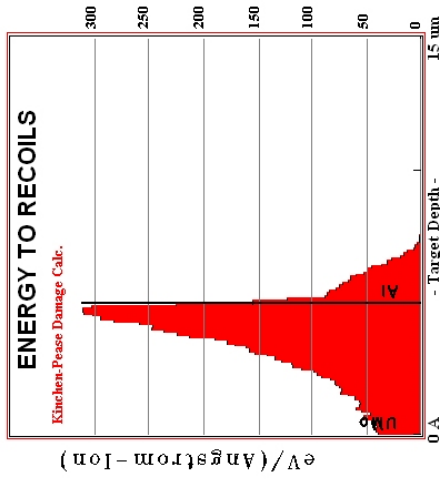
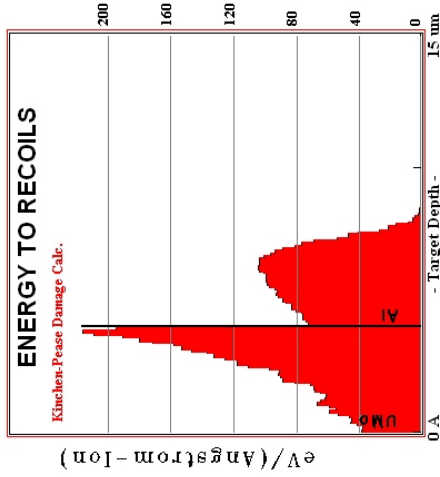


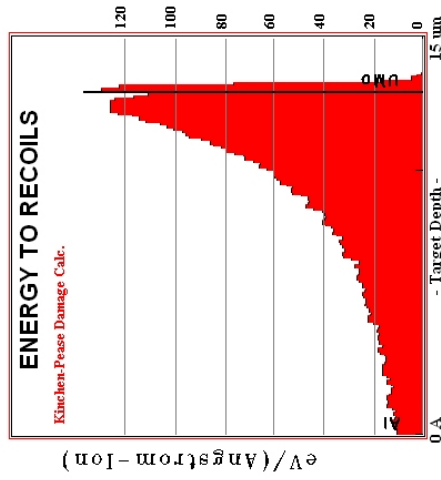
Figure 2.4: Electronic energy loss in UMo/Al (a-c) and Al/UMo (d-f) layer systems of different thicknesses.



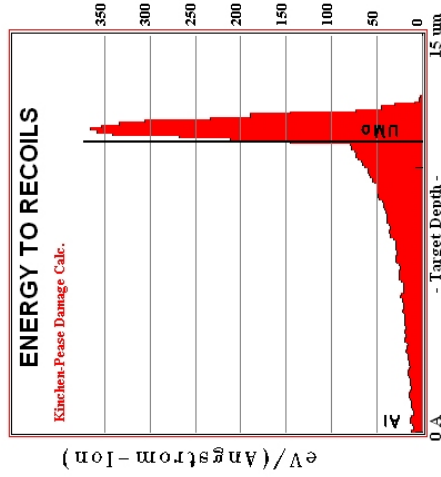
(a) 3 μm UMo on Al



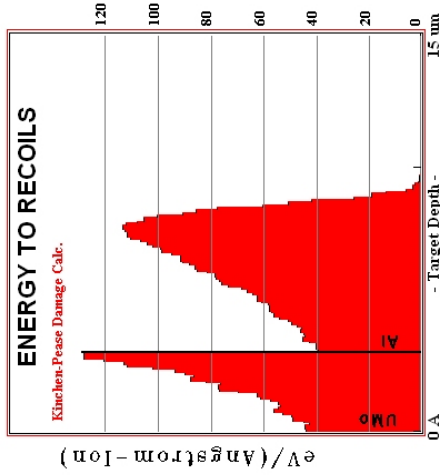
(b) 4 μm UMo on Al



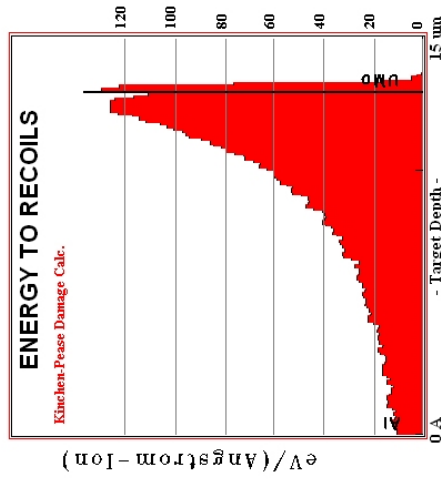
(c) 5 μm UMo on Al



(d) 6 μm Al on UMo



(e) 11 μm Al on UMo



(f) 13 μm Al on UMo

Figure 2.5: Energy transferred to recoils in UMo/Al (a-c) and Al/UMo (d-f) layer systems of different thicknesses.

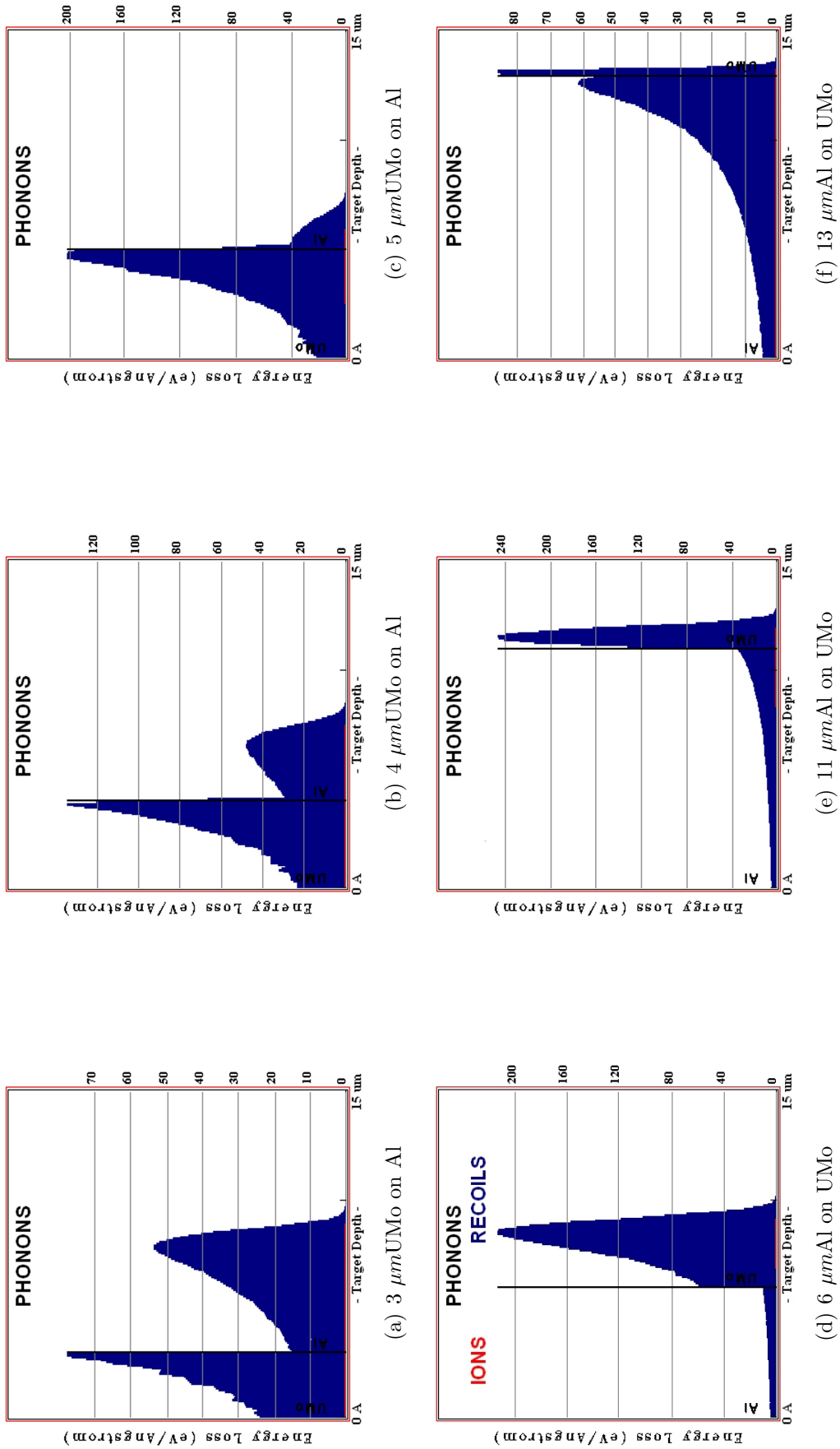


Figure 2.6: Phononic energy loss in UMo/Al (a-c) and Al/UMo (d-f) layer systems of different thicknesses.

2.2 Uranium and uranium alloys - Phase behavior

This section aims at presenting an overview of the different phases and phase transitions occurring in pure uranium and uranium alloys. In the following discussion the phase nomenclature introduced by Lehman and Hills [72] will be used, avoiding the alphabetic subscripts whose primary function is to distinguish between morphologically different variants of a phase [49, 73]. Some crystallographic parameters of pure uranium and different uranium alloys and compounds together with the terminology used in this work have been summed up in table 2.2.

2.2.1 Pure uranium

Pure uranium metal occurs in three allotropes between room temperature and the melting point at 1132 °C: the α -phase has got an orthorhombic structure and is stable up to 667 °C. It possesses four atoms per unit cell, the space group symbol is Cmcm (compare Fig. 2.7(a)). The lattice parameters are $a=2.852 \text{ \AA}$, $b=5.865 \text{ \AA}$ and $c=4.945 \text{ \AA}$ with thermal expansion coefficients of $35.6 \cdot 10^{-6}/^{\circ}\text{C}$, $-8.4 \cdot 10^{-6}/^{\circ}\text{C}$ and $31.6 \cdot 10^{-6}/^{\circ}\text{C}$ for the main axis, respectively. It is noteworthy, that, while the a and c parameters increase with temperature, the b parameter decreases. This anisotropic expansion is also important in explaining the growth of fine-grained highly textured uranium during thermal cycling between room temperature and $\approx 500-600^{\circ}\text{C}$, compare Fig.2.8³ [22, 27, 73–79].

From 667 °C up to 775 °C the β -form of uranium exists. It is tetragonal with 30 atoms per unit cell (compare Fig. 2.7(b)). For the space group, 3 candidates have been suggested between 1948 and 1971: $P4_2nm$, $P\bar{4}n2$ and $P4_2/mnm$ [79–83]. The precise space group could not be determined until 1988 by Lawson who used neutron instead of X-ray scattering. He concluded that the space group is $P4_2/mnm$ with lattice parameters of $a=b=10.7589 \text{ \AA}$ and $c=5.6531 \text{ \AA}$ at 682 °C. For a and b the thermal expansion coefficient is $23.6 \cdot 10^{-6}/^{\circ}\text{C}$, for c it is $10.4 \cdot 10^{-6}/^{\circ}\text{C}$ [84].

The high-temperature γ -phase of uranium is stable from 775 °C to the melting point at 1132 °C. It has got a simple body-centered cubic structure (compare Fig. 2.7(c)) with a lattice parameter of $a=b=c=3.49 \text{ \AA}$ at 800 °C. Extrapolated to room temperature, a lattice parameter of $a=b=c=3.474 \text{ \AA}$ has been calculated. The space group symbol is $Im\bar{3}m$. The thermal expansion coefficient is $21.6 \cdot 10^{-6}/^{\circ}\text{C}$ [22, 27, 73, 77, 79, 84–86]. At temperatures below 43K the α -phase exhibits a charge-density-wave distortion [84, 87]. However, since such a low temperature does not occur in-pile, this phase transition is of minor interest for this study.

2.2.2 Uranium alloys

This section aims in presenting the phases and phase transitions occurring in alloys of uranium with different metals. The alloy system can be roughly classified as follows [90]:

³Although the growth of uranium during irradiation (compare Fig. 1.2) and during thermal cycling lead to the same net result, the two effects are considerable different at a microscopic scale. The two effects have been compared by Holden in his textbook *Physical Metallurgy of uranium*, chapter 12 [27].

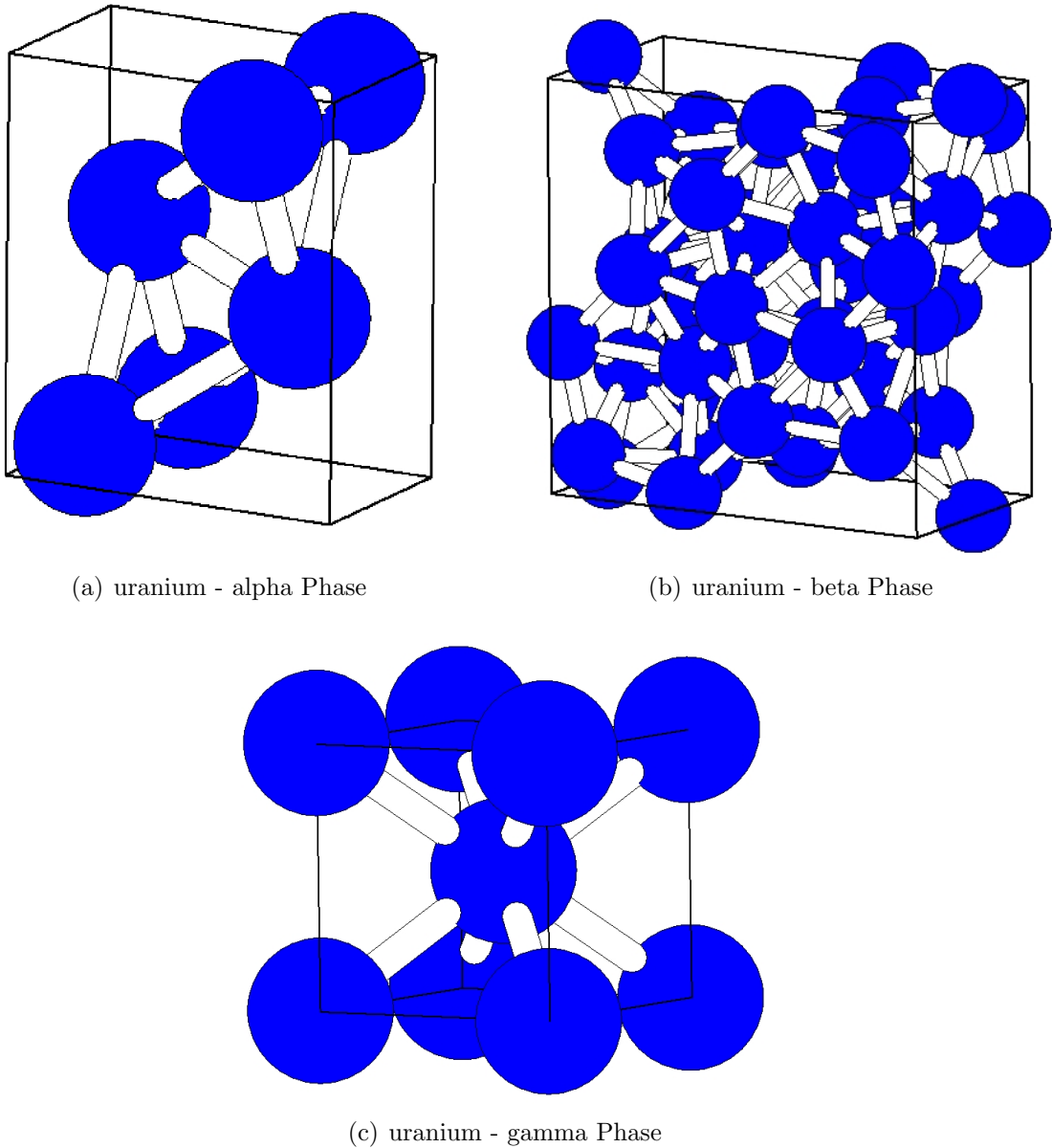


Figure 2.7: The three figures show sketches of the three phases of pure uranium. Figure 2.7(a) shows the orthorhombic low temperature α -phase of uranium which is stable up to 667 °C.

Figure 2.7(b) shows the complex tetragonal structure of β -uranium which is stable between 667 °C and 775 °C.

At temperatures higher than 775 °C up to its melting point at 1132 °C uranium is present in its body-centered cubic γ -phase (figure 2.7(c)) [22, 74–76, 79, 88].



Figure 2.8: Growth of a highly textured, fine grained α -uranium rod during thermal cycling. After 300 cycles from 50 °C to 550 °C the rod grew from 5 cm to 30 cm length [89]. The scalebar shown in the picture is in inch.

- *Compound free systems.* This group includes alloys of Mg, Ca, Ag, Na, Ta, Ce and some others. The common feature of these elements is the low miscibility with uranium. Indeed, the maximum solubility of these elements in uranium is <1 at% for all of the three uranium allotropes. To the authors best knowledge no intermetallic compounds form between uranium and members of this group of elements.
- *Low-miscibility systems with intermetallic compounds.* The common feature of these elements is again their low (<1 at%) solid solubility inside uranium. Nevertheless, they tend to form stoichiometric compounds of the UX_2 , UX_3 , U_6X and UX type. The most important elements in this group are Al and Si, but also Be, Bi, Fe, Mn, Ni and some others show this behavior. While all of the UX_3 compounds possess a face-centered cubic structure like $AuCu_3$, the compounds of type UX_2 form either the cubic zincblende structure (UMn_2 , UFe_2) or the hexagonal wurtzite structure (UNi_2). A similar behavior is not observed for the U_6X and UX type compounds.
- *Highly gamma-miscible systems.* The solubility of elements of this group inside γ -U is in general higher than 10at%. They are characterized by stabilizing the high-temperature γ -U structures at room temperature. For example an alloy of Mo with U retains the γ -phase of uranium at room temperature between 4.5 and 15.5 wt%Mo addition to the uranium. Ti, Nb, Zr, Ru, Re, Rh and many other transition metals behave in a similar way. These alloys are of considerable interest in reactor fuel element technology since they possess a good resistance to dimensional changes during thermal cycling and irradiation. Furthermore their resistance to aqueous corrosion and diffusion mechanisms is higher than for pure uranium [23, 91]. Especially the UMo alloy with 7-12 wt%Mo has been used as a metallic fuel in high-temperature reactors [92]. Recently, interest in this alloy renewed as it is a possible candidate for a future high-density fuel for research and test reactors operating at low temperatures (≈ 100 °C).

Here uranium-molybdenum alloys will serve as a model system for the phase behavior of highly gamma-miscible systems. Other systems, e.g. the U-Nb-Zr system have been reviewed elsewhere [73, 93]. The low-miscibility systems, the compound free systems and in general the metallurgy of uranium and uranium alloys have been discussed before [27, 73, 74, 90, 94].

Representative for all highly γ -miscible systems the uranium-molybdenum equilibrium

phase diagram is shown in Figure B.9. Alloys containing up to 30 at% of Mo form solid solutions of two different phases as the temperature and/or the alloy content are increased. For example at equilibrium conditions at room temperature for an U10at%Mo alloy a mixture of α -uranium plus a δ -phase, which is U_2Mo , is expected. In contrast, uranium alloys quenched from the γ -phase region to room temperature, i.e. in a non-equilibrium state, show a sequence of crystal structures as the alloy content is increased [95, 96]. The sequence progresses from $\alpha \rightarrow \beta \rightarrow \alpha' \rightarrow \alpha'' \rightarrow \gamma^\circ \rightarrow \gamma \rightarrow \delta$ [97–99].

Here

- α' is a distorted state of the orthorhombic α -phase that forms martensitically and is characterized by the contraction of the b_0 lattice parameter [72, 100].
- α'' is a monoclinic distortion of α' . The main feature is the further contraction of the b_0 parameter, the slight expansion of the a_0 and c_0 parameter and the increase of the γ angle from 90° to values between 90.5 and 93° [100–103].
- γ° is a bc-tetragonal distortion of the bc-cubic γ -phase. The main feature of this phase is the approximate doubling of the a_0 and b_0 lattice parameter compared to the lattice parameter of the γ -phase: $a_{\gamma^\circ} \approx 2 \cdot a_\gamma$ and $c_{\gamma^\circ} \leq c_\gamma$. The space group symbol is P4/nbm. The lattice structure is depicted in Figure 2.9 [101, 102, 104–106].
- the δ -phase is often also denoted ϵ or γ' , the latter because of its similarity to the γ -phase. Normally the intermetallic compounds of uranium in the highly γ -miscible systems are called δ -phase. These compounds must not be mixed up with the intermetallic compounds that form in the low-miscibility systems, e.g. UAl_2 or UAl_3 for which, however, often the same nomenclature is used. In the highly γ -miscibility systems several prototypes of intermetallic compounds exist:
 - *The U_2Ti system with hexagonal unit cell:* Beside titanium zirconium (UZr_2), hafnium(UHf) and mercury(UHg_2) belong to this group. The space group symbol is P6/mmm [73, 107–109].
 - *The U_2Ru system with monoclinic unit cell:* The lattice parameters of this phase are $a=13.106 \text{ \AA}$, $b=3.343 \text{ \AA}$, $c=5.202 \text{ \AA}$, $\beta = 96^\circ 9.6'$, the space group is either P2/m or P2₁/m [110].
 - *The U_2Re system:* To the authors best knowledge, the crystal structure of U_2Re is still unknown. However apparently it is related to the γ -U phase: XRD diagrams on alloys that are believed to be pure U_2Re showed a displacement of the γ -reflections towards higher θ -values and a splitting into two or more reflections. The displacement of the peaks indicates a contraction of the unit cells while the line splitting indicates a deviation from the bcc structure towards more complicated systems [88, 99].
 - *The U_2Mo system with tetragonal unit cell:* This intermetallic compound is stable in the range of 30–35 at% Mo. The space group symbol is I4/mmm. The lattice parameters reveal a high similarity to the γ -phase: $a_\delta = 3.427 \text{ \AA} \approx a_\gamma$ and $c_\delta = 9.834 \text{ \AA} \approx 3 \cdot a_\gamma$ [73, 111–113]. It is noteworthy that this phase

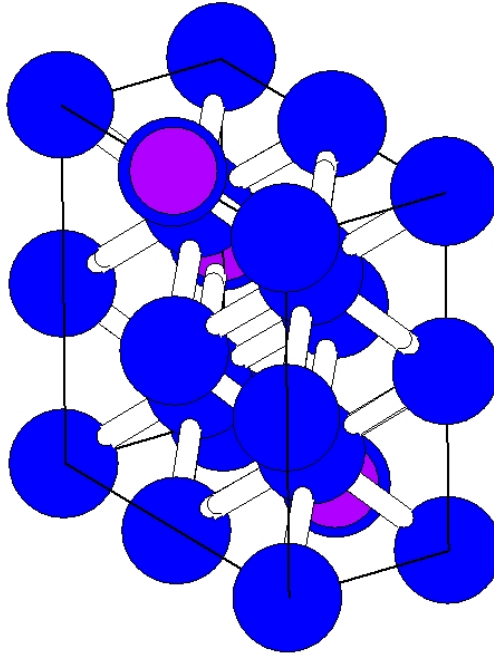


Figure 2.9: Tetragonal disordered γ° -phase of U10wt%Mo. Blue balls indicate the position of U-atoms, purple balls indicate the position of Mo-atoms. Note that the Mo atoms are statistically distributed in the lattice [88, 115].

transforms to a randomly ordered γ solid solution upon bombardment with thermal neutrons [114]. This effect will be discussed later in more detail.

Not every of these phases occurs in all highly γ -miscible uranium alloy systems at room temperature, e.g. no intermetallic U-Nb compound exists [116] or the α' -phase does not occur in the U-Ru system.

The occurrence of the single phases depends on the alloying element, on the at% of element addition to the uranium, on the cooling rate (in Kelvin/sec.) from the γ -phase temperature regime and also on the temperature at which the cooling started.

The sequences of the metastable phases occurring at room temperature in different quenched uranium alloys are depicted in Figure 2.10 and summed up in table 2.2. The composition limits for the occurrence of the single phases given here depend strongly on the experimental procedure. Therefore, the values may vary slightly when comparing different literature resources, e.g. [73, 74, 102, 117].

All of these phases, with exception of the δ -phase intermetallic compounds, are metastable and will readily decompose into phases closer to the thermal equilibrium. The decomposition can be induced by different procedures, typically mechanical working or heating to 300-500 °C. For example the metastable β -phase in the U-Ru system decomposes into α' when stresses as during mechanical polishing are induced [96]. It has been also observed, that γ -U20at%Mo decomposed into γ° upon a sequence of hot and cold rolling work [104]. The decomposition of the retained γ -phase in the UMo system upon annealing will be discussed in more detail since it affects the behavior of the UMo fuels that are regarded in this thesis.

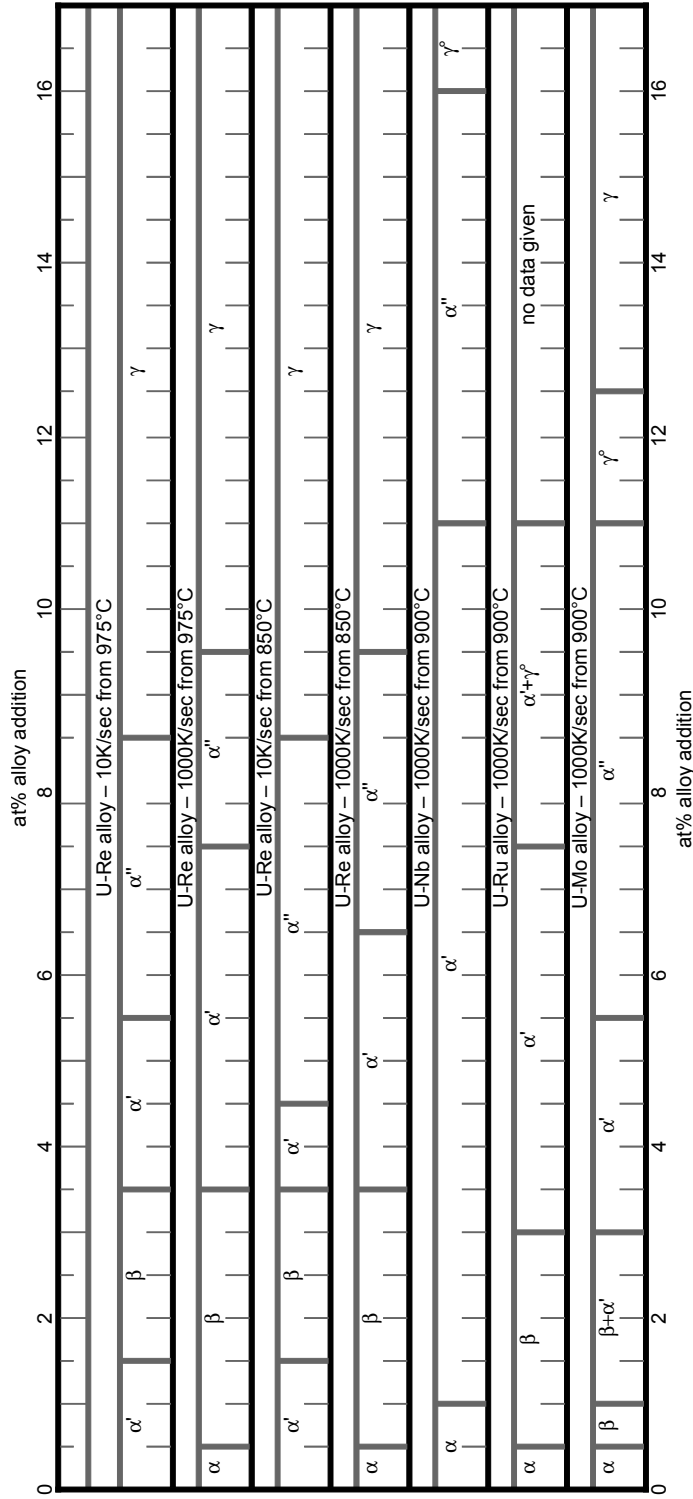


Figure 2.10: Sequences of different metastable phases observed at room temperature in different quenched uranium alloys. Diagram has been redrawn according to [97]. Data on U-Nb [95], U-Ru [96] and U-Mo [101] have been added.

It has been shown that it is possible to fully retain the high-temperature bcc γ -phase at room temperature if the alloy content is high enough. This is, for example, the case with an alloy of at least U12.74at%Mo⁴ quenched from 900° to room temperature inside water. Three different empirical formulas have been found in literature which allow to calculate the bcc γ -UMo lattice parameter at room temperature from the Mo content in at%.

An internal CEA report suggests the following formula [118]:

$$a(\text{\AA}) = 3.4878 - 0.0034[\text{Mo}](\text{at}\%) \quad (2.8)$$

On the other hand, A.E. Dwight suggested [112]:

$$a(\text{\AA}) = 3.4808 - 0.00314[\text{Mo}](\text{at}\%) \quad (2.9)$$

Third, S.T. Konobeevsky found [119]

$$a(\text{\AA}) = 3.481 - 0.00333[\text{Mo}](\text{at}\%) \quad (2.10)$$

Comparing the results obtained from the three different formulas the error can be estimated to be 0.5%.

The bcc γ -UMo phase is metastable and decomposes into the thermal equilibrium phases which are a mixture of α -U and U₂Mo [120]. Figure 2.11 shows the time-temperature transformation (TTT) diagram of a U10wt%Mo alloy. The diagram shows the phases occurring with time during the decomposition of the U10Mo. Below the critical temperature of U10Mo at 575 °C the decomposition is relatively complex. It involves several different reaction mechanisms which are separated by so called “C-curves” . Since during the production of typical UMo/Al fuel plates not too high temperatures are involved (max. 500°) to avoid strong UMo/Al interaction only the low temperature reactions will be regarded here. The topic has also been reviewed by D. Blake and R.F. Hehemann in “Transformation of uranium base alloys” [74].

At temperatures of 375-575 °C the decomposition is initiated by a cellular reaction in which γ -UMo decomposes austenitically into α -U plus γ -UMo enriched in Mo. As the reaction progresses, the γ -UMo is further enriched in Mo until U₂Mo (denoted γ' in Figure 2.11) occurs. The thermal equilibrium is reached when all of the γ -UMo has been transferred into α -U plus U₂Mo after at least 500 hours. Figure 2.12 gives an example for this reaction at 550 °C. This transformation occurs primarily at grain boundaries and consumes bit by bit the complete γ -phase. It is noteworthy that the cells consist initially of α -U and Mo enriched γ -UMo rather than α -U and U₂Mo which occurs during normal eutectoid reactions [122].

At temperatures below 375 °C no signs of the transformation are visible upon metallographic optical inspection (e.g. by using polarized light microscopy). However, X-ray diffraction studies show that the decomposition starts with the formation of U₂Mo. It occurs homogeneously inside the entire UMo grains. Later, in addition to γ -UMo and U₂Mo α -U forms. Also this stage of the reaction can not be revealed by optical inspection. Again, the decomposition is completed when only the thermal equilibrium products are present: α -U and U₂Mo. Depending on the annealing temperature, this

⁴The Mo content must not exceed 30 at%. Otherwise, U₂Mo will form. The samples regarded in this thesis normally contain around 20 at% Mo.

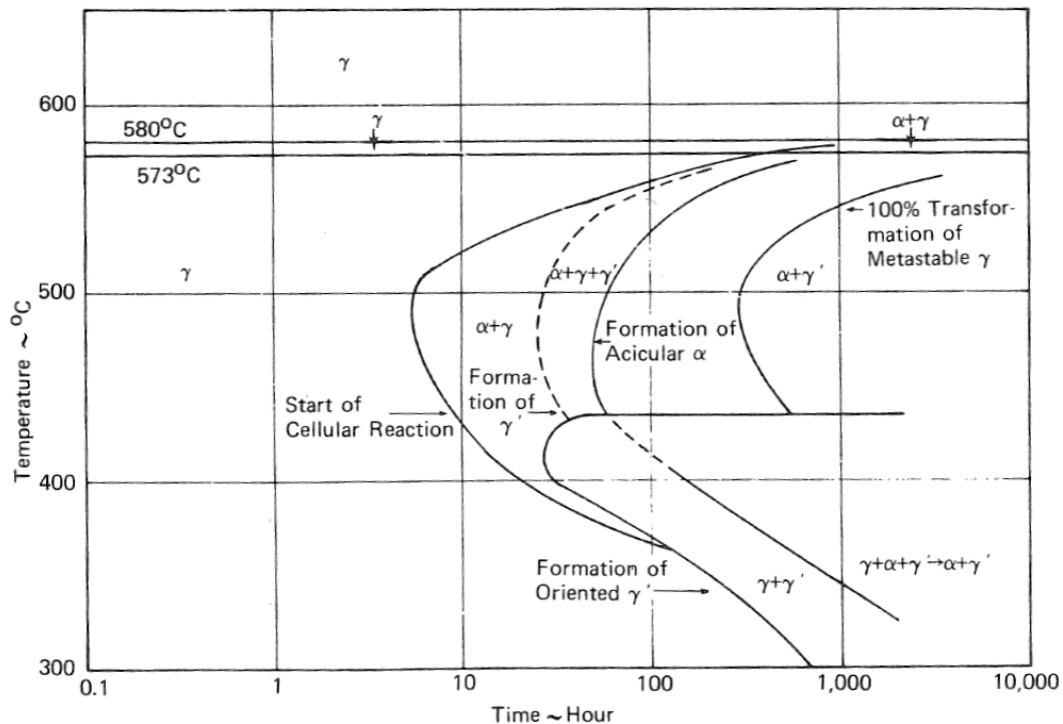


Figure 2.11: TTT diagram showing the decomposition kinetics of the γ -phase of the U10wt%Mo alloy [74, 121].

will not happen before some thousand hours of heating.

At temperatures between 375 °C and 450 °C both mechanisms occur: the cellular and the low temperature mechanism. The decomposition starts with the cellular reaction. However this reaction stops as the γ -UMo is transformed into a uniform mixture of γ UMo and U_2Mo by the low temperature mechanism [74, 123].

It has been observed by Russian [124] and US-American [60] groups already in the mid-fifties of the last century that a mixture of α -U+ γ -UMo or α -U+ U_2Mo is transformed into γ -UMo during pile irradiation. The effect occurs at low irradiation temperatures around 200 °C [60] as well during irradiation at high temperature between 600 °C and 800 °C. It has been found that the effect depends on the fission rate at high temperatures above 600 °C. However, at low temperatures it does not [24]. This fact can easily be understood: during irradiations at high temperatures the decomposition of γ -UMo into α -U and U_2Mo and the formation of γ -UMo from α -U and γ -UMo due to irradiation compete with each other.

J. Bloch observed during irradiation of a mixture of α -U and U_2Mo that the cell parameter of the U_2Mo is continuously shifted towards the cell parameter of γ -UMo with increasing burn-up. The U_2Mo phase and the γ -UMo phase have not been observed at the same time. Therefore, the phase transformation occurs to be continuously [114].

V.D. Dmitriev examined this phase transformation on UMo alloys containing between 0 and 8.95 wt%Mo after irradiation between 100 and 200 °C and an integral neutron

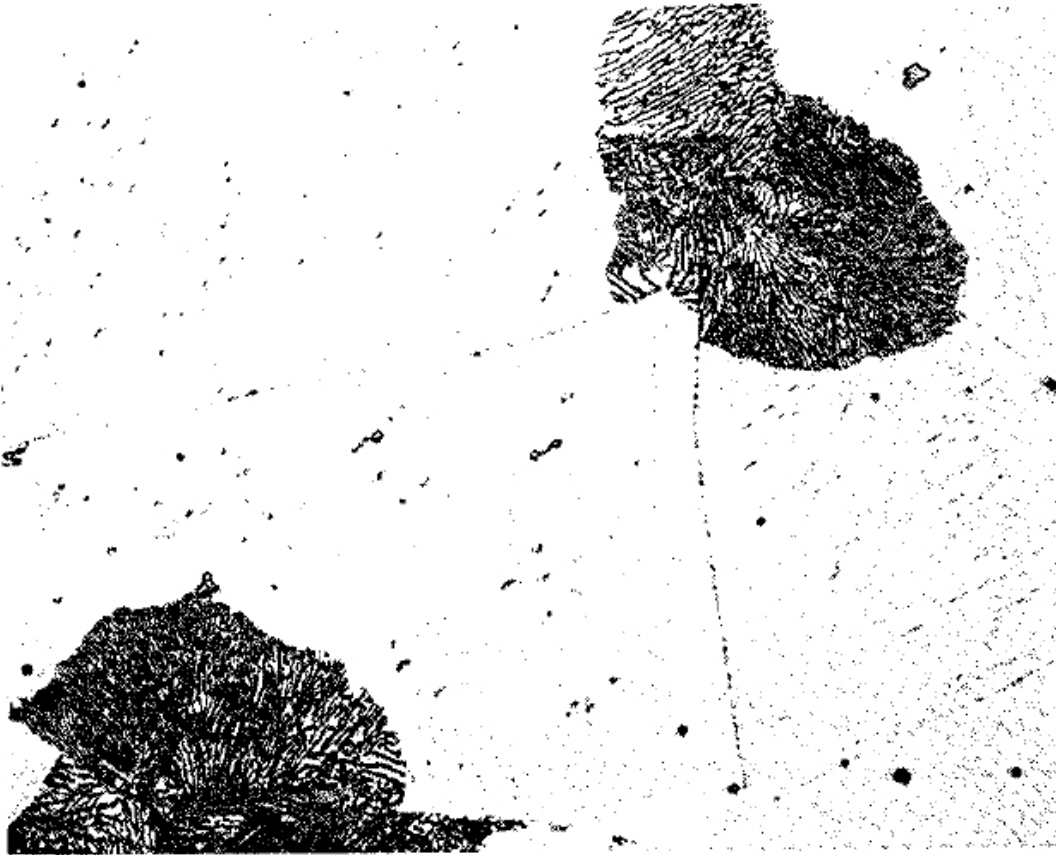


Figure 2.12: Cellular decomposition product in a U10Mo alloy annealed for 240 hours at 550 °C [74].

flux between 0.5 and $1.0 \cdot 10^{20}$ neutrons/cm². At alloy compositions between 0 and 1.02 wt%Mo no change of the phase composition before and after irradiation was measurable. In case of pure γ -retained UMo (7.0 and 8.95 wt%Mo) no change inside the γ -UMo phase was measurable after irradiation. The other cases present before irradiation, α -U plus γ -UMo, α U+U₂Mo and α t, all ended up in being transformed into a mixture of α -U plus γ -UMo. The Mo content of the γ -UMo phase after irradiation was lower than the Mo content of the γ -UMo or the U₂Mo before irradiation. It can therefore be concluded that γ -UMo has formed during irradiation on cost of α -U [125]. Two different explanations for this phenomenon have been suggested by S.T. Konobeevsky [66, 126, 127] and by M.L. Bleiberg [60]. Both base on the theory of radiation damage inside metals initially developed by Seitz [52–54] and Brinkman [59] (compare section 2.1). The two different explanations will be discussed briefly: On the one hand, S.T. Konobeevsky [66, 126, 127] argued in 1956 that the phenomenon of phase reversal during irradiation results from the kinetic energy of the two fission fragments produced during irradiation. According to him, the path of the fission fragments through the crystal lattice can be divided into two regions [59, 66]: An initial thermal spike along the trace of the PKA (in this case a fission product) which is followed by a displacement spike. Here, a region of $0.6 - 1.0 \cdot 10^{-15}$ cm³ can reach a

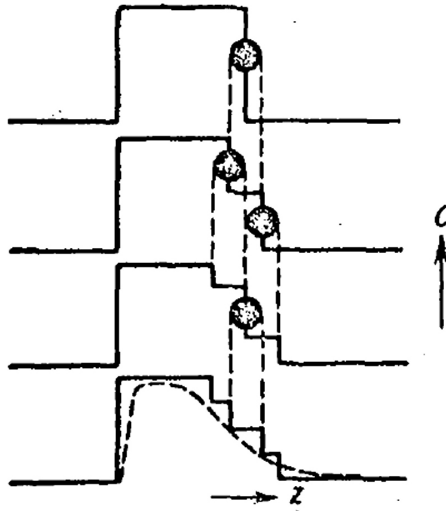


Figure 2.13: Schematic of the diffusion that takes place under the influence of the “thermal spikes” (circles) caused by a fission event [66].

temperature of more than 2000 °C for a time period of $\approx 1 \cdot 10^{-10}$ due to the thermal spike mechanism. During this time period, the atoms inside the thermal spike region are heavily intermixed and will solidify in the original lattice surrounding the thermal spike. If a fission event takes place at the boundary between the α -U and the U_2Mo , a material average is established throughout the region of the thermal spike. Since the heat is carried away from the region of the thermal spike in a very short time the occurrence of a spontaneous center of crystallization in the thermal spike region is very unlikely. The spike region therefore crystallizes in the structure of one of the neighboring lattices. It can thus crystallize either in the form of a supersaturated α -like UMo alloy, or in the form of U_2Mo . With increasing number of spikes the average composition is smoothed out (compare Fig. 2.13). In our case the concentration of the Mo inside the U_2Mo will gradually be reduced and the concentration inside the α -U will increase. In the U_2Mo region, the reduced molybdenum concentration causes an unstable U_2Mo -phase which transforms into γ -UMo. If the Mo concentration in the region of the α -phase reaches a value close to 10 at% it will be unable to crystallize in the α -phase. Therefore the γ -phase occurs. This effect increases with the integral dose until a complete homogeneous solid solution will have developed.

On the other hand, M.L. Bleiberg took the idea of the displacement spike out of Brinkmans model and adapted it: a displacement spike occurs at the end of the trail of a fission fragment through the crystal lattice [59, 60]. After the original particle slows down and its free path becomes comparable to the interatomic spacing, the energy loss to collisions increases so much that all the remaining energy of the particle is set free at once, being distributed by means of collisions between a large number of atoms and causing a local temperature increase. This region is called a “displacement spike” by Brinkman⁵ [66]. Bleiberg suggested that this disturbed region may be pictured as a large hole surrounded by a shell of lattice atoms which are in turn surrounded by the interstitial atoms created by knock-on collisions. These interstitial atoms increase the

⁵This region is called “thermal spike” in more recent literature, compare section 2.1

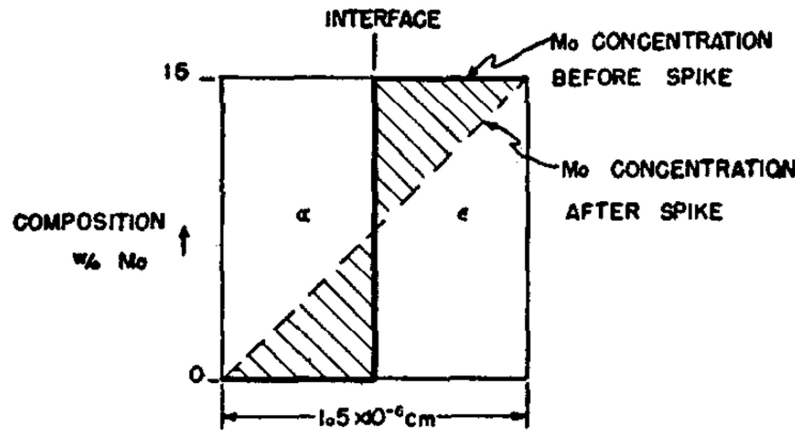


Figure 2.14: Model of the effect of a displacement spike occurring on the interface of the alpha and U_2Mo lamella against Mo concentration [60]

normal atomic density about 10% and give rise to high pressures. As a result, the spike collapses and recrystallization of the region according to the surrounding crystal lattice occurs. The atoms in the center of the spike end up on the outside and the atoms on the outside are moved to the inside. The volume of the displacement spike can be estimated to be $\approx 2.2 \cdot 10^{-18} \text{ cm}^3$ for γ -UMo. If the displacement spike occurs at the interface of α -U and U_2Mo or γ -UMo homogenization of the two phases occurs, compare Fig. 2.14 [60].

Both authors used their models to derive the kinetics of the phase transformation during irradiation. Further experiments on the α -U plus U_2Mo diffusion during irradiation by Bleiberg showed that both models, the one based on the thermal spike and the one based on the displacement spike, explain equally well the phase transformation effect. Bleiberg concluded that both models are consistent with the experimental observations of his experiment and can be used to derive the diffusion equations which describe the kinetics of the phase reversal [128]

It must be noted that both authors explained this phase transformation using the best knowledge of their time. However, since then diffusion and phase transformation mechanisms during irradiation have been the topic of detailed studies including numerical simulations as well as experiments. However, the models suggested by Konobeevsky and Bleiberg are still instructive in understanding the basic mixing principle.

2.3 Uranium - Aluminum diffusion

The alloying of uranium and aluminum when brought into contact with each other and exposed to reactor conditions is a well known fact since the very early days of nuclear engineering. First reports on this effect date back to the 40s of the last century where uranium-aluminum diffusion has been identified as the cause of fuel element rupture inside the X-10 Graphite pile⁶ at the Oak Ridge National laboratory - the second nuclear

⁶The reactor is also known as Clinton pile

Table 2.2: Terminology of different uranium and uranium-alloy phases. The nomenclature of the phases follows the one suggested by Lehmann and Hills [72]. UX stands for an alloy of U with a minor addition of a transition metal X.

Compound	Phase	Structure	Symbol	Lattice constants [Å]			Ref.
				a	b	c	
U	α	orthorhombic	Cmcm	2.852	5.865	4.945	[22, 27, 73, 75, 77, 79, 88]
U	β	tetragonal	P42/mmm	10.76	10.76	5.65	[22, 27, 73, 77, 79, 84, 88]
U	γ	bcc	Im-3m	3.474	3.474	3.474	[22, 27, 73, 77, 79, 84-86, 88]
UX	α	does not exist	-	-	-	-	[22, 73, 113, 129]
UX	β	does not exist	-	-	-	-	[22, 73, 113]
UX	α'	distorted orthorhombic	α				[74, 100-102]
UX	α''	monoclinic distorted	C21/m	2.89	5.68	4.99	$90^\circ \leq \gamma \leq 93^\circ$ [74, 100-103]
UX	γ°	tetragonal distorted	P4/NBM	$2a(\gamma)$	$2a(\gamma)$	$\leq a(\gamma)$	[73, 74, 101, 102, 104, 105]
U10at%Mo	γ°	tetragonal	P4/NBM	6.94	6.94	3.41	[73, 101, 102, 106]
U12.5at%Mo	γ°	tetragonal	P4/NBM	6.88	6.88	3.44	[73, 102, 106]
U8.5at%Ru	γ°	tetragonal	P4/NBM	7.00	7.00	3.40	[73, 103]
U16.25at%Nb	γ°	tetragonal	P4/NBM	7.01	7.01	3.37	[73, 103]
U19at%Nb	γ°	tetragonal	P4/NBM	6.95	6.95	3.43	[73, 103]
U ₂ Mo	$\gamma', \delta, \epsilon$ ^a	tetragonal	I4/mmm	3.427	3.427	9.834	[73, 111-113]
U ₂ Ti	$\gamma', \delta, \epsilon$	hexagonal	P6/mmm	4.828		2.847	[73, 107-109]
UAl ₂		cubic	Fd-3mS	5.487	5.487	5.487	[88]
UAl ₃		fcc	PM-3M	4.27	4.27	4.27	[88]
UAl ₄		orthorhombic	Imma	4.4	6.246	13.716	[88]

^a γ' is also tagged as δ or ϵ [23, 72]

reactor that has been built in the United States of America [32]. Since then, diffusion between different uranium alloys and compounds and aluminum during reactor operation has been observed many times, e.g. [33, 49, 130, 131]. The Al-U binary equilibrium phase diagram is shown in B.6.

Diffusion mechanisms Two different mechanisms have been identified to cause uranium-aluminum diffusion:

- First diffusion occurs when uranium and aluminum are brought into contact and exposed to elevated temperature. Significant thermal diffusion occurs at temperatures of 450 °C and higher. The diffusion process is in general accelerated when the temperature is raised. Typically the intermetallic compounds of uranium and aluminum (UAl_2 , UAl_3 , UAl_4) plus some other phases form - depending on the particular uranium and aluminum alloy and on the annealing temperature. In the U8Mo/Al system typically UAl_3 , UAl_4 , $\text{U}_6\text{Mo}_4\text{Al}_{43}$ and $\text{UMo}_2\text{Al}_{20}$ form [132, 133]. It has been found that in the UMo/Al system the diffusion is enhanced once the γ -UMo decomposes into α -U and γ -UMo enriched in Mo. The α -U/Al diffusion is thereby much higher than the γ -UMo/Al diffusion [134]. Uranium-aluminum diffusion can cause severe problems inside reactors running with metallic uranium-aluminum fuel elements at high temperatures. For example, the previously mentioned X-10 Graphite reactor used metallic uranium rods canned in aluminum. During operation, some of the cans ruptured resulting in the release of fission fragments. In this case, excessive uranium-aluminum diffusion at the hot-spots of the reactor has been identified to be the cause of the problem. Especially the formation of the brittle UAl_4 intermetallic compound resulted in the rupture of the fuel cans [32]. Already back then, different means to avoid uranium-aluminum diffusion have been examined. They will be discussed in a later paragraph [35]. The thermal diffusion effect is widely technically used during the development and qualification process of new reactor fuels in so called diffusion couples - small pieces of uranium or uranium alloys which are pressed onto aluminum and heated. This method is especially adapted to determine the high-temperature behavior of a nuclear fuel.
- Secondly uranium-aluminum diffusion occurs also inside fuels operated at low temperatures where thermal diffusion can normally be excluded [33, 130]. In this case, the diffusion process is radiation enhanced thermal diffusion [135] and caused by the high-energetic fission fragments. The diffusion process is based on thermal spike diffusion as described in section 2.1. Focus on this effect has been drawn during the ongoing development of high-density fuels based on UMo alloys dispersed in an aluminum matrix. This fuel-type suffers from excessive swelling due to the formation of an interdiffusion layer (IDL) at the interface between the UMo particles and the surrounding Al, compare Fig. 2.15. Although the formation of the interaction layer is radiation enhanced it is not temperature independent. For example, the reaction product inside UMo/Al fuel has been found to be crystalline after irradiation at higher temperatures in rod-type fuel [29]. In contrast, the interaction layer is amorphous inside plate-type fuel where the fuel temperature was around 100 °C during irradiation [28]. Moreover, no

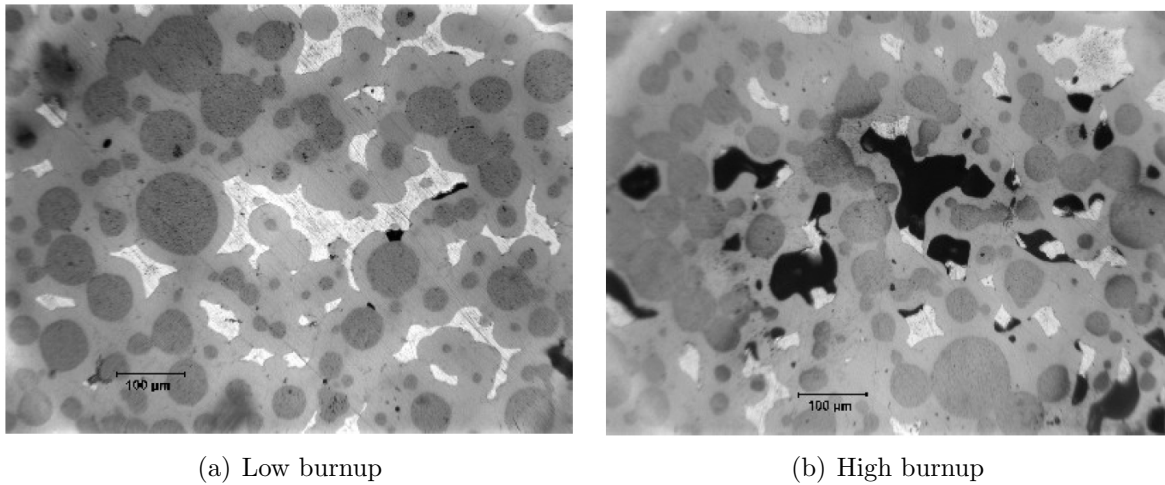


Figure 2.15: SEM micrography of in-pile irradiated UMo/Al fuel. The UMo particles (dark gray) are surrounded by a Al-rich diffusion layer (light gray) that formed during pile-irradiation. Almost the complete Al-matrix (white) has been consumed. Large fission gas bubbles (black) have formed [137].

UMo -Al interaction has been observed inside samples irradiated with Iodine at 80MeV at liquid nitrogen temperature [136], in contrast to samples irradiated in the same way at 150 °C where an IDL can be readily grown with heavy ions [46], compare section 4.1. It has been shown that the radiation induced diffusion due to fission products can be very well emulated using swift heavy ions [48]. This method is especially adapted to examine the diffusion behavior of fuel samples in a temperature range from liquid nitrogen temperature up to 250 °C.

UMo-Al diffusion During in-pile irradiation of UMo -Al dispersion fuel a huge IDL grows at the interface between the UMo and the aluminum. Figure 2.15 shows an example. UMo particles (dark gray) are surrounded by an IDL (light gray). The Al matrix (white) has been almost completely consumed. Fission gas bubbles (black) start to form inside the fuel. The thickness of the IDL and the size of the fission gas bubbles depends on the burn-up as can be seen by comparing Fig. 2.15(a) (low burn-up) and Fig. 2.15(b) higher burn-up [137]. At highest burn-ups the complete Al matrix can be consumed by the IDL. The IDL is in general Al rich, the exact composition depends, however, on the irradiation conditions. In general, a IDL composition $\text{Al}/(\text{U}+\text{Mo}) = 3$ is regarded as desirable and stable. The UMo/Al diffusion has been recently reviewed in detail by Porter and Ewh [138].

The IDL influences the fuel behavior in different ways:

1. It is generally believed that the IDL exhibits a low thermal conductivity below the respective values for pure Al (235 W/m/K) and UMo (13 W/m/K) [104,139–142]. Therefore the IDL will hinder the heat transport out of the nuclear fuel resulting in an increased fuel temperature.
2. The density of the IDL is lower than the density of UMo or Al. Therefore, the build-up of the IDL leads to swelling of the nuclear fuel [37].

3. The ability of the IDL to retain fission gases is lower than the ability of UMo. Therefore, large fission gas bubble form at the interface IDL-Al or IDL-UMo, depending on the irradiation conditions (compare Fig. 2.15). These fission gas bubbles lead to excessive swelling and can even cause pillowing, break-away swelling and fuel element rupture [137, 143].

The UMo/Al nuclear fuel has been, in principal, investigated in three different configurations:

1. Plate type fuel prepared with atomized UMo powder, e.g. [144]
2. Plate type fuel prepared with ground UMo powder, e.g. [145, 146]
3. Rod-type fuel prepared with atomized powder, e.g. [29, 147]

The temperature inside the plate-type fuel elements is in general lower than inside the rod-type fuel elements. However, the heat load also depends on the respective material test reactor, the irradiation position and the chosen irradiation conditions. Moreover, the production parameters of the respective fuel types are different regarding plates/rods produced by different groups. For example the fuel plates produced in the US are in general exposed to higher temperatures during production than the ones produced in France. These facts make it often very difficult to directly compare the results of the single irradiation experiments.

It has been found that the IDL consists of a mixture of UAl_3 and UAl_4 inside rod-type fuel elements [29]. In contrast, the IDL inside plate-type fuel elements is amorphous [28, 148], most likely due to the lower irradiation temperatures. The IDL composition ranges between $Al / (U+Mo) = 3.2 - 4.3$ [143].

Inside plate type fuel prepared with atomized UMo powder nanometer sized fission gas bubbles have been found to form a bcc superlattice inside the UMo. This bubble-lattice has got a lattice constant of ≈ 10 times the γ -UMo lattice constant and forms according to the γ -UMo atomic lattice [28]. No signs of nano-bubbles are found inside the IDL. Instead large fission gas bubble form at the interface IDL-Al [149]. Fission gas that is incorporated inside the UMo in form of nano-bubbles contributes only very little and in a predictable way to the fuel swelling. However, once the UMo with the incorporated nano-bubbles is consumed by the IDL, the fission gas follows the heat gradient towards the Al matrix. At the interface IDL-Al large fission gas bubbles are formed that will cause break-away fuel swelling. In contrast, no nano-bubble lattice has been found inside ground UMo powder [150], most likely due to the disturbance of the UMo lattice structure during the grinding process. In consequence, larger gas bubbles form already inside the UMo. Those bubbles are not transported towards the IDL/Al interface once they get incorporated inside the IDL but rather stay at their original position. It is believed that part of the improved swelling behavior of fuel plates prepared with ground powder to similar plates prepared with atomized powder is due to the changed fission gas transport mechanism [148, 151].

Means to avoid the formation of the interdiffusion layer Shortly after the cause of the slug-rupture problem in the X-10 graphite reactor had been identified, a research program was established to identify means to avoid uranium-aluminum diffusion [35]. Since then, many different means to reduce this undesired diffusion in

the different fuel systems have been suggested. For the UMo/Al system there are three different possibilities:

1. Addition of a diffusion limiting element to the aluminum matrix
2. Insertion of a diffusion barrier at the UMo/Al interface
3. Further alloying the UMo with a third element X to stabilize the UMo/Al diffusion.

Of course also every combination of option 1-3 is possible.

A diffusion barrier around the UMo particles inside dispersed UMo/Al fuels must be rather thin (around 1 μm). First, the thicker the diffusion barrier the higher is the amount of non-fissile material inside the fuel which will reduce the maximal possible uranium density. Secondly, the diffusion barrier may decrease the thermal coupling between the UMo and the Al.

On the other hand it is possible to apply thick diffusion barriers in the order of magnitude of 20 μm at the interface UMo/Al when the fuel plate consist of a pure UMo foil covered with Al cladding (further called monolithic fuel) [152]. However, there is no guarantee that diffusion barriers which are efficient in the dispersed system will also be efficient in the monolithic system and vice versa. It is therefore necessary also to take into account the thickness when examining a particular diffusion barrier material.

In the following paragraphs different diffusion limiting elements will be suggested. The discussion will be order by elements. A summary can be found in in Tables 2.3, 2.4 and 2.5. A collection of the binary equilibrium phase diagrams of alloys of the respective elements with Al and U is given in appendix B.

Silicon It has been shown many times before that silicon is efficient in reducing the uranium-aluminum diffusion kinetics since Si has got a higher chemical affinity to U than Al to U. The Al-Si and U-Si binary phase diagrams are shown in Figs. B.3 and B.12. Si suppresses the formation of the UAl_4 which is brittle and reveals a huge swelling under irradiation and enhances the formation of more stable UAl_3 when incorporated into the diffusion layer [43]. Furthermore, Si will not influence the reactor neutronics due to its low absorption cross section for thermal neutrons of $\sigma_{abs} = 0.24$ barn.

It has been shown first by Williams [35], Bierlein [153], Green [154] and de Luca [36] in the 50s of the last century that alloying aluminum with some wt% Sillicon reduces the uranium-aluminum diffusion kinetics in can-type fuel elements. This effect has also been found inside UMo-Al fuel plates: some wt% of Si added to the aluminum matrix efficiently reduce the growth of the IDL [37, 38, 155]. It will be shown in section 4.3 that the Si inside UMo/Al dispersed fuel plates diffuses towards the UMo and forms a protective layer at the UMo-Al interface. Therefore, indirectly a diffusion barrier is formed.

$U(Al,Si)_3$ and U-Si have been used in the early days of nuclear engineering as diffusion barrier in can type fuel elements that have been frequently used in graphite-pile type reactors [156]. The Belgian BR1 reactor is the last reactor world wide which uses this type of fuel. It is operated since 1956 with the first core loading. Recently Leenaers

et.al. showed that even after 50 years of operation the fuel is in excellent condition, i.e. no signs of undesired uranium-aluminum interaction are visible and the burn-up is less than 1% [157,158]. Recently van den Berghe suggested to apply a thin Si layer ($<1 \mu m$) around atomized UMo particles by sputtering instead of alloying the Al matrix with Si. It is believed that the total amount of Si inside the fuel can be minimized by applying the Si where it is needed to avoid UMo-Al diffusion: directly at the UMo/Al interface [159].

It has also been suggested to alloy UMo with Silicon. On the one hand, this will make some Si available inside the IDL. On the other hand, Si stabilizes the γ -phase of UMo upon annealing which will result in a reduced α -U formation and in turn in a reduced α U-Al diffusion [25, 31, 43, 160, 161]. However, it has been shown that the decomposition of γ -UMo is reversed during in-pile operation even at low burn-ups which indicates that the phase stabilizing effect is most probably of minor importance [60, 124].

Titanium It has been found by Williams 1950 that uranium-Al2.5wt%Ti diffusion couples showed a significant reduced diffusion compared to pure U-Al couples [35]. Later, titanium has been used by Thurber 1959 [43] and Keiser [42] as a diffusion barrier. Thurber concluded that in case Ti is incorporated into an U-Al diffusion layer the build-up of UAl_4 will be suppressed and UAl_3 will be promoted. Keiser concluded that Ti is a very promising diffusion barrier during annealing and Hot Isostatic Pressing (HIP-ing) at 550 °C. No barrier thickness has been given in his communication but it can be suspected that the thickness was several $10 \mu m$ since the study was performed on monolithic fuel plates.

Titanium has also been suggested several times as addition to the UMo. Thurber concluded in 1959 that Ti will not influence the γ -stability. Recently, UMoTi alloys with minor Ti addition (1-2 wt%) have been examined by several authors. It has been found that the alloys show a promising behavior in UMoTi/Al diffusion couples [31, 45, 161]. However, the amount of Ti directly available in the UMo alloy is diminished by the formation of Ti-rich precipitates [45, 162]. Yang recently presented results from the KOMO-4 irradiations which indicate that the addition of 1 wt% of Ti to U7Mo dispersed in Al5Si will reduce the UMo/Al interaction compared to pure U7Mo. He concluded that Ti and Si react preferential with each other forming a protective layer at the UMo/Al interface. This layer hinders the UMo/Al diffusion [147].

Bismuth The addition of 2 and 5wt% bismuth to the aluminum has been suggested by Williams, 1950. In this study performed on U/Al-X diffusion couples the addition of bismuth resulted in the lowest U-Al diffusion observed. Williams concluded that Bi is also “especially recommended because of its low neutron cross section” of only 0.016 barns for thermal neutrons [35].

Zirconium Zirconium or zirconium-alloys have been used as diffusion barrier inside dispersed [40] or monolithic [42] fuel plates where they showed very promising results both during in-pile and out-of pile experiments. Initially Zr showed a weak adhesion to UMo inside monolithic fuel. However, this problem has been overcome

by now [152, 163]. Zirconium reduces the γ -stability of UMo [31, 43, 161, 164]. This fact must be kept in mind when using Zirconium as a diffusion barrier. Nevertheless, Yang presented recently results from the KOMO-4 irradiation tests. The addition of 1 wt% Zr to U7Mo dispersed in Al5Si reduced significantly the UMo-Al diffusion compared to U7Mo/Al5Si. The results are similar to the one obtained on U7Mo1Ti/Al5Si samples irradiated during the same test. Like Ti, Zr reacts preferential with Si which forms a protective layer at the UMo/Al interface. This layer hinders the UMo/Al diffusion [147].

Niobium Nb has been used as diffusion barrier on dispersed [40] or monolithic [42] fuel. It showed a similar good behavior as zirconium. However, Nb, in contrast to Zr, enhances the γ -UMo stability upon annealing as has been shown several times over the past 50 years [44, 123, 161, 162, 164]. Therefore it is especially recommended as a ternary addition to the UMo.

Tantalum Tantalum, another member of the group of transition metals, has been considered to be the most effective diffusion barrier by Saller in 1955 [41]. Also Keiser suggested Ta as a possible diffusion barrier in 2007 [42]. However, to the author's best knowledge no detailed study was performed on this element so far.

Platinum 1-2 wt% platinum added to UMo have been found to enhance the γ -stability of UMo. It can therefore be expected, that it will also improve the UMo-Al diffusion behavior [20, 44, 123].

Uranium-oxide An uranium oxide layer at the interface U-Al or UMo-Al has been found to reduce the the U-Al diffusion both, during diffusion couple annealing experiments and during in-pile irradiation experiments. However, an oxide layer is only applicable with dispersed UMo particles that are completely surrounded by an Al matrix. An oxide layer at the interface UMo-Al inside monolithic fuel will reduce the adhesion between the UMo foil and the Al cladding. When an oxide layer is applied around UMo particles dispersed inside Al attention must be paid not to use a layer thicker than $\approx 1\mu m$. Otherwise, the oxide layer will be cracked during plate production which reduces its efficiency [35, 40, 156, 161].

Zirconium-Nitrite Izhutov showed in 2009 that there is a significant reduction up to 8-9 times of the UMo-Al diffusion compared with the unprotected case when ZrN is used as a diffusion barrier around UMo particles dispersed in Al. The thickness of the ZrN layer was around $1\mu m$ [39].

Recently it was shown by KAERI that in general nitriding of the UMo surface reduces the UMo/Al diffusion in annealing experiments. In fact, during the KAERI study uranium nitride formed which is very dense and hard. It therefore separates the UMo

and the Al mechanically [165].

Antimony Antimony has been suggested by Williams in 1950 as a possible addition to the aluminum. During annealing experiments with U-AlSb and U-AlBi diffusion couples Sb addition to the Al has been found almost equally powerful in suppressing U-Al diffusion than Bi. However, Sb forms an intermetallic compound with Al, which reduces the density of the Al and makes it brittle [35].

Beryllium Williams considered also beryllium addition to the aluminum. The results in his diffusion couple experiment was very promising, beryllium showed a similar potential than bismuth. [35].

Some other elements, namely tin, germanium, aluminum, palladium, ruthenium and osmium, have been suggested in the past as possible additions to the UMo in order to stabilize the γ -phase and suppress the UMo-Al diffusion. However, most of them were not the subject of extensive studies so far [20, 25, 26, 31, 38, 43, 160, 164].

The fourth possibility to avoid an UMo-matrix diffusion is the usage of an alternate matrix material. Here, magnesium is especially recommended since Mg does not form compounds with U (compare B.8) and Mg has got a similar neutronics and processability than aluminum. However, there are Al-Mg intermetallic compounds that form at 450° (compare Fig. B.2). It has been shown by Wiencek et.al. that it is possible to produce a UMo based fuel plates with a Mg matrix instead of an Al matrix and an Al6061 cladding. During an annealing test the UMo did not react with Al. However, there was a huge interaction between the Mg matrix and the Al cladding in that study which resulted in fuel plate swelling during the annealing test [6, 166].

Table 2.3: A list of possible options to reduce the UMo-Al interaction by adding a second element to the Al matrix.

Element	Remark	Ref.
Silicon	Si added to the Al matrix reduces the UMo-Al interaction. Uncertainties about the best concentration, the size of the Si particles and the behavior of the Si during the production and irradiation remain to be examined.	[35–38, 153–155]
Titanium	Ti added to the Al matrix performed good; study performed between 1948-50 on uranium-aluminum diffusion couples.	[35]
Bismuth	Bi added to the Al matrix has been considered “to be especially recommended because of its low neutron cross section” and showed most promising results in the past.	[35]
Beryllium	Be showed similar good results than Bi.	[35]
Antimony	Sb showed similar good results than Bi, but Sb forms a compound with Al which results in a loss of density of the Al matrix and a loss of free aluminum.	[35]

Table 2.4: A list of possible options to reduce the UMo-Al interaction by insertion of a diffusion barrier at the interface UMo-Al.

Element	Remark	Ref.
U-Oxide	An U-oxide layer at the interface UMo-Al showed promising results in the past.	[35, 40, 156, 161]
Tantalum	Ta has been considered the most effective diffusion barrier by H.A. Saller, 1955.	[41, 42, 167]
Zirconium	Zr showed good results with dispersed fuel, but had a weak adhesion when rolled to UMo foils. Can be overcome by sputtering Zr onto UMo	[40, 42, 152, 167].
Titanium	Considered to be the best diffusion barrier.	[42, 167]
Niobium	Nb showed promising results, similar to Zr.	[40, 42]
Zr-nitrite	There is a “significant reduction up to (8-9) times” of the UMo-Al diffusion compared with the unprotected case when ZrN is used as a diffusion barrier around UMo particles dispersed in Al.	[39]
U(Al,Si) ₃	Good diffusion barrier between U and Al within rod-type fuel elements	[156]
U-Si	Initial protection of the fuel inside BR1	[156, 158]
Si	Applied directly at the UMo-Al interface by sputtering	[159]

Table 2.5: A list of possible options to reduce the UMo-Al interaction by further alloying the UMo with a third element

Element	Remark	Ref.
Titanium	Shows promising results, no influence on the γ -stability of UMo	[31, 43, 45, 147, 161, 162]
Niobium	Enhances the γ -stability of UMo.	[44, 123, 161, 162, 164]
Platinum	Shows good results, enhances the γ -stability of UMo.	[20, 44, 123]
Silicon	Second choice, enhances the γ -stability of U-Mo.	[25, 31, 43, 160, 161]
Tin	Second choice	[38, 43, 160]
Germanium	Second choice	[38, 43]
Aluminum	Second choice, reduces the γ -stability of U-Mo.	[25, 31, 38]
Palladium	Second choice	[26]
Ruthenium	Second choice	[20, 26, 164]
Osmium	Second choice	[26]
Zirconium	Reduces the γ -stability of U-Mo. Promising results when used in combination with Al ₅ Si matrix.	[31, 43, 147, 161, 164]

Chapter 3

Experiment

3.1 Sample preparation

To identify the best candidate for a future in-pile test in total 21 different fuel plate samples have been produced according to tables 2.3, 2.4 and 2.5. We decided to divide those options into three parts and to pick the most interesting ones (compare table 3.1). For each option, one miniplate has been produced by AREVA-CERCA.

The first part consists of atomized U7wt%Mo powder dispersed in an Al matrix with and without addition of secondary elements. 2wt%Si, 5wt%Si and 7wt%Si have been chosen as addition to the Al matrix to find the best silicon concentration. Furthermore, 2wt%Ti, 2wt%Bi and 5wt%Bi have been added to the Al matrix, respectively, to check the positive effect of these elements. It has been reported, that the addition of magnesium to aluminum accelerates the diffusion at the U-Al interface. In consequence, 2wt%Mg has been added to the matrix to check this effect [35, 38]. In each case the samples have been prepared with and without an oxide layer (UOx) of $\approx 2 \mu\text{m}$ thickness around the UMo particles, to check its effectiveness as a diffusion barrier – second part. It was not possible to obtain UMo particles coated with metals like Zr or Ti to check their effectiveness as a diffusion barrier.

The third part consists of ternary U8wt%Mo-x ground powder dispersed in a pure Aluminum matrix. To study the principal effect of alloying the UMo with minor additions of a third element, 1wt%Ti, 1,5wt%Nb, 3wt%Nb and 1wt%Pt have been added according to table 2.5.

One miniplate consisted of UMo dispersed in magnesium, covered with AlFeNi. The meat of this sample was grayish and very brittle which indicates that the magnesium reacted with the Aluminum cladding to a low temperature eutectic phase [6, 161, 166]. The miniplate broke apart during cutting and polishing and it was not possible to obtain a sample for heavy ion irradiation from this miniplate. Therefore, this option was completely given up and will be disregarded.

The spherical atomized powder used during this study has been obtained from KAERI. Details on atomization process can be found elsewhere [168]. A part of the atomized powder has been intentionally oxidized to obtain the protective oxide layer. For this, the UMo powder has been heated while exposed to air for some time. Details on the process can be found elsewhere [161, 169].

The ground powder has been produced by AREVA-CERCA using a process similar to the one used to produce the UMo powder for the IRIS-TUM and IRIS-1 full size

plates [145, 146]. The ingot production has been followed by a thermal treatment consisting of heating and quenching steps to increase the homogeneity and to retain the γ -phase of the UMoX-alloy. Afterwards, the ingots were ground slowly under an inert atmosphere. In contrast to the atomized powder, which has got a spherical shape, the ground powder grains have an irregular shape after the grinding process and are covered with an oxide layer¹. Depleted uranium has been used in both cases. The miniplate samples have been produced using the AREVA-CERCA standard procedure which consists of the following steps:

1. **Al-powder:** In case a second element was added to the matrix this has been performed by blending powders of Al and the particular element. Powders of the highest purity and the smallest grain size (-mesh325) commercially available have been used². An exception is the 2wt%Si case where a pre-alloyed powder from a commercial supplier has been used. Picture 4.20 gives an example of mixed powder just after blending. A laser granulometry performed on the Al and the Si powder shows that the grain size of the particular product is in good agreement with the values given by the supplier (compare pictures 4.21(a) and 4.21(b)).
2. **UMo-powder:** The Al powder and the UMo powder have been mixed under an inert atmosphere to prevent oxidation. In the cases where oxidized UMo powder has been used to evaluate the possible interest of uraniumoxide as a diffusion barrier the UMo powder has been exposed to air in a controlled way under elevated temperature prior to the mixing step.
3. **Compact production:** The UMo-Al powder has been poured into a profile and high-pressure has been applied to produce a dense compact.
4. **Plate-processing:** An AlFeNi frame has been placed on a AlFeNi Plate and the compact has been placed into the frame. Afterwards they have been covered with another AlFeNi plate. By pressing a relatively thick, air-tight sealed compact has been produced. The compact production is followed by hot-rolling at ≈ 400 °C to reduce the total thickness of the sample to 1.4 mm and to finally seal the miniplate. The hot-rolling has been followed by a blister test (1–2h at ≈ 425 °C) to test if the sealing was successful. After this step, the UMo particles are tightly covered with Aluminum from every side. Figure 3.1 shows a sketch respectively a photograph of a typical miniplate.

To get access to the meat layer, the cladding had to be removed prior to the experiments. The procedure is described in Appendix A.

3.2 Heavy ion irradiation

All samples have been irradiated at the tandem accelerator of the Maier-Leibnitz Laboratory (MLL) in Garching which is operated in cooperation between the Ludwig-

¹Although the grinding is performed under an inert atmosphere an oxide layer develops around the UMo particles picking up residual oxygen contaminations inside the glovebox. The oxidation is crucial for the success of the grinding process [170].

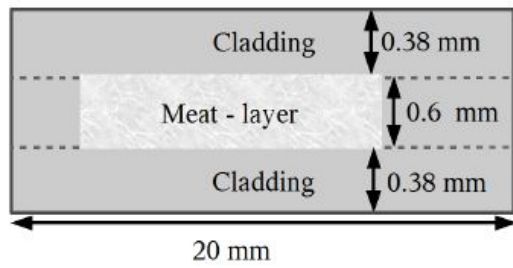
²Details on the powders used can be found on the suppliers website [171].

Table 3.1: Complete list of the samples prepared for the material down selection program MAFIA-I. Unless otherwise identified, atomized UMo powder has been used for sample preparation.

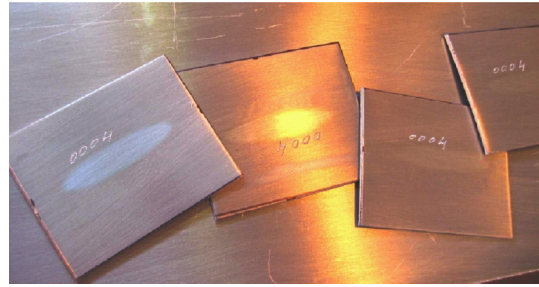
Name	Alloy	Matrix	Comment
MAFIA-I-1	U-7wt%Mo	Al	Reference samples.
MAFIA-I-2	U-7wt%Mo(ox) ^a	Al	
MAFIA-I-3	U-7wt%Mo	Al-2wt%Si	Different Si concentrations to find the most promising value.
MAFIA-I-4	U-7wt%Mo(ox)	Al-2wt%Si	
MAFIA-I-5	U-7wt%Mo	Al-5wt%Si	
MAFIA-I-6	U-7wt%Mo(ox)	Al-5wt%Si	
MAFIA-I-7	U-7wt%Mo	Al-7wt%Si	
MAFIA-I-8	U-7wt%Mo(ox)	Al-7wt%Si	
MAFIA-I-9	U-7wt%Mo	Al-2wt%Mg	
MAFIA-I-10	U-7wt%Mo(ox)	Al-2wt%Mg	
MAFIA-I-11	U-7wt%Mo	Al-2wt%Ti	To study the influence of Ti on the diffusion process.
MAFIA-I-12	U-7wt%Mo(ox)	Al-2wt%Ti	
MAFIA-I-13	U-7wt%Mo	Al-2wt%Bi	Different Bi concentrations in the Al matrix to find the most promising amount.
MAFIA-I-14	U-7wt%Mo(ox)	Al-2wt%Bi	
MAFIA-I-15	U-7wt%Mo	Al-5wt%Bi	
MAFIA-I-16	U-7wt%Mo(ox)	Al-5wt%Bi	Test of a different matrix material [6, 161, 166].
MAFIA-I-17	U-7wt%Mo	Mg	
MAFIA-I-18	U-8wt%Mo-1wt%Ti ^b	Al	Study the principal effect of alloying and grinding the UMo on the irradiation behavior.
MAFIA-I-19	U-8wt%Mo-1.5wt%Nb ^b	Al	
MAFIA-I-20	U-8wt%Mo-3wt%Nb ^b	Al	
MAFIA-I-21	U-8wt%Mo-1wt%Pt ^b	Al	

^a(ox) indicates that the UMo particles have been intentionally oxidized before the sample preparation to test the effectiveness of an oxide layer around the UMo particles as a diffusion barrier.

^bGround powder



(a) Sketch of a miniplate



(b) Typical miniplates

Figure 3.1: Figure 3.1(a) shows a cut-through sketch of a miniplate with the typical dimensions of the meat and the cladding, figure 3.1(b) shows a photograph of typical miniplates provided by AREVA-CERCA [46].

Maximilians Universität München (LMU) and the Technische Universität München (TUM). Figure 3.2 shows the lay-out of the accelerator laboratory.

Negatively charged ions are produced inside the ion source (1) by sputtering. Afterwards, they are injected into a tandem linear accelerator (2), which provides a maximum voltage of almost 15MV. It is called “tandem-type” since the accelerating voltage is used twice: The middle of the accelerator, the so called “terminal” is positively charged and kept at a voltage of several MV compared to the front or rear end of the accelerator, which are at ground potential. The negatively charged ions are injected at the front end and accelerated towards the terminal. The terminal contains a “stripping-medium”, either a thin metal foil or a dilute gas (air at some mBar). By passing this medium, the negatively charged ions lose some of their electrons and become positively charged. The number of stripped electrons depends thereby on the stripping medium and the sort of ions and follows a statistical distribution. Behind the terminal the now positively charged ions are accelerated again towards the rear-end of the accelerator. The ion beam is split into single lines according to the ions charge and energy at position (3) by a 90° analyzing magnet resulting in an almost mono energetic ion beam. The ion beam is allocated into the single beam-lines at position (4). Our irradiation setup has been build up at position (5) in the middle of the $+10^\circ$ beam line.

^{127}I at 80MeV has been used for every beam time. Iodine has been chosen because it has an atomic weight comparable to common fission products (compare Fig. 2.1). Furthermore, the tandem accelerator at the MLL can provide a high flux of ^{127}I ions which keeps the time needed for the irradiation of a single sample as low as possible. An energy of 80MeV has been chosen because it is a typical energy of fission products [47, 48]. Furthermore, ^{127}I ions at 80MeV are well beyond or only slightly above the Coulomb barrier energies of Al, Mo and U which are at 73.6MeV, 200.1MeV and 373.4MeV, respectively. Even though, an activation of the aluminum inside the sample was not measurable [46]. All irradiations have been performed under high vacuum ($< 2 \cdot 10^{-6}$ mbar).

To improve the safety and reliability, the irradiation chamber used during former experiments has been replaced by bigger a chamber combined with a fully automated system based on a programmable controller (SPS).

Figure 3.3 shows a picture of the chamber: The incoming ion beam direction is indicated with the arrow. Onto a turnable motor-driven mechanical feedthrough (1) with an attached cooling element (2) a wheel has been mounted. The different sample holders can be mounted on the wheel at in total eight possible positions. The cooling element limits the sample holder temperature to about 200 °C. Measurement of the sample and sample holder temperature and the beam current is possible via multiple electric feedthroughs (4). The size and shape of the beam spot can be detected with a crystal (5) that can be put into the beam. The cooling element (2) is fed with cooling water via two metal hoses (6).

The sample holders used for the irradiations are shown in Figure 3.5. To affix the sample to the sample holder an aperture plate is used. Both are made of aluminum to provide a good heat contact with the sample. The sample holder is available in 4 different versions to provide different irradiation angles (90, 30°, 45°, 60°; angle measured between the incident beam and the sample surface). To measure the temperature of the sample holder during irradiation, thermoelements (Pt100 type) have been used.

The programmable controller can be operated via a standard web browser (e.g. Fire-Fox) with Java. All valves, shutters, cup 1, cup 2 and the motor driving the wheel with the sample holders are controlled by it. Furthermore, the programmable controller monitors the pressure at different positions of the irradiation chamber, the sample holders and the wheels temperature and the beam current. A system of interlocks closes the beam tube shutter and stops the beam with a cup in case that any of the values monitored is outside a predefined range. The same interlocks prevents the beam tube shutter from being opened as long as the air pressure inside the irradiation chamber is above a certain limit avoiding an accidental forced venting of the beam tube. The motor can be driven either manually in both directions or a series of irradiations can be defined that will be followed automatically, afterwards. For the automated irradiation, it is possible to define an individual upper limit for the total integral fluency to be reached on every sample. After starting the program, the SPS will turn the samples on the wheel into the beam and start integrating and monitoring the current ion beam. When the desired fluency has been reached, the next sample is moved into the beam automatically until all samples have been irradiated. The measured temperature and current values are stored. With this program, it is possible to irradiate up to eight samples without having to open the irradiation chamber which saves time.

To direct the ion beam on the sample the following procedure has been used: a Faraday cup has been installed just in front (Cup 1) and after (Cup 2) the irradiation setup (compare Fig. 3.4) allowing the precise measurement of the ion beam current at the particular position. A plate with a hole identical to the one on the aperture plates used to mount the samples on the sample holder is installed at the exact same position where the samples are irradiated. Thus, the beam current measured at cup 2 is the same current that reaches the samples later during irradiation. By measuring the beam current at cup 1 or the complete beam current on the sample holder (with mounted sample) and calculating the ratio with the current on cup 2 (correction factor), it is possible to determine the current on the sample at any moment of the irradiation by measuring either the current on cup 1 or the complete current on the sample holder. The later continuous measurement is used during the automated irradiation program. To improve the homogeneity of the irradiation, the beam can be “wobbled” over the sample by applying an AC current to the magnetic lenses controlling the X-Y position

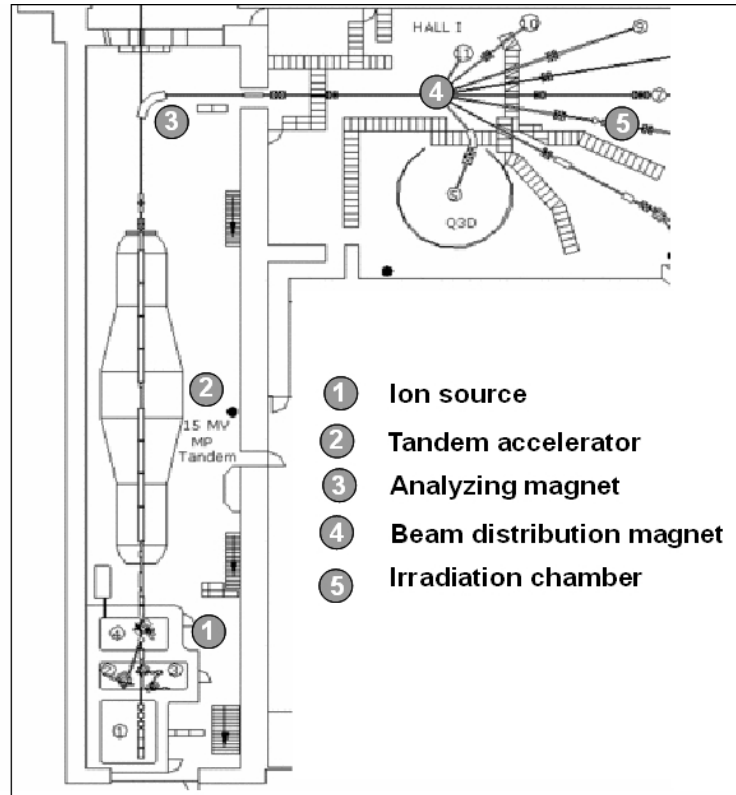
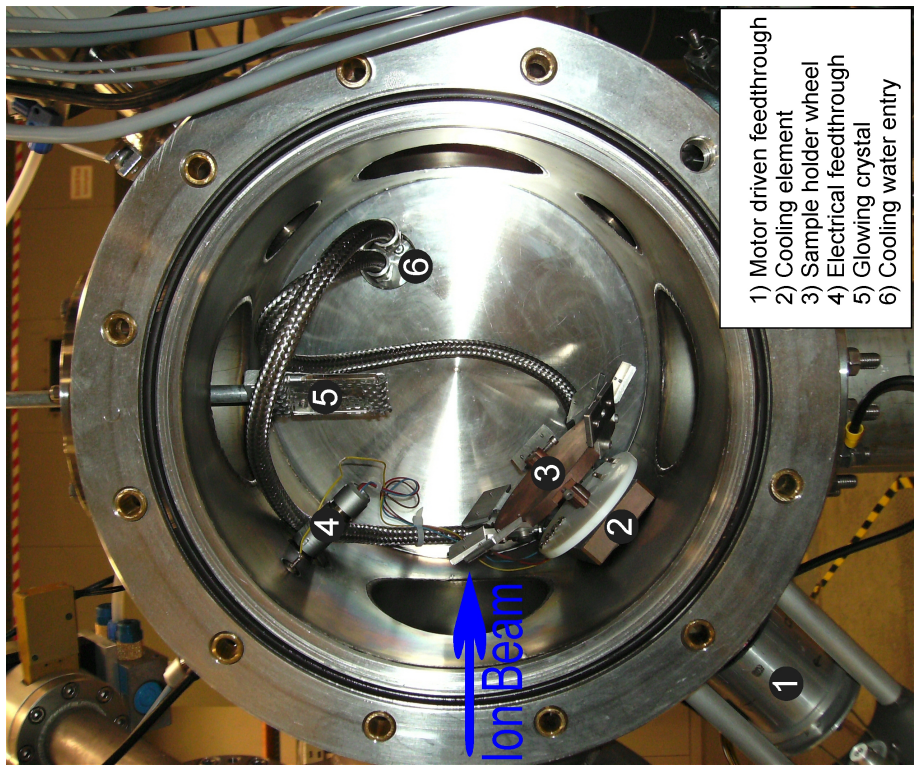


Figure 3.2: Floor plan of the tandem accelerator laboratory of the MLL [173].

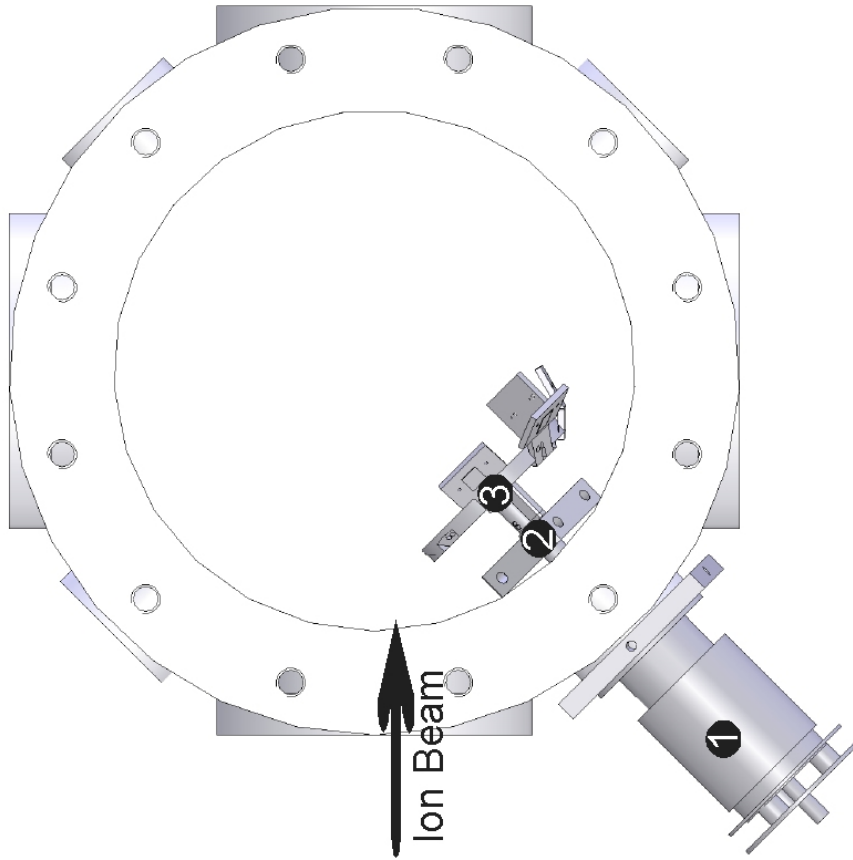
of the beam. Furthermore, the size and shape of the beam spot can be confirmed using a crystal behind the aperture plate (compare Fig. 3.3(a), 5).

Since with the sample holder wheel only irradiations at temperatures around 200 °C are possible which was not satisfying for every planned experiment a liquid nitrogen cooled sample holder has been used to irradiated samples at lower temperatures. This sample holder can be mounted instead of the crystal (5) in Figure 3.3(a) and allows to reach irradiation temperatures between 120 °C and -180 °C. It works with the cold finger principal (compare Figure 3.6): a copper block is installed into a flange (size CF100). The upper end of the copper block is in contact with liquid nitrogen in a dewar vessel. The sample is directly mounted on the copper block to ensure a good thermal contact. The temperature of the sample holder is controlled by the amount of liquid nitrogen filled into the dewar. With this sample holder, only one sample can be inside the irradiation chamber at one time. Furthermore, it is only possible to measure the temperature of the sample holder, not the ion beam current.

Unless different notated, all samples presented in the following chapters have been irradiated at the same conditions: the total integral fluency is $1 \cdot 10^{17}$ ions/cm² which corresponds to a full burn-up [46,172]. The beam spot size was 4mm in diameter, the irradiation angle was 30° between incoming beam and sample surface. The irradiation temperature ranged between 180 and 250°C.



(a)



(b)

Figure 3.3: A photo (3.3(a)) and a sketch (3.3(b)) of the high vacuum chamber in which the irradiation of the MAFIA-I samples has been performed. The incoming ion beam direction is indicated with the arrow.

3.3 Pre- and Postirradiation examinations - Methods

All samples have been examined before and after irradiation with heavy ions with a standard set of laboratory scale methods. Furthermore, the most promising samples have been examined with synchrotron radiation at different beam lines of the European Synchrotron Radiation Facility (ESRF, Grenoble, France) and of the Swiss Light Source (SLS) of the Paul Scherrer Institute (PSI, Villigen, Switzerland). The methods used are described hereafter. Results are presented in chapter 4.

1. **Optical Microscopy:** The quality of the sample polishing and the state of the sample surface just after heavy ion irradiation have been controlled using a light microscope.
2. **Scanning Electron microscopy (SEM) with energy dispersive X-ray spectroscopy (EDX):** For the examinations, two different electron microscopes have been used: a Zeiss EVO MA 25 at the Institut für Radiochemie of the Technische Universität München in Garching and a FEG-SEM Philips XL30 at the “Laboratoire UO₂” of CEA in Cadarache. The Zeiss EVO MA 25 is equipped with a ultra-dry silicon drift detector by Thermo Fisher than enables EDX analysis. Details on the technique and the models can be found elsewhere [174–176]. SEM pictures and EDX of the fresh and the irradiated sample surface have been made. Furthermore, cross sections of irradiated samples have been prepared at the “Laboratoire UO₂” of CEA in Cadarache to observe the in-depth behavior of the IDL (compare Figure 3.7). Standardless EDX point measurements as well as EDX mapping and line scans have been used to determine the elemental composition and element distribution inside the samples.
3. **Laboratory scale X-ray diffraction analysis (XRD):** The crystallographic phases present in each sample have been determined before and after irradiation with heavy ions using X-ray diffraction analysis. The examinations have been performed at the crystallography section of the Earth- and Environmental Sciences Department of the Ludwigs-Maximilians-Universität (LMU) in Munich using their powder X-ray diffraction setup (compare Figure 3.8) in the standard Bragg-Brentano reflection configuration. The samples have been rotated during the measurement to prevent errors from local impurities and preferred orientations. For the measurement, molybdenum K- α radiation with a wavelength of $\lambda = 70,93$ nm has been used. Before the examination, the samples have been masked with Kapton tape to prevent contamination and have been glued onto small glass sample holders to ease the handling. The size of the X-ray beam has been adapted to the irradiated area on the sample. To identify the phases present in the samples Rietvelds method and the Fullprof software suite have been used. Details on the XRD-setup, on the Rietveld method and on the programs used can be found in references [139, 177, 178].
4. **μ -XRD examinations:** To access the crystallographic composition of the samples on a micrometer scale single UMo particles (irradiated and not irradiated) have been examined using micro-focused synchrotron radiation at the Swiss Light

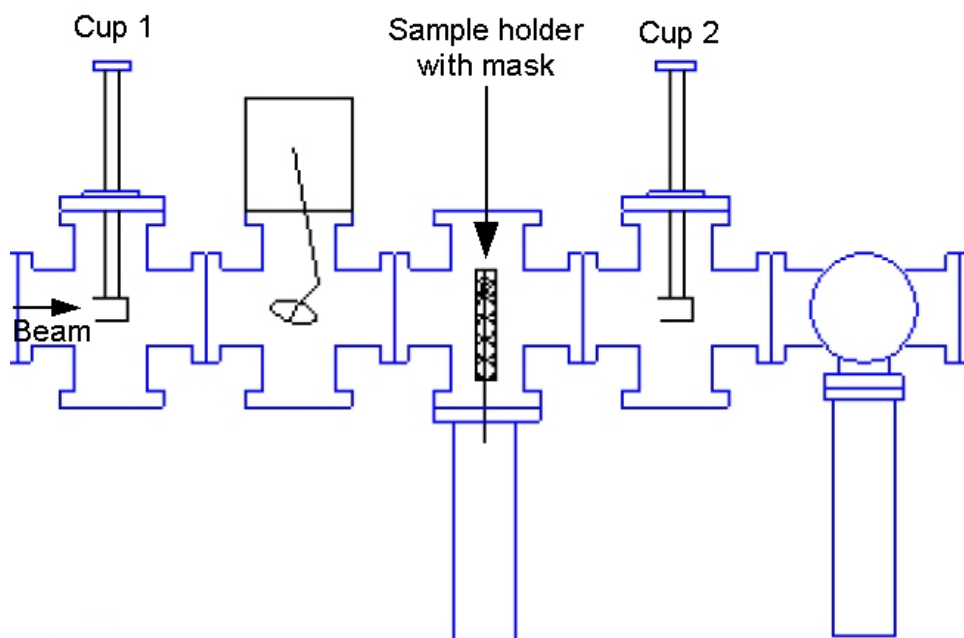
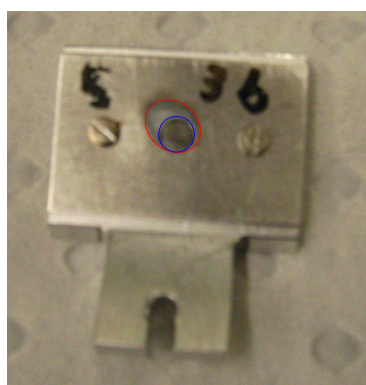
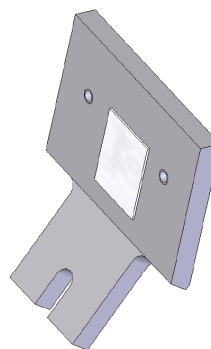


Figure 3.4: Schematic of the aiming procedure [139].



(a)



(b)

Figure 3.5: Photo (3.5(a)) and sketch (3.5(b)) of a sample holder with mounted sample. On the photo, the sample is partially covered with an aperture plate. The beam spot is indicated in red, the irradiated part of the sample in blue.

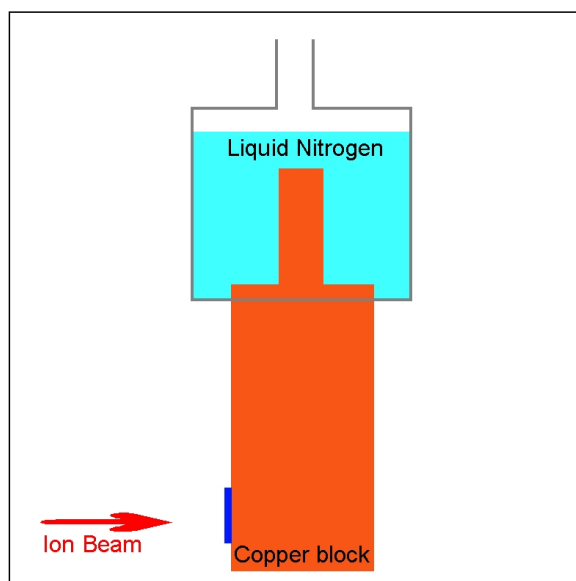


Figure 3.6: Liquid nitrogen cooled sample holder working with the cold-finger principal.

source μ -XAS beamline [179] (PSI, Switzerland) and at different beamlines (e.g. ID22, ID18 F) of the ESRF. ID18F has been closed 1. March 2011 [180, 181]. The beam time has been obtained by our collaboration partner H. Palancher from CEA who also performed the measurements and the data treatment. The samples have been characterized by XRD in transmission mode. For this, the UMo particles have been glued on top of glass capillaries and brought into the beam (compare Figure 3.9). Afterwards, the beam has been scanned over the particle to identify the different crystallographic compositions. Also here the Rietveld method and the Fullprof software suite have been used for data treatment [177, 178]. Further details on the method can be found in [182] and [183]. Since different setups have been used during this work, the exact size of the beamspot used and the beam energy will be indicated with the particular results in chapter 4.

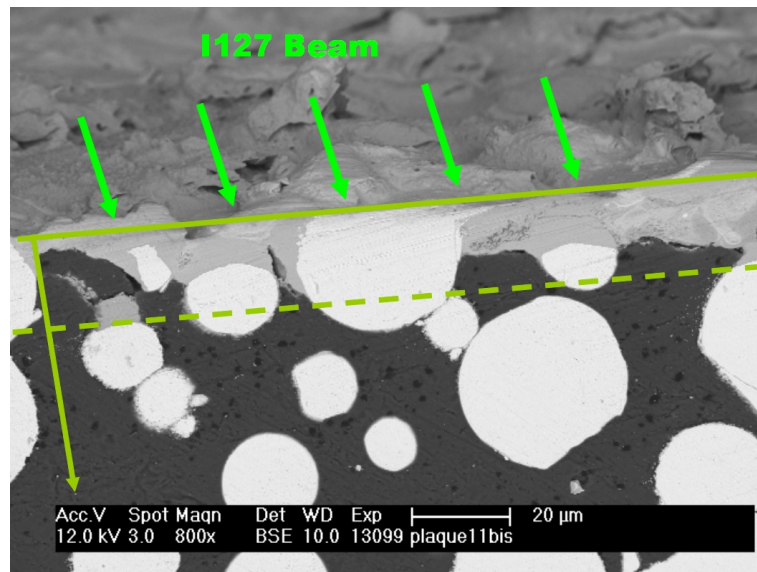


Figure 3.7: Cross section through the irradiated part of a sample. The incoming ion beam is indicated by green arrows, the penetration depths of the heavy ions by a dashed line [184].

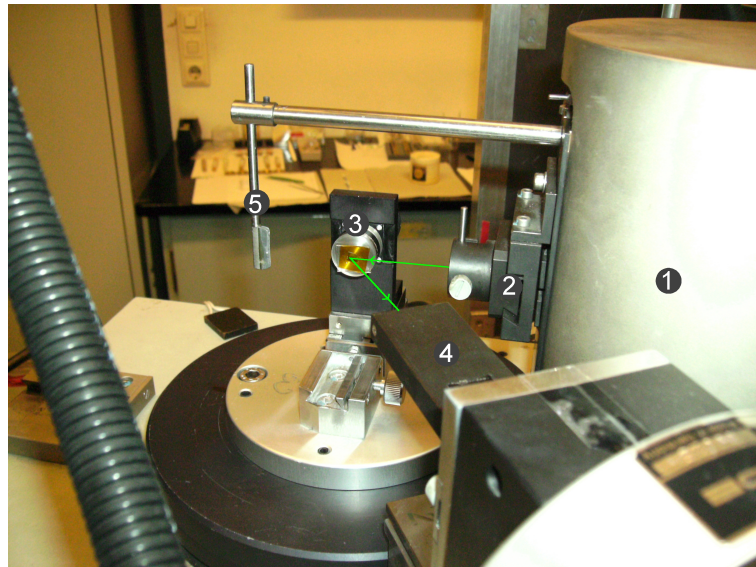


Figure 3.8: The laboratory scale XRD setup used during this work. The X-ray beam (green arrows) passes the monochromator (1) and a slit system (2) before it is reflected by the sample (3). A counting tube serves as detector (4). The primary beam catcher (5) protects the detector when measuring at small angles.

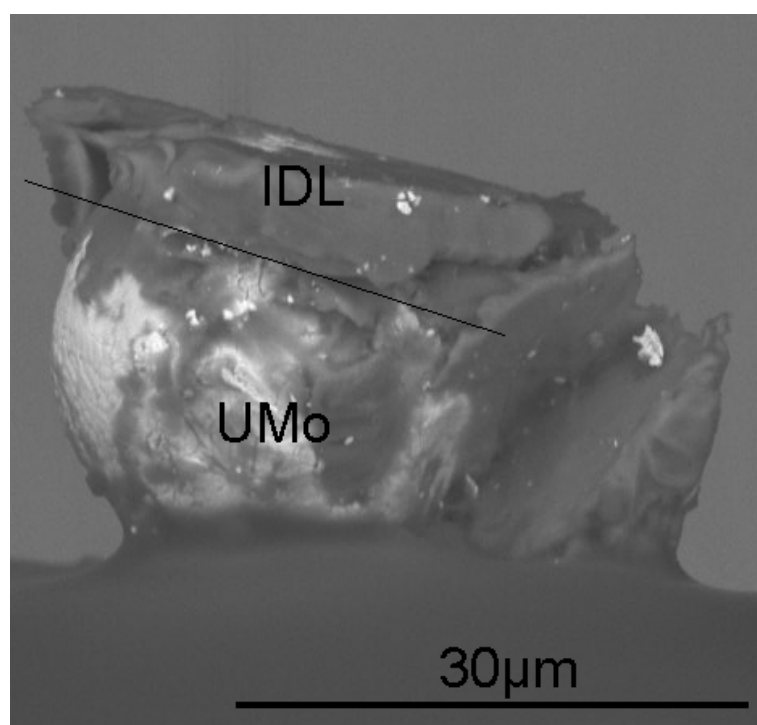


Figure 3.9: SEM picture of a UMo particle with a small piece of IDL glued on top of glass capillary.

Chapter 4

Results and discussion

In this chapter, the results of the single irradiation campaigns will be presented and discussed. At first, the results of a methodology test to determine the heavy ion irradiation conditions that are closest to the in-pile irradiation conditions will be presented. Afterwards, the results of the material down selection program MAFIA-I will be shown.

4.1 Irradiation conditions - Methodology

Irradiation of dispersed UMo/Al samples with ^{127}I at 80 MeV has been used to simulate the in-pile growth of the IDL out of pile [47,48,185]. However, after the proof of principle had been successful, attention had to be turned on making the results of the heavy ion irradiations more representative for the in-pile irradiation phenomena and to understand the influence of the single irradiation conditions which are:

1. Ion flux
2. Irradiation angle
3. Integral fluency
4. Irradiation temperature

The main objective was to establish the use of ion irradiation as a routine method to discriminate technological solutions envisaged for limiting the growth of the UMo/Al IDL. For this reason, a research project to determine the influence of the single irradiation parameters on the formation of the IDL has been accomplished in cooperation between partners from the Commissariat à l'Énergie Atomique (CEA), AREVA-CERCA and the FRM II. This work has mainly been driven by our partners from CEA and has already been presented before in [184] and [136].

4.1.1 Experimental method

The samples used consist of atomized U7Mo particles dispersed in an Al matrix provided by AREVA-CERCA. They have been prepared according to the standard procedure described in section 3.1.

Pre- and post irradiation examinations were carried out at the “Laboratoire UO₂”

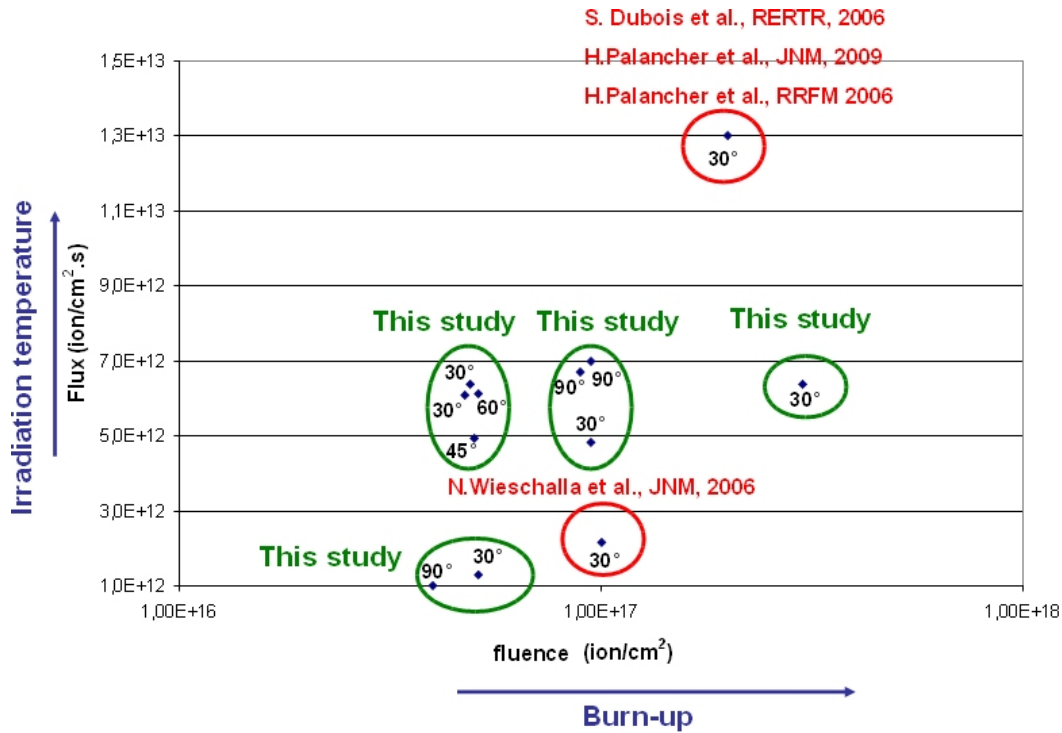


Figure 4.1: Irradiation conditions during this and during previous studies [47, 48, 161, 184, 186]. The samples irradiated with the cooled sample holder are not regarded in this picture.

of CEA in Cadarache. Microscopy was performed using a FEG-SEM-Philips XL30 coupled with an Energy Dispersive X-ray Spectrometer (EDS). XRD measurements were obtained using a diffractometer D8 Advance Brüker. μ -XRD analyses using synchrotron radiation in reflection mode on the ID22 beamline at ESRF (European Synchrotron Radiation Facility) in Grenoble (France) have completed the data. The photon energy was set to 17 keV and the size of the beam spot was in the order of $1 \times 20 \mu\text{m}^2$. To fulfill safety requirements the samples were covered with Kapton tape. To test the influence of ion flux, the irradiation angle and the integral fluency the sample holder wheel and to test the influence of the irradiation temperature the liquid nitrogen cooled sample holder have been used (compare section 3.2). ^{127}I odine at 80 MeV has been used as projectile, the beam spot diameter on the sample was 4mm or 6mm. Beam wobbling has been used during the irradiations to increase the homogeneity of the irradiation. The ion flux was tested from $1 \cdot 10^{12}$ up to $7 \cdot 10^{12}$ ions/(cm².s). The ion fluency was tested between $3 \cdot 10^{16}$ and $3 \cdot 10^{17}$ ions/cm² with an irradiation angle between the sample surface and the ion beam ranging from 30° to 90°. The irradiation conditions (angle, fluency and ion flux) of this and previous studies are depicted in figure 4.1. The irradiation temperature was $\approx 180 \text{ }^\circ\text{C} - 220 \text{ }^\circ\text{C}$. The influence of the temperature has been tested in the range between $-160 \text{ }^\circ\text{C}$ and $50 \text{ }^\circ\text{C}$ using the liquid nitrogen cooled sample holder. The total integral fluency was $1 \cdot 10^{17}$ ions/cm².s, the irradiation angle was 90°.

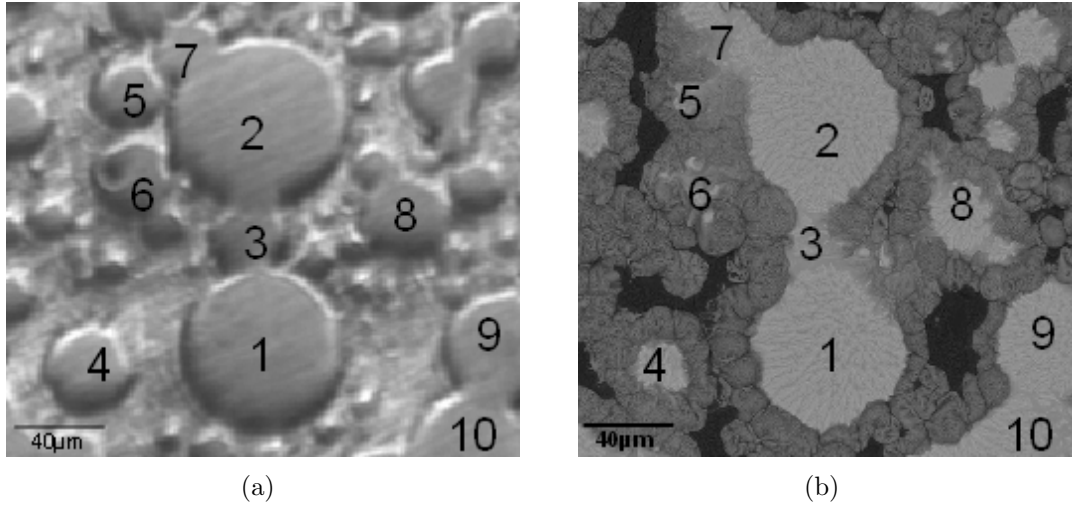


Figure 4.2: Influence of the heavy ion irradiation. Microscopy images have been taken on the same zone before (4.2(a): OM observation of the sample surface) and after irradiation (4.2(b): SEM observation in BSE mode of the irradiated sample surface). The dark gray colored zones on SEM observations correspond to the interaction compounds.

4.1.2 Results

Surface observations: Flux and fluency

Both, optical (OM) and scanning electron microscopy (SEM) have allowed to distinguish clearly the irradiated from the non-irradiated zones on the sample surface. Whatever the experimental conditions (in particular for each irradiation angle), the irradiation has systematically led to the growth of an IDL around the UMo particles. Because of the use of a lower flux, no ripples have appeared at the sample surface contrary to previous similar experiments [46, 48]. Since different and relatively high fluencies have been considered in this work, the fluency does not seem to have an impact on this ripple phenomenon.

For the lowest flux values tested during this campaign, the global organization of the sample is preserved after irradiation (compare figure 4.2). For the highest fluxes, the interaction compounds are not strictly limited to the periphery of the UMo particles but also cover the surface. In this last case, post irradiation experiments and results are difficult to interpret. Thus, moderate flux has been preferred for the major part of these irradiation experiments.

It has been confirmed that the total integral ion fluency has a direct influence on the IDL thickness. If we compare two samples irradiated under the same conditions except for the ion fluency (compare 4.3), we can note an unambiguous evolution of the IDL thickness which ranges from $3 \mu m$ for $3 \cdot 10^{16}$ ions/cm² to around $15 \mu m$ for $3 \cdot 10^{17}$ ions/cm². It does not depend on the size of the particles since smallest particles may fully be consumed (compare Figure 4.3(b)).

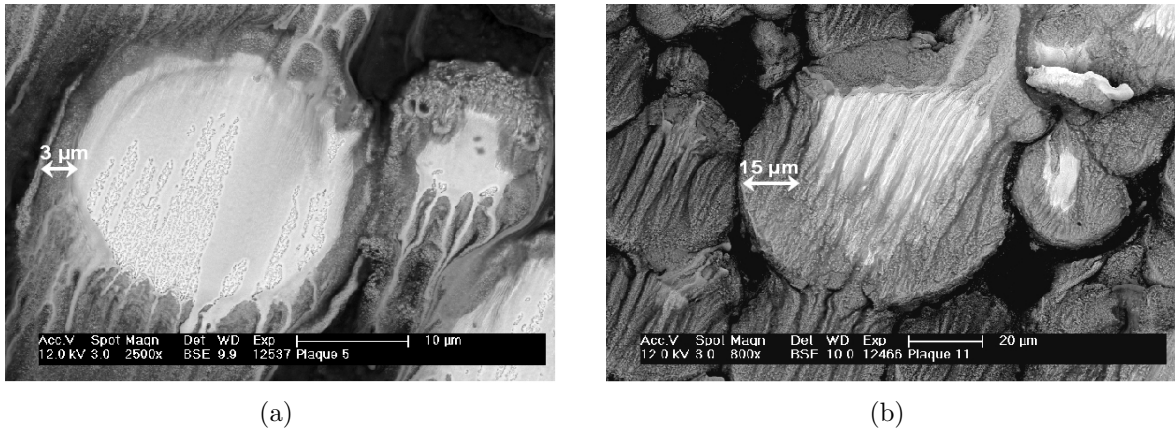


Figure 4.3: Influence of the ion fluency on the interaction layer thickness. Comparison of two plates irradiated at 30° with an ion flux fixed at about $4 \cdot 10^{12}$ ion/(cm²·s) and different ion fluencies. 4.3(a): SEM observation of a fuel plate irradiated at $3 \cdot 10^{16}$ ions/cm²; 4.3(b): SEM observation of a fuel plate irradiated at $3 \cdot 10^{17}$ ions/cm².

Surface observations: Irradiation angle

During a precedent study an angle of 30° had been chosen to irradiate dispersed UMo-Al samples [46]. To check the influence of the irradiation angle on the formation of the IDL different irradiation angles have been tested during this study.

The morphology of the IDL at the surface is strongly affected by the irradiation angle (compare Figure 4.4). With normal incidence, the IL is homogeneously organized around the particle; however in the others cases and especially for the lowest incident angle (30°), the interaction morphology has clearly changed. In case the irradiation angle is other than 90° a “flowing” effect of the IDL on the surface parallel to the direction of the incoming ion beam occurs. It can be concluded that the irradiation conditions control the morphology and the thickness of the IDL. However, surface examinations are not fully adapted for analyzing the samples irradiated with the highest fluencies since strong surface modifications prevent the measurement of the interaction layer size.

Sample cross section examinations - Proof of principal

In case of 90° incidence angle the penetration depth of ^{127}I ions at 80 MeV reaches $5 \mu\text{m}$ inside γ -UMo and $13 \mu\text{m}$ in Al. Calculations of the ions penetration depth using the SRIM code [63] show that this distance changes with the beam incidence angle as shown in table 4.1.

The surface observations allow having an overview of the irradiation effect but they do not allow understanding the behavior in depth. Consequently, they do not describe a significant part of the modification induced by irradiation in this material. In-depth analyses are thus required.

Indeed one would expect that each UMo/Al interface located at a depth ranging from the surface down to $13 \mu\text{m}$ (in the normal incidence case) would be affected by uranium-aluminum diffusion. Therefore transversal cross sections of the UMo/Al plates have

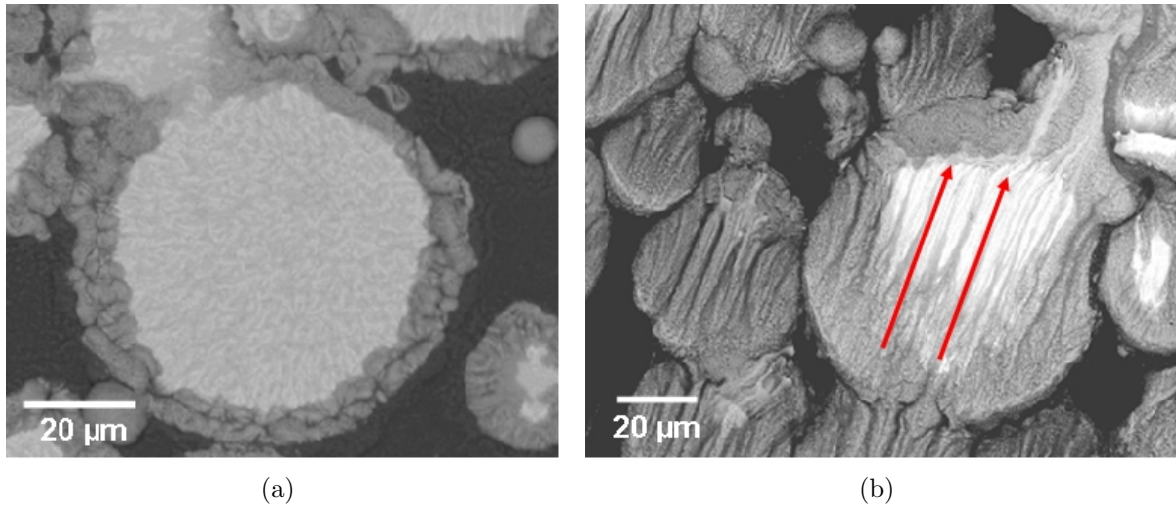


Figure 4.4: Influence of the irradiation angle on the morphology of the interaction layer. SEM observations in BSE mode of a fuel plate irradiated at (a) 90° and (b) at 30° . The direction of the ion beam is indicated by the red arrows.

Table 4.1: Penetration depth of ^{127}I at 80MeV into UMo and Al, calculated with the SRIM code [63].

Angle	90°	60°	45°	30°
UMo	$5.0 \mu\text{m}$	$4.6 \mu\text{m}$	$3.5 \mu\text{m}$	$2.5 \mu\text{m}$
Al	$12.7 \mu\text{m}$	$11.0 \mu\text{m}$	$9.0 \mu\text{m}$	$6.4 \mu\text{m}$

been prepared in the irradiated zone and afterwards been observed with SEM. For samples irradiated using a beam normal to the surface, we can observe the formation of an IDL around UMo particles down to $13 \mu\text{m}$ (figure 4.5(a)). When UMo particles are present at the sample surface and are thinner than $5 \mu\text{m}$, an interaction layer has grown below the particles (figure 4b). This IDL has also been identified above UMo particles that are buried in the Al matrix (figure 4.5(b)). It is important to note that deeper zones are not affected by interaction phenomena. The results are totally in agreement with the SRIM calculations reported in table 4.1.

An asymmetric IDL profile has been detected inside samples irradiated under low angles of 30° and 45° (figure 4.6). At the left side of the biggest particle, the IDL has been formed up to $11 \mu\text{m}$ whereas at the right side only $5 \mu\text{m}$ have been affected by the diffusion. Again, the formation of the IDL is in accordance with calculated values in table 4.1.

In case of the highest ion fluency ($3 \cdot 10^{17}$ ions/cm 2), the profile is slightly different to samples irradiated with moderate ion fluency. In fact, we see in the figure 4.7 a quasi continuous IDL from the surface to the first micrometers under the sample surface.

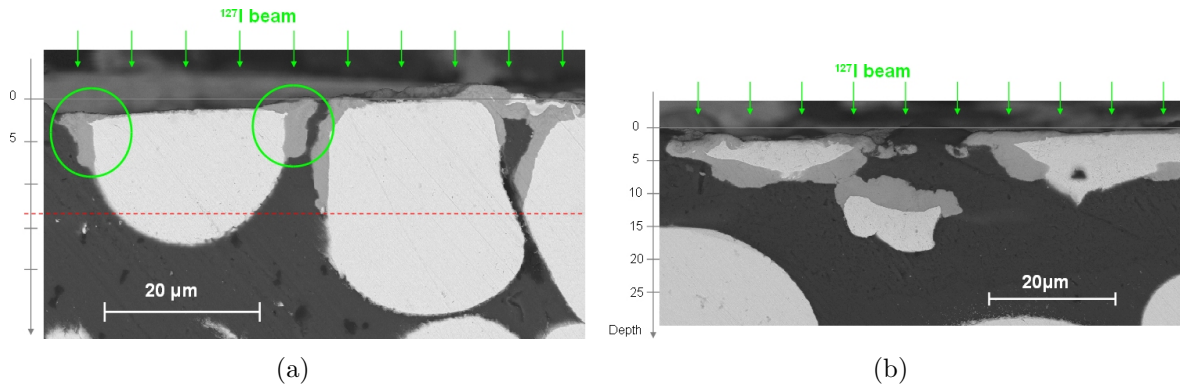


Figure 4.5: SEM observations of transversal cross sections prepared with irradiated UMo/Al samples. The irradiation angle was 90° . The formation of the IDL is in accordance with the penetration depth of ^{127}I in UMo and Al as shown in Table 4.1, respectively.

Phase behavior under irradiation

An X-ray diffraction analysis of the irradiated surface revealed the following phase composition: α -U, γ -UMo, Al, UO_2 and UAl_3 . This composition is in accordance with results obtained before on heavy ion irradiated UMo-Al samples [47, 48, 185]. Nevertheless, the phase composition is not identical to results obtained with neutron diffraction or transmission electron microscopy on in pile irradiated samples: on the one hand, no UAl_4 and no ternary $\text{U}_x\text{Mo}_y\text{Al}_z$ compound has been found [187], on the other hand, the IDL is at least partially crystalline, in contrast to in pile irradiated fuel plates [28, 70]. This behavior indicates, that the irradiation temperature has to be reduced to avoid a recrystallization of the IDL.

Despite the fact, the only UAl_3 has been identified in the diffraction patterns the Al/(U-Mo) ratio as determined using SEM/EDX is always considerable higher than 3. Most often, values between 3.5 and 5 are found. The composition of the IDL is temperature dependent. This temperature dependence was the issue of a further examination and will be discussed in more detail in section 4.1.2.

Furthermore, XRD diagrams of fresh and irradiated fuel have been obtained on both, samples containing atomized (Figure 4.8 and Table 4.2) and ground UMo powder (Figure 4.9 and Table 4.3). The overall α -U content is higher in ground powder when compared with atomized, compare also section 4.7. However, the ratio $U(\alpha)/U(\gamma)$ decreases in both cases after irradiation.

- For samples containing atomized U7wt%Mo powder, the ratio $U(\alpha)/(U(\alpha)+U(\gamma))$ decreases from 17.3% to 4.6%, the γ -UMo cell parameter increases from 3.425Å to 3.431Å.
- For samples containing ground U8wt%Mo powder, the ratio $U(\alpha)/(U(\alpha)+U(\gamma))$ decreases from 31.7% to 16.3%, the γ -UMo cell parameter increases from 3.396Å to 3.423Å.

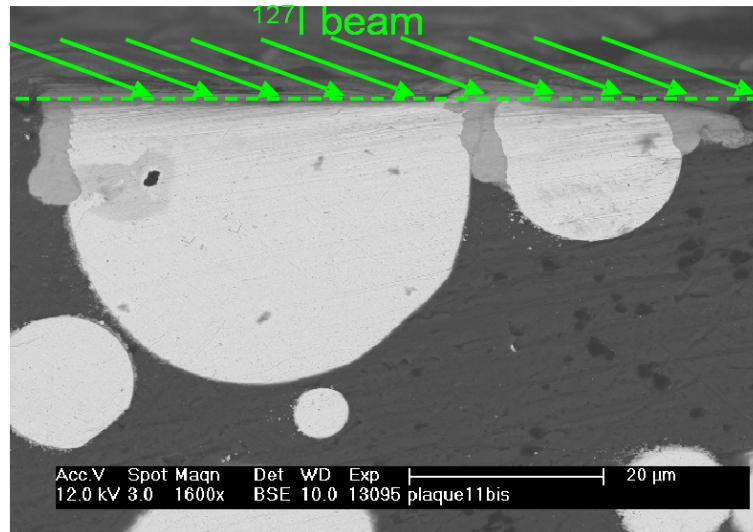


Figure 4.6: Influence of the angle between the sample surface and the ion beam during irradiation on the morphology of the IDL in depth.

The following empirical formula [90, 119] connects the Mo content in γ -phase UMo alloys with the lattice parameter:

$$a_0 = 3.481 - 0.00333 \cdot (Mo) \quad (4.1)$$

where (Mo) is the atom per cent of molybdenum and a_0 is the lattice parameter. The increase of the lattice parameters after irradiation corresponds therefore to a depletion of Mo in the UMo from 7.5wt%Mo to 6.6wt%Mo in the case of atomized powder and from 12.1wt%Mo to 7.8wt%Mo in the case of ground powder. This behavior can be interpreted by the stabilization of the γ -UMo phase during irradiation:



Where $\gamma - \text{UMo}_a$ has a higher Mo content than $\gamma - \text{UMo}_b$. This stabilization of γ -UMo occurs also in-pile [60, 124, 127]. For details on this reaction compare section 2.2.

Influence of the irradiation temperature

During XRD and μ -XRD examinations of heavy ion irradiated samples only UAl_3 has been found. This is somewhat in contrast to results obtained on in-pile irradiated plate type samples in which the IDL was amorphous [70]. Moreover, the composition of the IDL grown by heavy ion irradiation as determined by EDX has an $\text{Al}/(\text{U}+\text{Mo})$ ratio between 3.5 and 5 in the most cases. It can therefore be suspected that a part of the IDL turned amorphous which would lead to an increased background at low scattering angles. However, this signal would have interfered with the amorphous background originating from the glue used for mounting the samples. Furthermore, the samples

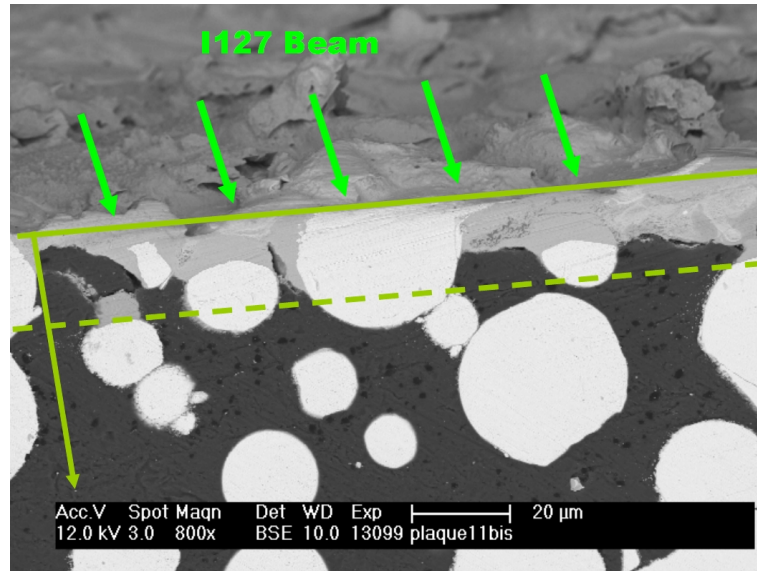


Figure 4.7: Influence of the ion fluency on the IDL in depth. Case of the highest final fluency tested ($3 \cdot 10^{17}$ ions/cm²)

had to be covered with Kapton tape to exclude instrument contamination during most measurements which also gives an amorphous background. Therefore an amorphization of the sample IDL could not be proven using simple XRD setups.

So far higher UMo-Al compounds like $U_6Mo_4Al_{43}$ and UMo_2Al_{20} have not been identified in IDLs grown by heavy ion irradiation - in contrast to what has been found inside samples after annealing [132].

To examine the temperature dependent growth of the IDL by heavy ion irradiation, pure UMo/Al samples have been irradiated at different temperatures. This work has been initiated by Dr. H. Palancher from CEA Cadarache. The post irradiation examinations on these samples are still ongoing, especially complete results on the XRD and μ -XRD examinations are not yet available. However, the result of preliminary cross section analysis is available and will be the topic of this section [136, 188, 189].

In total 5 samples have been irradiated at temperatures between -170°C and 120°C with Iodine at 80 MeV up to a total integral fluency of about $1 \cdot 10^{17}$ ion/cm² which corresponds to a full burn-up in a high performance research reactor. The irradiation conditions can be found in table 4.4.

The results of the surface and cross section analysis using SEM are shown in Figs. 4.10 - 4.14. The sample irradiated at 120°C developed a conventional IDL at the UMo/Al interface during heavy ion irradiation according to the penetration depth of the ions. no excessive surface oxidation is visible (Fig. 4.10).

Inside the sample irradiated at 80°C (Fig. 4.11) also a conventional IDL grew at the UMo/Al interface. However, the surface was affected by considerable UMo oxidation - despite the fact that the irradiation has been performed under the usual high vacuum of $\approx 5 \cdot 10^{-7}$ mbar.

The sample irradiated at -38°C (Fig. 4.12) did not develop any IDL at the UMo/Al interface during irradiation. Instead, the UMo particle surface picked up a lot of oxygen during irradiation and shows signs of beginning creep.

Table 4.2: Comparison of the composition of the irradiated and the non irradiated zone of an atomized U7wt%Mo fuel plate irradiated at the maximum ion fluency. The weight fractions had been deduced from the semi-quantitative analysis of the μ -XRD diagrams depicted in Figure 4.8 using the Rietveld method [177, 178]. The Mo content has been calculated using the lattice parameter (LP) and equation 4.1.

	Weight fractions (%)					U(α)/ (U(α)+U(γ)) (%)	γ -UMo LP(Å)	Mo cont. (wt%)
	U(α)	UO ₂	γ -UMo	Al	UAl ₃			
Non irradiated	13	3	62	22	-	17.3	3.425	7.5wt%
Irradiated	3	9	62	22	4	4.6	3.431	6.6wt%

Table 4.3: Comparison of the composition of the irradiated and the non irradiated zone of an ground U8wt%Mo fuel plate. The weight fractions had been deduced from the semi-quantitative analysis of the XRD diagrams depicted in Figure 4.9 using the Rietveld method [177, 178, 186].

	Weight fractions (%)				U(α)/ (U(α)+U(γ)) (%)	γ -UMo LP(Å)	Mo cont. (wt%)
	U(α)	UO ₂	γ -UMo	Al			
Non irradiated	20	27	43	10	31.7	3.396	12.1wt%
Irradiated	8	25	41	26	16.3	3.423	7.8wt%

Figure 4.13 shows the sample irradiated at -75°C . In this case surface oxidation (red circles) and UMo creep occurred (blue circles). Fig. 4.13(b) shows the cross section that corresponds to surface oxidation and creep as shown with the red circles, Fig 4.13(c) corresponds to the case marked with the blue circles. Here, voids have formed inside the UMo particles just below the surface.

The sample irradiated at -170°C is shown in figure 4.14. Here, no surface oxidation is visible. However, considerable UMo creep occurred. Thereby, porosities formed inside the UMo (Fig. 4.14(b)) and the sample surface has been modified due to UMo surface creep ((Fig. 4.14(c))).

4.2 Oxidized particles

All MAFIA-I samples with addition of second elements to the matrix have been produced with and without an oxide layer around the UMo particles. The particles have been oxidized by heating while being exposed to air. In this section the general effect of oxidizing atomized UMo particles on the fuel behavior will be discussed. Even-

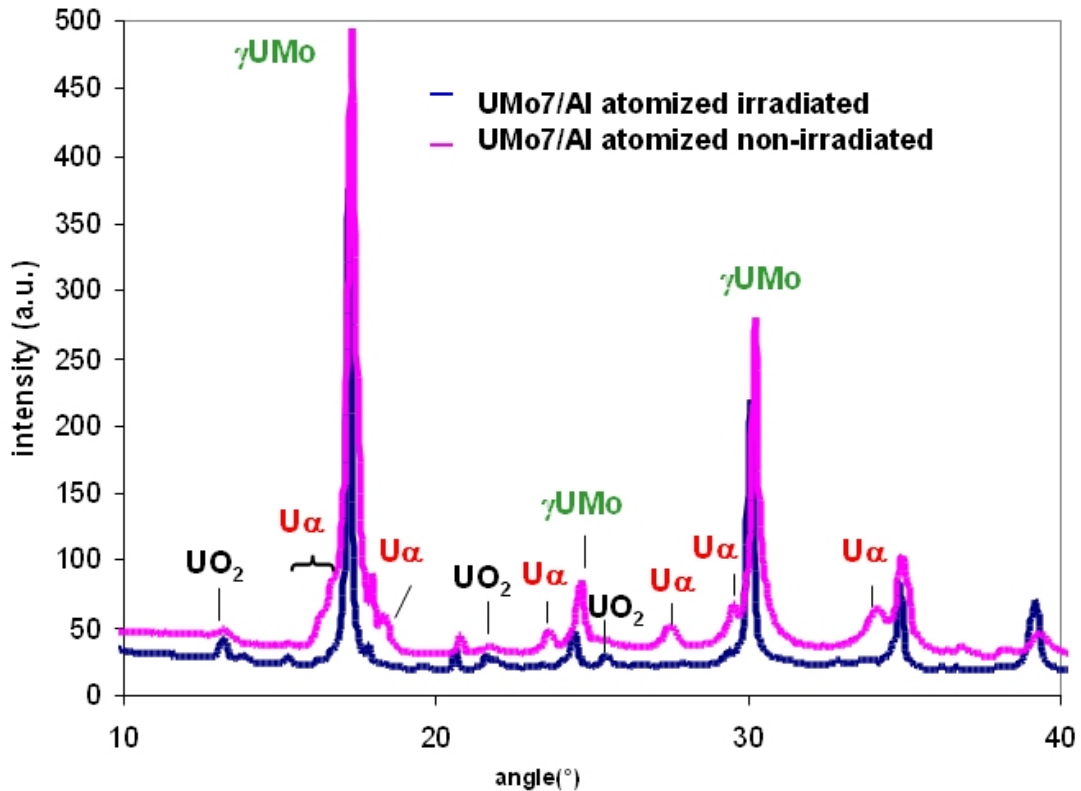


Figure 4.8: μ -XRD diagram of an irradiated and non-irradiated atomized U7Mo/Al sample. The α -U content is strongly decreased after irradiation.

tual interactions between the different matrix additions and oxidized particles will be discussed in the section dealing with the particular matrix admixture. Since the occurrence of oxide is an intrinsic effect of ground UMo powder it will be discussed in the section dealing with this special kind of powder (section 4.7).

At first the sample microstructure before irradiation with heavy ions will be regarded. Afterwards, the influence of the oxide layer on the fuel behavior during heavy ion irradiation will be discussed.

4.2.1 Pre-irradiation state

Two classes of oxide layers have been found around the UMo particles:

- Thin oxide layers with a thickness $\leq 1\mu\text{m}$ have been found around some of the particles that have not been intentionally oxidized. In this case, the oxidation must have occurred spontaneously during the sample manufacturing process. Already the thin oxide layers reveal cracks (compare Fig. 4.15).
- Thicker oxide layers with a thickness up to $5\mu\text{m}$ have been found around the UMo particles that have been oxidized on air by heating. This kind of oxide layer is very brittle and shows large cracks (compare Fig. 4.16).

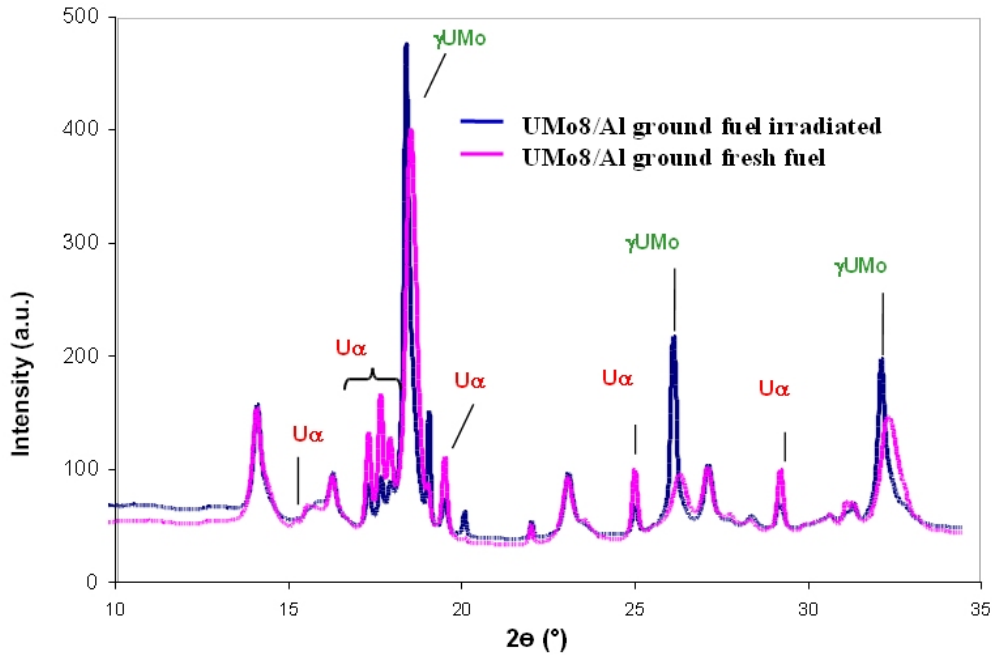


Figure 4.9: XRD diagram of an irradiated and non-irradiated ground U8wt%Mo/Al sample. The α -U content is strongly decreased after irradiation [186].

Furthermore the oxidized UMo particles tend to loose contact with the matrix: gaps between the UMo and the oxide layer have been observed (Fig. 4.16). The oxide layer sticks rather to the Al matrix than to the UMo particles. This behavior is most obvious at spots where a UMo particles has been ripped out during the polishing: the oxide layer remained inside the resulting hole (compare Fig. 4.17).

Cracks appear inside the thin and thicker oxide layers but the tendency to form gaps between the UMo and the Al matrix has only been found in case of thicker oxide layers. Therefore the oxide layer has already been cracked during the sample manufacturing process. However, the appearance of gaps between the UMo and the Al matrix is most likely also influenced by the forces occurring during the polishing process. In this case the sample preparation process would have influenced the sample behavior. It is likely that those kind of gaps will not be present in the bulk material.

Table 4.4: Irradiation conditions of the samples used during the temperature test.

Sample	Flux(10^{12} ion/($\text{cm}^2\cdot\text{s}$))	Irradiation temperature ($^{\circ}\text{C}$)
18	7	120
C11	1.8	80
C18	1.35	-38
C21	1.35	-75
S2	1.35	-170

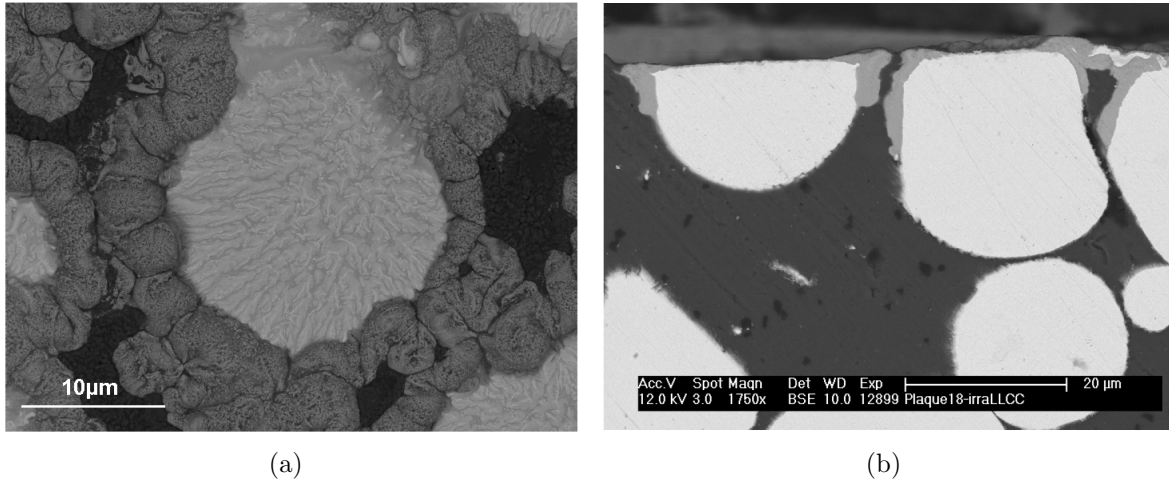


Figure 4.10: Surface analysis (a) and cross sections (b) of the sample 18 irradiated at 120°C. A conventional IDL formed according to the penetration depth of the heavy ions [189].

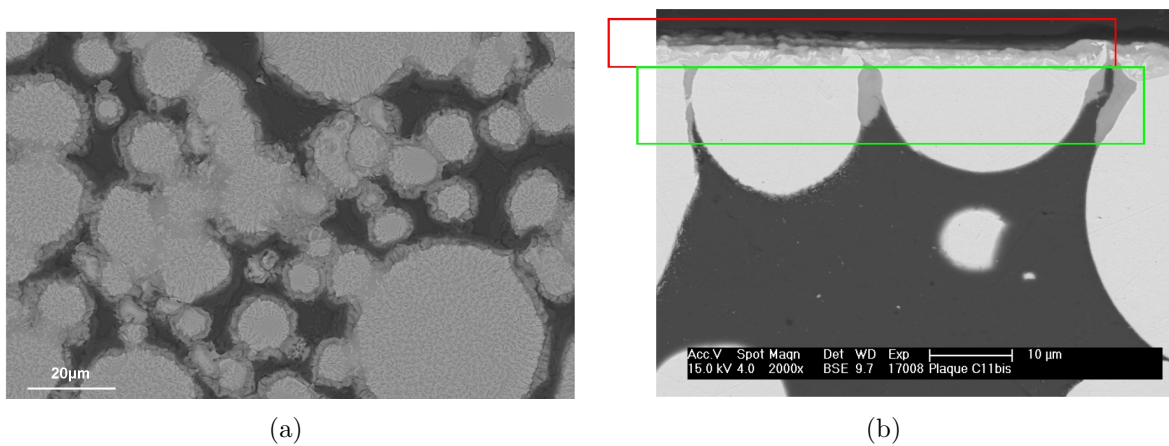


Figure 4.11: Surface analysis (a) and cross sections (b) of the sample C11 irradiated at 80°C. A conventional IDL formed according to the penetration depth of the heavy ions (green frame). However, considerable surface oxidation occurred (red frame) [189].

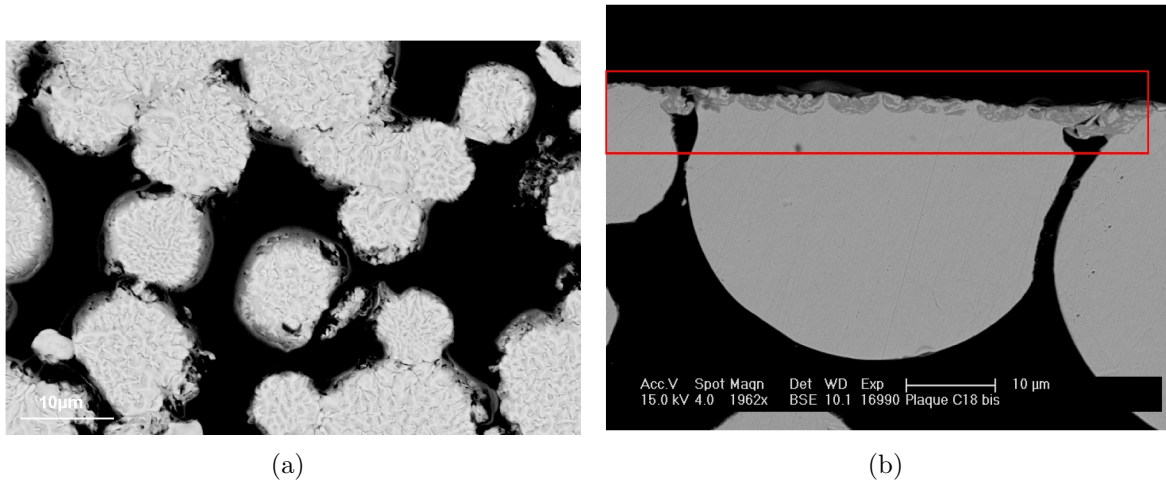


Figure 4.12: Surface analysis (a) and cross sections (b) of the sample C18 irradiated at -38°C . No sign of any UMo-Al interaction is visible. Instead, considerable surface oxidation occurred (red frame) [189].

The α -U, γ -UMo and UO_2 contents of each sample have been determined - compare table 4.5. In general and as expected the UO_2 content found inside the samples that have been intentionally oxidized is higher than in the non-oxidized samples. In average $\text{UO}_2/(\alpha\text{-U}+\gamma\text{-UMo}+\text{UO}_2)$ ratios of $24\pm 9\%$ and $10\pm 5\%$ have been found. The $\alpha\text{-U}/(\alpha\text{-U}+\gamma\text{-UMo}+\text{UO}_2)$ has also been determined for the oxidized and non-oxidized samples. Values of $10\pm 4\%$ and $8\pm 3\%$ have been found, respectively. This behavior is fully in accordance with the production parameters: the oxidation has been performed by heating the UMo powder which also results in a decomposition of the γ -UMo into α -U (compare section 2.2.2). However, no signs of cellular decomposition have been found which is most likely due to the low amount of decomposition products.

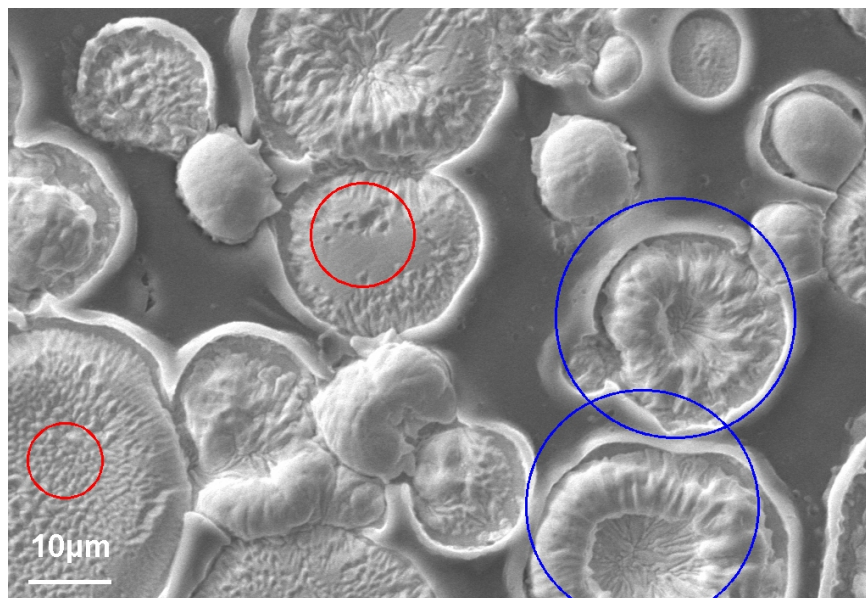
Table 4.5: α -U, γ -UMo and UO_2 phase composition of the MAFIA-I samples prepared with atomized powder with and without intentional pre-oxidation. The values have been determined using laboratory scale XRD together with Rietveld analysis.

	$\text{UO}_2/(\alpha\text{-U}+\gamma\text{-UMo}+\text{UO}_2)$	$\alpha\text{-U}/(\alpha\text{-U}+\gamma\text{-UMo}+\text{UO}_2)$
With oxide layer	24 ± 9	10 ± 4
Without oxide layer	10 ± 5	8 ± 3

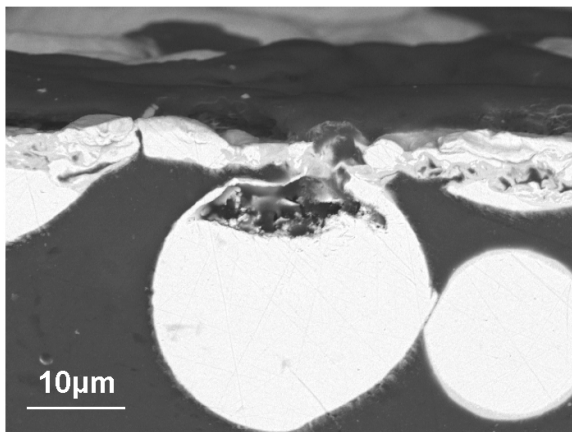
4.2.2 Post-irradiation state

The samples have been irradiated with Iodine at 80 MeV to an integral ion fluency of $1\cdot 10^{17}$ ions/cm² at the MLL tandem accelerator in Garching.

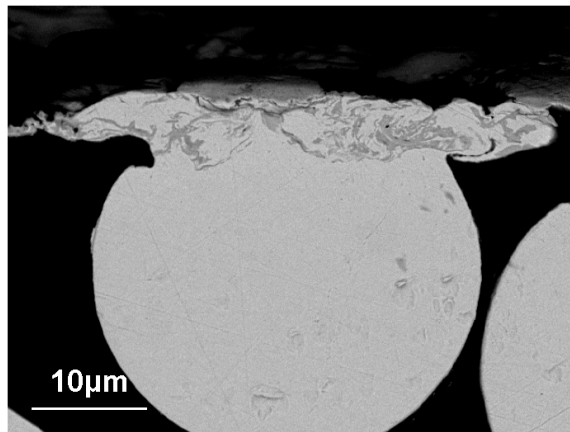
The behavior of the samples with a large oxide layer around the UMo particles differed considerable from the behavior of the samples containing atomized powder without



(a)

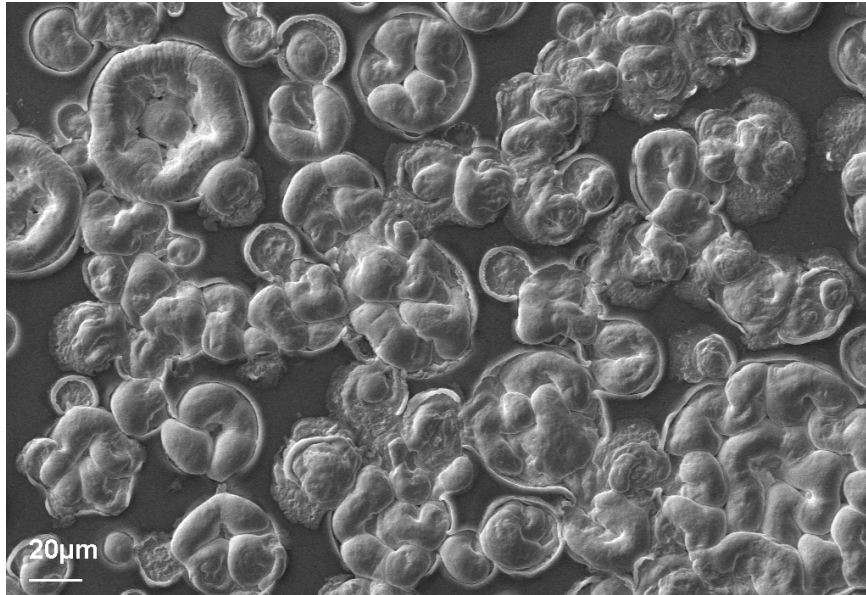


(b)

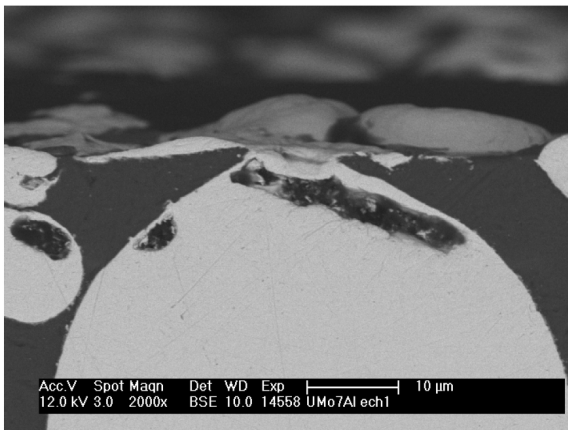


(c)

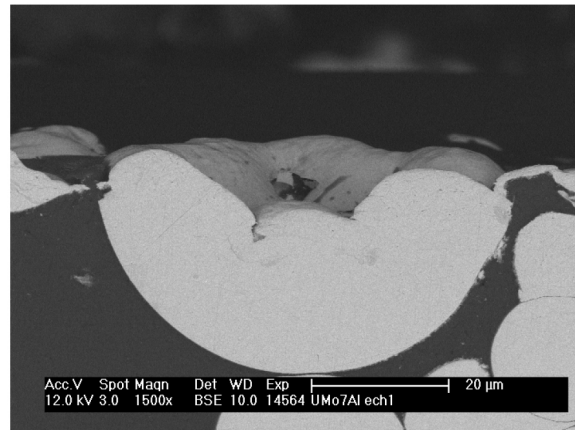
Figure 4.13: Surface analysis (a) and cross sections (b,c) of the sample C21 irradiated at -75°C . Surface oxidation (red) and UMo creep occurred (blue circles). Fig. (b) corresponds to surface oxidation and creep as shown with the red circles, Fig (c) corresponds to the case marked with the blue circles [189].



(a)



(b)



(c)

Figure 4.14: Surface analysis (a) and cross sections (b,c) of the sample S2 irradiated at -170°C . No surface oxidation is visible. Considerable UMo creep occurred. Thereby, porosities formed inside the UMo (b) and the sample surface has been modified due to surface creep (c) [189].

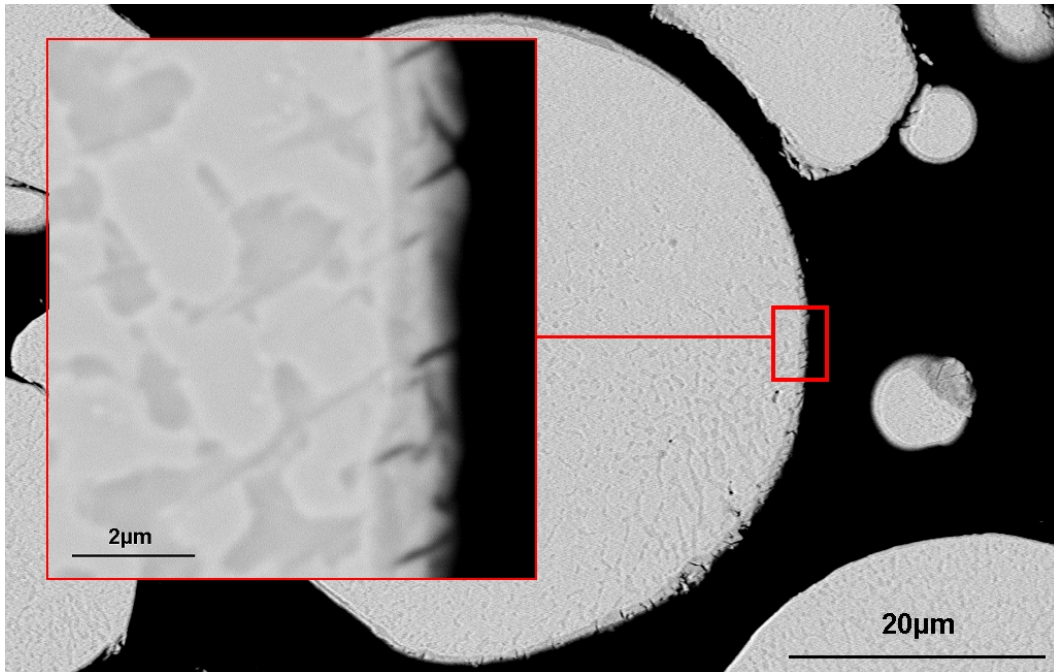


Figure 4.15: SEM picture of a thin oxide layer covering a UMo particle. The oxide layer reveals cracks.

or with only a small oxide layer and from the samples containing ground powder. In contrast to the other samples examined a “glittering” of the irradiated surfaces has been observed upon visual inspection after heavy ion irradiation. A more detailed SEM analysis including also cross sections through the irradiated surface prepared at CEA revealed that the UMo particles had frequently lost contact with the Al matrix and stick out of the surface (compare Fig. 4.18). Some particles seem even to have fallen of.

However, particles covered with thin oxide layers did not loose contact with the Al matrix during irradiation. In these cases the oxide layer got incorporated into the IDL that grew during irradiation (compare Fig. 4.19). The oxide has not moved during irradiation relative to the original UMo/Al interface: it staid at the original position.

XRD analysis of the irradiated samples confirmed that in addition to a slightly increased UO_2 content due to surface oxidation the only new phase was UAl_3 . It can therefore be concluded that the IDL consists mainly of this phase.

4.2.3 Discussion

Samples prepared with atomized UMo powder that has been oxidized prior to plate manufacturing by heating on air have been examined before and after irradiation with heavy ions. A thick oxide layer with cracks has been found to have grown around the UMo particles. The oxide layer tends to loose contact with the UMo particles which results in particle ripped out of during polishing or the formation of gaps between the UMo particles and the oxide layer. It is noteworthy that in these cases the oxide layer rather sticks to the surrounding Al matrix than to the UMo particles. Comparing

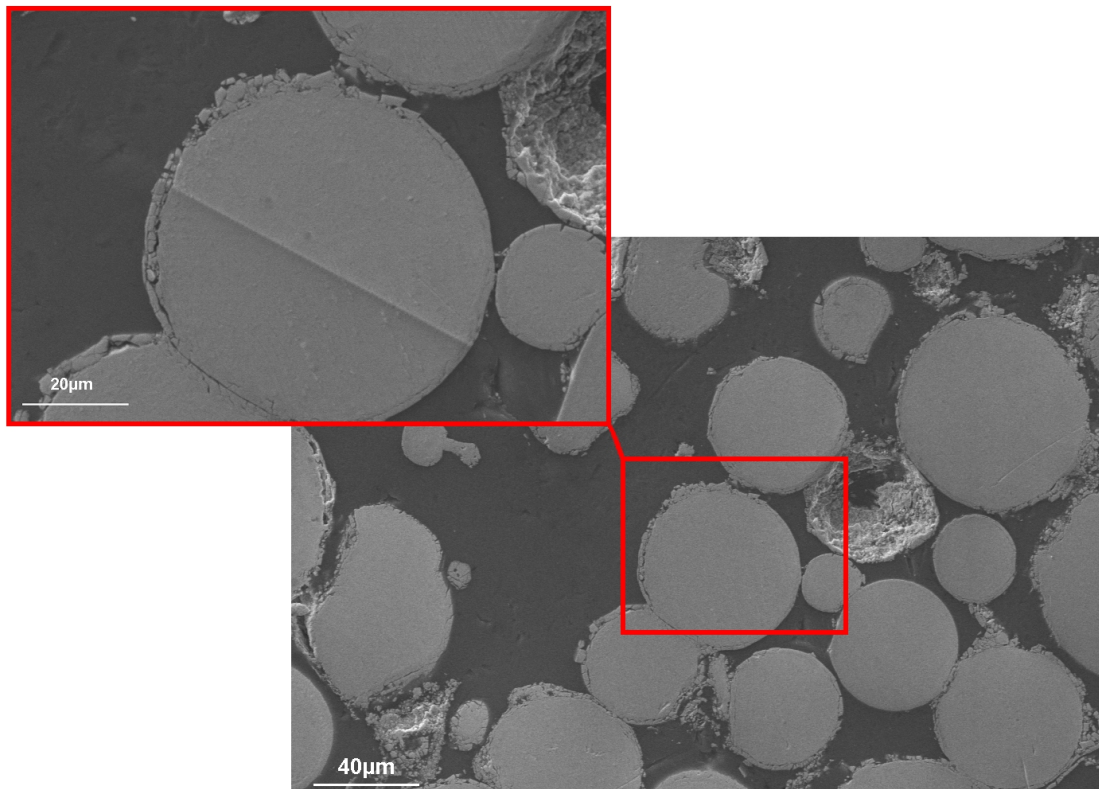


Figure 4.16: SEM picture of a thick oxide layer. The layer is very brittle and reveals cracks. The thicker oxide layers layer tend to loose contact with the UMo particles.

XRD results of samples that have been intentionally oxidized to those which have not a higher UO_2 content together with a higher α -U content is found within the former. After irradiation a IDL formed around the UMo particles that consists mainly of UAl_3 . Thin oxide layers get incorporated into the IDL close to the original position. However, particles covered with thick oxide layers tend to loose contact with the Al matrix during irradiation and stick out of the irradiated surface.

An improved irradiation performance - especially a reduction of the IDL growth - of samples prepared with oxidized powder can not be deduced from the heavy ion irradiation experiments.

It can be concluded that the improved swelling behavior of in-pile irradiated plates results not simply from a reduction of the IDL growth but from an improved fission gas retainment [144,161]. The oxide layer gets incorporated into the IDL during burn-up and may positively influence its ability to retain fission gases.

At this point, the drawback of using heavy ion irradiation as out of pile technique to examine the behavior of UMo/Al nuclear fuels becomes visible: the build-up of UMo-Al interaction can be emulated very well using Iodine at 80MeV. However, the accumulation of gaseous fission products which influence the fuel performance to great extent is not simulated by this method. Further experimental steps are therefore needed to emulate also the fission gas behavior - e.g. by direct implantation of Xe ions into a previously grown IDL using a second particle accelerator.

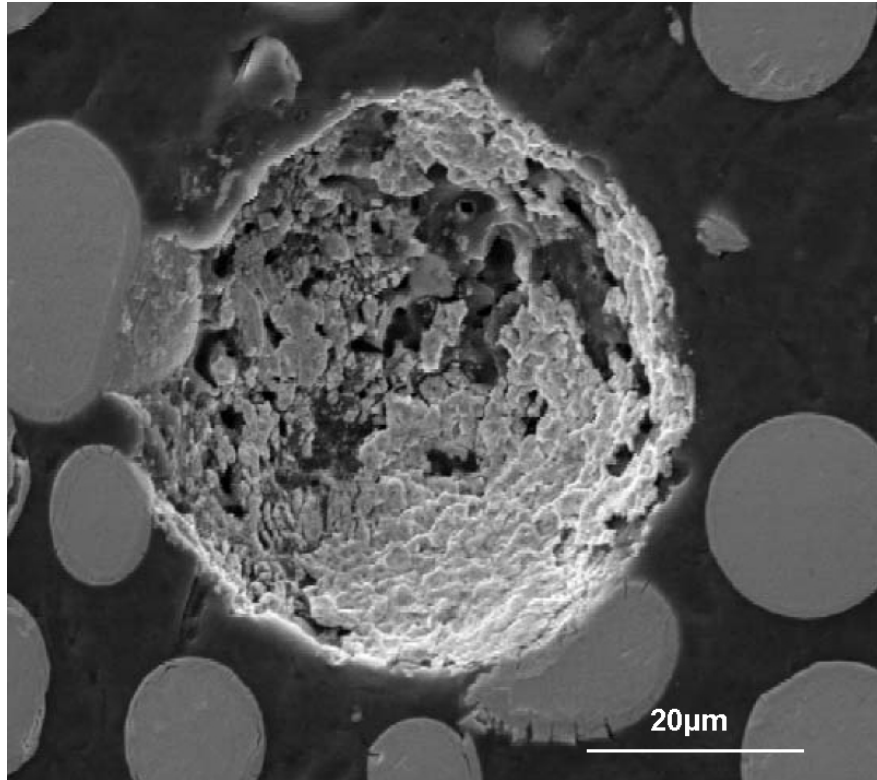


Figure 4.17: SEM picture of a sput where a particle has been ripped-out during polishing. A part of the oxide layer around the UMo particle remained inside the hole indicating that the oxide layer is very brittle and has a weak adhesion to the UMo particle.

4.3 UMo/AlSi

4.3.1 Sample production

It has been shown that Silicon limits the formation of the undesired diffusion layer forming during in-pile irradiation of UMo/Al dispersion test fuel plates. This section will focus on the effects of Silicon addition (2, 5 and 7wt%) into the Al matrix and the behavior under irradiation of the Si rich diffusion layer (SiRDL) grown around the UMo particles during fuel plate production. The results will be compared to in-pile irradiated samples (IRIS-3 [190], RERTR-6 [191] and RERTR-7 [192]). The results on the phase composition of the SiRDL and the behavior of the samples during irradiation with heavy ions as well as the interpretation of the data would not have been possible without our partners from CEA. The results have been presented before in two common conference contributions [193, 194].

Four cases are compared: UMo/AlSi2 (2wt% of Si into the Al matrix), UMo/AlSi5 UMo/AlSi7 and a standard UMo/Al used as reference. Furthermore, the influence of an oxide layer around the UMo particles on the formation of the SiRDL during fuel plate production will be discussed.

The UMo/AlSi2 miniplate has been produced using commercially available ready mixed powder (Al and Si powder mixed, sintered and crushed; the same powder has been used

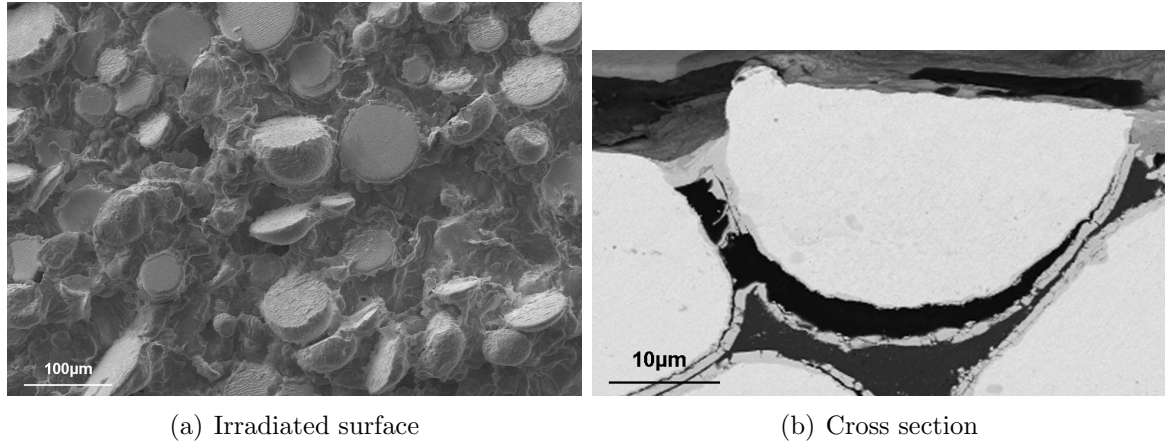


Figure 4.18: Surface analysis (a) and cross sections (b) reveal that UMo particles with huge oxide layers tend to loose contact with the matrix during heavy ion irradiation and fall out of the irradiated surface.

for e.g. for IRIS-3 and IRIS-TUM). The UMo/AlSi5 and UMo/AlSi7 samples have been produced by blending very fine (\sim mesh 325) Al and Si powders of the highest purity. The mean particle size of the aluminum and the silicon powder have been determined using a laser granulometer and found to be $21.4 \mu\text{m}$ and $7.3 \mu\text{m}$, respectively (compare Table 4.6 and Figure 4.21).

Figure 4.20 shows a SEM picture of the blended AlSi7 powder before sample manufacturing. The grain size of the particles is in accordance with values obtained using a laser granulometer. The Al powder has been produced by atomization, the Si powder by grinding.

All miniplates have been manufactured with the standard CERCA procedure described in section 3.1 which has also been used for IRIS and IRIS-TUM full sized plates production. The IRIS-3 and IRIS-TUM full size plates were manufactured with the same Al2%Si pre-alloyed powder like the 2wt%Si samples presented in this study. The rolling temperature and the heat treatment were the same. However, there are certain differences concerning the UMo powder (ground powder with IRIS-TUM [145]).

Table 4.6: Particle size of Al and Si powder used to produce the 5wt%Si and 7wt%Si miniplates determined by a laser granulometer.

Powder	Mean particle size	10% Diameter	90% Diameter
Silicon	$7.3 \mu\text{m}$	$1.2 \mu\text{m}$	$15 \mu\text{m}$
aluminum	$21.4 \mu\text{m}$	$10 \mu\text{m}$	$30 \mu\text{m}$

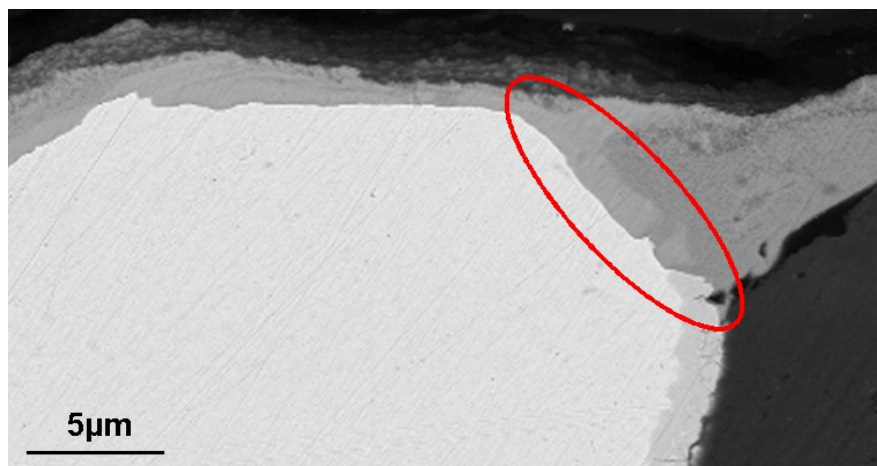


Figure 4.19: SEM/BSD picture of a thin oxide layer (medium gray) that got incorporated into the IDL (dark gray) that formed during heavy ion irradiation at the UMo (light gray) Al (black) interface.

4.3.2 Characterization before irradiation

SEM/EDX analyses

Figure 4.22 compares the three miniplates containing 2wt%Si, 5wt%Si and 7wt%Si using SEM and EDX mapping. Three different parts can be discussed:

- The growth of a Si rich layer around the UMo particles in the 5wt% and 7wt%Si case during production of the miniplates
- The presence of Si precipitates in the Al-matrix
- The occurrence of USiAl particles inside the matrix

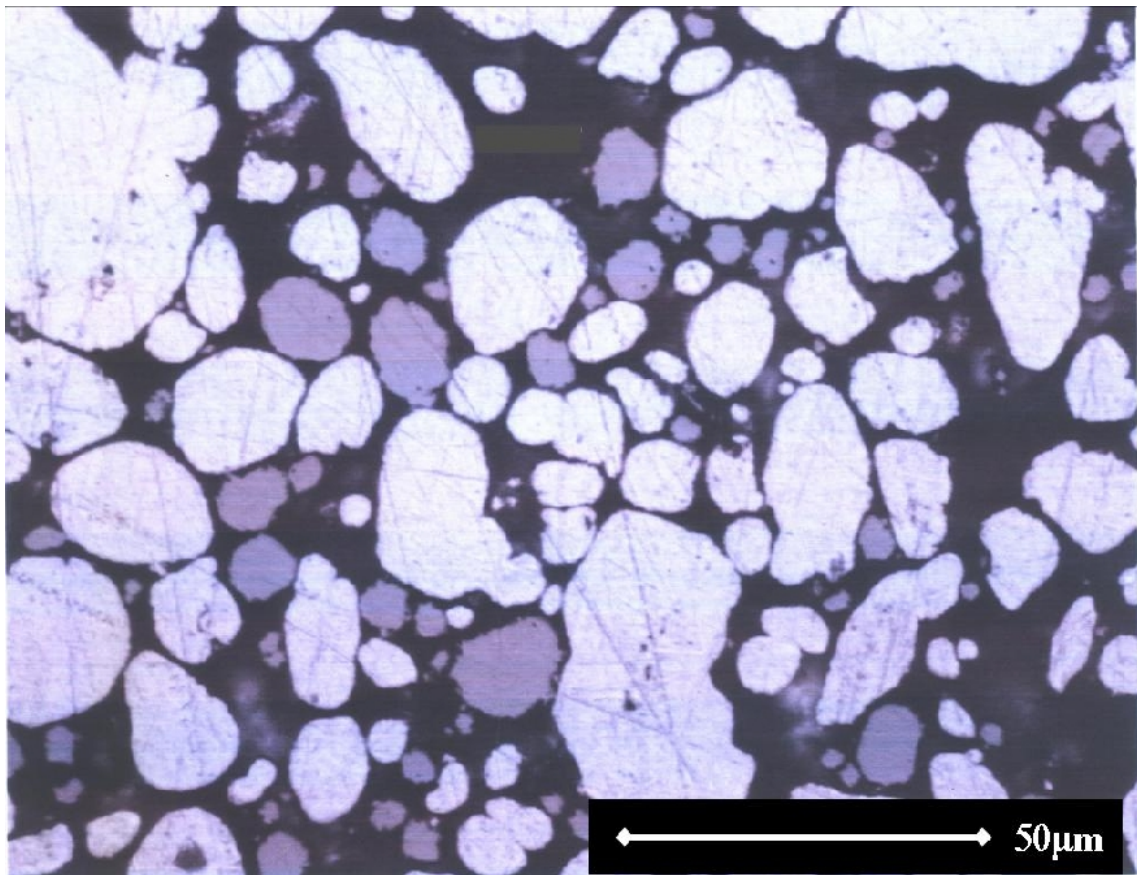
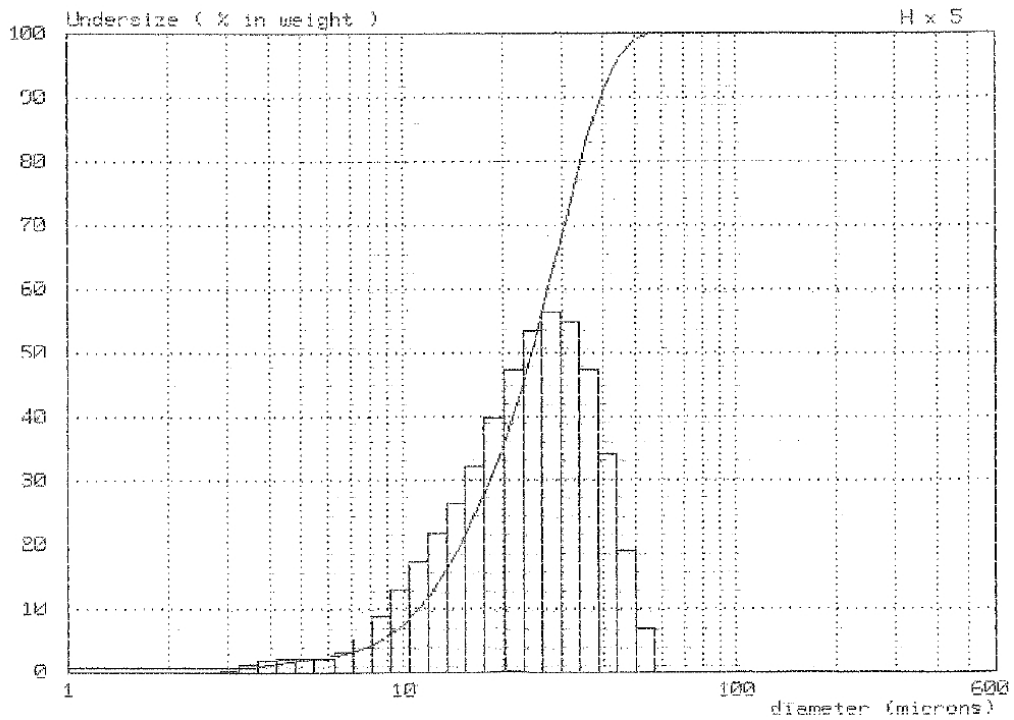
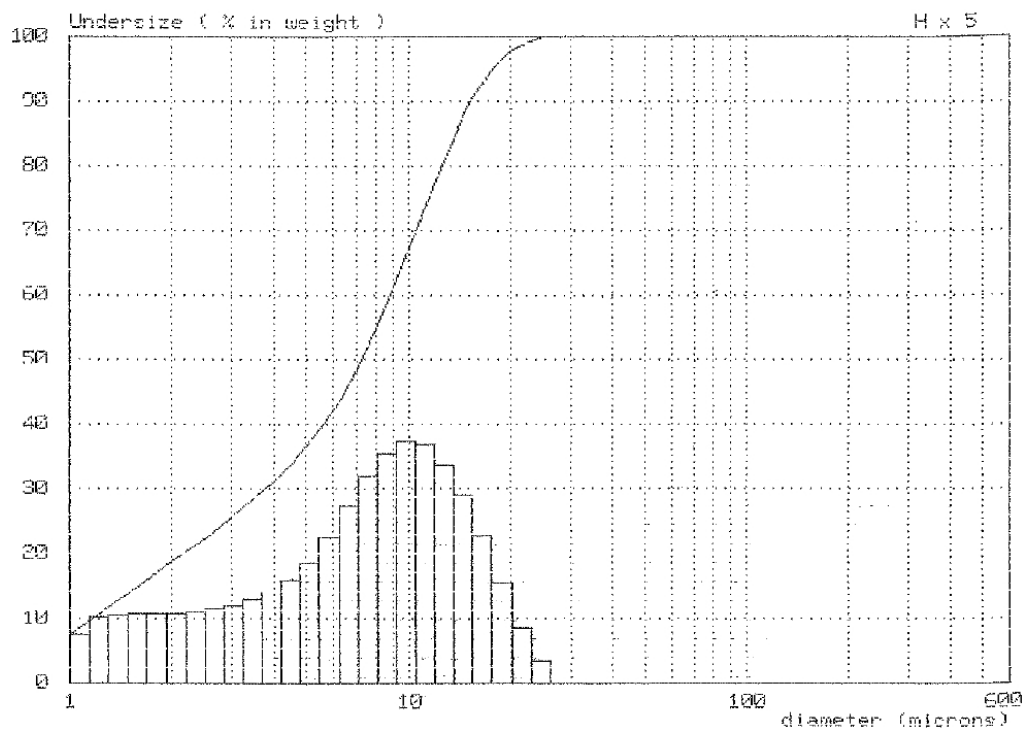


Figure 4.20: SEM picture of blended Al 7wt%Si powder before sample manufacturing. Si grains appear grey, Al grains appear white. The Al powder has been produced by atomizing, the Si powder by grinding. The picture has been provided by CERCA.



(a) Aluminum



(b) Silicon

Figure 4.21: Results of a laser granulometry measurement performed on the Al (4.21(a)) and Si (4.21(b)) powder used for sample manufacturing. The mean particle size is $21.4 \mu\text{m}$ for the Al and $7.3 \mu\text{m}$ for the Si powder which is in good agreement with values given by the supplier [171].

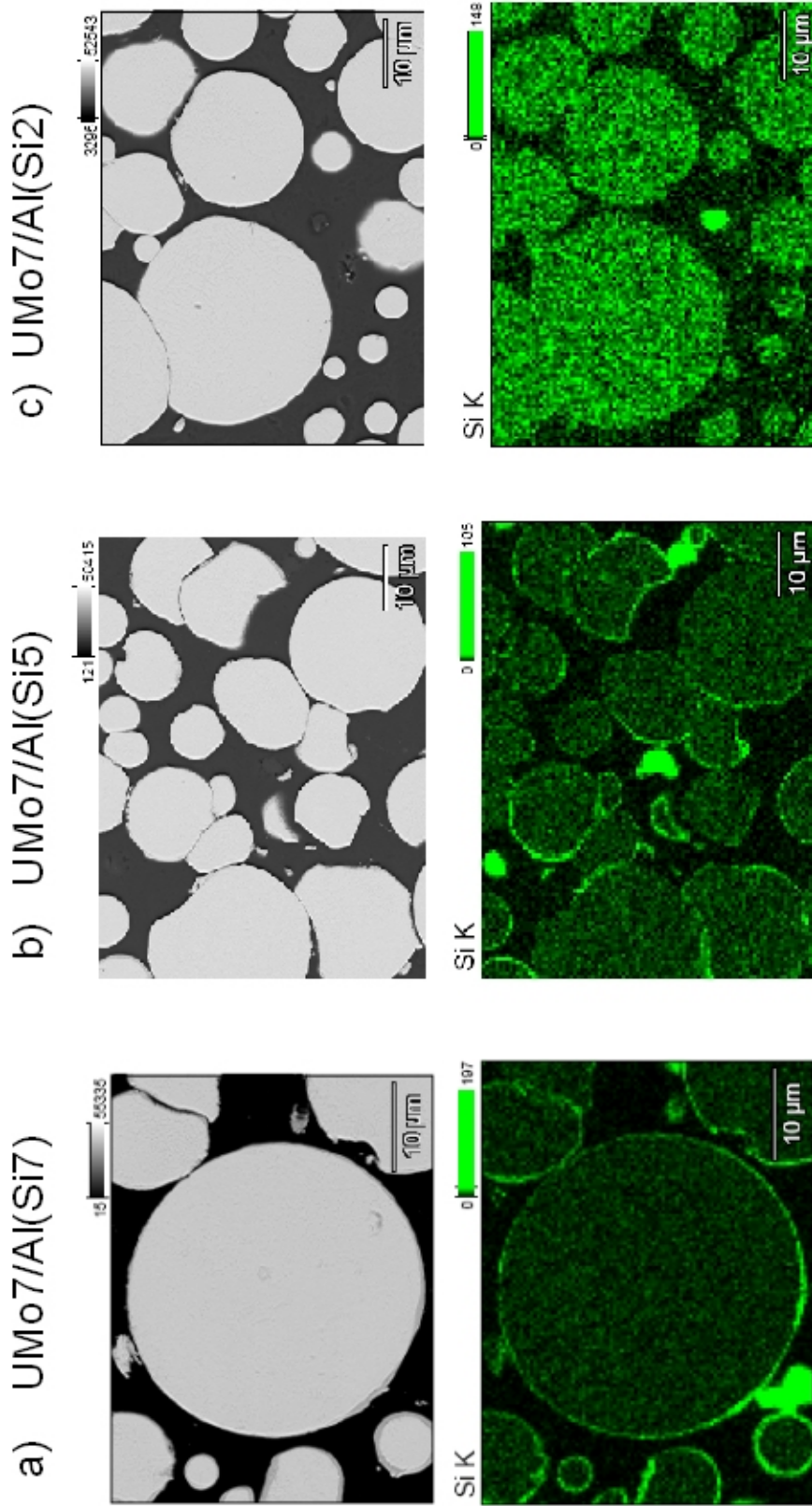


Figure 4.22: Comparison between the Si distribution in three not pre-oxidized UMo/AlSi miniplates. The pictures show BSE images with the corresponding EDX Si-K α maps. In the 7wt%Si and 5wt%Si case a SiRDL formed around the UMo particles. This is not the case in the 2wt%Si sample.

In the 2wt%Si case usually no Si rich layer has been observed around the UMo particles after hot rolling, even if a Si precipitate is located very close to the UMo (compare Fig. 4.23). Rarely a very thin Si rich layer ($< 0.5 \mu m$), limited to only a few grains and a very small fraction of the affected UMo grain surface has been observed. This behavior is consistent with data that has been presented before [186]. However, in the case of the IRIS-3 plate (Al2wt%Si), which was manufactured with the same AlSi powder used for the 2wt%Si sample in our study, a SiRDL was observed but not on all the UMo particles (heterogeneous presence) [195, 196]. The difference between the IRIS-3 plates and the case regarded here may be related to the difference in process parameters and the grain size of the UMo powder.

In the 5wt%Si case each particle is at least partially covered by a Si rich layer

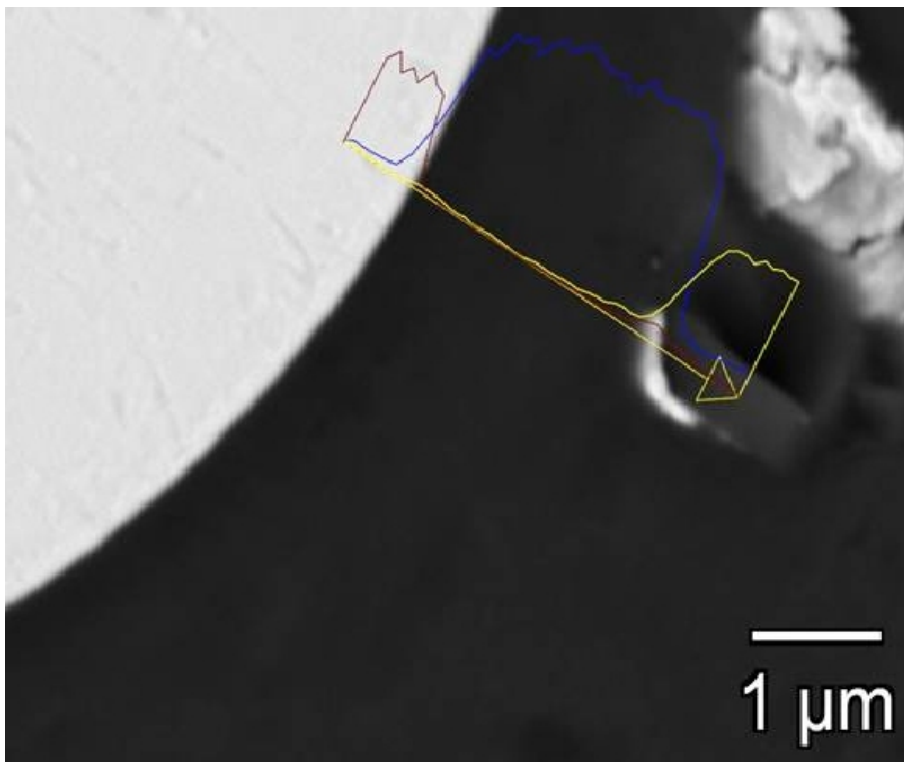


Figure 4.23: Si precipitate close to a UMo particle in the 2wt%Si case. The blue line indicates the Al content, the red line the U content and the yellow line the Si content. No Si rich layer has formed around the UMo particle

(compare Fig. 4.22 and 4.24(a)). However, smaller particles reveal a thicker and more homogenous layer than bigger particles. The biggest particles are frequently only partially covered by the Si-rich layer. The thickness of the layer varies from $0.4 \mu m$ to $1.2 \mu m$.

In the 7wt%Si case each particle is completely covered by the SiRDL (compare Fig. 4.22 and 4.24(b)). However, also here the layer around the smaller particles is thicker than around the bigger particles. In general the thickness of the Si rich layer is not very homogenous varying between $0.4 \mu m$ and $2 \mu m$.

The Si rich layer can also be found around particles very close to each other ($< 1 \mu m$), compare Fig. 4.25.

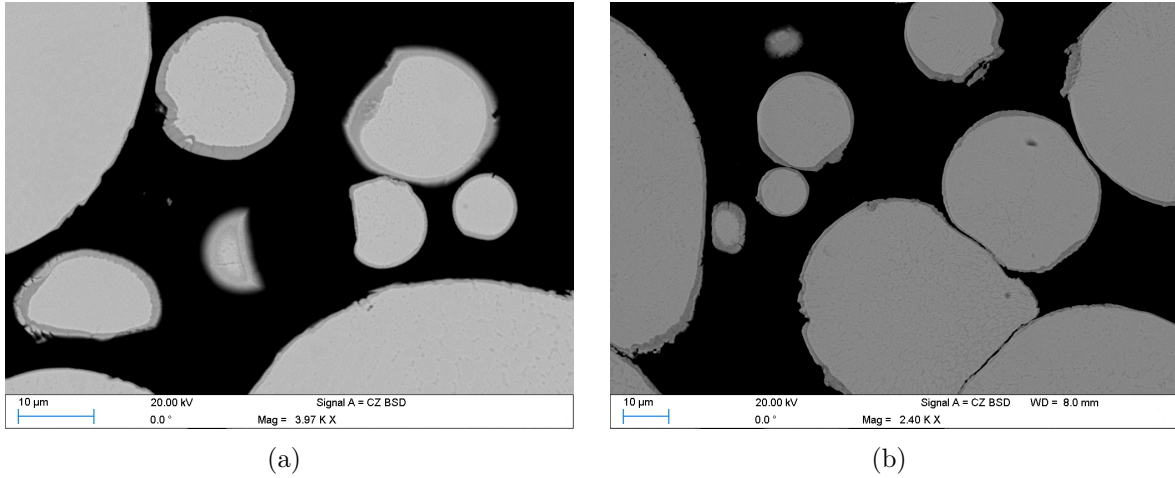


Figure 4.24: Si rich layer around UMo particles, BSE image. 4.24(a) shows the 5wt%Si case, 4.24(b) shows the 7wt%Si case.

Note that in general the layer is thicker for smaller particles (i.e. when looking at the top or the bottom of a cut through particle). This effect has been taken into account with the values given above. The composition of the Si rich layer has been determined by EDX analyses. Values are given in Table 4.7. The composition of the layer appears to be stable and is the same for the 5wt%Si and 7wt%Si case. Note that since the layer is sometimes very thin the probed volume may be influenced by the surrounding aluminum matrix such indicating a too high Al content inside the layer. However, the exact phase composition has been found using μ -XRD (see below).

Table 4.7: Elementary composition of the SiRDL

Si content wt%	O	Si	Al	Mo	U
5	13.7 ± 2.1	41.9 ± 2.3	7.9 ± 1.7	5.0 ± 0.5	31.8 ± 1.9
7	14.1 ± 2.7	39.0 ± 0.3	12.6 ± 4.1	4.7 ± 0.6	29.7 ± 1.7

XRD analyses

Laboratory scale and μ -XRD analyses with a full Rietveld refinement have been carried out on the samples before irradiation to access the crystallographic phase composition. The following phases have been found using a laboratory scale XRD setup:

- γ -UMo
- Al
- UO₂, slight surface contamination
- traces of α -uranium

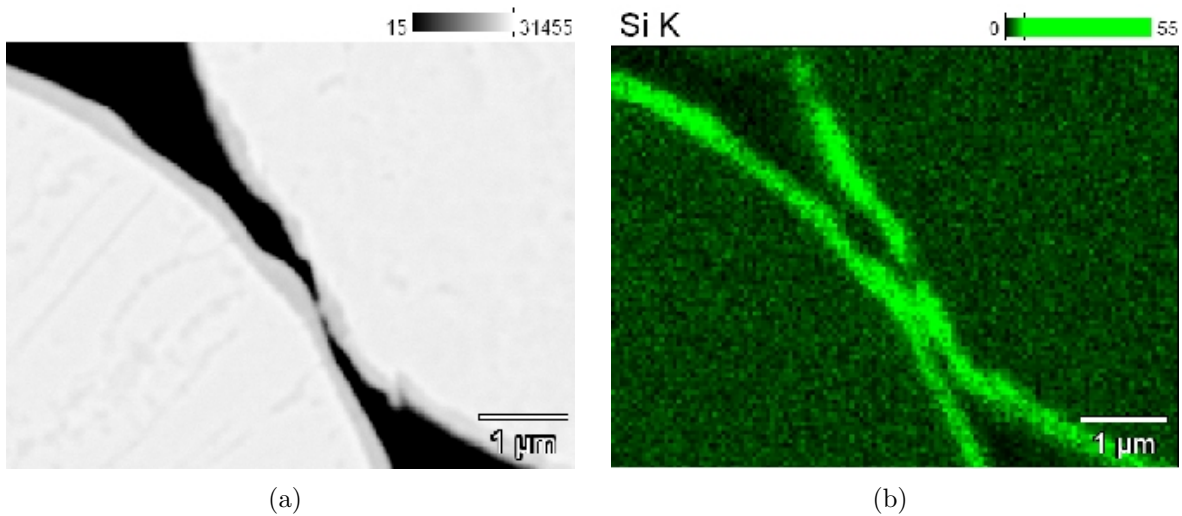


Figure 4.25: In the 5wt%Si and the 7wt%Si case, a Si rich layer is also present at spots, where two UMo particles are very close to each other. (a) BSE image, (b) EDX Si K- α mapping. The images show the 7wt% Si case

No traces of Si or Si containing phases could be found indicating that the global amount of Si or Si rich phases is very low. Therefore the SiRDL has been examined using the μ -XRD technique described in section 3.3 and [182, 183]. Note that for preserving the SiRDL during this operation, an Al layer around the particles has been kept.

Six particles have been characterized by XRD in transmission mode using a micro-focused X-ray beam ($3 \cdot 3 \mu\text{m}^2$) at the micro-XAS beamline at SLS [179] (Swiss Light Source, Villigen, Switzerland) during a beam time obtained by CEA. The X-ray beam energy was set to 19.7keV. Figure 4.26 shows an example of the data collected at the periphery of the particles. The size of the X-ray beam exceeded the thickness of the SiRDL which was lower than $2 \mu\text{m}$. Therefore the analyzed volume was not strictly restricted to the SiRDL but some parts of the UMo core and of the Al were also probed. UO_2 pollutions have also been observed.

In each studied sample the presence of USi_Y phase(s) exhibiting broad X-ray peaks has been observed. This indicates that:

- different USi_Y phases with strongly overlapping peaks can be found in the SiRDL,
- these phases are characterized by small sizes of the crystallites (a few tens of nanometers) and/or cell parameter gradients.

On the one hand, no significant amount of $\text{U}(\text{Al},\text{Si})_3$ or of any ternary phase $\text{U}_x\text{Mo}_y\text{Al}_z$ has been identified in the diagram 4.26(c), and very little in the other diagrams collected on these particles.

On the other hand, the presence of the USi_{2-x} or U_3Si_5 (P6/mmm, $a=b=3.89\text{\AA}$, $c=4.017\text{\AA}$) phase could be assessed. However this phase alone does not reproduce the measured XRD diagram.

Among all the previously reported USi and UAlSi crystal structures, only one was found to improve significantly the fit of the measured data: stoichiometric USi_2 [197, 198].

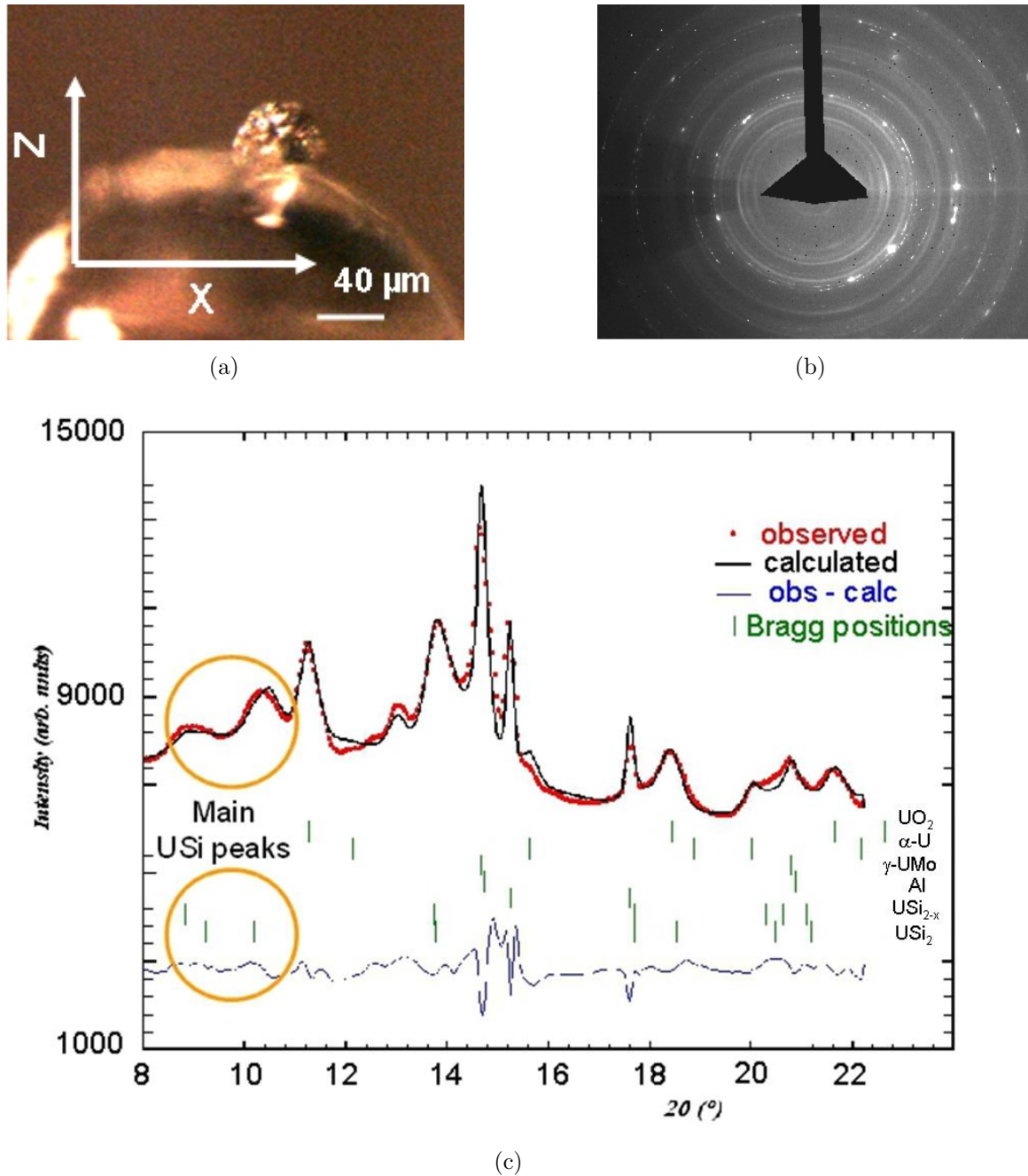


Figure 4.26: μ -XRD characterization of the SiRDL in an UMo₇/AlSi₇ particle. Optical microscopy of the UMo particle on a glass capillary (a), collected μ -XRD image (b) and Rietveld analysis of the associated 1D pattern (c).

Table 4.8: Crystal structure of USi and USiAl phases

Structure	Space group	a(Å)	b(Å)	c(Å)	Unit cell volume(Å ³)	Ref.
USi ₂	P6/mmm	4.028	4.028	3.852	55.12	[197, 198]
USi _{2-x} GdSi ₂ -type (β)	P6/mmm	3.839	3.839	4.072	51.97	[199]
USi _{2-x} (USi _{1.88})	I41/amd	3.99	3.99	13.15		[199]
ThSi ₂ -type (α)		3.98	3.98	13.74		[200]
		3.922	3.922	14.152		[201]
U ₃ Si ₅ (USi _{1.66}) GdSi ₂ -type (β)	hP3, P6/mmm	3.89	3.89	4.017	52.8	[199]
U ₃ Si ₂ Al ₃	I4	7.6292	7.6292	10.85		[202]

Indeed strong distortion in the cell parameters or in the intensities (compare Table 4.8), should have been assumed for using other USi or UAlSi compounds. For example, an almost cubic USi_{2-x} or U₃Si₅ phase (P6/mmm, a=b=3.95Å c=3.97Å) with smaller grain size would have lead to the same refinement quality than using USi₂ and USi_{2-x} or U₃Si₅ (P6/mmm, a=b=3.89Å c=4.013Å). However the presence of such a distorted compound has never been reported up to now.

Dwight mentions that the presence of stoichiometric USi₂ remains controversial [199] and that it is stable only up to 450°C [197, 198], which is in agreement with the temperatures used in the manufacturing process. When heated at temperatures above 450°C, USi₂ decomposes into a mixture of USi_{2-x} and USi₃.

Discussion

Up to now, the composition of the SiRDL around atomized UMo particles taken from four different fuel plates are reported in literature:

- UMo7/AlSi₂, UMo7/AlSi₅ from RERTR9A miniplates [134]
- UMo7/AlSi₂ from IRIS-3 full size plates [203]
- UMo7/AlSi₇ miniplates [194]

The temperature used during the production process was higher than 480°C for the RERTR9A plates and lower than 450°C for the other experiments.

Comparing the results from these four experiments, the Si content inside the matrix influences the composition of the SiRDL. With 2%wt Si (IRIS-3) the SiRDL consists of U(Al,Si)₃ and USi_{2-x}/USi₂ phases. With 7wt% Si (this study), the SiRDL evolves and it consists of USi_{2-x}/USi₂ phases only. This influence of the Si content on the composition of SiRDL is consistent with previous studies performed on diffusion couples at a close temperature (450°C) [204]. However and contrary to what has been found on these diffusion couples, a Si rich phase (USi_{2-x} and/or USi₂) around UMo7 particles has been observed even at low Si concentration inside the Al matrix (2wt%).

In diffusion couples, a Si rich phase close to UMo has only been found at higher Si weight fractions in the Al alloy (partly at 5wt% and fully at 7wt%). The composition of the SiRDL in the UMo7/AlSi7 miniplate is closer to that found on a UMo7/AlSi7 diffusion couple obtained after annealing at 340° [133].

The temperatures involved in the fuel plates manufacturing process plays an important role not only on the composition but also on the size of the SiRDL by inducing or not the destabilization of the γ -UMo phase. Because of the relatively low temperatures involved in the fabrication of the IRIS-3 or MAFIA-I-UMo7/AlSi7 plates, extensive destabilization of the γ -UMo phase in the fissile particle has not occurred (compare section 4.3.2). For this reason and since the reaction between destabilized UMo and AlSi has probably to be avoided to increase the fuel performances [134], only the case of SiRDLs resulting from the interaction between γ -UMo and the AlSi matrix will be discussed in the following. In the RERTR09A full plates (especially in the UMo7/AlSi5 plates), some SiRDL resulting from the γ -UMo/AlSi interaction have been found with SEM and further analyzed using TEM [134]. These thin zones have been shown to consist of $USi_{1.88}$, $U(Al,Si)_3$, $U_3Si_2Al_3$ and U_3Si_5 . Even if the tetragonal $USi_{1.88}$ and the $U_3Si_2Al_3$ phases have not been identified (absence or low amount) neither in MAFIA-I-UMo7/AlSi7 miniplates nor in IRIS-3, this composition is quite close to that found in IRIS-3 fuel plates (USi_{2-x} and $U(Al,Si)_3$). The absence of USi_2 in the SiRDL around the RERTR9A particles is due to its instability above 450°C [197, 198]. However, since no clear data exists on the in-pile behavior of these phases ($USi_{1.88}$, $U(Al,Si)_3$, $U_3Si_2Al_3$, U_3Si_5 and USi_2), it is difficult to state which one should be promoted as the most promising diffusion barrier.

Influence of a pre-formed oxide layer

The presence of an oxide layer around the UMo particles clearly influences the shape and the formation of the SiRDL. The influence depends on the thickness and the brittleness of the oxide layer and on the amount and distribution of the Si inside the matrix.

Figure 4.27 compares three cases: if no oxide layer is present around the UMo particles a homogeneous SiRDL grows at the interface UMo-Al (cf. Fig. 4.27(a)). In case an oxide layer is present around the UMo particles the SiRDL, if at all, always grows between the UMo particle and the oxide layer (cf. Fig. 4.27(b)). In this case the thickness of the SiRDL is reduced and not homogeneous. As presumed by Ripert et.al. [144] it is essential that the oxide layer reveals cracks perpendicular the the UMo particle surface to make path for the Si diffusion: in case of an even thin ($\approx 1 \mu m$) but dense oxide layer no SiRDL could be found even at high Si concentrations inside the matrix (cf. Figure 4.27(c)).

This effect is even more pronounced when the thickness of the oxide layer is increased (cf. Figure 4.28). Figure 4.28(a) shows a SE-image of a UMo particle covered with a thicker oxide layer ($> 1 \mu m$) inside an aluminum matrix with 5wt%Si addition to the matrix (MAFIA-I-6). A linescan has been overlaid. The oxide layer is dense at the left side of the particle, no Si can be found there. In contrast, the brittle and cracked oxide layer on the right side made path for a Si diffusion but the SiRDL is thinner than in the cases where the UMo particle is not covered with an oxide layer. However, EDX maps at different positions of the sample revealed in general no SiRDL around the UMo particles (cf. Fig. 4.28(b)). This behavior is identical on the samples containing

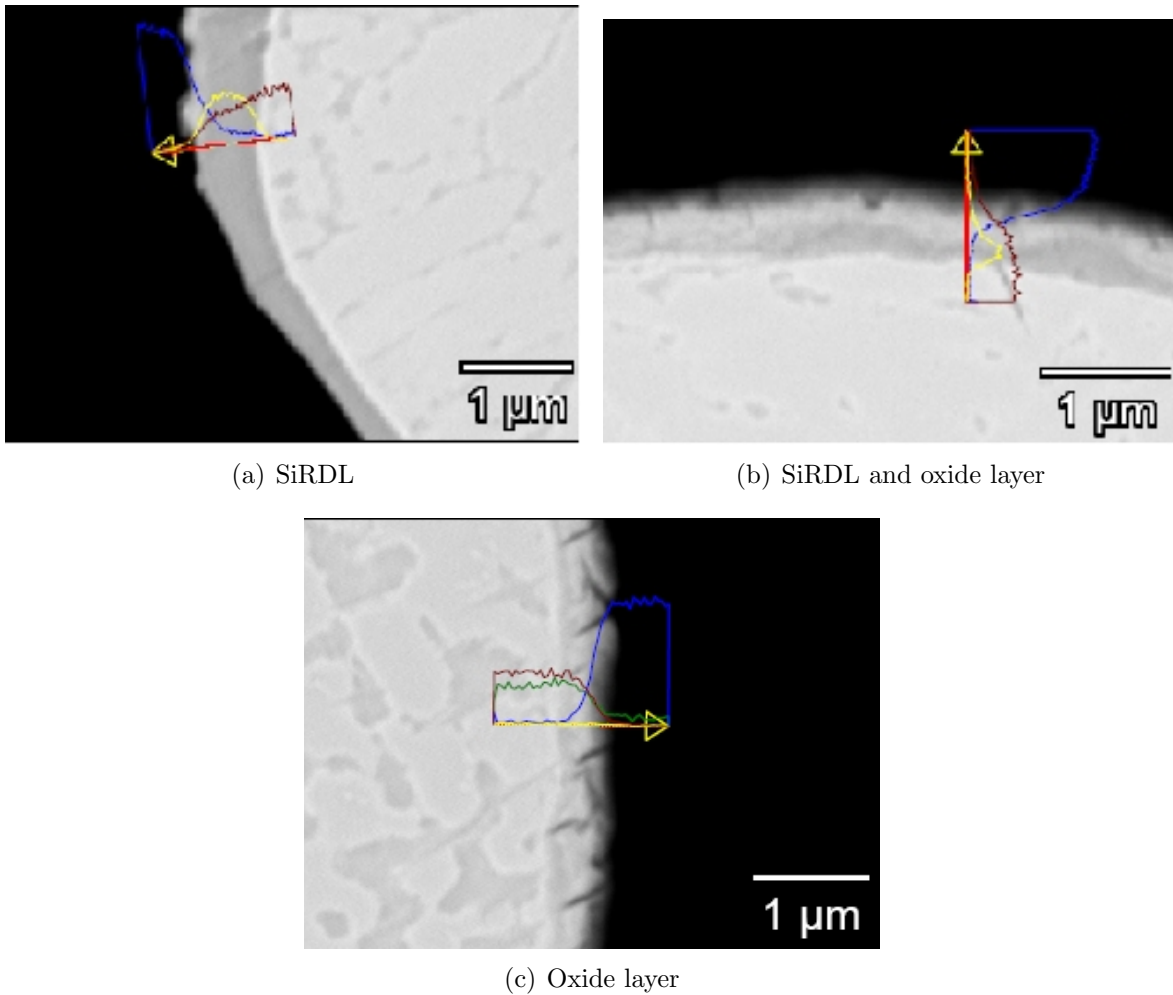


Figure 4.27: Behavior of the SiRDL in combination with an oxide layer. 5wt%Si addition to the matrix. EDX linescans overlaid: Yellow indicates the Si content, blue the aluminum content, green the Oxygen content and red the uranium content.

- (a) A conventional SiRDL grown at a non-oxidized part of a UMo particle.
- (b) A thin SiRDL grew between the UMo particle and the oxide layer around the particle. Note that the oxide layer reveals cracks to make path for the Si diffusion.
- (c) A thin oxide layer around the UMo particle prevented the growth of the SiRDL.

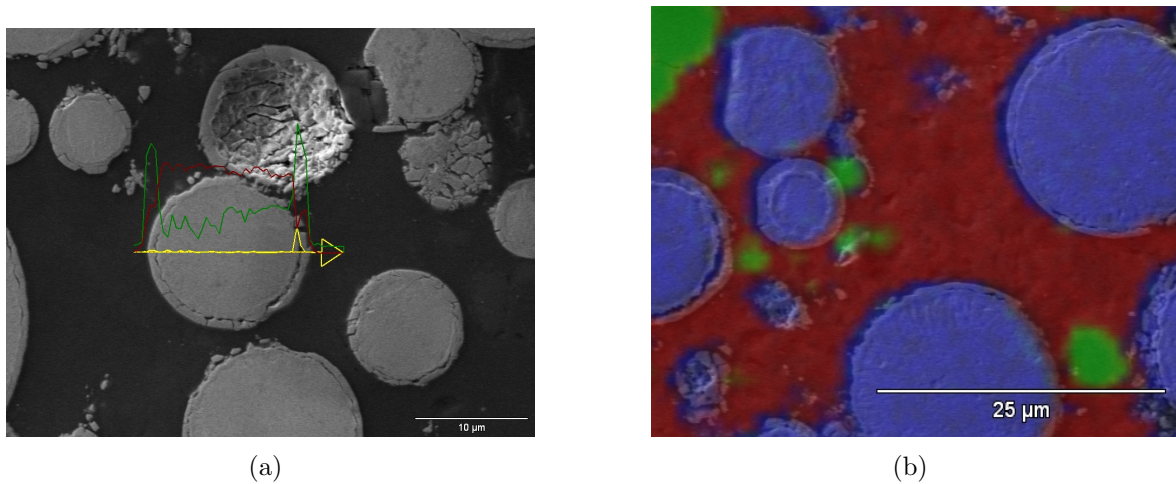


Figure 4.28: The thickness of the oxide layer clearly influences the formation of the SiRDL in case of 5wt%Si inside the matrix.

(a) SE-image of a UMo particle with a thick oxide layer and overlaid EDX-linescan: Red indicates the U content, green the Oxygen content and yellow the Si content.

(b) SE-image, colorized accordingly to an EDX mapping of the same area: red indicates uranium, blue indicates aluminum, green indicates Silicon. No SiRDL is visible around the UMo particles.

oxidized particles with 5wt%Si (MAFIA-I-6) and 7wt%Si (MAFIA-I-8) added to the aluminum matrix.

As shown before, in case 2wt%Si have been added to the matrix with non-oxidized UMo particles (MAFIA-I-3), no SiRDL has been observed (compare Figure 4.22 and 4.29(a)). However, in case oxidized UMo particles have been used, a SiRDL has formed around most of the UMo particles (compare Figure 4.29(b)) and a Si depletion of the matrix around the UMo particles has been observed. This behavior is similar to what has been observed on fresh IRIS-3 samples¹ although there, no oxide layer was present around the UMo particles [195, 196].

This on the first view unexpected behavior may be understood by regarding the morphology of the pre-formed oxide layer in the particular cases: The oxide layer around the UMo particles in the 5wt%Si case (MAFIA-I-6) and the 7wt%Si case (MAFIA-I-8) is thick and all UMo particles are covered by it. No SiRDL could be found around the UMo particles in these two cases.

In the 2wt%Si case regarded here (MAFIA-I-4), the pre-formed oxide layer is thinner and not every UMo particle is covered by it. One can regard the UMo particles covered with an oxide layer as being “physically separated” from the AlSi matrix, i.e. the covered UMo particles can be regarded as “taken out of the system”. This means that the relative availability of UMo and Si for diffusion is higher in the case with oxidized particles (MAFIA-I-4) compared to the case with non-oxidized UMo particles (MAFIA-I-3). In consequence, this increased availability of silicon leads to the formation of a SiRDL at the parts of the UMo particles which are not covered by an oxide layer or where the

¹The IRIS-3 full size plates consisted of non-oxidized UMo powder dispersed inside an aluminum matrix with 2.1wt%Si

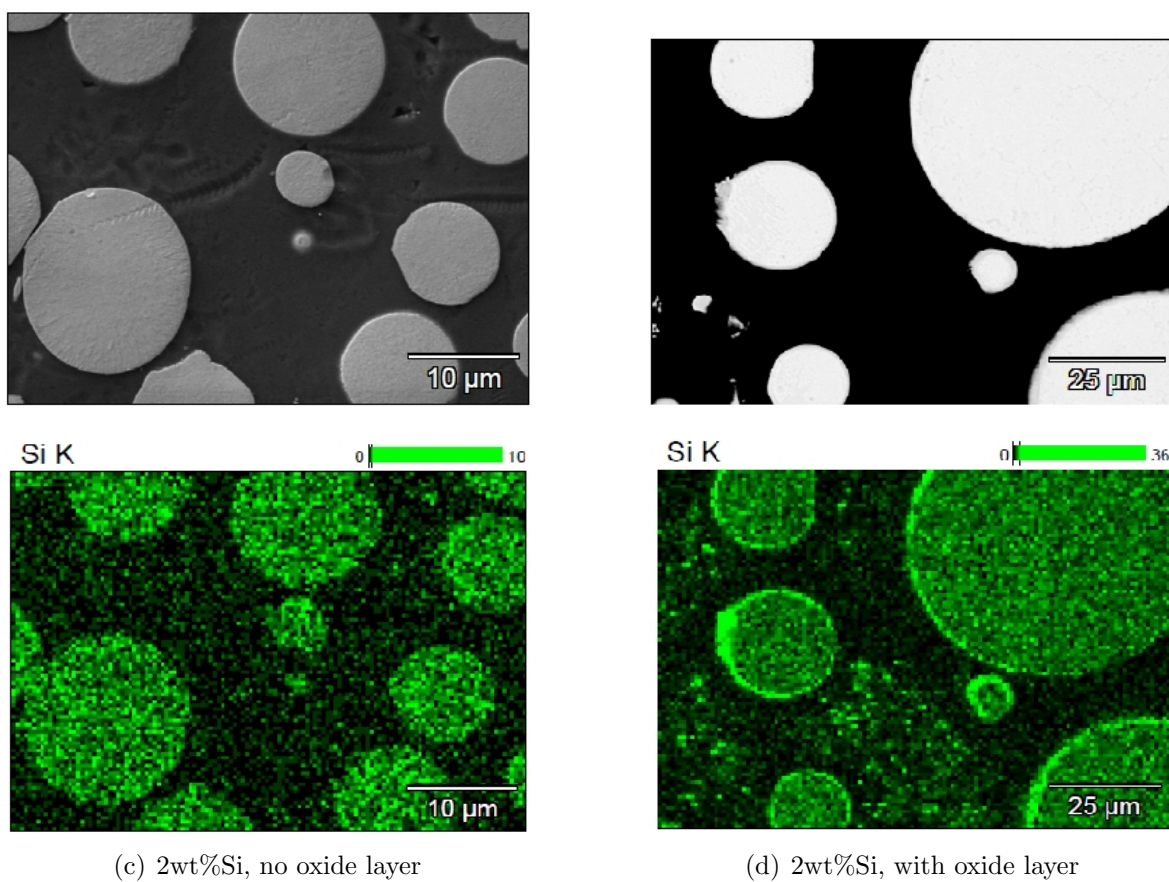


Figure 4.29: Influence of a thin oxide layer around the UMo particles in the 2wt%Si case, SEM images and EDX-map (Si-K- α):

(a) Without an oxide layer: No SiRDL formed.

(b) With an oxide layer: A SiRDL formed, precipitate free zones around the UMo particles are visible.

oxide layer has got cracks²

It can be concluded, that the presence of an oxide layer around the UMo particles in general hinders the formation of the protective SiRDL. A combination of Si addition to the matrix with a pre-formed oxide layer does not cumulate the positive effects of the two single measures. This conclusion has also been drawn by Ripert et.al from comparing the swelling data obtained from the IRIS-4 in-pile test (oxidized UMo particles dispersed in Al with 0wt% or 2.1wt%Si addition [205] with the IRIS-2 (UMo with and without an oxide layer dispersed in pure Al [206]) and IRIS-3 test (UMo dispersed in Al with 0wt% or 2.1wt%Si addition [190]): “In the IRIS-4 case, we can imagine that the oxide layer might obstruct or impede the close contact between UMo particles and the Al matrix. The efficiency of silicon (inside the matrix) is (...) certainly reduced but not completely annihilated, because (...) some cracks in the oxide layer have been caused by the hot rolling process. Some pathways still exist for the silicon” [144].

4.3.3 Characterization after irradiation

XRD analysis

The samples have been examined after irradiation with heavy ions using laboratory scale XRD with Rietveld analysis. Beside the phases that were already present before irradiation, UAl_3 has been found. The lattice parameter of the UAl_3 is $\approx 4.23\text{\AA}$ for all three miniplates with Si addition to the matrix (UMo/AlSi2, UMo/AlSi5 and UMo/AlSi7) which indicates that there is almost no Si present inside this phase i.e. no Si in the IDL grown by heavy ion irradiation. The lattice parameter is in agreement with the results obtained previously on heavy ion irradiated UMo7/Al samples with no addition to the matrix [48]. The α -uranium content decreased, the UO_2 contamination on the sample surface increased during irradiation with heavy ions (compare section 4.1).

SEM/EDX analysis

To observe the behavior of the IDL grown during heavy ion irradiation cross sections through the samples have been prepared. Figure 4.30 compares SEM observations on transversal cross sections of UMo/AlSi2 and UMo/AlSi7 heavy ion irradiated miniplates. The porous part of the IDL is the result of oxidation during the irradiation. Note that because of the irradiation conditions and the important IDL production, some IDL has flown above the particles at the sample surface.

The properties of the IDL in the UMo/AlSi2 miniplate are very close to that observed in the UMo/Al reference: no Si has been found in the IDL and the IDL is just slightly thinner. Only when a Si precipitate was located close to the UMo/Al interface, a significant reduction of the size of the IL could be found. Compared to a very similar sample irradiated however at a higher dose and flux [186], the influence of the addition of 2%wt Si into the matrix is less obvious.

As in the fresh fuel, very few differences between the UMo/AlSi5 and the UMo/AlSi7 miniplates could be found after heavy ion irradiation. Since all UMo particles were

²The total ratio UMo over Al+Si must of course be the same within both samples to apply this argument. This is the case.

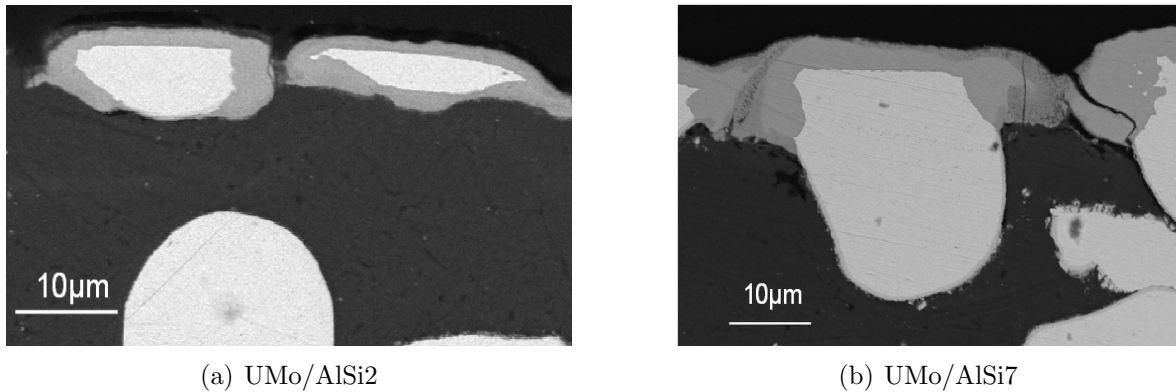


Figure 4.30: SEM observations of UMo/AlSi2 and UMo/AlSi7 heavy ion irradiated miniplates.

covered by a SiRDL in these miniplates, the behavior under heavy ion irradiation of this SiRDL could be investigated. Observations of transversal cross sections show that the SiRDL has vanished in the zones affected by the highest fluencies and a conventional IDL has formed. EDX measurements in the IDL (in the areas larger than $1\mu m^2$) do not show the presence of measurable Si quantities except when a Si precipitate is close to this area.

Considering first the irradiation conditions and in particular the value of the irradiation angle (30°) and second the different iodine penetration depth into UMo and Al (shadowing effect by UMo particles), each UMo/Al interface has not seen the same final fluency. Moreover, at the periphery of the irradiated zone, the obtained final fluency is lower than in the middle of the beam spot. Therefore from the irradiation of one sample, the influence of the fluency on the growth of the IDL can be deduced. It appears that the interaction process may be divided into two main parts (cf. Figure 4.31):

- First, an interaction occurs between the SiRDL and the Al matrix (cf. Figure 4.31(a)) until the SiRDL has disappeared (cf. Figure 4.31(b)). In this case, the IDL is often too thin for being probed with EDX, however it is likely that with the growth of the IDL, the Si concentration decreases (if no Si is located in the irradiated areas, close enough to the IDL as shown in Figure 4.32.). At this step, the UMo core of the particle is preserved from any interaction with Al.
- Afterwards, a conventional UMo/Al interaction appears (cf. Figure 4.31(c)). The UMo particle is consumed now.

Discussion

The presence of the SiRDL around an UMo particle does not prevent by itself the growth of a conventional IDL (generally silicon free) with however a lower thickness. This result is in agreement with those obtained on the IRIS-3 and RERTR7 test fuel plates [190, 191]. Main conclusions of these experiments are:

- the SiRDLs, present in the fresh fuel have been destroyed

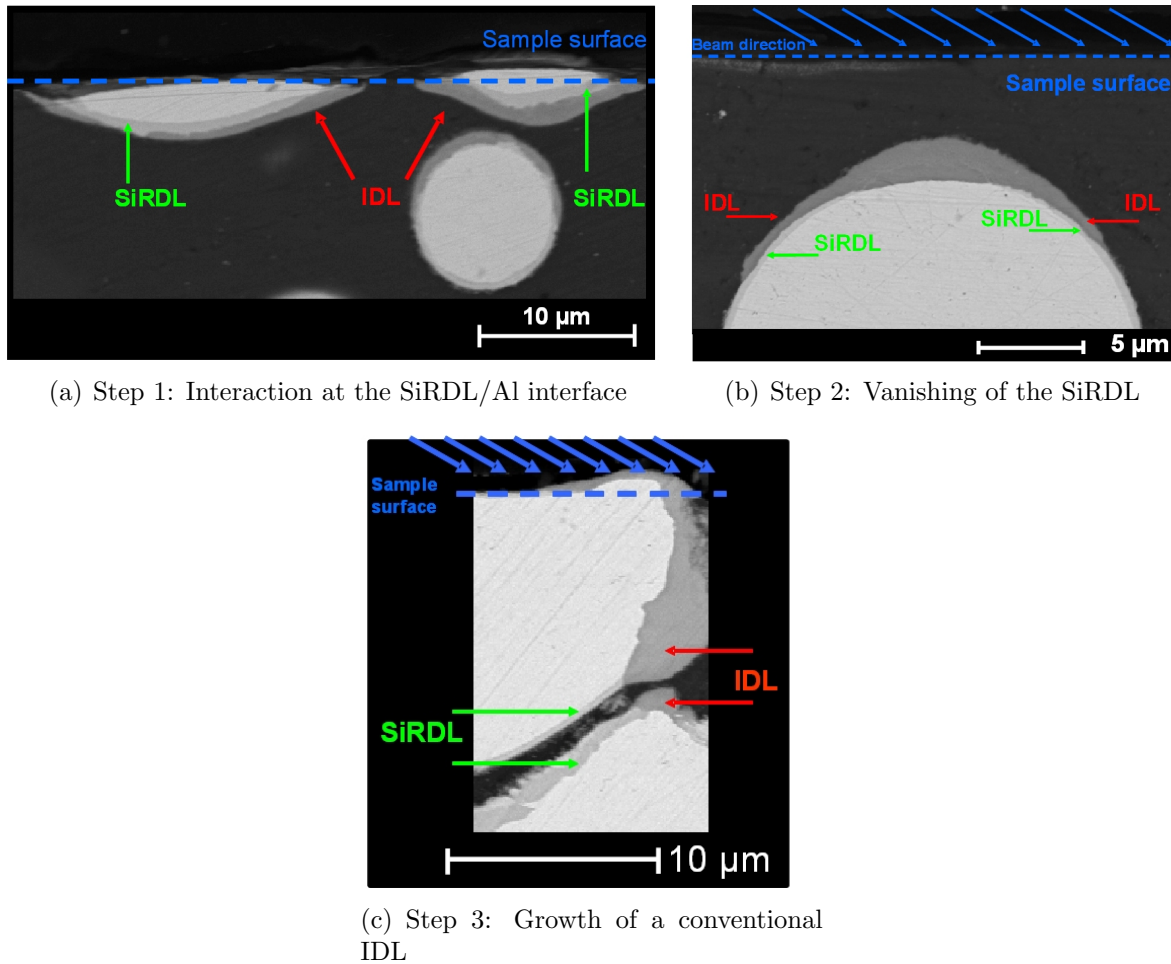


Figure 4.31: IDL growth around UMo particles protected by a SiRDL in three steps. Details of the transversal cross section of the heavy ion irradiated part of the UMo/AlSi7 miniplate. An IDL has formed according to the penetration depth of the heavy ions (red arrow). A SiRDL is visible around the UMo particle (green arrows). (a) The two UMo particles located at the sample surfaces are surrounded by first a SiRDL and then an IDL. Area taken at the periphery of the irradiated zone i.e. where the final fluency is lower.

(b) In the upper part of UMo particle embedded in the Al matrix, the SiRDL has been destroyed by the heavy ion irradiation and the IDL is directly in contact with the UMo particle core.

(c) A standard UMo/Al interaction occurs and the shape of the UMo particle indicates clearly that UMo has been consumed in the interaction.

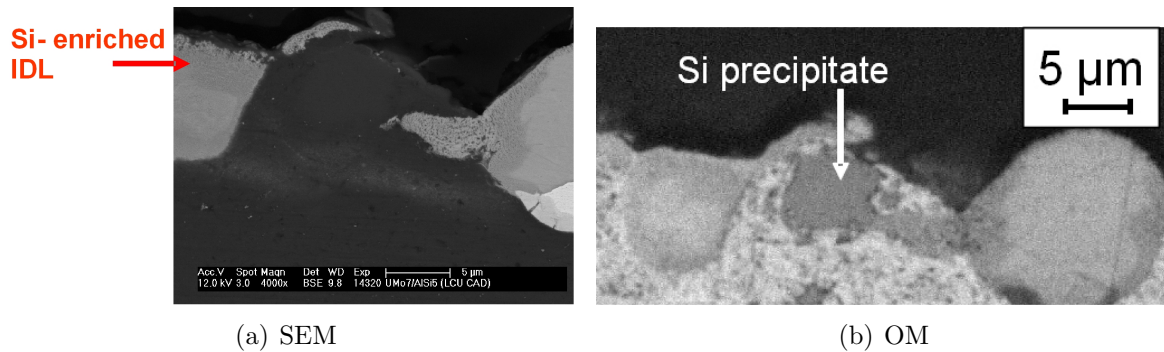


Figure 4.32: Presence of a significant Si concentration inside the IDL when a Si precipitate is located close to this IDL. SEM (a) and optical micrography (b) of the same irradiated area of the UMo/AlSi5 miniplate.

- Si is generally not present in the IDL except when Si precipitates were found to be in close contact with the UMo particles. In this case the thickness of the IDL is reduced.

This result underlines the important role played by Si precipitates located inside the zone affected by the fission fragment recoil around the UMo particles - approximately $12\mu\text{m}$: It has been shown that the Si present inside the SiRDL is not sufficient to stabilize the IDL. Therefore the Si precipitates in this zone act as a Si source that feeds the IDL with Si during the in-pile irradiation. To increase the total amount of Si located inside the fission fragment recoil zone and to assure a homogeneous availability of Si the AlSi alloy used as a matrix should be characterized by the presence of a high number of homogeneously dispersed small Si precipitates rather than large Si precipitates. The best results could be expected when all the Si available inside the fuel plate is present near the UMo particles. This could be achieved e.g. by using UMo particles covered with pure Si as has been suggested by van den Berghe et.al. [159].

4.3.4 Conclusions

In the following, the main results and conclusions drawn from the heavy ion irradiation of UMo/Al miniplates with 2wt%, 5wt% and 7wt% silicon addition to the matrix and from the comparison of the results with a pure UMo/Al standard sample are listed:

- Miniplates containing 2wt%, 5wt% and 7wt% of Si inside the Al matrix have been examined before and after irradiation with heavy ions
- A Si rich layer has formed around the UMo particles without a pre-formed oxide layer during the production of the miniplates in case of 5wt% and 7wt%Si. This is not the case for 2wt%Si. This is in contradiction to what has been found on IRIS-3 full-size plates with 2wt%Si inside the matrix [195, 196]. The difference can be ascribed to the fact that the production parameters for full-size plates and miniplates (as in our case) are not fully identical.
- The composition of the SiRDL has been found to be USi_2 (P6/mmm, $a=b=4.028\text{\AA}$, $c=3.852\text{\AA}$) and USi_{2-x} or U_3Si_5 (P6/mmm, $a=b=3.89\text{\AA}$, $c=4.013\text{\AA}$).

- The presence of an oxide layer around the UMo particles hinders the formation of the protective SiRDL.
- The positive effect of the oxide layer and the SiRDL are non-cumulative.
- The SiRDL does not by itself protect the UMo particle from the growth of an IDL during heavy ion irradiation since the SiRDL is dissolved inside the IDL. The degree of decomposition is dose-dependent. When the SiRDL has been completely dissolved, a normal UMo/Al diffusion occurs in case there is no Si particle nearby.
- The IDL consists of UAl_3 with a lattice parameter of ≈ 4.23 Å for all miniplates with Si addition to the matrix. This indicates that the Si concentration inside the IDL is very low.
- In case that a Si particle is close to the UMo, the resulting IDL is Si rich. Furthermore, the thickness of the IDL is significantly reduced.

4.4 UMo/AlBi

Williams concluded in 1950 that “Bi would seem to be especially recommended” as an addition to the Al matrix for reducing the U/Al interaction [35]. On top of excellent behavior under thermal treatment, the author underlines its low neutron absorption cross section of only 34mBarn for thermal neutrons at 25 meV. This value is a factor 4 lower than the total absorption cross section of Si for thermal neutrons (160mBarn) [207]. In that study this element was thus preferred to Si for limiting the in-pile U/Al interaction.

Even if this work dealt with the U/Al and not the UMo/Al interaction, a further analysis of adding Bi into the Al matrix was of interest. The effect of 2 and 5wt%Bi addition to the matrix on the formation of the IDL during heavy ion irradiation has therefore been investigated. The binary phase diagram of Al-Bi and U-Bi are shown in Figs. B.1 and B.7.

The results presented in this section have been also shown before during a common conference contribution with our cooperation partners [194].

4.4.1 Characterization before irradiation

Figure 4.33 compares the non-irradiated state of the UMo/AlBi samples and of a reference sample. Beside the UMo, small (< 1 μm) Bi and Bi-oxide particles are visible in BSE images (Fig. 4.33(a)) and the Al matrix itself is virtually Bi free. Indeed, this behavior was expected from the phase diagram: the solubility of Bi inside Al is $< 1\text{at}\%$ [208]. Compared to the pure Al sample, the matrix is very brittle and uneven in case of Bi addition (cf. Fig. 4.33(c) and 4.33(d)). Furthermore, the UMo particles begin to lose contact with the matrix. A high oxygen content of up to 75at% is observed with EDX inside the matrix with Bi addition³(cf. Fig. 4.33(b)). The

³Without Bi addition a Oxygen content of around 10at% has been measured with EDX standardless analysis.

reason for this abnormal behavior is the Bi content of the matrix: on the one hand, Bi acts as a powerful catalysator during oxidizing reactions, on the other hand, one of the Bi-oxides, Bi_2O_5 releases O_2 gas upon heating and reduces to Bi_2O_3 [209]. Further SEM/EDX inspection of the blended Al-Bi powder just after the mixing step at room temperature revealed that the Bi already started to oxidize, however, the Al powder is still non oxidized. The oxidizing of the Al-matrix must therefore have occurred during the hot-rolling step of the sample production.

The brittle Al-oxide grows in layers around the UMo particles (compare Fig. 4.34(a)). To identify the crystalline phase composition of this layer, a UMo particle with adherent Al-oxide has been extracted from the samples and glued onto a glass capillary (compare Fig. 4.34(b) for examination with a μ -X-ray beam at the beamline ID18F of the ESRF [181]. An X-ray beam of $2.5\mu\text{m}^2$ size has been scanned over the particle in transmission mode. The beam time has been obtained by our partner CEA. However, in the diffraction pattern only peaks corresponding to γ -UMo, α -U, U-oxide and Al have been identified which indicates that the Al-oxide phase could be amorphous.

4.4.2 Characterization after irradiation

Heavy ion irradiation strongly modified the matrix microstructure, dissolving the Bi based precipitates. This can be clearly seen in transversal cross sections prepared in the irradiated zone (compare Figure 4.35(c)), where the number of Bi precipitates is lower in the part affected by the heavy ions (close to the surface) than in the non-irradiated part (deeper than $12\mu\text{m}$). However, as in the non-irradiated zone, no evidence for Bi dissolved into the Al is found.

As in the reference UMo/Al plates, an IDL grew around the UMo particles during heavy ion irradiation. The Al/(U+Mo) ratio has been determined to be about 4.3 ± 0.6 , the IDL to consist mainly of UAl_3 (laboratory scale XRD). The ratio (Al)/(U+Mo) inside the IDL is therefore higher than could be expected by the occurrence of UAl_3 . No significant influence of the Bi on the thickness of the IDL has been found.

An EDX mapping performed on the irradiated surface revealed a Bi rich layer at the interface between the IDL and the Al matrix (Figure 4.35(b)). Cross section examinations confirm that this layer is present at each IDL/Al interface (Figures 4.35(a) and 4.35(c) whatever the IDL thickness, and not only at the sample surface. The thickness of this Bi-rich layer is $\approx 1\mu\text{m}$. The Bi is only located in this Bi-rich layer, the IDL itself being Bi free.

4.4.3 Conclusions

In contrast to the observation of Williams [35], no significant reduction of the UMo/Al diffusion could be achieved by adding 2 or 5wt% of Bi to the Al matrix. However, there are certain differences in the experimental procedure:

- Fine grained α -uranium has been used by Williams. We used γ -UMo.
- Williams prepared a mixture of Al and Bi by melting and mixing both elements. Although no real alloy can form according to the Al-Bi phase diagram [208], a finer distribution of the Bi in the Al can be expected from this procedure than

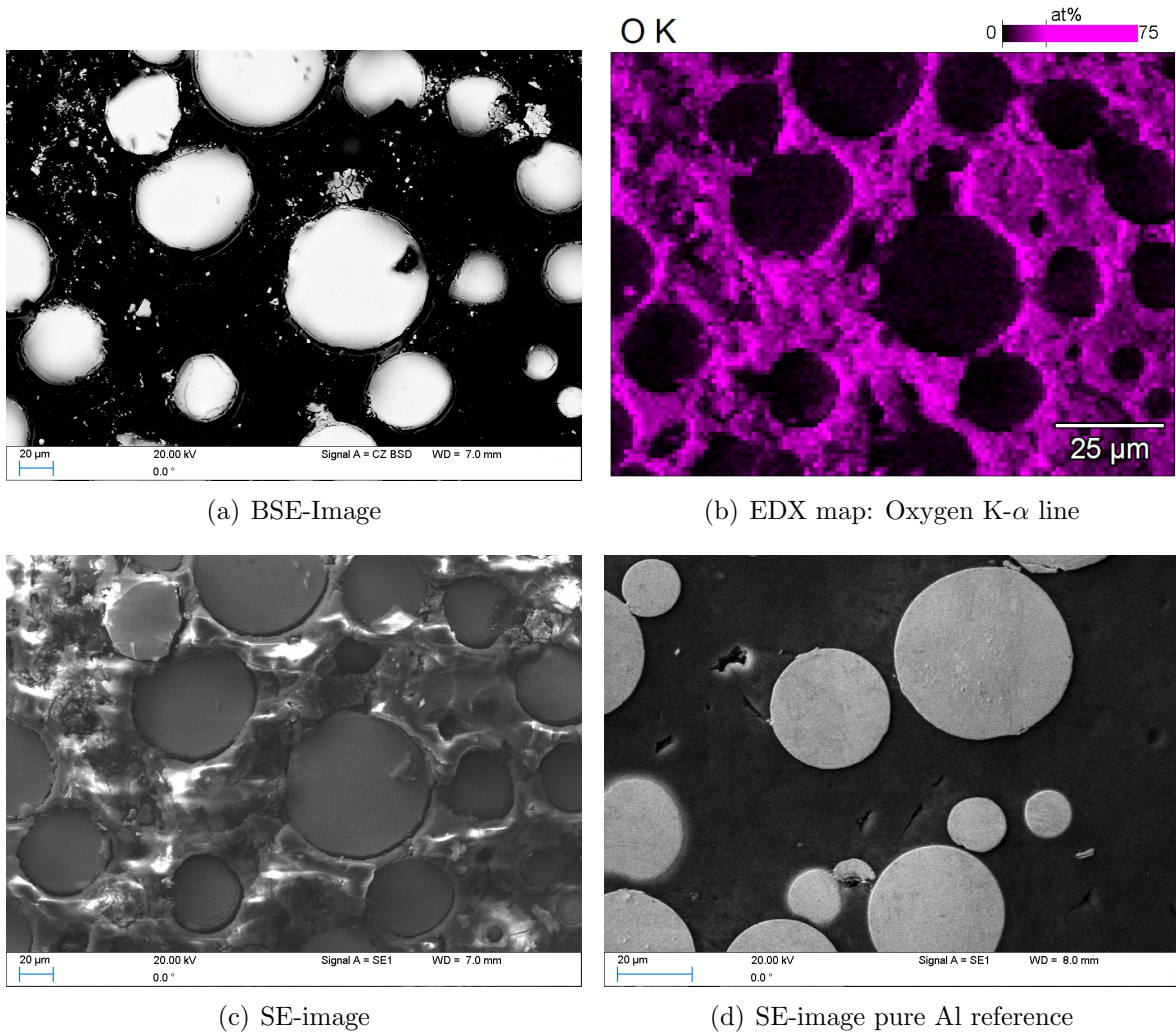
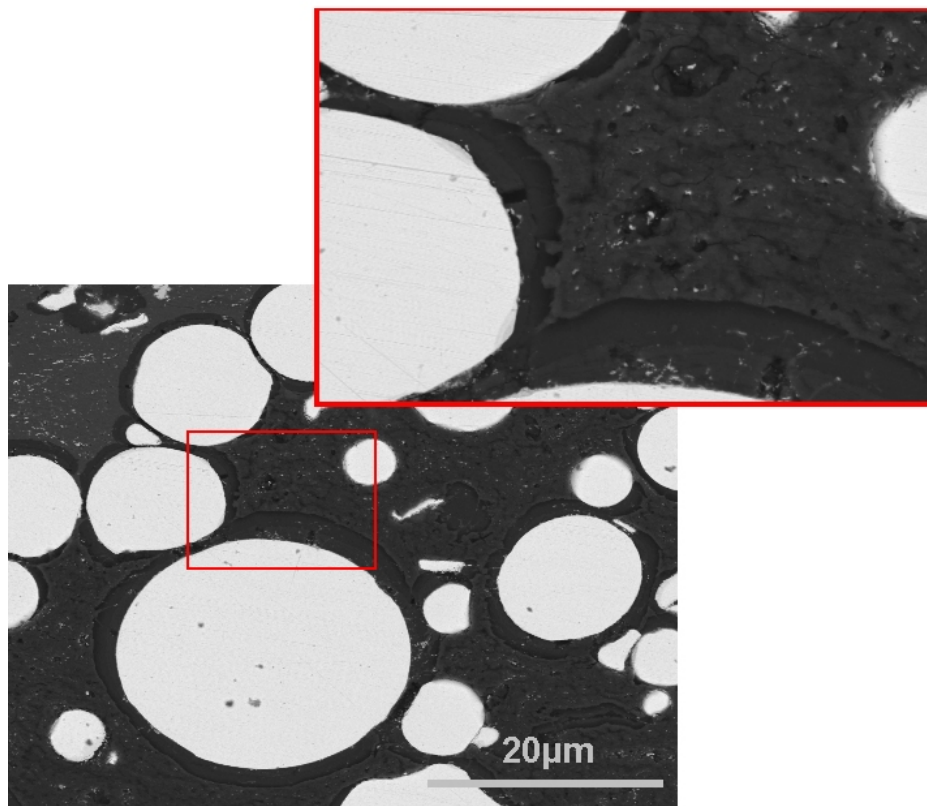
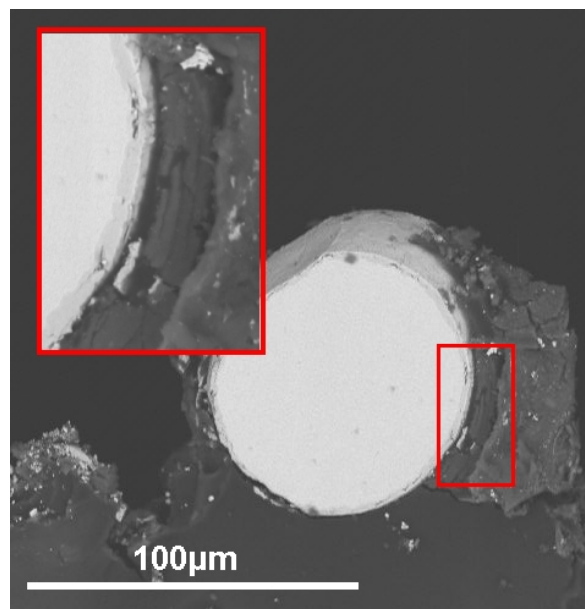


Figure 4.33: (a-c) Typical state of the UMO/AlBi samples after polishing before heavy ion irradiation.

(d) SE-image of a pure UMO/Al sample as comparison.



(a) BSE-Image



(b) Extracted particle

Figure 4.34: (a) Brittle Al-oxide layer around UMo in fresh UMo/AlBi miniplates
(b) UMo particle with adherent Al-O layer, glued on a glass capillary before μ -XRD examination.

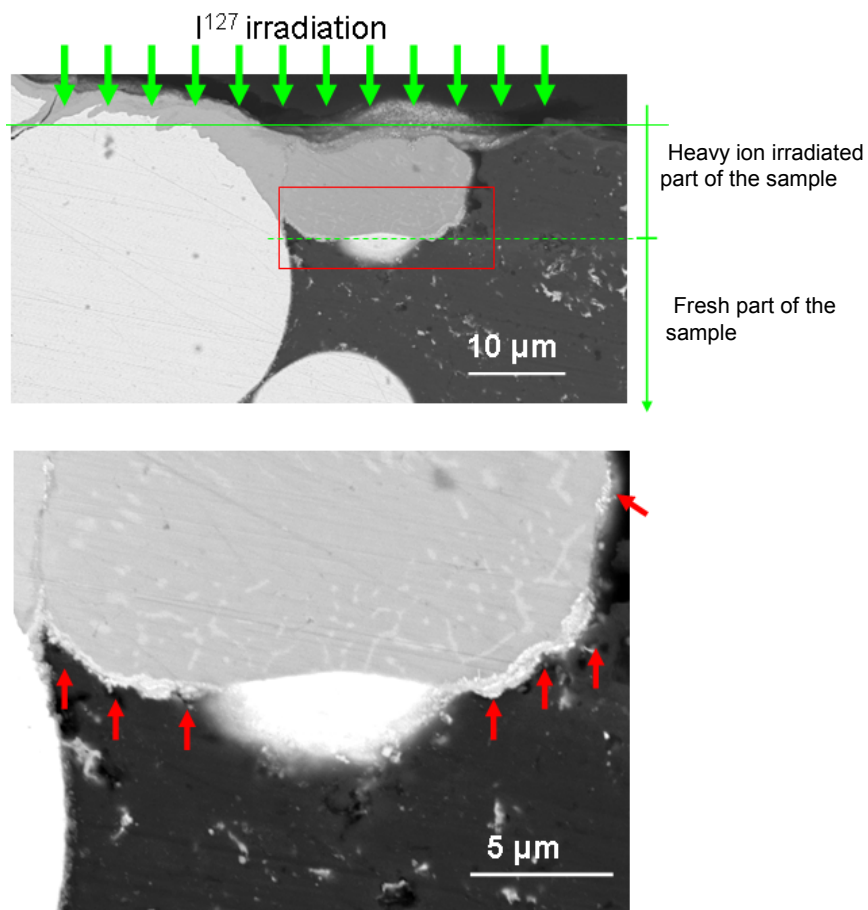
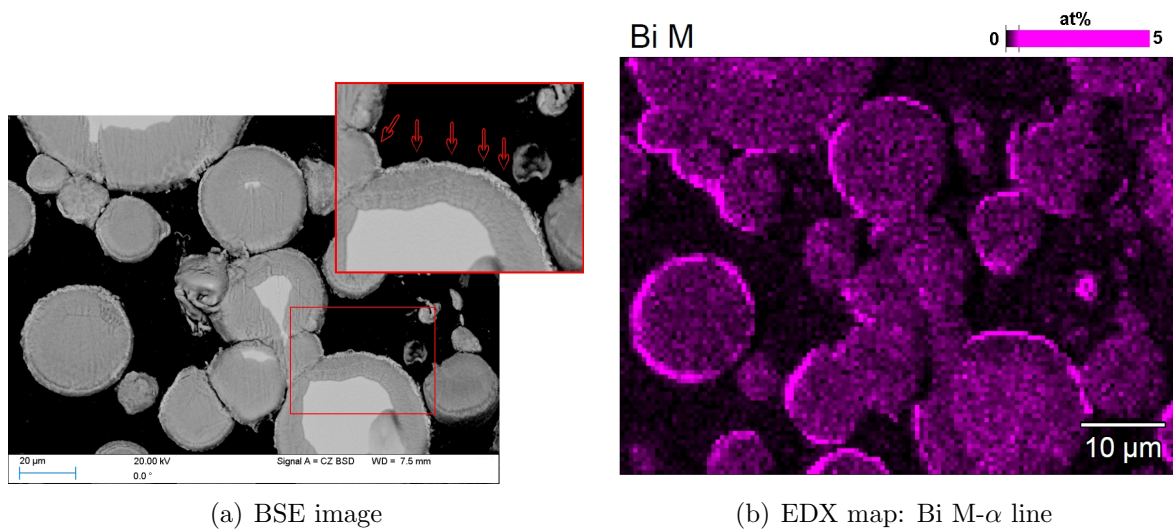


Figure 4.35: SEM characterization of the heavy ion irradiated U/Mo/AlBi₅ miniplate. (a,b) Surface examination, (c) cross section analysis. Red arrows show the Bi rich layer at the interface IDL-Al matrix induced by heavy ion irradiation.

from blending Al and Bi powders as we did. Although, oxidation of the Bi and subsequent oxidation of the Al is avoided by the melting procedure.

- Williams prepared U-AlBi diffusion couples from U and AlBi plates. He induced the U-Al diffusion by heating the samples under inert atmosphere to 250°C, 350°C, 450°C and 550°C for several hundred hours, respectively. Our samples consisted of round UMo particles dispersed in an AlBi matrix. The UMo/Al diffusion has been induced by heavy ion irradiation.

Before concluding definitely on the possible interest of Bi for reducing the UMo/Al diffusion, a second study should be performed. It is crucial that an oxidation of the Al-Bi powder is avoided during the production process.

The use of AlBi powder that has been produced by melting both elements would be desirable for the future, however, no such powder is readily available from commercial providers and requires a custom-made product.

Nevertheless, handling of the Al, Bi and UMo powder under inert atmosphere in glove boxes during the whole production process would easily avoid oxidation and therefore improve the quality of the Al matrix of the hot-rolled samples. Furthermore, the ready polished samples must be stored under non-oxidizing atmosphere before and after heavy ion irradiation to retain the quality of the sample surface.

4.5 UMo/AlTi Systems

Ti in general retards the uranium-aluminum diffusion. In former studies, the positive effect of titanium could be observed by adding titanium to the aluminum [35], by further alloying the UMo with titanium [31, 43, 45, 161] and by introducing titanium as a diffusion barrier at the interface between UMo and aluminum [42]. However, the total absorption cross section of titanium for thermal neutrons of 6.12barn is high compared to other possible stabilizing elements like Si (160mbarn), Bi (34mbarn) or Zirconium (187mbarn) which makes titanium less favorable from a neutronic point of view. Nevertheless, the influence of titanium on the UMo-Al metallurgy has been examined during this study. The phase diagrams of Al-Ti and U-Ti are shown in Figs. B.4 and B.13:

- Conventional dispersed UMo/Al2wt%Ti samples have been produced by the conventional method described in section 3.1 and irradiated with heavy ions.
- It was not possible to obtain UMo powder directly coated with Ti to test the effectiveness of Ti as a diffusion barrier with dispersed samples during heavy ion irradiation. However, it became possible to produce thin Al/Ti/UMo layer system by DC magnetron sputtering. The compatibility of Ti with Al and UMo in the non-irradiated state has been examined [152, 172, 210].
- Dispersed samples consisting of ground U7wt%Mo1wt%Ti ternary alloys have been produced. The samples have been examined before and after irradiation with heavy ions. The principal effect of using ground powder compared to atomized powder in dispersed UMo/Al samples will be discussed in section 4.7 together with the influence of Ti, Nb and Pt addition to UMo in the fresh and irradiated state.

4.5.1 Matrix addition: UMo/Al2wt%Ti

Atomized UMo powder and blended Al-Ti powder have been used to prepare the samples. Blended Al-Ti powder of the finest grain size available had to be used since no pre-mixed Al2wt%Ti powder was commercially available. Since the solid solubility of Ti in Al is lower than 0.7at% [116], the presence of Ti precipitates was anticipated. However, the size of the Ti precipitates is larger when using blended powder (5-10 μm) and the distribution is more inhomogeneous as could be expected when using melted Al-Ti. No reaction of the aluminum matrix or of the UMo particles with the titanium precipitates during the production process could be observed, compare figure 4.36(a). A surface inspection of the irradiated sample using SEM and EDX element mapping reveals the usual flowing of the IDL on the surface as has been observed before on pure UMo/Al reference samples irradiated at an angle of 30° (compare section 4.1). However, in case a titanium particle is present, the IDL seems to float around the particle. The titanium particle itself is not consumed by the diffusion process (compare figure 4.36(b)).

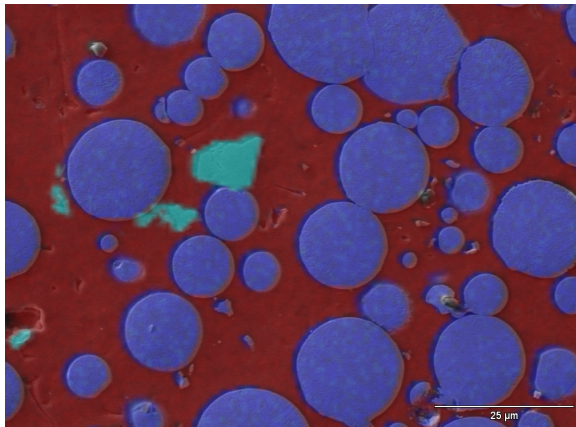
A cross section examination confirms that the titanium particles are not affected by the diffusion process (compare figure 4.36(c)): The IDL around the UMo particles forms according to the shape of the Ti particles nearby. This IDL consists of two layers, a porous outer layer and a dense inner layer. The outer layer contains significantly more oxygen than the inner layer. This oxidation has occurred during the irradiation process and has also been observed inside others samples, compare e.g. figure 4.30. However, it has been confirmed by EDX that both layers are virtually free of titanium: the Ti content has been determined to be below 1at% in both layers. Furthermore, during heavy ion irradiation, there is no interaction of the titanium particles with the surrounding aluminum matrix, or, in case of close contact, with the UMo particles.

XRD measurements showed the presence of UAl_3 after irradiation with heavy ions in addition to the phases present already before irradiation - γ -UMo, Al, UO_2 and a slight α -U contamination. However, the Al/(U+Mo) ratio in the IDL has been found to be 5.27 ± 0.59 by EDX measurements which is higher than could be expected by the occurrence of UAl_3 . No signs of titanium could be found using XRD due to the small overall amount inside the sample.

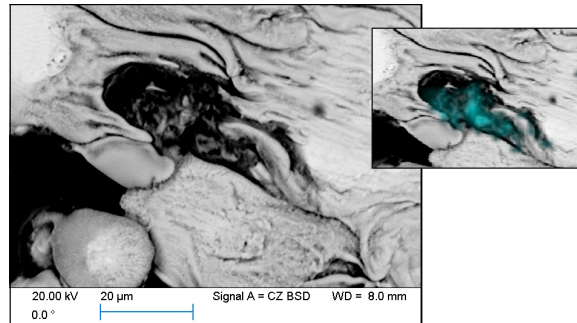
4.5.2 Ti as diffusion barrier

Titanium has been considered to be one of the most effective diffusion barriers to stop or delay the UMo/Al diffusion process [42]. Using the DC magnetron sputtering technique it was possible to obtain thin Al/Ti/UMo layer systems (for details on the process compare reference [152]): these samples served as model systems to test on the one hand the compatibility of titanium with aluminum and UMo, on the other hand the bond strength of titanium sputtered onto aluminum and of UMo sputtered onto titanium have been determined.

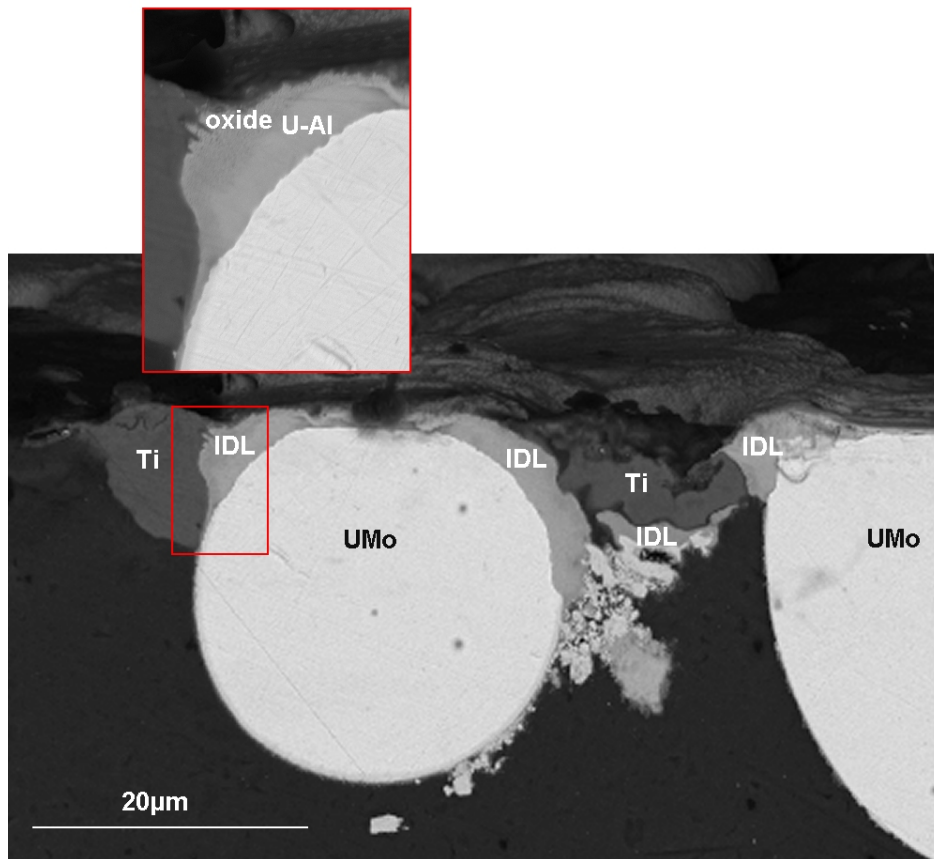
To test the compatibility of titanium with aluminum and UMo, thin layers, each around 5 μm , of titanium and UMo have been sputtered onto an aluminum substrate. Cross sections have been prepared and examined using SEM/EDX, compare figure 4.37. No interaction of the titanium with the UMo or the aluminum substrate occurred during the production process. Furthermore, no spontaneous debonding of the sputtered layers



(a) Before irradiation, SE image, colorized



(b) After irradiation, BSE image, colorized



(c) Cross section

Figure 4.36: Influence of Ti addition to the matrix:

(a) SE image, colorized: red indicates aluminum, blue indicates UMo, cyan indicates titanium precipitates.

(b) BSE image of the irradiated surface, partially colorized: a titanium precipitate (cyan) has stopped the floating of the IDL.

(c) Cross section examination through the irradiated surface: titanium precipitates in contact with UMo and the IDL.

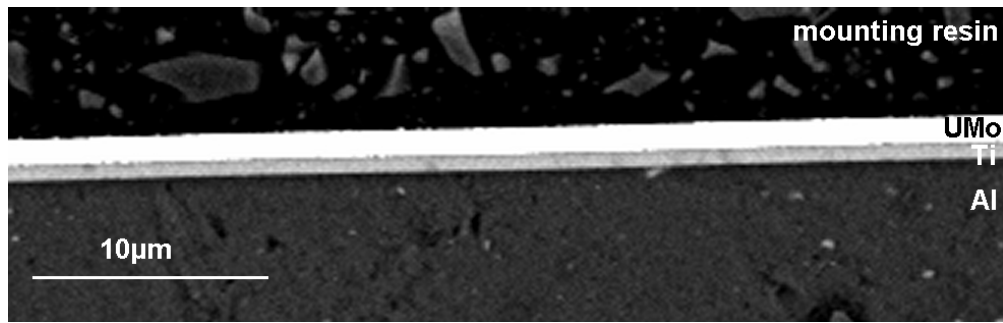


Figure 4.37: UMo and titanium sputtered onto a pure aluminum substrate, cross section [172].

has been observed [172].

In a second step, the bonding strength between titanium sputtered onto aluminum substrates and between UMo sputtered onto titanium substrates have been tested by tensile tests. More details on the experimental procedure can be found in references [163, 210]. Values between 40-70MPa have been found in the first case, a value of 67MPa has been found in the second case. The bond strengths of UMo and Ti to the substrate are therefore at least as high as the adhesion between UMo and aluminum that has been reached using conventional techniques [210, 211].

4.5.3 Discussion

The titanium precipitates present in the dispersed UMo/Al samples did neither react with the aluminum, nor with the UMo during the production process and during the heavy ion irradiation. Furthermore, no reaction between the titanium and the IDL could be observed after heavy ion irradiation. The positive effect of a titanium addition to the matrix is insofar limited that as soon as the IDL gets in contact with a titanium precipitate the diffusion stops.

A finer and more homogeneous distribution of titanium in the aluminum matrix as could be achieved by co-melting and casting Al and Ti would be of no avail: the smaller titanium precipitates would most probably be incorporated into the IDL. However, further examinations showed the possibility to apply Ti as a diffusion barrier between the UMo and the Al.

For the future, in a first step the heavy ion irradiation of sputtered UMo/Ti/Al layer systems of different thickness is recommended to confirm the effectiveness of titanium as a diffusion barrier (compare section 5.2). In case of success, the coating of atomized UMo powder with a thin titanium layer should be assessed in a second step as described in references [40, 152, 159]. Afterwards, dispersed samples produced with this coated UMo powder should be tested using heavy ion irradiation.

4.6 UMo/AlMg

Earlier [35] and recent literature [38] agree that an addition of some wt% of magnesium to the aluminum should be avoided since the uranium/UMo-aluminum diffusion

accelerates in these cases. However, these experiments regarded only thermal diffusion at temperatures of 400°C-500°C. To verify this effect also for irradiation induced diffusion, UMo/Al samples with 2wt%Mg addition to the matrix have been prepared. Again, blended aluminum and magnesium powder of the finest grain size (-mesh325) have been used.

An inspection of the sample surface before heavy ion irradiation revealed that the magnesium powder has completely and uniformly dissolved in the aluminum matrix (compare Figure 4.38(a)). No Mg particles or precipitates could be found. EDX measurements showed a medial Mg content inside the aluminum of $1.87 \pm 0.75\text{wt}\%$ which is in good accordance with the expected value of 2wt%. Since the solid solubility of Mg in Al at room temperature is $\approx 2\text{wt}\%$ this behavior was expected [208] (compare Fig. B.2).

A cross section analysis of the heavy ion irradiated samples reveals that a diffusion layer has grown around each irradiated UMo particle. However, the diffusion layer is not thicker than the one that has been observed in the reference samples and only slightly thicker than the one that has been observed inside the samples with Si addition to the matrix. This result is clearly in contradiction to what has been found before in diffusion couple experiments: the thickness of the diffusion layer when adding 2-3wt%Mg to the aluminum was at least two times higher compared to the reference samples with pure aluminum and up to 50 times higher compared to the optimal case with 10wt% silicon addition to the aluminum [35, 38].

The phase composition of the samples has been determined by XRD before and after irradiation with heavy ions. In addition to the phases present before irradiation - γ -UMo, Al, UO₂ and a slight α -U contamination - UAl₃ was present after heavy ion irradiation. However, an EDX analysis of the IDL revealed a (Al+Mg)/(U+Mo) ratio of 4.73 ± 1.01 . The Mg/(Al+Mg) was 2.62 ± 0.72 which is, within the error bars, the same ratio than in the Al matrix. Magnesium has therefore not preferably been built into the IDL compared to aluminum. The ratio (Al+Mg)/(U+Mo) inside the IDL is higher than could be expected by the occurrence of UAl₃.

4.7 UMo Ground powder

Beside UMo/Al samples based on atomized powder also samples based on ground powder have been examined prior and after irradiation with heavy ions. Beside pure ground U8Mo-powder although ternary UMoX (X=Ti, Nb and Pt) alloys have been regarded to study the influence of further alloying the UMo on the fuel behavior. The samples containing ternary UMo alloys have been prepared in the framework of the MAFIA-I material screening campaign while the samples containing ground U8Mo powder originate from the non-irradiated spare test-fuel plates of the IRIS-TUM irradiation campaign.

4.7.1 Pre-irradiation state of ground UMo fuels

In this section the micro structure of non-irradiated ground UMo-Al samples will be discussed. At first attention will be drawn to general features of this fuel type on

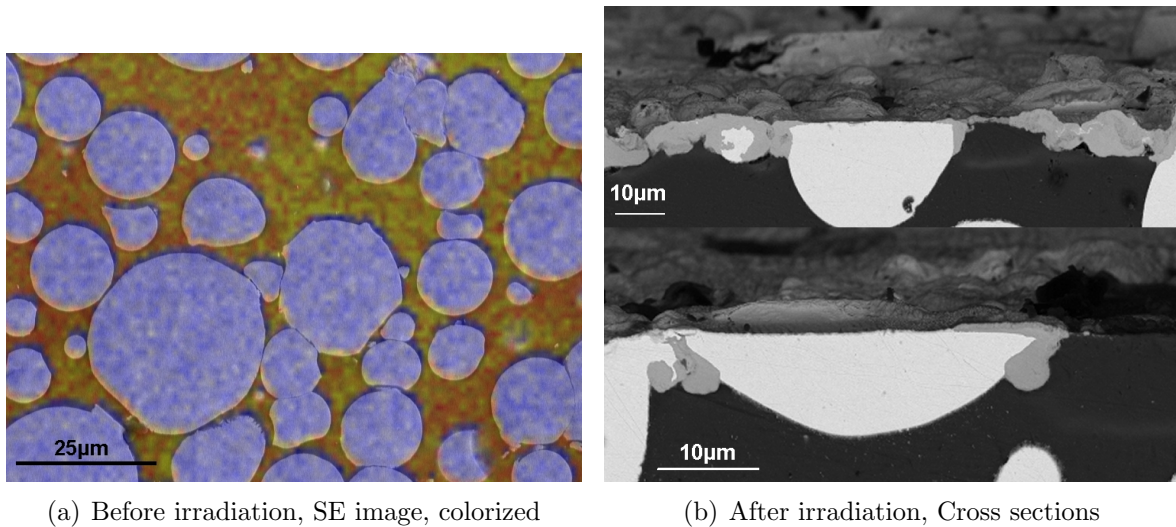


Figure 4.38: Influence of 2wt%Mg addition to the matrix:

- (a) SE image, colored according to an EDX map: blue indicates uranium, red indicates aluminum, yellow indicates magnesium.
- (b) Cross section through the irradiated surface at two different positions, BSE image.

the example of samples originating from non-irradiated IRIS-TUM test fuel plates. Afterwards, the influence of further alloying the UMo will be discussed. The results will be compared to samples prepared with atomized powder. The microstructural examinations of the IRIS-TUM samples as well as the post irradiation examinations of the MAFIA samples have been performed in cooperation with X. Iltis and H. Palancher from CEA, Cadarache. The results have been presented before in a common conference contribution [212].

Non-irradiated IRIS-TUM samples

Introduction In the framework of the IRIS-TUM irradiation campaign – a cooperation between the Technische Universität München (FRM II), the Commissariat à l’Energie Atomique (CEA) and AREVA-CERCA – five full size test fuel plates have been irradiated under conditions approaching those of EOL in high flux research neutron sources, i.e. a maximum heat flux of $260\text{W}/\text{cm}^2$ and a maximum burn up between 56.3% and 88.3% (LEU equivalent). The irradiation took place in the OSIRIS test reactor of CEA at Saclay. Although the plates suffered from a large swelling at the end of the irradiation campaign, none of them showed a cladding failure and no fission products were released [145]. The results of the post irradiation examinations on these plates have been presented recently [143, 148–150].

For this examination samples taken from the middle and the edge of the fuel zones of the non-irradiated spare fuel plates have been examined. The results will be compared to the in-pile irradiated state and to results obtained on non-irradiated samples containing atomized UMo powder and ground UMoX powders of different elementary compositions [193]. Furthermore the evolution of the UMo phases during plate manufacturing will be discussed in detail.

Table 4.9: Parameters of the five irradiated IRIS–TUM plates as shown in [145]

Plate number	8001	8002	8501	8503	7002	7003
uranium density [gU/cm ³]	8.5	8.4	8.3	8.3	7.3	7.3
Meat Porosity [vol%]	8.1	7.9	9.0	8.9	6.5	6.4
Si in Al content [wt%]	0.07	0.07	2.1	2.1	0.07	0.07
Vol% of Al in the meat	38.2	38.0	38.7	38.6	45.0	45.2
Meat thickness [mm]	0.49	0.49	0.49	0.49	0.54	0.54
Mo in UMo [wt%]	8.1	8.1	8.1	8.1	8.2	8.2

Plate definition In order to improve the irradiation performance of UMo/Al dispersion fuels which suffered from excessive swelling due the build-up of a large interaction layer at the UMo/Al interface during former irradiation test [34, 213] four different actions that have shown to be efficient in limiting the plate swelling have been taken up in the IRIS-TUM irradiation campaign:

1. Addition of 2wt%Si to the Al matrix [161]
2. Oxidation of the UMo powder⁴ [161]
3. Increase of the Mo content to 8wt% to further stabilize the γ -UMo phase
4. Use of ground UMo powder instead of atomized powder [146, 214]

Point 1-3 aim at limiting the build up of the undesired UMo/Al interdiffusion layer (IDL) which is regarded as the cause for the excessive plate swelling while point 4 – compared to atomized powder – induces more porosity into the meat which takes up the plate swelling at the beginning of the irradiation. Furthermore, the fission gas behavior is improved when using ground powder [143]. Since in the case of dispersed fuel it is only possible to convert the FRM II from the use of highly enriched uranium (HEU) to an enrichment of $\approx 50\%$ (MEU) [215] it has been decided to use an enrichment of 49.3% for the IRIS-TUM plates. The plates were produced by AREVA-CERCA, the main features are given in table 4.9. The plates have been labelled and categorized in the following way where x, y and z are running numbers:

- 700x: 7.3gU/cm³, no Si addition to the matrix
- 800y: 8.5gU/cm³, no Si addition to the matrix
- 850z: 8.3gU/cm³, 2.1wt% Si addition to the matrix

⁴The UMo powder has not been intentionally oxidized but the oxidation is an intrinsic effect of the grinding process. However, it has been shown before that an oxide layer around the UMo particles improves the fuel in-pile behavior [206]

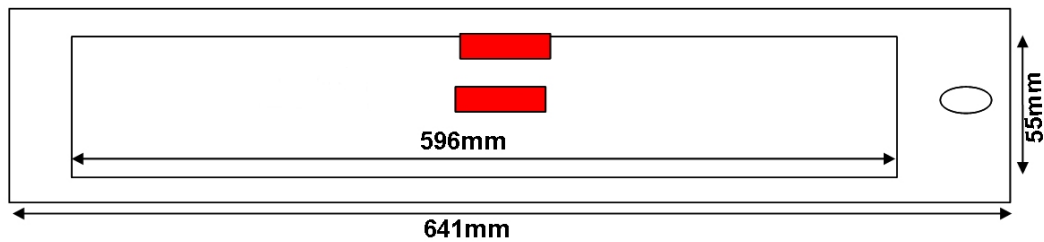


Figure 4.39: Sampling positions at the fresh IRIS-TUM fuel plates. The size of the samples (red) was $28 \times 10 \text{mm}^2$.

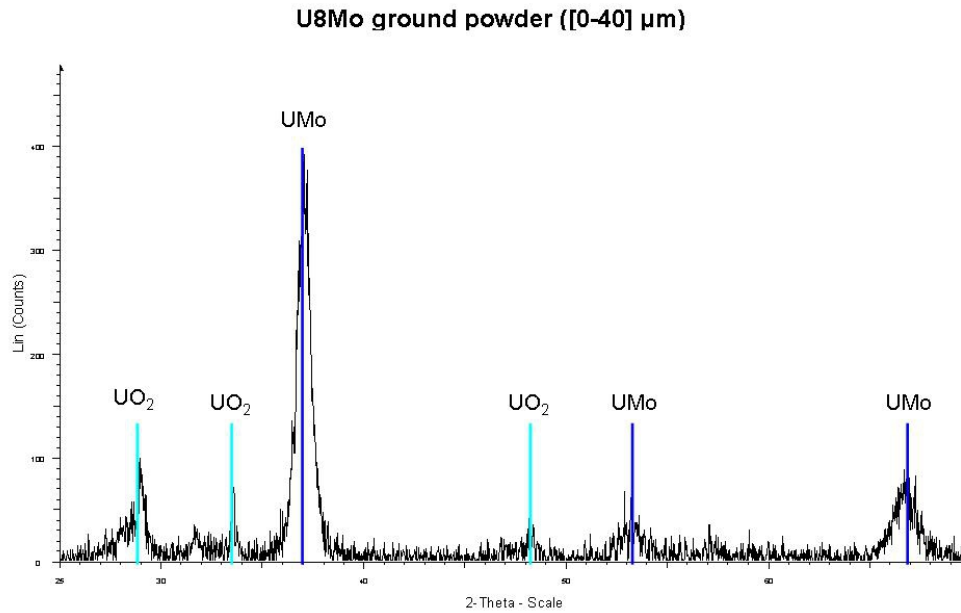
In addition to the five plates depicted in Table 4.9 three identical twin plates – one of each kind – named 7002, 8003 and 8502 have been produced and remained non-irradiated. From each of these plates two samples have been taken from the middle of the fuel zone and from a zone close to the picture frame, respectively – see Fig. 4.39. Cross sections have been prepared from each sample and have been examined using SEM/EDX and laboratory scale XRD. Furthermore, samples from the original ground UMo powder provided by AREVA-CERCA have been examined using SEM/EDX, XRD and laser granulometry.

UMo ground powder: State before plate fabrication Samples of the ground UMo powder used for the IRIS-TUM plate production have been examined. They were sieved in order to obtain two classes: (0-40 μm , most probable size $36\mu\text{m}$) and coarse ones (40-125 μm , most probable size $110\mu\text{m}$). The two sieved powders were characterized by:

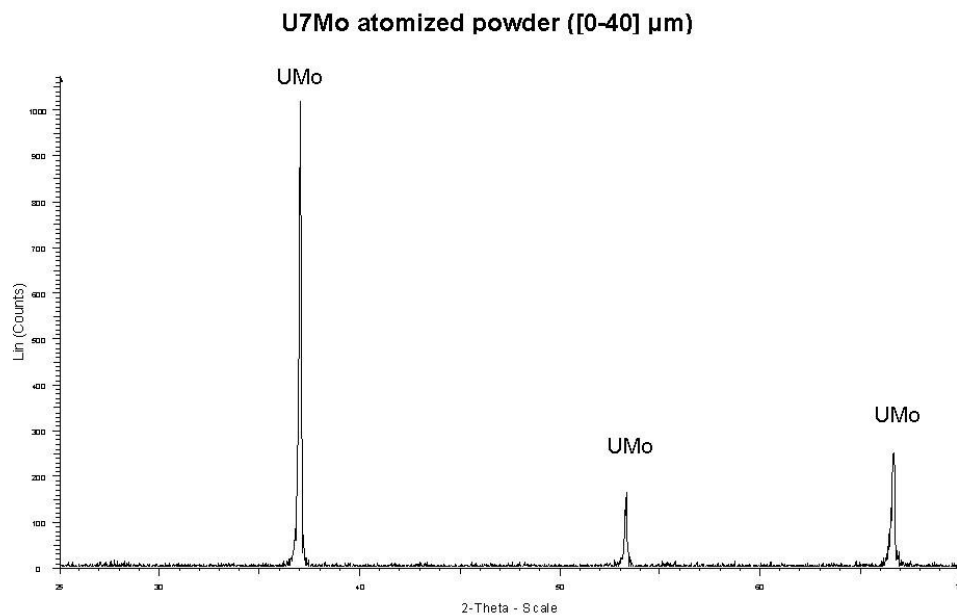
- laser granulometry to determine the size distribution of the particles,
- laboratory scale XRD to determine the phase composition.

Granulometry measurements showed that a significant amount of very fine particles characterized by a size of a few μm to $10\mu\text{m}$ were present in the [0-40 μm] class, while, in the [40-125 μm] class, some particles larger than $125\mu\text{m}$ were also present. In both cases, XRD analysis evidenced only two phases: γ -UMo and UO_2 . No signs of α -U have been found (compare Fig. 4.40). Comparing the a XRD analysis of atomized UMo powder and ground UMo powder with almost the same Mo content the peaks are broader in case of ground UMo and there is a higher background noise [216]. It can be concluded that the lattice structure of the UMo inside the ground powder is strongly disturbed, most probably due to defects accumulated during the grinding process.

IRIS-TUM plate samples: SEM/EDX analysis The typical microstructure of UMo/Al plates prepared with ground UMo powder has been found within all three samples: UMo particles of different size up to $\approx 150\mu\text{m}$ and irregular shape are dispersed inside the Al matrix. The particles contain cracks and sometimes look even “folded” due to the high mechanical forces applied during grinding. Furthermore, the particles often contain oxide stringers and are in general oxidized at the interface UMo-Al. Also a considerable amount of porosity is visible inside the matrix (compare Fig.



(a) Ground powder



(b) Atomized powder

Figure 4.40: XRD analysis of fresh (a) ground U8Mo powder and (b) atomized U7Mo powder prior to plate manufacturing [216]

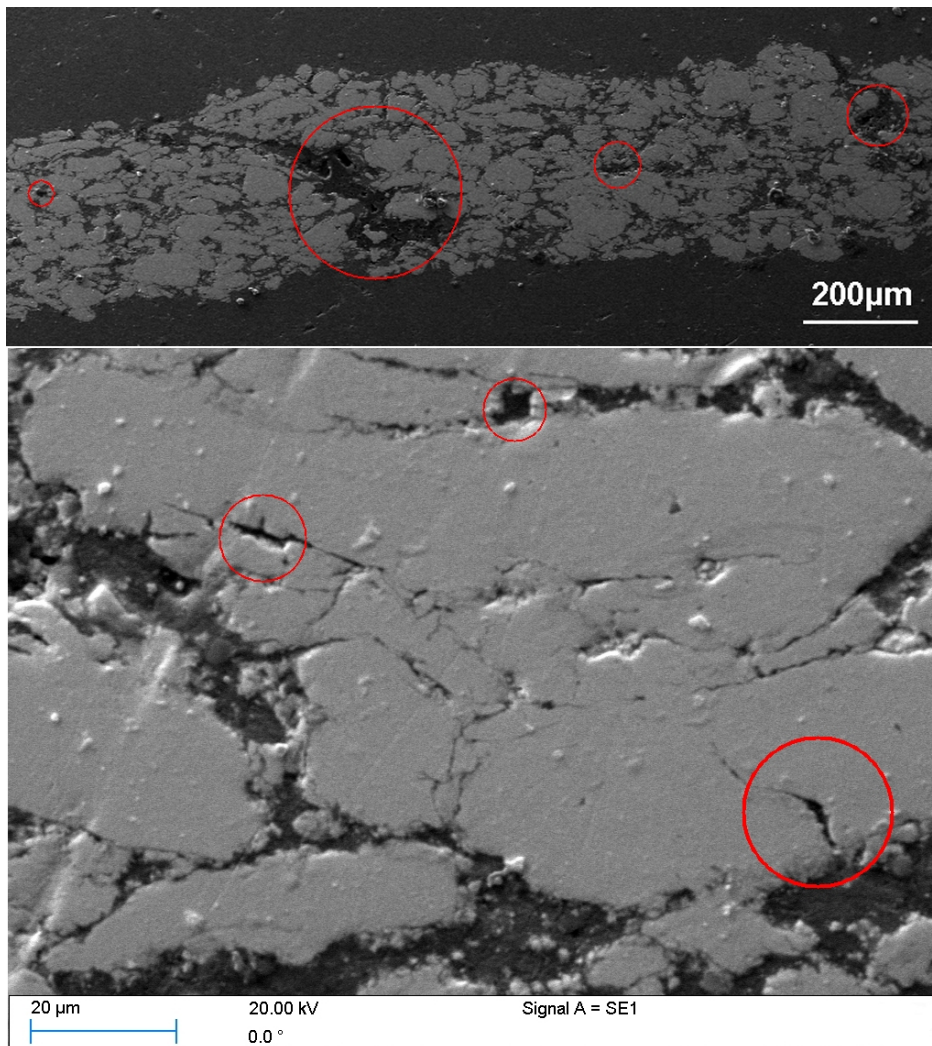


Figure 4.41: Low (upper part) and high (lower part) magnification picture of the typical as prepared matrix state of the IRIS-TUM samples. The irregular size and shape of the ground UMo particles, the presence of porosity (red circles) and the high UMo loading are noteworthy.

4.41 and Fig. 4.42).

The surface percentage of porosity, UMo and Al have been determined for each of the three samples by analyzing SE-SEM pictures, results are given in Table 4.10. It is noteworthy that the amount of UMo and Al determined by image analysis is consistent with the values given in Table 4.9 according to [145], although the values are not the same (surface % vs. vol. %). As expected, the UMo fraction is higher in the plates 8003 and 8502 compared to plate 7001. The percentage of porosity could not be determined precisely by image analysis.

No signs of granular γ -phase destabilization could be observed inside all three as-fabricated IRIS-TUM plates. An UMo-matrix interaction occurred only on plate 8502 – the one with 2.1wt% Si inside the matrix.

Here, in addition to the features described above, Si from the matrix reacted with the UMo: on the one hand a silicon rich layer (SiRDL) formed at the interface between

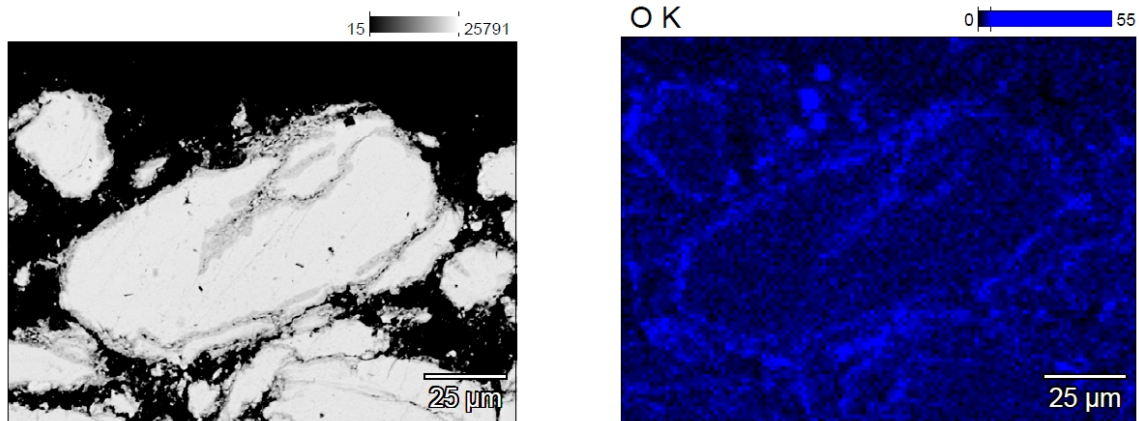


Figure 4.42: BSE image (left) and EDX map on the Oxygen K- α line (right) of the same area. The UMo particles are oxidized and contain oxide stringers due to the grinding process.

Table 4.10: UMo, aluminum and porosity surface % as determined using image analysis on SEM secondary electron pictures.

Plate	UMo [surf.%]	Al [surf.%]	Porosity [surf.%]
8003	68 ± 4	26 ± 5	5 ± 5
7001	54 ± 12	45 ± 12	2 ± 1
8502	69 ± 6	28 ± 5	2 ± 1

the UMo and the Al of larger UMo particles. The thickness is around $1\mu\text{m}$. On the other hand, instead of small UMo particles a lot of small USi_x particles (up to $10\mu\text{m}$ in size) dispersed inside the matrix have been found - compare Fig. 4.43. Furthermore, no small Si (around $1\mu\text{m}$ in diameter) precipitates are visible inside the matrix, in contrast to what has been found inside similar fuel plates prepared with atomized UMo powder and the same Al2.1wt%Si alloy. In those plates a SiRDL formed around the spherical UMo particles leaving a Si depleted zone around the UMo particles. However, there were still small Si precipitates present inside the matrix, especially at regions more than $5\mu\text{m}$ away from the UMo [138, 193, 195]. It can therefore be concluded that in the plates examined here all the Si inside the matrix has reacted with the available UMo, especially with small UMo particles which are not present inside plates prepared with atomized UMo powder.

The Si/(U+Si) content of the SiRDL and the reacted UMo particles has been determined by standardless EDX analysis to be 42at%. This value is only slightly lower than values obtained previously on samples with 5wt% (Si/(U+Si)=50at%) and 7wt%Si (Si/(U+Si)=54at%) addition to the matrix (compare Table 4.11) [193]. The value is furthermore in full accordance with values found by Palancher et.al. on different fuel plates with similar Si additions to the matrix [217].

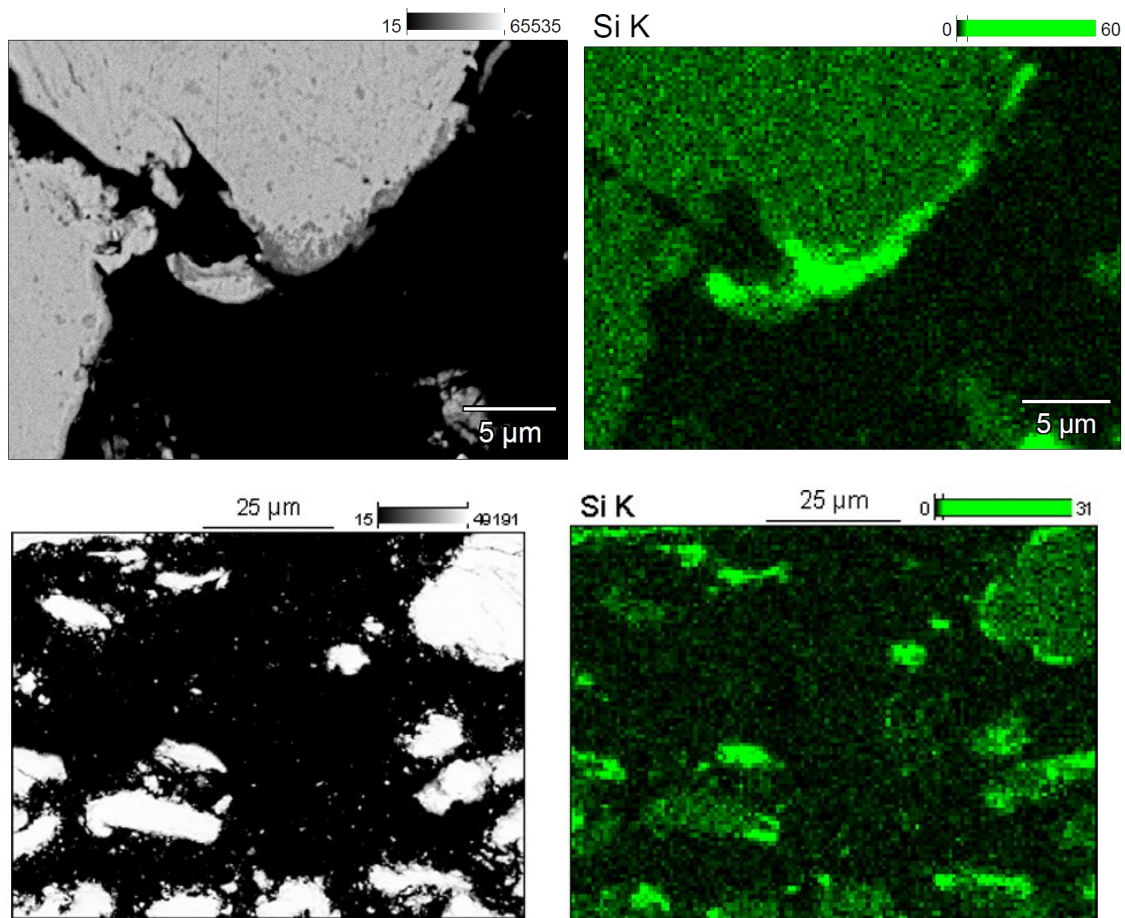


Figure 4.43: IRIS-TUM 8503 (2.1wt%Si inside the matrix): BSE images (left) and EDX maps on the Si K- α line (right) of the same area. Edges and small UMo particles reacted with the Si inside the matrix and formed a U-Si compound.

Table 4.11: Si content of the SiRDL found on IRIS-TUM samples containing 2.1wt%Si inside the matrix compared to previous work on similar samples [193].

	2,1wt%Si	5wt%Si	7wt%Si
	IRIS-TUM 8502	MAFIA-I-5	MAFIA-I-7
Si/(U+Si) (at%)	42	50	54

Table 4.12: Phase composition of different ground UMoAl samples as determined by laboratory scale XRD and Rietveld analysis before irradiation.

Plate	Al (wt%)	α -U (wt%)	γ -U-Mo (wt%)	UO ₂ (wt%)	$\alpha/(\alpha + \gamma)$ (%)
IRIS-TUM 8003	50.6	19.2	24.2	6	44.2
IRIS-TUM 8502	44.7	19.9	26.9	8.5	42.5
U8Mo [184]	10	20	43	27	31.7
U8Mo atomized [184]	22	13	62	3	17.3
U8Mo1Ti	60.3	10.8	20	8.9	35.2
U8Mo1.5Nb	49.9	11.7	28.9	9.4	29.1
U8Mo3Nb	62.2	8.8	24.8	4.3	26.1
U8Mo1Pt	65.4	5.8	19.6	9.2	22.7

IRIS-TUM plate samples: XRD analysis Results of the XRD analysis are given in table 4.12 together with values obtained on samples containing ground and atomized powder presented earlier in section 4.1 and on samples containing ground powder from the MAFIA-I irradiation test⁵. The values obtained for the composition of the two examined IRIS-TUM plates are identical within the limitations of the method. No signs of Si or Si-containing phases have been found inside the plate with Si addition to the matrix due to the small overall Si content. Despite the fact that no granular γ -phase destabilization of the UMo has been observed by SEM, a high amount of α -U has been found inside the samples ($\alpha/(\alpha + \gamma)$ =44.2 and 42.5 %, respectively for the two samples examined). These values are higher than values obtained on samples containing atomized powder (U8Mo atom: $\alpha/(\alpha + \gamma)$ =17.3% [184]), but similar to values obtained on other samples containing ground powder (U8Mo $\alpha/(\alpha + \gamma)$ =31.7% [184] and U8Mo1Ti $\alpha/(\alpha + \gamma)$ =35.2%). However, it should be pointed out that this γ -phase destabilization occurring on samples containing ground UMo can be diminished by adding some wt% Nb or Pt to the UMo as has been done during the MAFIA-I test [20, 44, 164]. The lattice parameters of the α -U as determined by Rietveld analysis of the measured XRD diagrams are given in Table 4.13. The well-known orthorhombic structure of α -U (symbol Cmcm) has been used during the Rietveld analysis. However, compared to the lattice constants given in literature [218], the crystal lattice of the α -U inside ground UMo/Al samples is in general slightly deformed: the b-parameter is contracted while the a- and c-parameters are stretched. The Mo content of the

⁵For details see below

Table 4.13: α -U cell parameters of different ground UMo powders as determined by laboratory scale XRD and Rietveld analysis before irradiation. Orthorhombic structure, symbol Cmc_m.

Plate	a(Å)	b(Å)	c(Å)	$\gamma(^{\circ})$
IRIS-TUM 8003	2.8603	5.8543	4.9651	90
IRIS-TUM 8502	2.8637	5.8543	4.9651	90
U8Mo1Ti	2.8640	5.8506	4.9642	90
U8Mo1.5Nb	2.8642	5.8542	4.9706	90
U8Mo3Nb	2.8599	5.8542	4.9732	90
U8Mo1Pt	2.8615	5.8478	4.9601	90
α -U [218]	2.8536	5.8698	4.9555	90

remaining γ -UMo phase has been calculated using the following expression [118]:

$$a(\text{Å})=3.4878-0.0034[\text{Mo}](\text{at}\%)$$

Calculated values are given in Table 4.14. It is noteworthy, that the calculated Mo content for the two IRIS-TUM samples of 11.8 and 11.1wt%, respectively is higher than the value expected from the production parameters given in [145] (8wt%Mo). This behavior is consistent with the values calculated from the γ -UMo lattice parameter of other samples prepared with ground powder.

However, a certain uncertainty on the calculated Mo content has to be considered. Comparing the expression used for this calculation with that determined by A.E. Dwight [112]

$$a(\text{Å})=3.4808-0.00314[\text{Mo}](\text{at}\%)$$

or another by S.T. Konobeevsky [119]

$$a(\text{Å})=3.481-0.00333[\text{Mo}](\text{at}\%)$$

the error can be estimated to be about 0,5 wt%. Even with such an uncertainty, the Mo content of the γ -phase remains still significantly higher than the mean alloy composition (8 wt%).

IRIS-TUM XRD analysis – Discussion of the results In this section the phase behavior of ground UMo will be discussed. First, the main results are summed up:

- XRD analysis of the ground UMo powder prior to plate production revealed only the presence of γ -UMo and UO₂. However, the broad peaks and the high background noise indicate that the lattice structure of the UMo powder is strongly disturbed due to defects accumulated during the grinding process.
- XRD analyses of two as-fabricated plates (with and without Si addition) reveal the presence of α -U besides γ -UMo in the samples. The ratio $\alpha/(\alpha + \gamma)$ was about 43-44% for each of them.

Table 4.14: γ -UMo lattice parameter as determined by laboratory scale XRD and Rietveld analysis and corresponding calculated Mo content before irradiation.

Plate	a(Å)	Mo(at%)	Mo(wt%)
IRIS-TUM 8003	3.4027	25.0	11.8
IRIS-TUM 8502	3.4077	23.6	11.1
U8Mo [184]	3,4	27,0	13,0
U8Mo1Ti	3,4007	25,6	12,2
U8Mo1.5Nb	3.4007	25.6	12.2
U8Mo3Nb	3.3964	26.9	12.9
U8Mo1Pt	3.4017	25.3	12.0

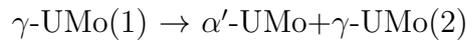
- The lattice constants of the α -U inside the samples differs somewhat from the lattice constants of α -U given in literature: the b-parameter is contracted while the a- and c-parameters are stretched.
- By calculating the Mo content of the remaining γ -UMo from its lattice constant a higher Mo content than expected has been found: 11-12wt%Mo instead of 8wt% as expected from the alloy ingredients composition and subsequent chemical analysis.

On the first view, the phase transformation occurring in ground UMo powder upon plate production of the initial γ -phase into α -U and γ -UMo enriched in Mo resembles strongly to the austenitic decomposition of γ -stabilized UMo according to the TTT diagram that occurs upon annealing for several hours at temperatures between 375°C and 550°C (compare Fig. 2.11 and section 2.2.2: γ -UMo decomposes first into α -U and γ -UMo enriched in Mo. Later, as the α -U content increases U_2Mo appears beside γ -UMo. Thermal equilibrium is reached when the entire γ -UMo has been transferred into a mixture of α -U + U_2Mo [74,116]. However, a detailed view on the data obtained on the IRIS-TUM samples excludes this simple interpretation:

- The fuel plates have reached 425°C for 1-2h during the production process. The γ -UMo decomposition according to the TTT diagram can therefore be excluded since it would take longer to initiate this reaction.
- Already the beginning of γ -UMo decomposition according to the TTT diagram (γ -UMo(1) \rightarrow γ -UMo(2) + α -U where UMo(2) has a higher Mo content than UMo(1)) leads to the formation of a cellular decomposition product [102], which has not been observed on the IRIS-TUM samples.
- The solubility of Mo in α -U is <1at% [116,219]. Under this condition and the fact that over 40% of the UMo decomposed into α -U (Table 4.12), the rise from the expected \approx 18at% to the measured \approx 25at% Mo inside the γ -UMo is too small to assume that the α -U can be free of Mo. However, two α -U like phases are known with Mo contents of 2.95-6.20at%Mo (α' , orthorhombic structure) and 7.20-11.18at%Mo (α'' , monoclinic structure) - compare section 2.2.2 [100,101].

- The measured cell parameters do not fit to values reported for pure α -U in literature: the b-parameter is contracted while the a- and c-parameters are stretched. However, this is characteristic of the α' -UMo phase reported in literature [72]. This phase is basically orthorhombic α -U with a lattice distortion due to the presence of Mo atoms on lattice sites [73].

Good results during the Rietveld analysis have been obtained using the orthorhombic structure of α -U (Space group Cmc₂m). No line splitting compatible with a monoclinic structure has been observed. Therefore the following γ -phase transformation mechanism is suggested for the samples containing ground U8Mo alloys:



where γ -UMo(1) has got a lower Mo content than γ -UMo(2).

Thus, the UMo particles inside the as-fabricated IRIS-TUM plates consist of a mixture of $\approx 40\%$ α' -UMo with a Mo content of $\approx 6\text{at}\%$ and of $\approx 60\%$ γ -UMo further enriched in Mo. This mixture of phases is still far from the thermal equilibrium state which would be α -U and U₂Mo [120].

By comparing the results to the lattice parameters of the α -U phase obtained on other samples containing ground UMo powder - the ground MAFIA-I samples and ground U8Mo samples examined earlier - and taking into account the fact that the γ -UMo in these plates is also enriched in Mo (compare Table 4.12, Table 4.13 and Table 4.14) one can conclude that this behavior is a general feature of this type of fuel plates.

The phase transformation from γ -UMo to α' -UMo + γ -UMo during the plate production occurred most likely due to the annealing of the lattice defects during the hot-rolling step that were induced by the grinding. Therefore we did not observe a decomposition of the γ -UMo phase but rather a recrystallization into two new phases.

A similar conclusion has been drawn by Palancher et.al. who examined IRIS-TUM samples using synchrotron radiation at 87keV in transmission mode. Details on the experimental procedure together with their results can be found in [217]. The authors concluded that the samples have recrystallized into a mixture of α' -U, γ -UMo and U₂Mo. It is probable that the three phases identified by Palancher et.al. can also be found in our samples⁶ - however, the U₂Mo phase and the γ -UMo phase can hardly be distinguished by laboratory scale XRD equipment due to the limited resolution compared to experiments using synchrotron radiation.

No signs of α -U or α -U-like phases have been found during the post irradiation examinations of the IRIS-TUM plates [70]. The phase transformation γ -UMo(1) \rightarrow α' -UMo + γ -UMo(2) has therefore been reversed. This effect has been observed before after in-pile and heavy ion irradiation [60, 126, 184].

Influence of further alloying the UMo

It has been suggested to further alloy the UMo with ternary element to increase the γ -phase stability and by this mean reduce the UMo-Al interaction (compare section 2.3). To test this hypothesis ternary U8MoX alloys have been created where X=1,5wt%Nb, 3wt%Nb, 1wt%Ti and 1wt%Pt. In this section, the microstructure prior to heavy ion

⁶In fact, they examined samples originating from the same fuel plates

irradiation of these samples will be discussed.

On first view, the SEM reveals the typical microstructure of ground powder: particles of irregular sizes and shapes are dispersed in the Al matrix. The particles are oxidized and contain oxide stringers, compare e.g. Fig. 4.41 and Fig. 4.42. In addition to what has been observed on the fresh IRIS-TUM samples a Fe-Co-Ni-W contamination has been found at some spots, most likely due to the wear of the grinding tools.

No signs of Nb or Pt precipitation have been found inside the samples containing U8Mo1.5Nb and U8Mo1Pt. These two additions have dissolved uniformly inside the UMo - compare Fig. 4.44.

In contrast, Nb precipitates (size $\approx 1 - 5 \mu m$) and larger Nb stringers have been found inside the U8Mo3Nb (compare Fig. 4.45(a)). The small precipitates indicate that the solubility limit for Nb inside U8Mo may be reached: segregation of small round precipitates of a second phase inside a dominant first phase frequently occurs upon cooling from a single phase to a two phase regime [208]. The rather large Nb stringers indicate, however, that the initial homogenization step, which consisted of frequent remelting and cooling followed by a final heat treatment of the U8Mo3Nb alloy, was not sufficient to fully homogenize the sample.

The mean composition of the Nb stringers and the Nb precipitates is shown in table 4.15. All values show a huge standard deviation since the single measured values varied considerable. While the stringers consist almost exclusively of Nb and contain only traces of Mo and U the precipitates contain a considerable amount of U and Mo. This behavior underlines the hypothesis that the stringers consist of Nb that has not been dissolved during the melting and annealing step whereas the precipitates occurred during cooling due to phase segregation.

Precipitation has also been found inside the sample containing U8Mo1Ti. Here, Ti rich precipitates of about $1 \mu m$ diameter have been found inside the UMo (compare Fig. 4.45(b)). In contrast to the U8Mo3Nb alloy, no stringers have been found. The composition of the Ti rich precipitates is given in table 4.16. The precipitates consist mainly of Ti (82at%) and U (14at%) and are depleted in Mo (4at%) Again, the values varied considerable when measuring different particles as can be seen from the huge standard deviation.

A similar precipitation behavior has been observed before by A. Ewh [162]: The authors examined a U8wt%Mo3wt%Nb and a U7wt%Mo3wt%Ti alloy after 96h and after 96h+quenching+96h at $950^\circ C$. Inside the U8Mo3Nb alloy, the authors found after annealing for 96h Nb-Mo rich precipitates (size $\approx 1 - 2 \mu m$) with an average composition of 37at%Nb and 62at%Mo. After an additional anneal of 96h at $950^\circ C$ the composition of the precipitates did not change but the amount increased from 4.4 surface% to 6.6 surface%. Inside the U7Mo3Ti alloy the authors found Ti rich precipitates with an average composition of 37at%Ti, 52at%Mo and 11at%U. After an additional anneal of 96h at $950^\circ C$ the composition of the precipitates did not change but the amount increase from 5.6 surface% to 9.0 surface%.

The composition of the precipitates observed by A. Ewh differs somewhat from the composition observed in our samples. This deviation is most likely due to the different heat treatments: in our case the annealing time was shorter. It is most likely that the thermal equilibrium has not yet been reached in our samples.

Results of the XRD analysis are presented in tables 4.12, 4.13 and 4.14. By comparing the $\alpha/(\alpha + \gamma)$ values of the single samples in table 4.12 one finds that

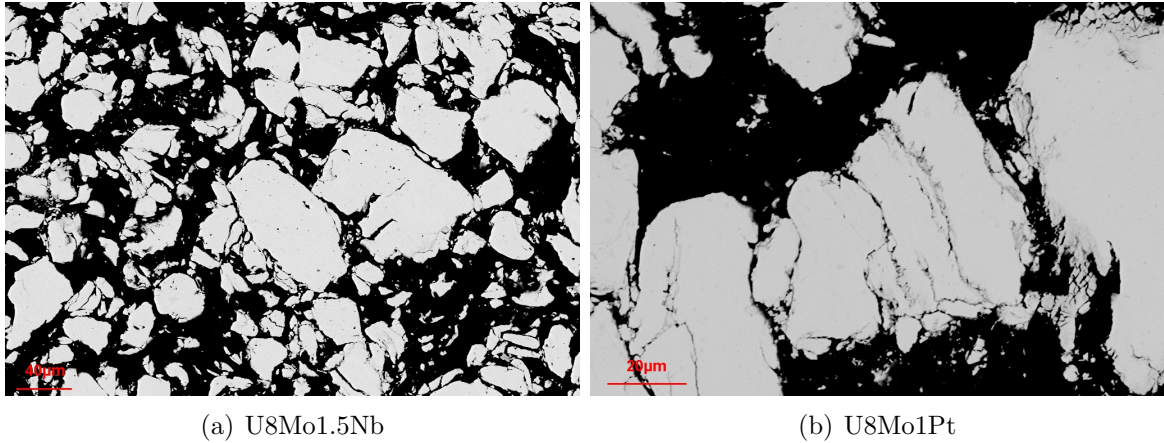


Figure 4.44: Ground U8Mo powder with 1.5wt%Nb (a) and 1wt%Pt (b) addition. The third element has been completely dissolved inside the UMo, no precipitation is visible.

Table 4.15: Composition of the Nb precipitates and stringers

	Nb(at%)	Mo(at%)	U(at%)
Precipitate	75±9	4±3	22±9
Stringers	97±3	1.5±0.5	2±2

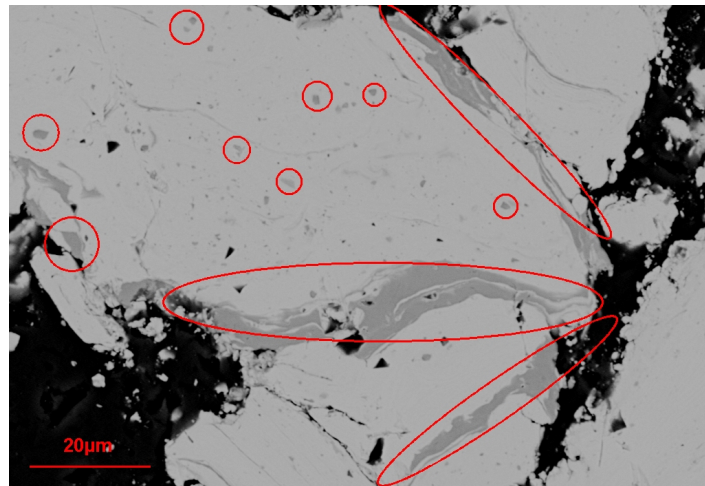
further alloying the UMo with a third element can stabilize the UMo- γ phase compared to pure UMo. The addition of 1.5wt% and 3wt% Nb lead to a stabilization of the γ -UMo where the higher alloy composition revealed slightly better results. However, since inside the 3 wt%Nb alloy already precipitation occurred, it is likely that the stabilizing effect has already reached its saturation.

In case of 1wt%Pt addition the stabilizing effect is even more pronounced. Here, a $\alpha U/(\alpha U + \gamma UMo)$ ratio of 22.7 has been found which is lower than the values found in pure U8Mo, U8Mo1.5Nb and U8Mo3Nb. Since no Pt precipitation occurred it is likely that the effect can be potentiated by adding 2-3wt%Pt.

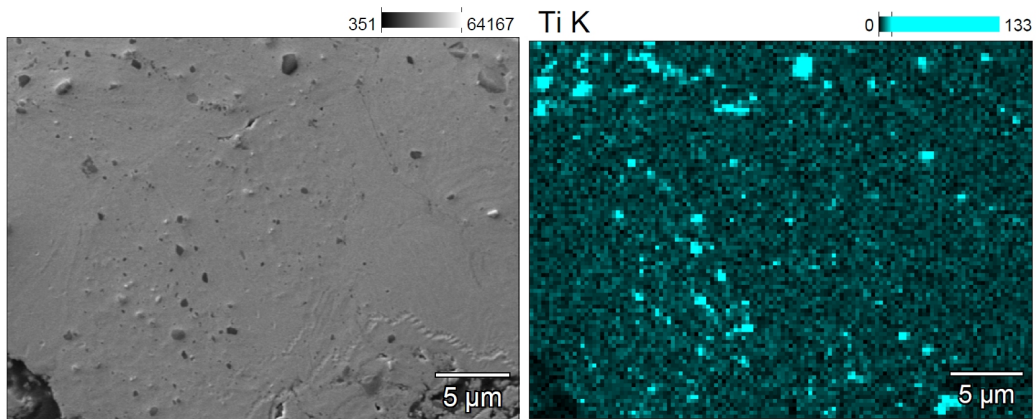
In case of 1wt%Ti addition no effect on the γ -UMo stability compared to unalloyed UMo could be deduced. An explanation for this behavior is most likely the occurrence of Ti precipitates which indicate that virtually no Ti is present inside the UMo lattice. Regarding the lattice parameters of the α -UMo phase (table 4.13) one finds the same behavior than inside the samples containing pure ground U8Mo: the b-parameter is contracted, the a and c parameter are stretched compared to pure α -U. The absolute values are approximately the same than inside the pure U8Mo samples. From the

Table 4.16: Composition of the Ti precipitates

	Ti(at%)	Mo(at%)	U(at%)
Precipitate	82±8	4±2	14±8



(a) U8Mo3Nb



(b) U8Mo1Ti

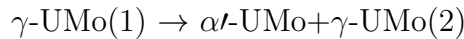
Figure 4.45: (a) BSE-image of the U8Mo3Nb alloy ground powder. Nb rich precipitates have formed (red marked positions).

(b) BSE image and EDX map on the Ti K- α line: Ti rich precipitates are visible.

Table 4.17: Composition of the IDL grown around samples containing ground powder after irradiation with iodine at 80 MeV.

Sample	U(wt%)	Mo(wt%)	Al(wt%)	Al/(U+Mo)(%)
U8Mo1Ti	11.7±2.0	2.2±0.6	71.2±7.7	5.3±1.2
U8Mo1.5Nb	10.3±1.3	2.0±0.2	75.2±2.5	6.2±0.8
U8Mo3Nb	10.5±2.1	2.2±0.4	73.0±4.8	6.0±1.8
U8Mo1Pt	11.8±1.8	2.0±0.5	70.7±2.8	5.2±0.7
IRIS-TUM 8003	15.3±2.6	2.6±0.7	66.2±4.9	3.9±0.9

lattice parameters of the γ -UMo the Mo content of the γ -phase has been calculated (compare table 4.14). As in the pure U8Mo case the calculated Mo values inside the ternary alloys are higher than what has been expected from the alloys composition⁷. Therefore the same γ -phase decomposition mechanism as in the samples containing pure ground U8Mo is suggested for the samples containing ground U8MoX ternary alloys:



where γ -UMo(1) has got a lower Mo content than γ -UMo(2).

4.7.2 Irradiation behavior of ground fuel - IDL formation and phase behavior

The four U8MoX ternary alloy samples have been irradiated with iodine at 80 MeV. In addition, one sample containing pure ground U8Mo powder originating from the IRIS-TUM spare test plates (plate identification 8003) has been irradiated and serves as a reference. After irradiation, the samples have been examined using SEM/EDX (surface and cross section analysis) and XRD.

As shown in figure 4.46, a thick UMo/Al interaction layer has grown at every UMo particle periphery affected by the ion beam inside each irradiated sample. The thickness of the IDL ranges between 7-15 μm . A reduction of the IDL thickness due to further alloying the UMo could not be deduced. However, due to the irregular shape of the UMo particles it is often very difficult to conclude on this point. The IDL elementary composition is given in table 4.17. The Al/(U+Mo) ratio varies inside the U8MoX ternary alloy samples between 5.2±0.7% and 6.2±0.8%. The value inside the pure U8Mo sample is 3.9±0.9%. From the different gray tones of the IDL in figure 4.7.2 it can be concluded that the IDL consists of different sublayers. EDX measurements have shown that the elementary composition of these sublayers only differs in oxygen content and not significantly in the Al/(U+Mo) ratio. The high oxygen content in the deepest part of the IDL is most probably a consequence of the uranium-oxide which is

⁷The formula used for calculating the Mo content from the γ -UMo lattice parameter is empirical and does not take into account ternary alloys. It has nevertheless been used to estimate the γ -UMo phase composition inside the ternary UMoX alloys under the assumption that the ternary alloy additions behave like the Mo atoms inside the γ -UMo lattice.

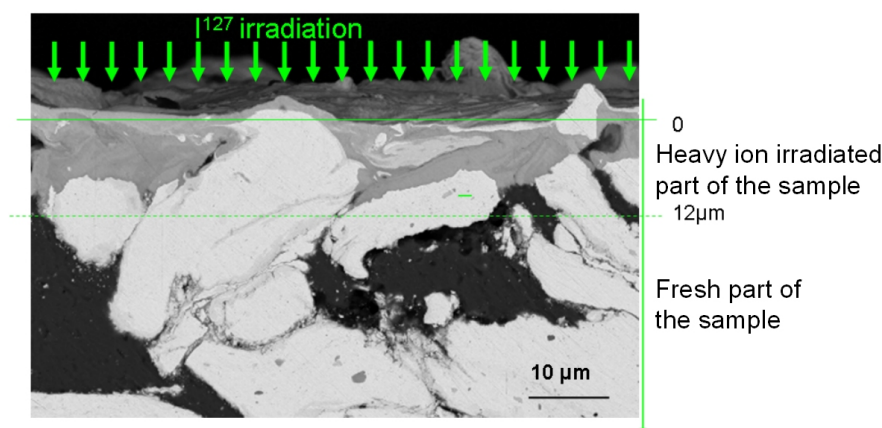


Figure 4.46: BSE image of a cross section through an ion irradiated sample from one IRIS-TUM plate without Si addition to the matrix. A large UMo/Al interaction is visible at the interface between the ground UMo powder and the Al.

present in the fresh ground UMo particles, compare Fig. 4.42.

The IDL Al/(U+Mo) composition has not been influenced by the different ternary alloy compositions. Indeed, no signs of the ternary element could be resolved inside the IDL using EDX, most probably due to the low overall content.

Regarding the samples which contained stringers and precipitates inside the UMo before irradiation (U8Mo1Ti and U8Mo3Nb) two different effects have been observed: in case of Nb, the precipitates and stringers have been dissolved inside the IDL and the UMo during irradiation - no signs of precipitates could be found inside the irradiated area.

In contrast the Ti precipitates did not dissolve and even got incorporated into the IDL - compare Fig. 4.47.

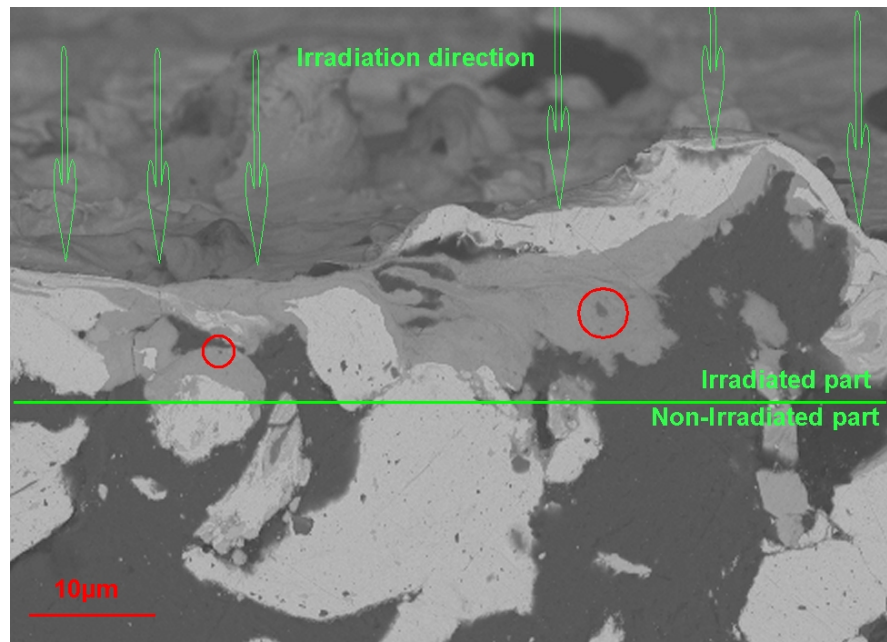
The phase composition of the irradiated samples is given in table 4.18 and can be compared to the values of the samples before irradiation given in table 4.12.

Inside all samples UAl_3 grew during irradiation - this phase had not been present in the fresh samples. The same phase has been observed inside the samples containing atomized UMo/Al powder after irradiation with heavy ions. It can therefore be concluded that the IDL consists mainly of this new phase. Again the Al/(U+Mo) ratio determined by EDX is higher than the Al/U ratio defined by UAl_3 .

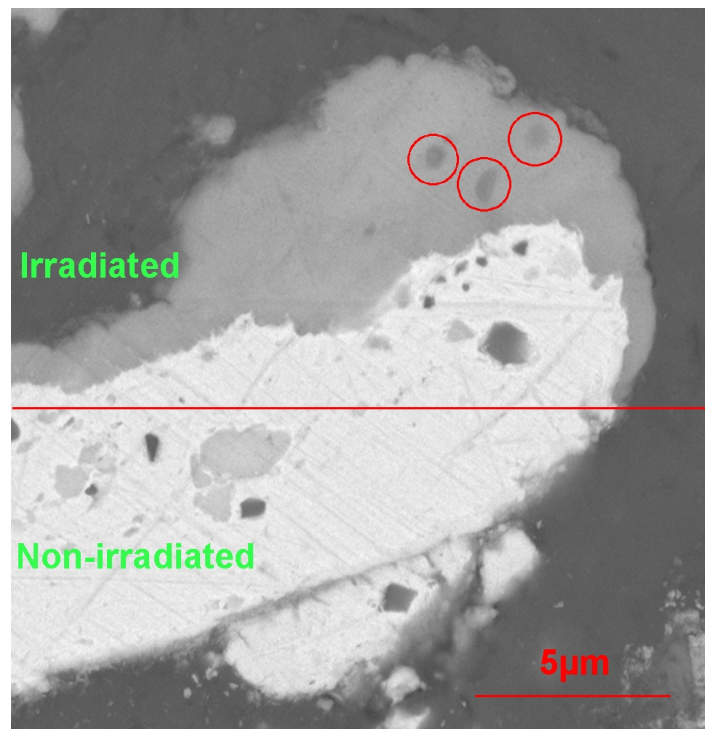
The ratio $\alpha\text{-U}/(\alpha\text{-U}+\gamma\text{-UMo})$ is lower than inside the unirradiated samples. The phase transformation $\gamma\text{-UMo}(1) \rightarrow \alpha\text{-UMo}+\gamma\text{-UMo}(2)$ has therefore been reversed during heavy ion irradiation. This effect has been observed before after in-pile and heavy ion irradiation and already been described in section 4.1 [60, 126, 184, 212].

The lattice parameters of the $\alpha\text{-U}$ and $\gamma\text{-UMo}$ after irradiation are given in tables 4.19 and 4.20. The $\alpha\text{-U}$ cell parameters may reveal a larger error due to the low overall $\alpha\text{-U}$ content after irradiation. It can be nevertheless observed that the lattice parameters differ from the values reported in literature for pure $\alpha\text{-U}$. Therefore we conclude that some Mo atoms are present inside the $\alpha\text{-U}$ lattice and that the α -like phase present after irradiation is identical to the one present inside the fresh samples: $\alpha\text{-UMo}$.

The lattice parameters of the $\gamma\text{-UMo}$ after irradiation are given in table 4.20. The



(a)



(b)

Figure 4.47: Low (a) and high (b) magnification image of an U8Mo1Ti/Al sample after irradiation with heavy ions. The Ti precipitates present inside the UMo did not dissolve during irradiation and got incorporated into the IDL.

Table 4.18: Phase composition of different ground UMoAl samples as determined by laboratory scale XRD and Rietveld analysis after irradiation with iodine at 80 MeV.

Plate	α -U (wt%)	γ -UMo (wt%)	UO ₂ (wt%)	UAl ₃ (wt%)	$\alpha/(\alpha + \gamma)$ (%)
U8Mo1Ti	3.3	23.3	5.7	4.6	12.8
U8Mo1.5Nb	2.6	23.6	6.7	6.7	8.9
U8Mo3Nb	3.8	34.9	8.9	3.5	10.0
U8Mo1Pt	1.1	7.2	3.2	1.6	13.4
U8Mo [184]	8	41	25	-	21

Table 4.19: α -U cell parameters of different ground UMo powders as determined by laboratory scale XRD and Rietveld analysis after irradiation. Orthorhombic structure, symbol Cmc₂m.

Plate	a(Å)	b(Å)	c(Å)	γ (°)
U8Mo1Ti	2.8604	5.8528	4.9809	90
U8Mo1.5Nb	2.8580	5.8538	4.9925	90
U8Mo3Nb	2.8621	5.8594	4.9803	90
U8Mo1Pt	2.8431	5.8239	4.9520	90
α -U [218]	2.8536	5.8698	4.9555	90

Mo content inside the UMo phase of the irradiated samples has been calculated from the γ -UMo lattice parameter. Compared to the non-irradiated case one finds that the Mo content inside the γ -UMo is reduced from around 12 wt%Mo to around 9wt%Mo - which is almost the value expected according to the production parameters (8wt%Mo). An exception is the sample containing U8Mo1Pt where no significant reduction could be observed.

This behavior confirms that the phase decomposition γ -UMo(1) \rightarrow α' -UMo+ γ -UMo(2) described earlier has been reversed during heavy ion irradiation.

Table 4.20: γ -UMo lattice parameter as determined by laboratory scale XRD and Rietveld analysis and corresponding calculated Mo content after irradiation with iodine at 80 MeV.

Plate	a(Å)	Mo(at%)	Mo(wt%)
U8Mo1Ti	3.4229	19.1	8.7
U8Mo1.5Nb	3.4171	20.8	9.6
U8Mo3Nb	3.4197	20.0	9.2
U8Mo1Pt	3.3972	26.6	12.8
U8Mo [184]	3.423	16.4	7.3

4.7.3 Conclusions on ground UMo fuels

- The non-irradiated samples in general contain UMo particles of irregular size and shape that are oxidized and include oxide stringers. Furthermore, the plates contain a considerable amount of porosity.
- No precipitation of the ternary phase has been found in case of 1.5wt%Nb and 1wt%Pt. Precipitates have been found in case of 1wt%Ti and 3wt%Nb.
- It has been found that the increased γ -phase decomposition that is in general observed inside UMo/Al plates prepared with ground UMo powder does not follow the normal decomposition path according to the TTT diagram. We found that a recrystallization of the γ -UMo that has accumulated many defects during the grinding process into two new phases occurs during the fuel plate production. The following phase transformation path has been suggested: γ -UMo(1) \rightarrow α -UMo + γ -UMo(2).
- Compared to the pure U8Mo case the addition of 1.5wt%Nb, 3wt%Nb and 1wt%Pt stabilizes the γ -phase with respect to the α -phase. No effect on the γ -phase stability could be found inside the sample alloyed with 1wt%Ti. This is most probably due to the formation of Ti precipitates which indicates that the UMo lattice is virtually Ti-free.
- After irradiation a thick IDL that consists mainly of UAl_3 formed around each particle affected by the ion beam. However, the Al/(U+Mo) ratio as determined by EDX analysis is in general higher than 3.
- In case of 1wt%Ti inside the UMo the Ti precipitates did not dissolve during heavy ion irradiation and even got virtually unchanged incorporated inside the IDL.
- The decomposition of the γ -UMo into an α -U like phase and γ -UMo enriched in Mo has been reversed during heavy ion irradiation as has been observed before.
- No influence of further alloying the UMo on the IDL formation could be deduced.
- The enhanced in-pile performance of full-size UMo plates prepared with ground powder compared to those prepared with atomized powder has to be ascribed to the improved fission gas behavior: the higher initial porosity content inside plates prepared with ground powder takes up part of the swelling. Furthermore, the IDL formed inside these plates can retain the fission gases more effectively than the one grown around atomized UMo particles. This effect should be checked by implanting rare gases into an IDL grown with heavy ion irradiation inside both, atomized and ground samples.

Chapter 5

Summary and outlook

5.1 Summary

The aim of this thesis was the identification of promising material combinations to suppress the undesired UMo/Al interaction and to find a candidate for a future in-pile test. The success of this work was only possible due to the close cooperation with colleagues from the Commissariat à l'Énergie Atomique (CEA) and AREVA-CERCA, France. During this thesis, 20 different candidates for a future high-density nuclear for research and test reactors have been examined. All samples based on UMo powder dispersed in an Al matrix. Thereby, different additions to the Al matrix or to the UMo have been examined with regard to their effectiveness in suppressing the undesired UMo-Al interaction. Furthermore, the effectiveness as a diffusion barrier of an uranium oxide layer at the interface UMo-Al has been studied. For this, more than 60 samples have been prepared whereof more than 40 samples have been irradiated with Iodine at 80 MeV at the tandem accelerator in Garching. For these irradiations ≈ 6 weeks of beam time have been granted. All samples have been characterized before and after irradiation using SEM/EDX (surface and cross section examinations) and laboratory scale XRD. In addition, the most interesting samples have been examined with μ -XRD at the ESRF in Grenoble, France and at the SLS/PSI in Villigen, Switzerland. In addition, it has been studied to which extent the growth of the irradiation induced UMo/Al diffusion layer is influenced by the particular irradiation conditions like irradiation temperature, ion flux, integral fluency and irradiation angle. For this work, additional beam time at the tandem accelerator in Garching, at the ESRF and at the SLS/PSI has been granted.

Most interesting results have been obtained on the samples with **Si addition** to the matrix. It could be shown that during the production process a SiRDL forms at the interface UMo/Al that protects the UMo particle during irradiation. Thereby the samples with the highest Si concentrations showed the best behavior.

It has been shown that **Ti addition** to the matrix prevents the growth of a conventional IDL in case the Ti particles are in direct contact with the UMo particles. Furthermore, no diffusion between the UMo and the Ti and between the Ti and the Al occurred. Ti can be therefore regarded as a promising diffusion barrier but is rather worthless as a matrix addition.

The most promising results concerning **Bi addition** to the aluminum obtained by Williams [35] on uranium-aluminum diffusion couples could not be verified. The Bi ox-

idized during the production process which resulted in a brittle Al matrix with finely dispersed Bi-oxide and Bi-metal. However, during irradiation these precipitates dissolved and a Bi-rich layer formed at the interface between a normal IDL and the Al, leaving the IDL Bi free. Nevertheless, a reduction of the IDL layer thickness could not be deduced.

Magnesium addition to the matrix resulted in a complete and homogeneous dissolution of the Mg inside the Al. However, an influence on the IDL formation kinetics could not be deduced.

In case an **oxide layer** has been used as a diffusion barrier the particles showed the tendency to loose contact with the matrix and to tilt out of the irradiated surface. Furthermore, even before irradiation the oxide layer revealed cracks and gaps formed at the interface UMo-matrix. This effect was more pronounced in case of thick oxide layers. It can only be suspected whether this effect already occurred during the production process of the miniplates or during the polishing of the samples. In case the UMo particles did not loose contact with the matrix an IDL layer formed at the interface UMo-Al. A reduction of IDL thickness could not be deduced due to the presence of the oxide layer. This oxide layer got incorporated into the IDL and altered its microstructure. It can only be suspected that the improved in-pile behavior of test plates prepared with oxidized UMo particles may result from an improved fission gas retaining inside the IDL with incorporated oxide. However, irradiation with Iodine alone is to be adapted to verify this effect.

The addition of **ternary elements** to UMo can tremendously reduce the γ -UMo phase decomposition during plate production. However, no positive effect on the IDL formation kinetics could be deduced. This can most likely be accounted to the fact that during irradiation with heavy ions or in-pile the γ -phase decomposition is completely reversed, i.e. α -UMo transforms back to γ -UMo.

Based on the results of this thesis and studies of other groups the following conclusions can be drawn:

- On close view, additions to the Al matrix and/or additions to the UMo can be reduced to the self-acting formation of a protective layer at the UMo/Al interface in dispersed fuel. These layers form already during the production process or latest during pile irradiation. In case of second element addition to the Al it is therefore advised to chose an element with a higher affinity to uranium than to aluminum. On the other hand, in case of ternary additions to UMo it is recommended to chose elements with higher affinity to aluminum than to uranium. In case additions to the UMo and the aluminum are chosen they should have a very high affinity to form compounds with each other compared to the other elements in the system in order to form a protective layer around the UMo particles [31, 38, 147, 159].
- In order not to reduce the available U-density too much it is recommended to use thin layers in the order of magnitude of $1\mu m$ as diffusion barriers inside dispersed UMo/Al fuels. Thin, stable layers like U-oxide or U-nitride have been used successfully [165]. The other option is to directly apply a reactive layer like Si, USi or ZrN on the UMo particles before plate production [39]. Since the fission products easily penetrate such a thin layer ion beam mixing will occur. Therefore, these layers will never be able to suppress completely the U-Al diffusion. However, they

can control the formation kinetics and lead to the formation of stable diffusion compounds when incorporated into the diffusion layer.

- In case of monolithic fuel it is possible to insert a rather thick diffusion barrier at the interface UMo-Al. The thickness can be much higher than the penetration depth of the fission products. An order of magnitude is $20\text{-}50\mu\text{m}$. It is advised to use materials that do not form easily compounds with uranium and aluminum like zirconium, titanium or tantalum. In this way, the UMo-Al diffusion can be completely suppressed. Here, especial attention must be paid on the adhesion of the single layers. For example, a oxide layer at the interface UMo-Al would reduce the adhesion. In contrast, a Zr layer enhances the fuel-cladding bonding [163].
- Ternary additions to the UMo in order to stabilize the γ -UMo upon heating are of minor importance. In-pile irradiation at low temperatures reverses the phase decomposition of UMo. These additions are only valuable in case they form a protective layer at the UMo/Al interface or in case of annealing of the fuel element prior to the irradiation. In the later case they will reduce or avoid an initially present, thermal grown interaction layer.

Table 5.1: List of conclusions drawn from the MAFIA-I material down selection program

Name	Alloy	Matrix	Result
MAFIA-I-3	U-7wt%Mo	Al-2wt%Si	
MAFIA-I-5	U-7wt%Mo	Al-5wt%Si	SiRDL formed during production at the interface between UMo and Al in case of 5wt%Si and 7wt%Si. The SiRDL protects the UMo during irradiation but gets consumed.
MAFIA-I-7	U-7wt%Mo	Al-7wt%Si	
MAFIA-I-9	U-7wt%Mo	Al-2wt%Mg	Mg completely dissolved inside Al - no effect on UMo-Al diffusion.
MAFIA-I-11	U-7wt%Mo	Al-2wt%Ti	Ti addition to Al matrix prevents growth of IDL only in case Ti is in direct contact with UMo. Ti therefore a good diffusion barrier but rather worthless as a matrix addition.
MAFIA-I-13	U-7wt%Mo	Al-2wt%Bi	Promising results from Williams [35] could not be reproduced - brittle Al matrix already during production, no reduction of IDL growth
MAFIA-I-15	U-7wt%Mo	Al-5wt%Bi	
MAFIA-I-17	U-7wt%	Mg	Mg matrix reacted with AlFeNi cladding during miniplate production to a brittle compound - it was not possible to obtain samples for irradiation.

Name	Alloy	Matrix	Result
MAFIA-I-4	U-7wt%Mo(ox)	Al-2wt%Si	
MAFIA-I-6	U-7wt%Mo(ox)	Al-5wt%Si	
MAFIA-I-8	U-7wt%Mo(ox)	Al-7wt%Si	
MAFIA-I-10	U-7wt%Mo(ox)	Al-2wt%Mg	
MAFIA-I-12	U-7wt%Mo(ox)	Al-2wt%Ti	
MAFIA-I-14	U-7wt%Mo(ox)	Al-2wt%Bi	
MAFIA-I-16	U-7wt%Mo(ox)	Al-5wt%Bi	

Oxidized UMo particles lost contact with Al matrix during irradiation in case of thick oxide layers ($>1\mu\text{m}$). Thin oxide layers get incorporated into IDL and change morphology.

Name	Alloy	Matrix	Result
MAFIA-I-18	U-8wt%Mo-1wt%Ti	Al	
MAFIA-I-19	U-8wt%Mo-1.5wt%Nb	Al	Third element addition increased γ -phase stability during sample production. However, no effect on IDL formation visible. γ -phase decomposition which occurs during production is reversed during heavy ion irradiation.
MAFIA-I-20	U-8wt%Mo-3wt%Nb	Al	
MAFIA-I-21	U-8wt%Mo-1wt%Pt	Al	

5.2 Further prospects for heavy ion irradiation

In this thesis, the importance of heavy ion irradiation as a method to test the irradiation behavior of nuclear fuels has been further developed. In principal every method effective in reducing the UMo/Al interaction can be reduced to the formation of a protective layer at the UMo/Al interface.

Recently it became possible to produce different UMo/Al layer systems using the sputtering technique. These new type of samples may serve very well as model systems for dispersed samples and also for monolithic samples (compare Fig. 5.1(a)). Hereby, the disadvantage of heavy ion irradiated dispersed samples is avoided: the uneven UMo/Al interface hinders the determination of exact IDL layer thicknesses. However, it is possible to grow in a very controlled way an IDL at the interface of UMo sputtered onto an Al substrate (compare Fig. 5.1(b)).

Using this technique different diffusion barriers can easily be down-selected. In case diffusion barriers for dispersed-type fuel plates should be tested sputtering of a thin ($\approx 1\mu m$) reactive layer between the UMo and the Al substrate is recommended. Here, Si, Zr or ZrN are promising candidates.

In case diffusion and bonding layers for monolithic type fuel plates are desired a layer of some $10\mu m$ thickness should be sputtered on an Al substrate and be covered with some μm of UMo. Of course, in this case no UMo/Al interaction will occur since the penetration depth of the heavy ions is lower than the layer thickness. Here, the possible evolution of a radiation induced diffusion layer at the interface UMo/barrier material can be studied. Suited candidates for this protective layers are inert metals with high melting point like Zr, Ti or Ta. However, noble metals like gold or platinum are also interesting candidates to prevent the IDL.

To fully emulate the in-pile behavior of UMo/Al nuclear fuels not only the build-up of the IDL layer must be regarded but also the accumulation of fission gas, especially xenon, is important. The accumulation of fission gas inside the fuel and the insufficient ability of the IDL to retain the fission gases is the mechanism that leads to unacceptable plate swelling and plate failures. So far, the rare gas behavior inside the IDL and the fuel has not been studied out of pile. However, it is possible to implant noble gases like argon or krypton into metals using particle accelerator. The accumulation and behavior of the noble gases can afterwards be examined using TEM and SEM. It should therefore be possible first to grow a IDL using Iodine at 80MeV and afterwards implant Ar or Kr to emulate the fission gas behavior inside the IDL, the UMo and the aluminum.

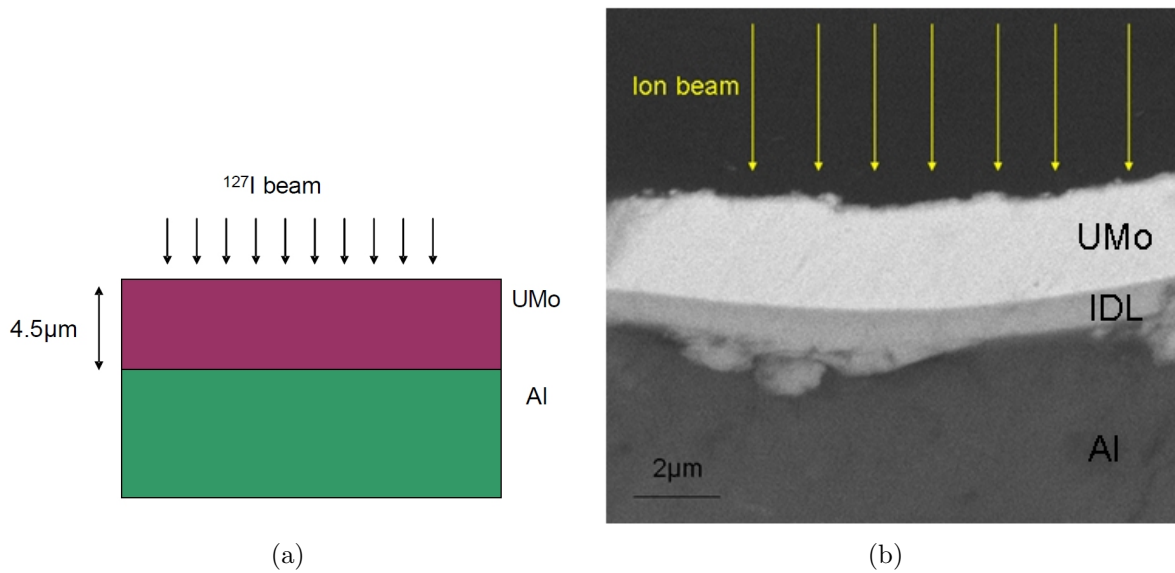


Figure 5.1: (a) Sketch of the transversal cross section of a sputtered UMo/Al sample with $4\mu\text{m}$ thick UMo layer on an Al substrate. An IDL can be inserted at the interface UMo/Al. (b) Transversal cross section of a heavy ion irradiated sample (Al substrate coated with UMo) showing the growth of an IDL.

Appendix A

Sample preparation

To get access to the meat layer the following steps have been performed prior to the heavy ion irradiation.

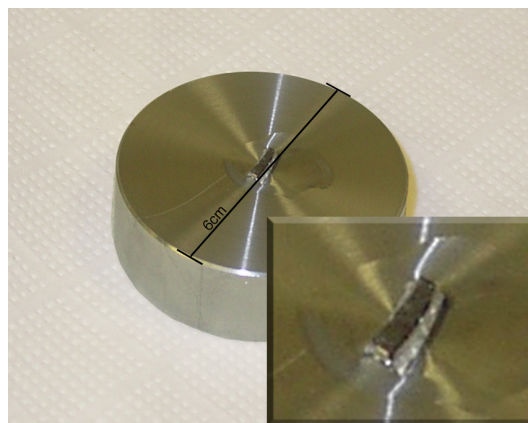
The miniplates provided by AREVA-CERCA have been transferred into a glovebox for the following handling to prevent contamination (figure A.1(a)). The miniplates have been cut into small pieces ($\approx 5 \times 5 \text{ mm}^2$) and glued onto an Aluminum block (compare figure A.1(b)). Afterwards, the sample has been flattened and the cladding has been removed using wet abrasive paper of subsequent smaller grains size (roughness 800 and 1000). Water has been used as cooling and cleaning fluid. The grinding step has been followed by in total 3 wet polishing steps in which the grain size of the particles has been reduced step by step. The polishing consumables have been obtained from Struers:

1. DP-Mol, a woven wool polishing cloth, together with DiaDuo, grain size $3 \mu\text{m}$. DiaDuo is an all-in-one Diamond suspension containing small diamonds of a definite size.
2. DP-Nap, a polishing cloth containing small-sized, rayon-viscose fibers, flocked on woven on textile, together with DiaDuo, grain size $1 \mu\text{m}$.
3. OP-chem, a neoprene foam polishing disk, together with OP-U, a suspension containing active oxide and colloidal silicon. The OP-U suspension has been mixed with demineralized water in a ratio 30:70 OP-U:water. This step combines chemical and mechanical polishing and results in a very good surface flatness with almost no scratches left [220].

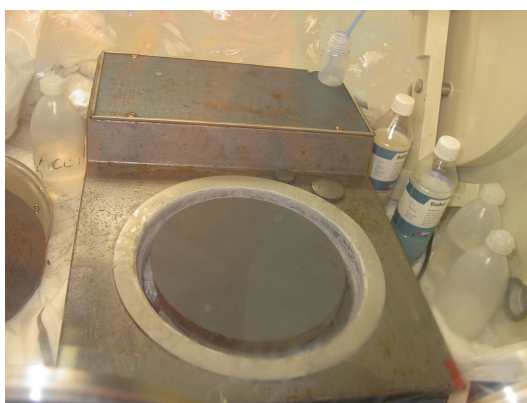
After the last polishing step, the samples have been removed from the Aluminum block using acetone and have been cleaned in an ultrasonic bath using water and Isopropanol, respectively.



(a) Glovebox used for polishing



(b) Sample before polishing



(c) Manual polishing disk, diameter 200 mm

Figure A.1: Pictures of the equipment used during polishing: A.1(a), a picture of the glove box used to prevent contamination during sample handling
A.1(b), a small piece cut out of a miniplate and glued onto an Aluminum block, just before polishing
A.1(c), the manual polishing disk used to prepare the samples

Appendix B

Phase diagrams

A selection of binary equilibrium phase diagrams of different U and Al based alloys is presented on the following pages. The phase diagrams have been chosen according to the materials examined in this thesis.

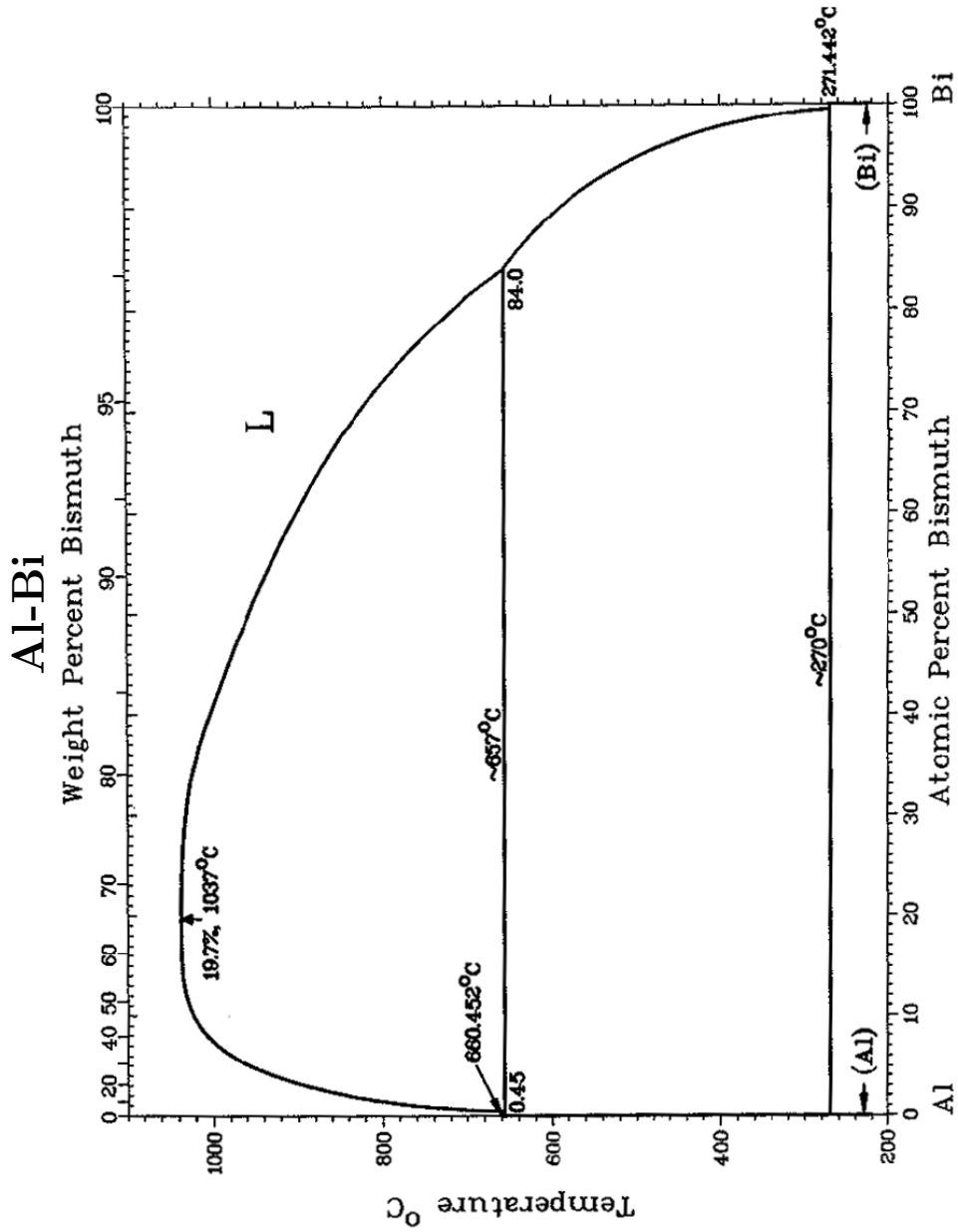


Figure B.1: Phase diagram of the aluminum-bismuth system. The solubility of Bi in Al is virtually nil at room temperature [208].

Al-Mg

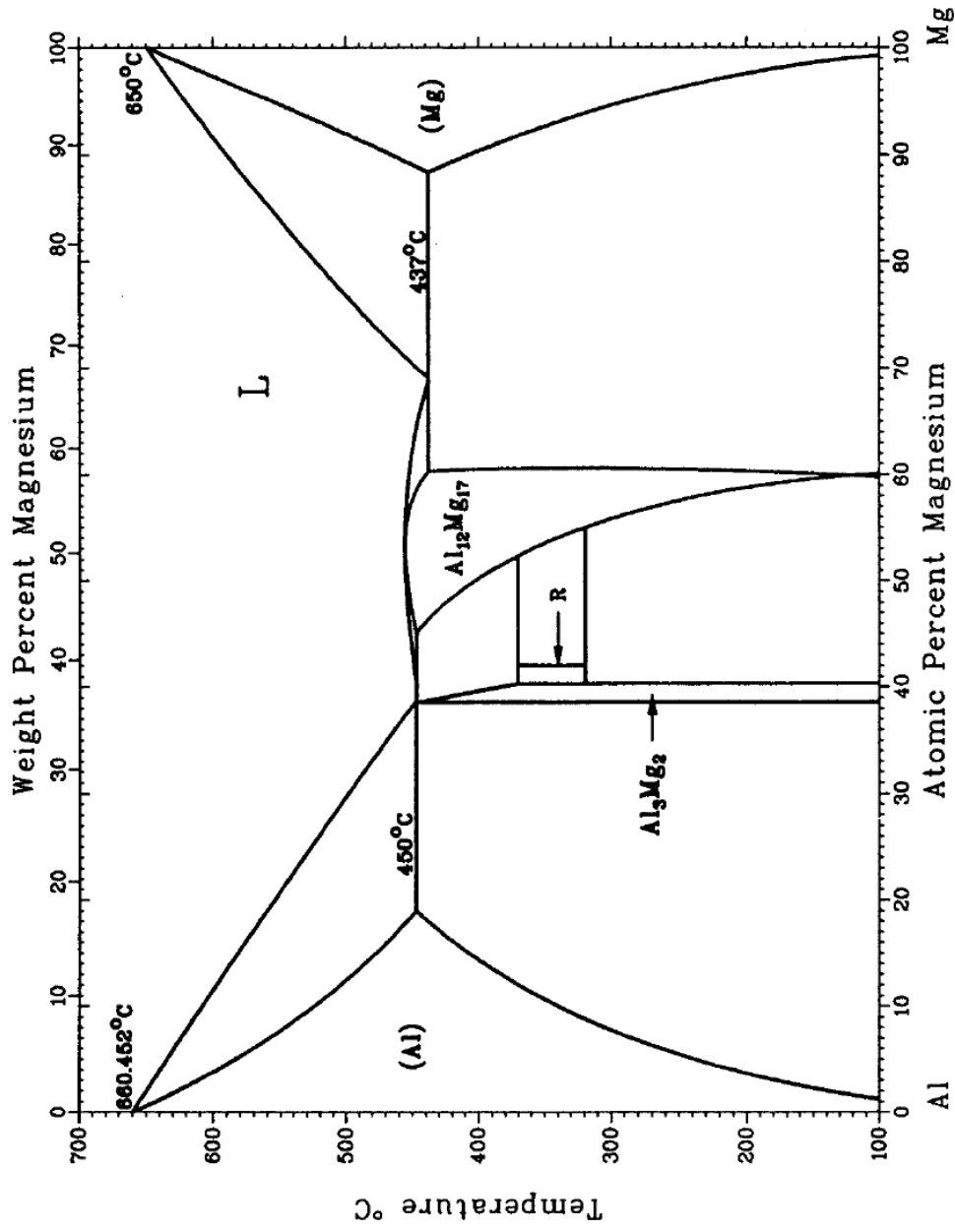


Figure B.2: Phase diagram of the aluminum-magnesium system. The solubility of Mg in Al is $\approx 2\text{at}\%$ at room temperature [208].

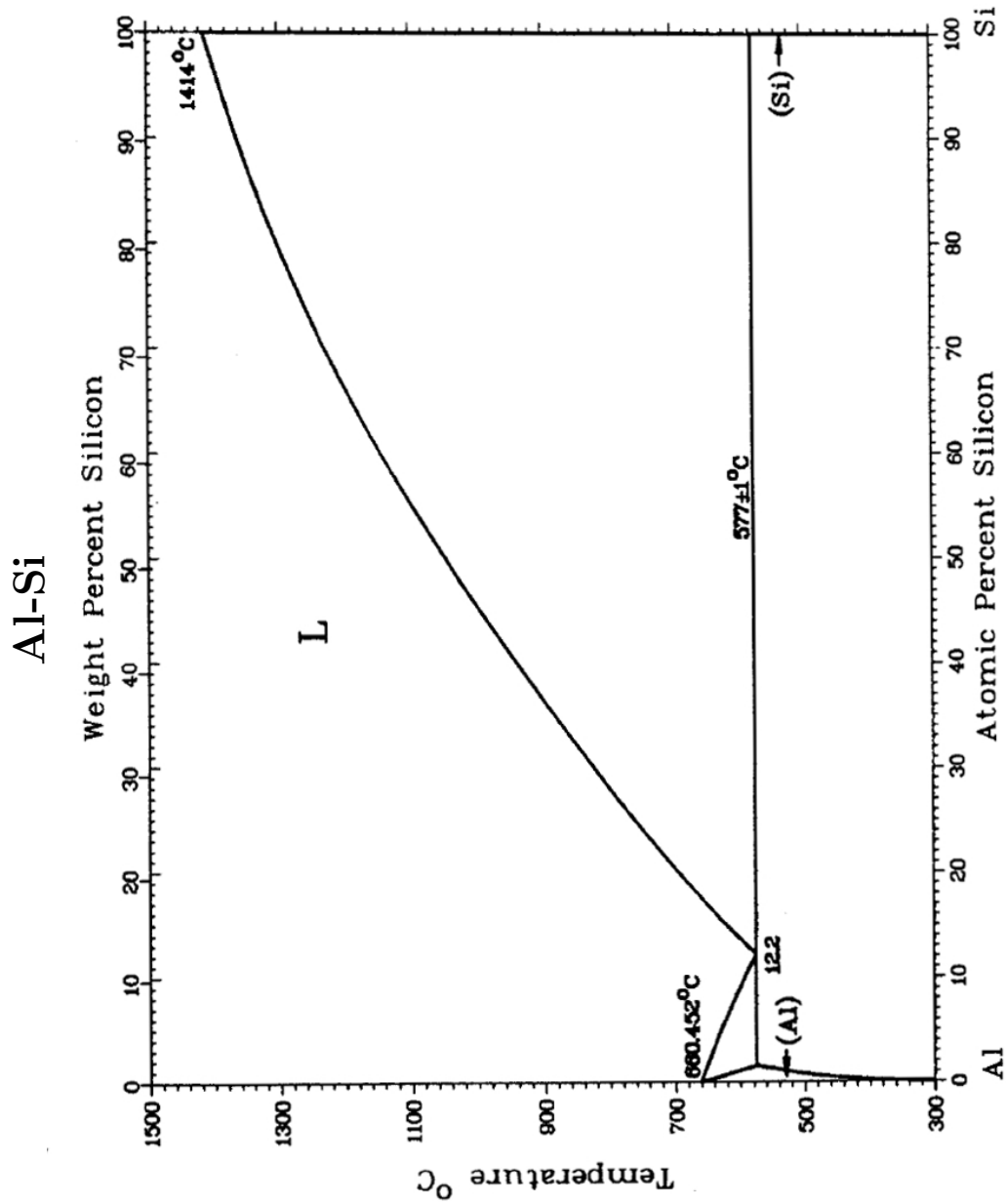


Figure B.3: Phase diagram of the aluminum-silicon system. The solubility of Si in Al is $< 0.1\text{at}\%$ at room temperature [208].

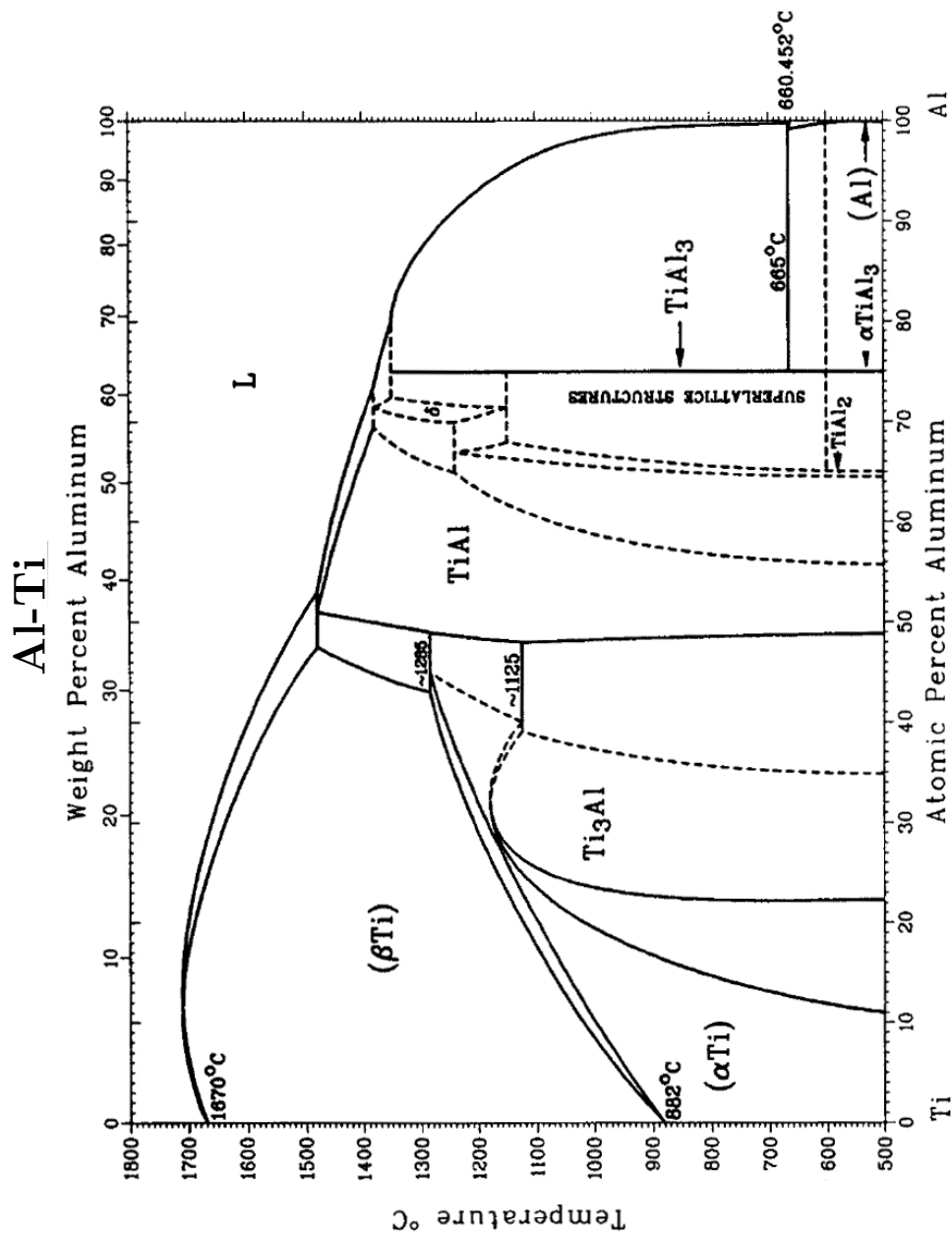


Figure B.4: Phase diagram of the aluminum-titanium system. The solubility of Ti in Al is $< 0.1\text{at}\%$ at room temperature [208].

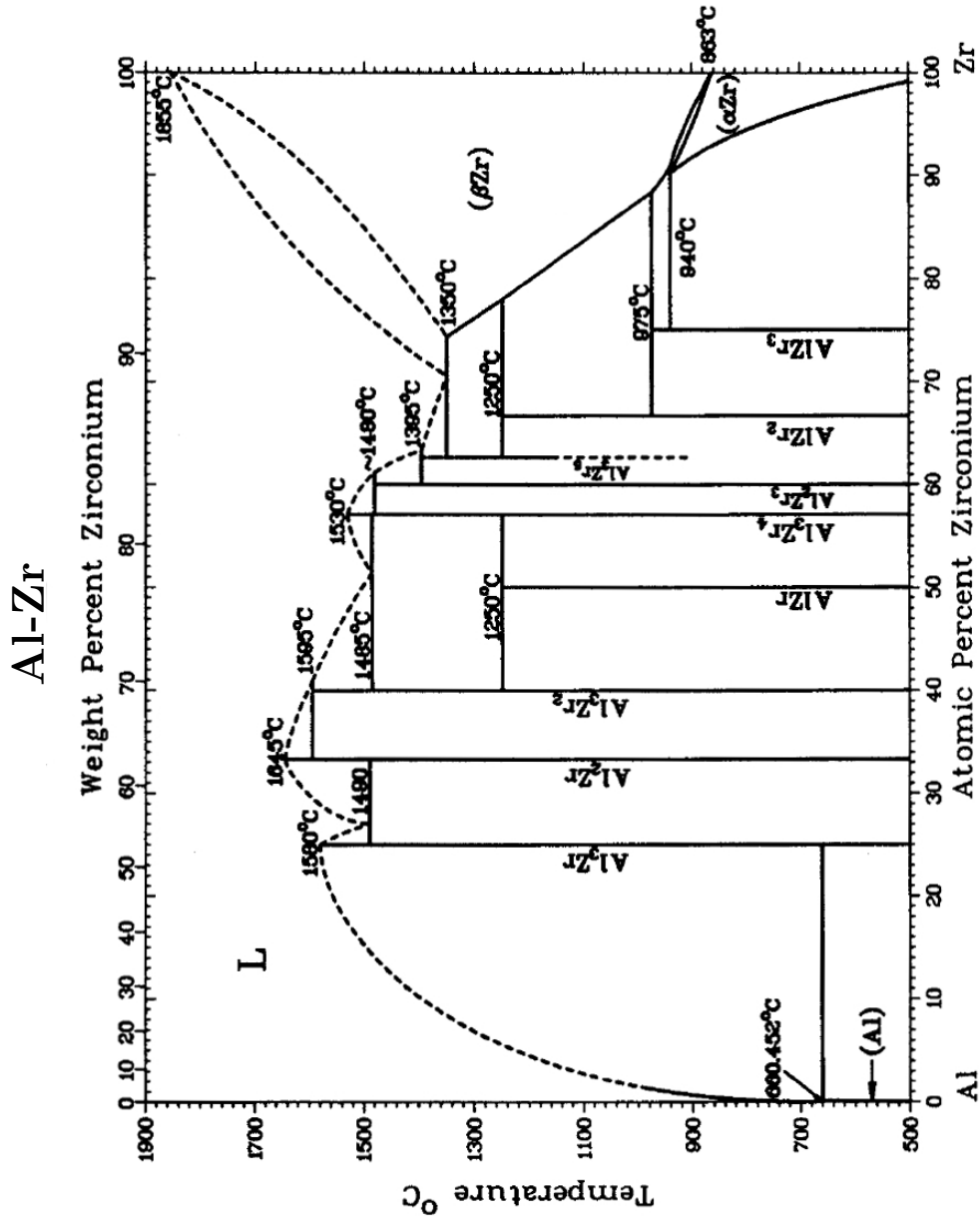


Figure B.5: Phase diagram of the aluminum-zirconium system. The solubility of Zr in Al is <0.1at% at room temperature [208].

U-Al

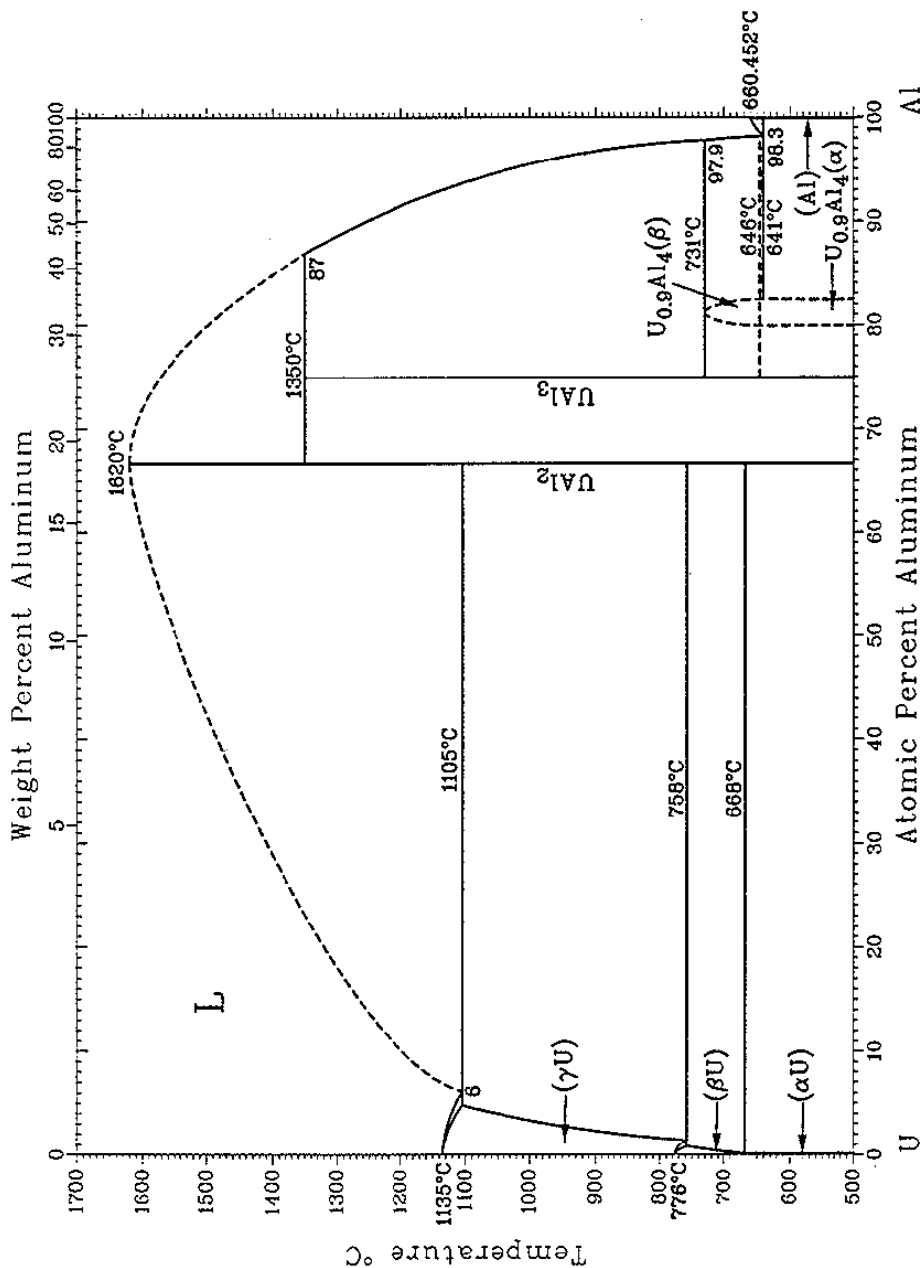


Figure B.6: Phase diagram of the uranium-aluminum system. The intermetallic compounds UA₁₂, UA₁₃ and UA₁₄ form readily during annealing experiments [208].

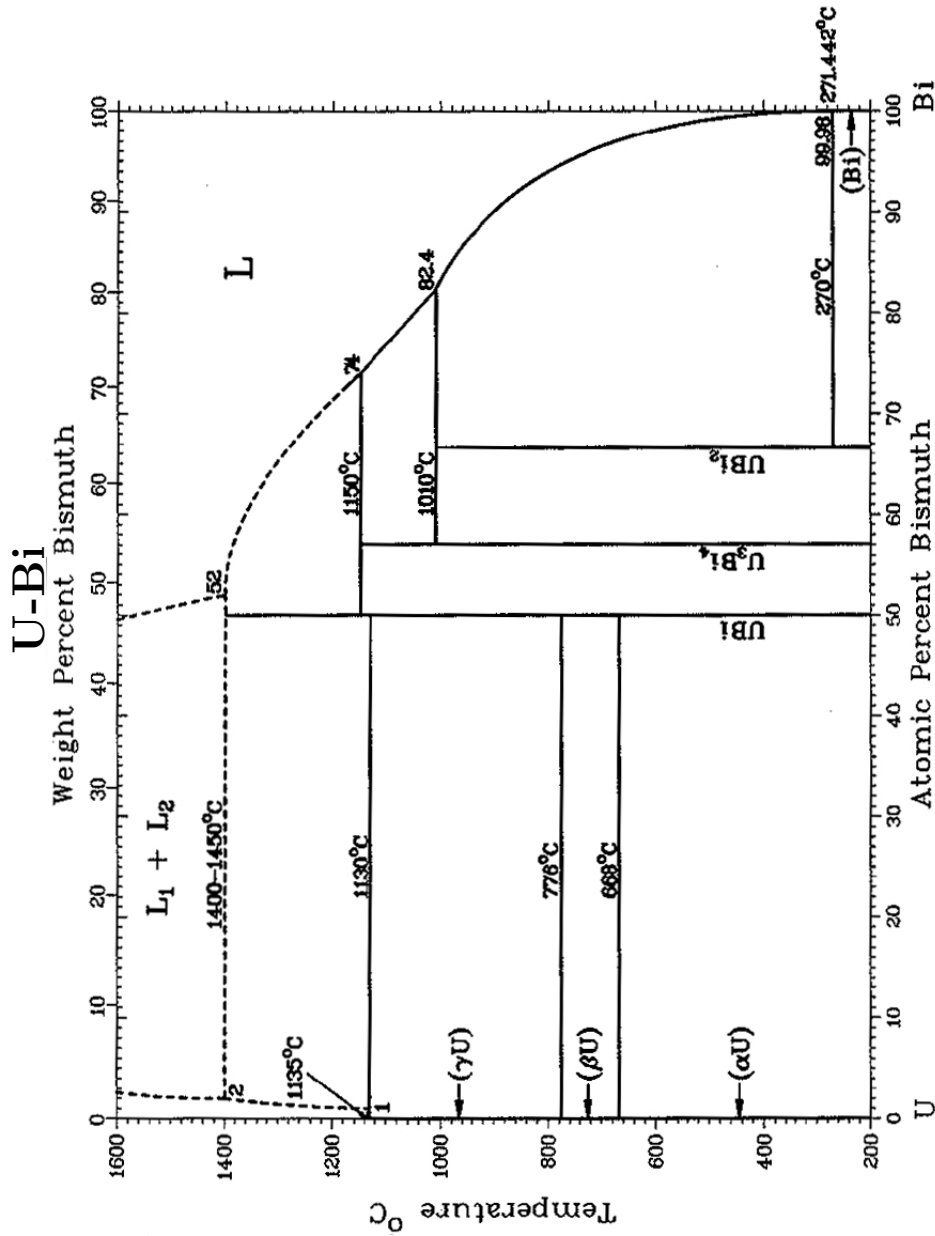


Figure B.7: Phase diagram of the uranium-bismuth system. Three intermetallic compounds exist at room temperature: UBi, U₃Bi₄ and UBi₂ [208].

U-Mg

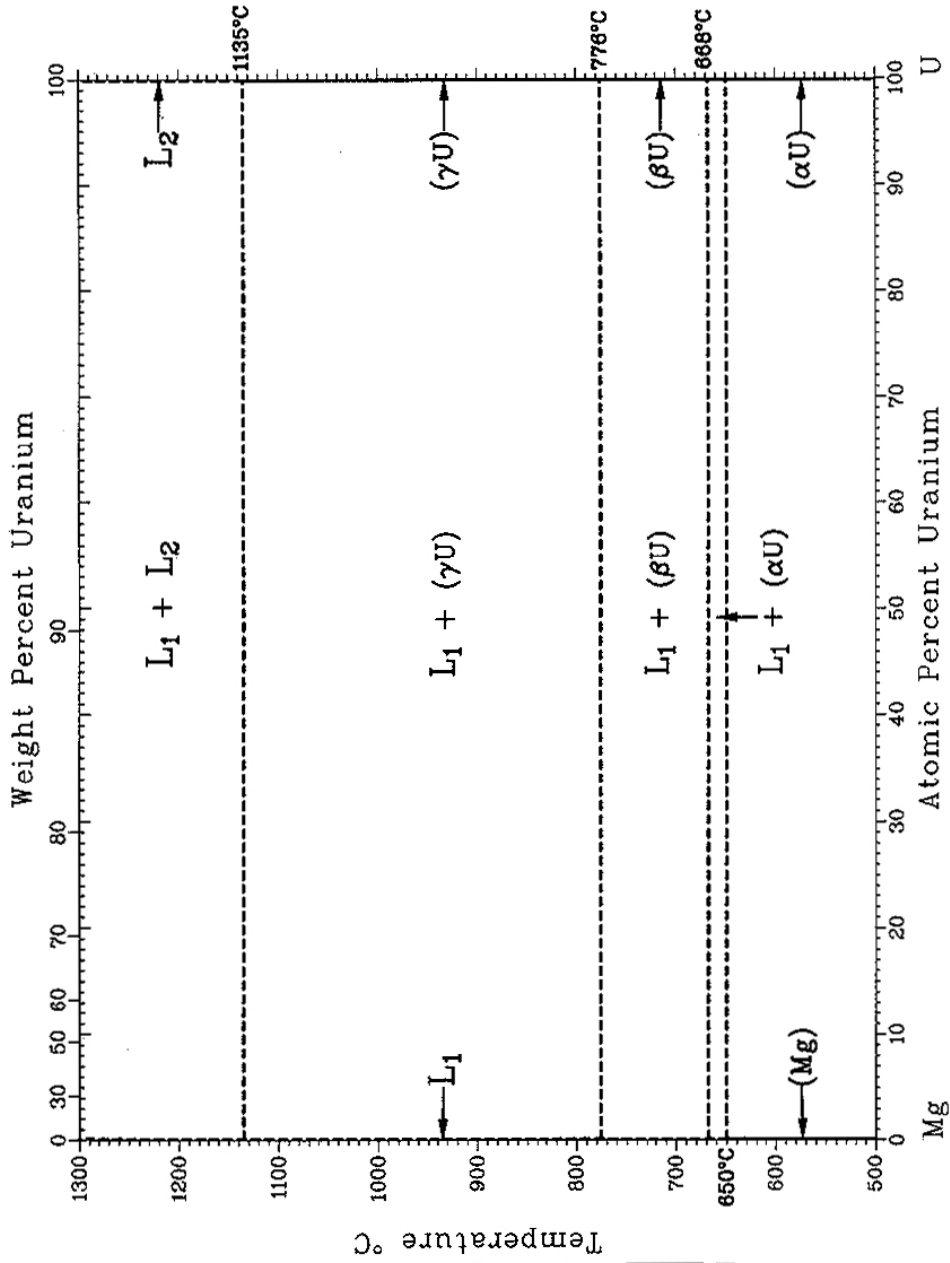


Figure B.8: Phase diagram of the uranium-magnesium system. The solubility of Mg in U and vice versa is below 1at%. There are no intermetallic compounds [116].

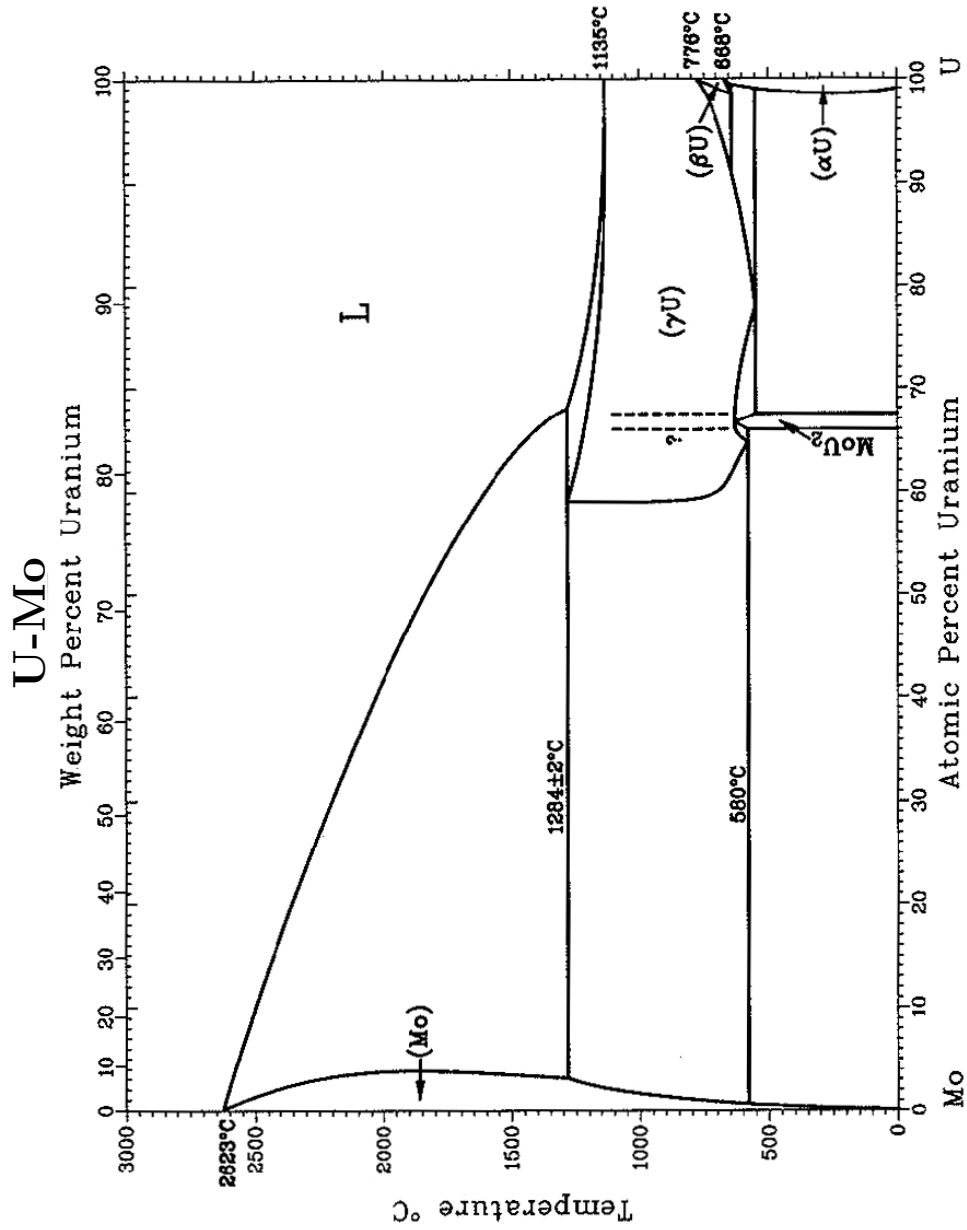


Figure B.9: Phase diagram of the uranium-molybdenum system. The samples regarded in this thesis normally contain between 7 wt% and 8 wt% of molybdenum [22, 27, 49, 116, 221].

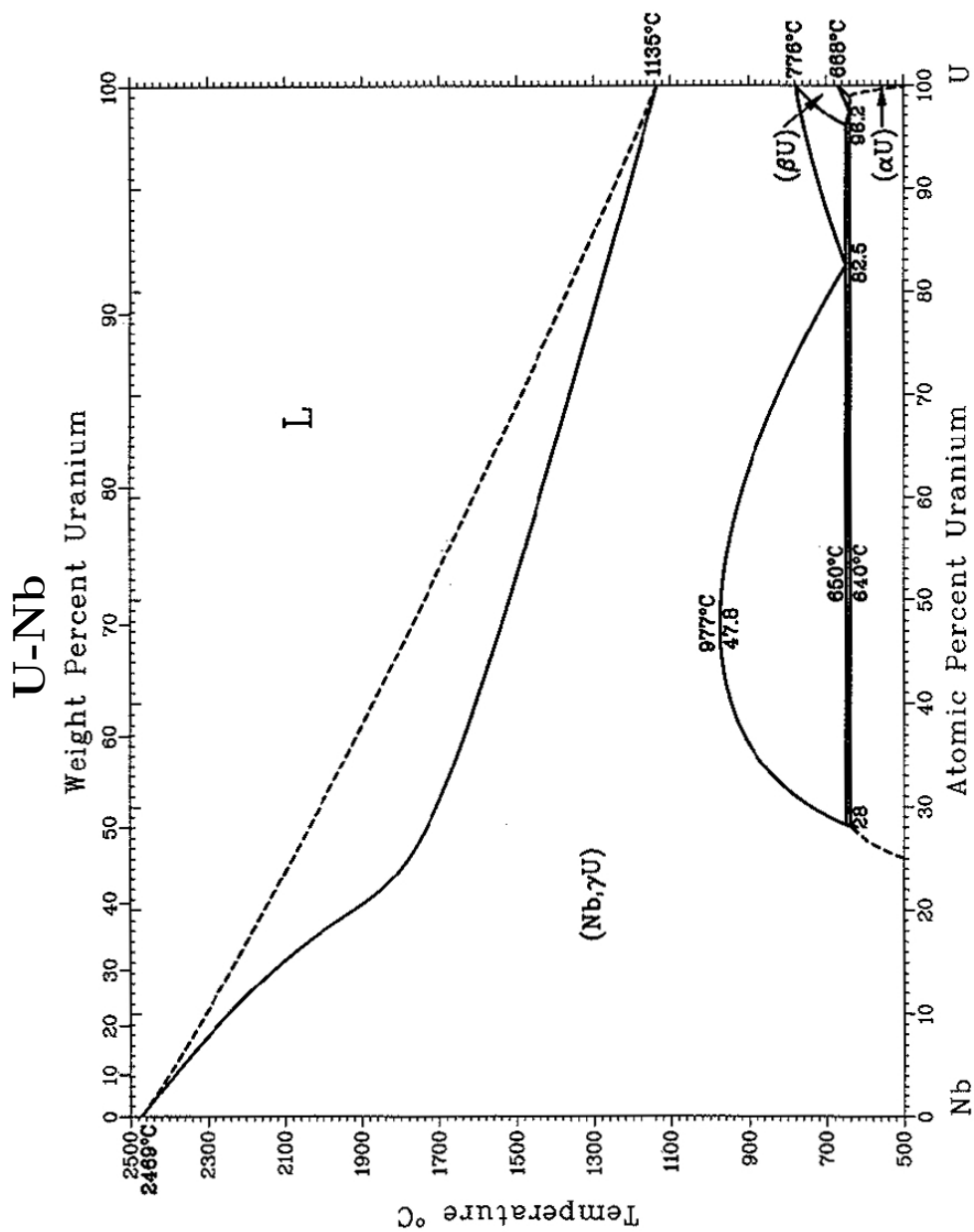


Figure B.10: Phase diagram of the uranium-niobium system [116].

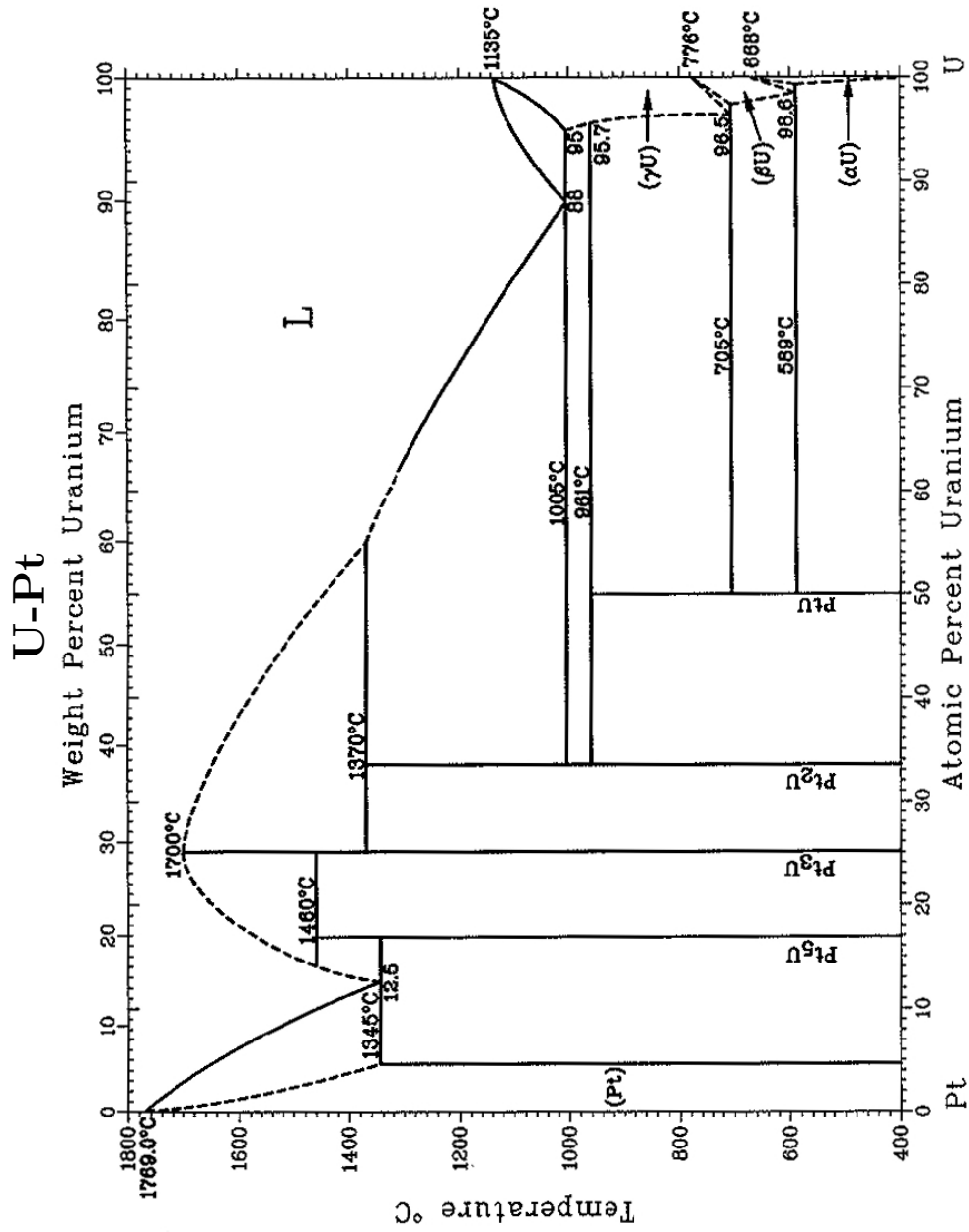


Figure B.11: Phase diagram of the uranium-platinum system. A maximum of 5at% Pt can be dissolved inside γ -U [116].

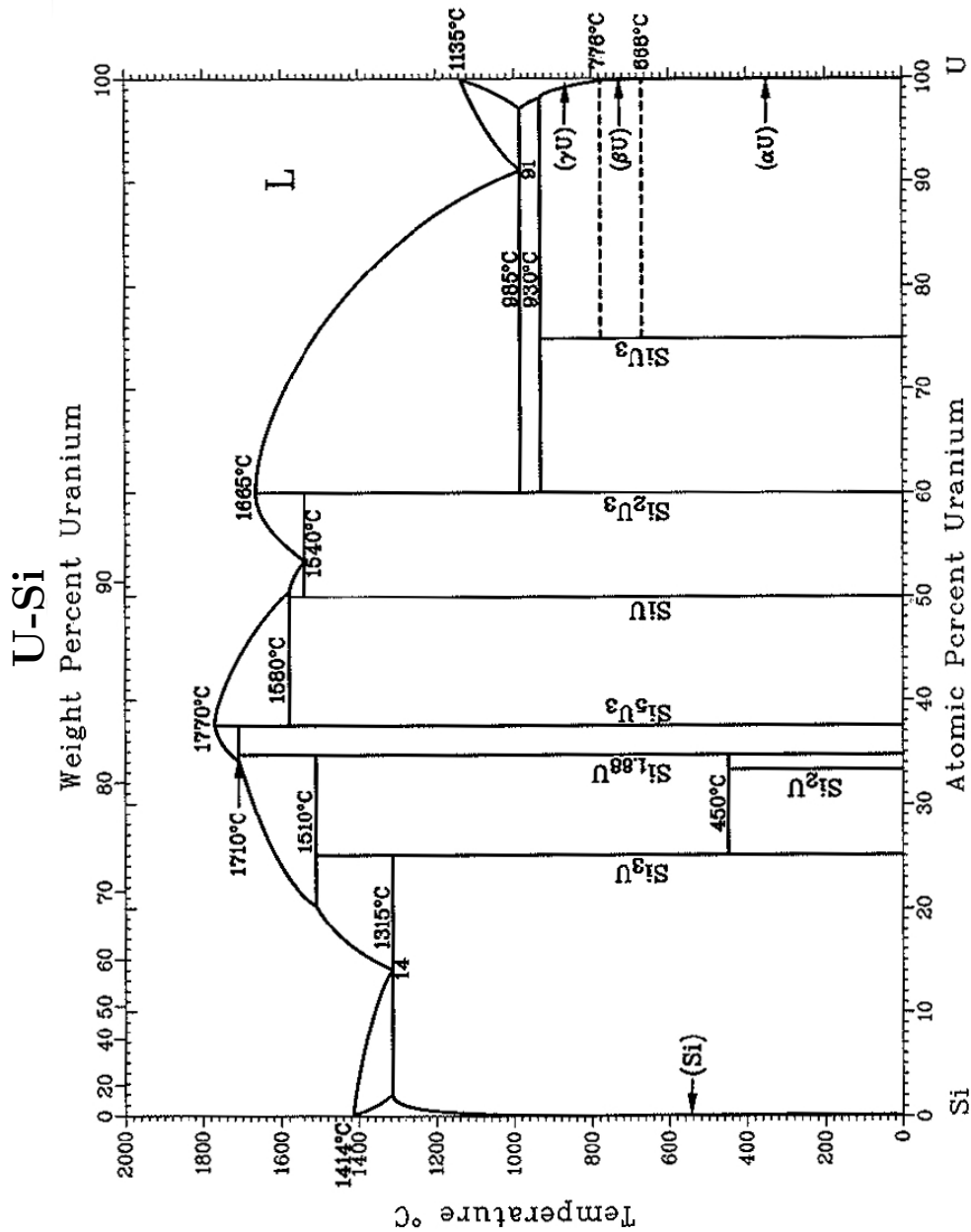


Figure B.12: Phase diagram of the uranium-silicon system. From the at least seven different intermetallic compounds that are known at room temperature U_3Si_2 is used as a nuclear fuel [116].

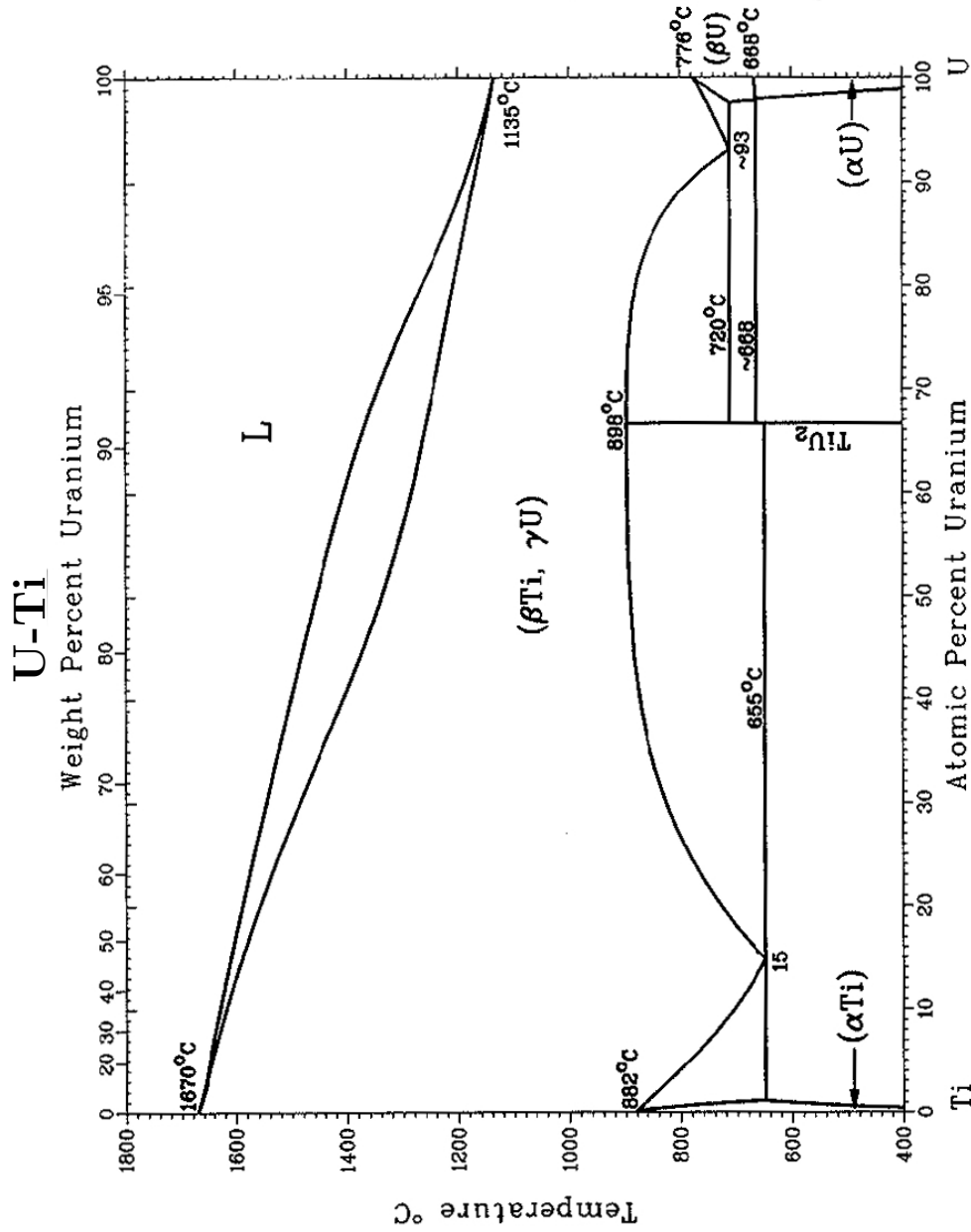


Figure B.13: Phase diagram of the uranium-titanium system. β -Ti and γ -U form a bcc mixture at high temperatures that can be retained at room temperature in case of high quenching rates [116].

Own Publications

- R. Jungwirth et al. **Progress in heavy-ion bombardment of U-Mo/Al dispersion fuel**, In *Proceedings of the International Topical Meeting on Research Reactor Fuel Management (RRFM)* Hambourg, 2008
- E. Welcomme, H. Palancher R. Jungwirth et al. **Heavy ion irradiation of UMo7/Al fuel: methodological approach**. In *Proceedings of the International Topical Meeting on Research Reactor Fuel Management (RRFM)*, Vienna, 2009
- C. Jarousse, L. Halle, W. Petry, R. Jungwirth, A. Röhrmoser, W. Schmid **FRM II and AREVA-CERCA common effort on monolithic UMo plate production**. In *Proceedings of the International Topical Meeting on Research Reactor Fuel Management (RRFM)*, Vienna, 2009
- R. Jungwirth H. Palancher et al. **Optimization of the Si content in UMo/AlSi fuel plates** In *Proceedings of the 31th International Meeting on Reduced Enrichment for Research and Test Reactors (RERTR)*, Beijing, 2009
- R. Jungwirth H. Palancher et al. **Study of heavy ion irradiated UMo/Al miniplates: Si and Bi additions into AL and UMo ground powders**, In *Proceedings of the International Topical Meeting on Research Reactor Fuel Management (RRFM)*, Marrakesh, 2010
- R. Jungwirth, X. Iltis et al. **IRIS-TUM: Microstructure of the Non-Irradiated plates**, In *Proceedings of the International Meeting on Reduced Enrichment for Research and Test Reactors (RERTR)*, Lisbon, 2010.

Acknowledgment

Only the continuous and outstanding support of a lot of people made the success of this thesis possible. I would like to take the chance to thank especially

- my supervisor **Prof. Dr. Winfried Petry** who, despite his overfull time schedule, always had the time for listening to my problems, giving me advices and finding solutions. I would like to thank you for all your support and especially for giving me the opportunity to work on this interesting topic.
- **Dr. Hervé Palancher** from the Commissariat à l'énergie atomique (CEA) who, during our cooperation, became my “voluntary advisor”. Your support was so great and so all-encompassing! Without you, this work would not have been possible. To keep it short: Thank you for everything!
- all the other colleagues from the CEA who supported my work: **Dr. P. Lemoine, Dr. F. Charollais, Dr. X. Iltis, Dr. E. Welcomme, Dr. A. Bonnin, Dr. C. Sabathier** just to mention some of them.
- **Christophe Jarousse, Michelle Grasse** and **Dr. Bertrand Stepnik** from AREVA-CERCA for providing the samples I worked on - free of charge! Thank you for all the discussions and the “small hints” you used to give me.
- **Dr. Christoph Lierse von Gostomski, Dr. Silvia Lehenberger** and **Florian Kortmann** from the Radiochemie München for the allowance to use their facilities and for all the aid during my thesis.
- **Frank Klein** who formerly worked at the Radiochemie München. Thank you for introducing me into the secrets of scanning electron microscopy.
- **Prof. Dr. Wolfgang Schmahl** from the Lehrstuhl für anorganische und biogene Geomaterialien for the allowance to use their XRD setup. Furthermore I would like to thank **Dr. Julius Schneider** for teaching me how to perform proper XRD analysis and **Dr. Soyhun Park** for her help during my measurements.
- **Dr. Hans-Friedrich Wirth** and **H.U. Friebel** - who always had time for me when I had to “quickly use the glove box inside the hot-lab once more”. Furthermore I would like to thank **Prof. Dr. Dietrich Habs** for the allowance to do so for a very long time.

- **Dr. Rainer Grossmann** who first was responsible for the radiation protection side of my work at the hot lab of the LMU in Garching and later joined our group as radiation protection responsible. Thank you for your help with this complicated topic!
- **Dr. Ludwig Beck, Dr. Andreas Bergmaier, Walter Carli and the entire team of the MLL tandem accelerator in Garching** - thank you for your sedulous efforts before, during and after my beam times, all the advices and the great working atmosphere.
- **Alexander Breitner from Elektronik-Software-Systemtechnik Breitner** for the construction and implementation of the automated irradiation setup which allowed the quick and safe irradiation of all of my samples.
- all my former and current colleagues from the HEU-MEU group of the FRM II: **Dr. Wolfgang Schmid, Dr. Harald Breitzkreutz, Dr. Anton Röhrmoser, Christian Bogenberger, Rosmarie Hengstler-Eger, Stefan Dirndorfer, Heiko Juranowitsch, Tobias Zweifel, Hsin-Yin Chiang, Robert Schenk, Tobias Hollmer, Jürgen Sarvas, Miriam Däubler, Bruno Baumeister, Christian Steyer, Matthias Fuchs and Sebastian Reinl** - we became a very large group in the last few years. Thank you for the great working atmosphere and all the discussions! Thank you for overtaking a lot of shifts during my beam times and also thank you all for the fun we had!
- **Dr. Nico Vollmer** who encouraged me to work on UMo fuels a long time ago
- my parents **Martina and Friedrich Jungwirth** and my brother **Michael**
- **Lilly**, my wife, for encouraging me the last years!

List of Figures

1.1	Drawing of the FRM II fuel element	12
1.2	Growth of a highly textured α -uranium rod during irradiation.	14
2.1	Fission fragment distribution	19
2.2	Iodine path in UMo	25
2.3	Penetration depths, energy to recoils and electronic energy loss	26
2.4	Electronic energy loss in layer systems	29
2.5	Energy transfered to recoils in layer systems	30
2.6	Phonon creation in layer systems	31
2.7	Sketch of the phases of pure uranium	33
2.8	Growth of a highly textured α -uranium rod during thermal cycling.	34
2.9	Tetragonal distorted γ° -phase of U10wt%Mo	36
2.10	U-alloy phases	37
2.11	TTT diagram of U10wt%Mo	39
2.12	Cellular decomposition	40
2.13	Thermal spike diffusion	41
2.14	Displacement spike diffusion	42
2.15	IDL grown in-pile	45
3.1	Typical miniplates	58
3.2	Floor plan of the tandem accelerator laboratory of the MLL	60
3.3	Irradiation chamber	61
3.4	Aiming procedure	63
3.5	Sample Holder	63
3.6	Liquid nitrogen cooled sample holder	64
3.7	Cross section of an irradiated sample	65
3.8	Laboratory scale XRD setup	65
3.9	UMo particle on top of glass capillary	66
4.1	Irradiation conditions methodology test	68
4.2	Sample surface before and after irradiation	69
4.3	Influence of the integral fluency	70
4.4	Influence of the irradiation angle	71
4.5	SEM observations of transversal cross sections on irradiated UMo-Al samples.	72
4.6	Influence of the irradiation angle	73
4.7	Influence of the fluency on the IDL	74

4.8	μ -XRD diagram of irradiated and non-irradiated atomized U7wt%Mo/Al sample	76
4.9	XRD diagram of irradiated and non-irradiated ground U8wt%Mo/Al sample	77
4.10	Sample 18: 120°C	78
4.11	Sample C11: 80°C	78
4.12	Sample C11: -38°C	79
4.13	Sample C21: -75°C	80
4.14	Sample S2: -170°C	81
4.15	SEM picture: Thin oxide layer	82
4.16	SEM picture: Thick oxide layer	83
4.17	Ripped-our particle	84
4.18	Oxidized particles getting loose during irradiation.	85
4.19	Thin oxide layer incorporated into IDL	86
4.20	SEM picture of blended Al7wt%Si powder	87
4.21	Granulometry of Si and Al powder	88
4.22	Si distribution in three UMo/AlSi miniplates	89
4.23	Si precipitate close to a UMo particle, 2wt%Si case	90
4.24	SiRDL around UMo particles, 5wt%Si and 7wt%Si case	91
4.25	SiRDL between two close UMo particles	92
4.26	μ -XRD characterization of the SiRDL	93
4.27	Behavior of the SiRDL in combination with an oxide layer.	96
4.28	No SiRDL in combination with a thick oxide layer even at high Si concentrations	97
4.29	Oxide layer influence in the 2wt%Si case.	98
4.30	Cross section of UMo/AlSi2 and UMo/AlSi7 samples.	100
4.31	IDL growth around UMo particles protected by a SiRDL in three steps.	101
4.32	Si concentration inside the IDL when a Si precipitate is located close to this IDL.	102
4.33	Pre-irradiation state of the UMo/AlBi samples	105
4.34	Al-O layer around UMo in fresh UMo/AlBi miniplates	106
4.35	Bi rich layer around UMo particles after irradiation	107
4.36	Influence of Ti addition to the matrix	110
4.37	UMo-Ti-Al multilayer	111
4.38	Influence of Mg addition to the matrix	113
4.39	Sampling positions at the fresh IRIS-TUM fuel plates.	115
4.40	XRD analysis of fresh ground and atomized powder	116
4.41	Typical as prepared matrix state of the IRIS-TUM samples	117
4.42	Typical state of oxidation of ground UMo particles.	118
4.43	SiRDL inside IRIS-TUM 8503 plate	119
4.44	Ground powder: No precipitates	125
4.45	Ground powder: Precipitates	126
4.46	Ground powder: IDL growth	128
4.47	Ground powder: Ti precipitates inside IDL	129
5.1	UMo-Al layer systems	140

A.1	Polishing procedure	142
B.1	Phase diagram of aluminum and bismuth	144
B.2	Phase diagram of aluminum and magnesium	145
B.3	Phase diagram of aluminum and silicon	146
B.4	Phase diagram of aluminum and titanium	147
B.5	Phase diagram of aluminum and zirconium	148
B.6	Phase diagram of uranium and aluminum	149
B.7	Phase diagram of uranium and bismuth	150
B.8	Phase diagram of uranium and magnesium	151
B.9	Phase diagram of uranium and molybdenum	152
B.10	Phase diagram of uranium and niobium	153
B.11	Phase diagram of uranium and platinum	154
B.12	Phase diagram of uranium and silicon	155
B.13	Phase diagram of uranium and titanium	156

List of Tables

1.1	Selected uranium compounds with densities higher than that of U_3Si_2 .	13
1.2	Selected uranium alloys with higher density than that of U_3Si_2 .	14
2.1	Iodine at 80MeV in U8Mo	28
2.2	Terminology of uranium Phases	43
2.3	Possible options to reduce the UMo-Al interaction - Matrix	51
2.4	Possible options to reduce the UMo-Al interaction - Diffusion barrier	52
2.5	Possible options to reduce the UMo-Al interaction - ternary UMoX alloys	53
3.1	List of MAFIA-I samples	57
4.1	Penetration depth of Iodine at 80 Mev in Al and UMo	71
4.2	Atomized powder: composition before and after irradiation	75
4.3	Ground powder: composition before and after irradiation	75
4.4	Irradiation conditions temperature test	77
4.5	Phase composition MAFIA-I	79
4.6	Particle size of Al and Si powder.	85
4.7	Elementary composition of the SiRDL	91
4.8	Crystal structure of USi and USiAl phases	94
4.9	Parameters of the six irradiated IRIS-TUM plates.	114
4.10	UMo, aluminum and porosity surface %.	118
4.11	Si content of the SiRDL found on IRIS-TUM samples containing 2.1wt%Si inside the matrix	120
4.12	Phase composition of ground UMoAl samples before irradiation	120
4.13	α -U cell parameters of different ground UMo powders before irradiation	121
4.14	IRIS-TUM γ -UMo lattice parameters before irradiation	122
4.15	Nb precipitate composition	125
4.16	Ti precipitate composition	125
4.17	IDL composition ground powder	127
4.18	Phase composition of different ground UMoAl samples after irradiation	130
4.19	α -U cell parameters of different ground UMo powders after irradiation	130
4.20	Ground powder γ -UMo lattice parameters after irradiation	130
5.1	Conclusions on MAFIA-I samples	136

Bibliography

- [1] Homepage of the Forschungsneutronenquelle Heinz Maier-Leibnitz (FRM II). <http://www.frm2.tum.de>.
- [2] A. Röhrmoser. Untersuchungen zur Kühlbarkeit eines neuartigen Kompaktkerns für Forschungsreaktoren. Diplomarbeit, Technische Universität München, 1984.
- [3] A. Röhrmoser. *Neutronenphysikalische Optimierung und Auslegung eines Forschungsreaktors mittlerer Leistung mit Zielrichtung auf einen hohen Fluß für Strahlrohrexperimente*. Disseratation, Technische Universität München, 1991.
- [4] A. Röhrmoser. Verifizierung der Rechenergebnisse für die 2d-Darstellung der Kompaktkernanordnung des FRM-II. Technical report, 1991. Technische Universität München - Forschungsneutronenquelle Heinz Maier-Leibnitz.
- [5] A. Röhrmoser. OPA-112: Reaktivitätsbilanz, regelstabcharakteristik und Abbrandzyklus des Kompaktkerns KKE7 bei 20MW. Technical report, 1990. Fakultät für Physik E21, Technische Universität München.
- [6] J.L. Snelgrove. Development of high-density low-enriched-uranium fuels. *Nuclear engineering and design*, 178:119–126, 1997.
- [7] Homepage of the RERTR Program. <http://www.rertr.anl.gov>.
- [8] Alexander Glaser et al. Nuklearterrorismus: Eine vermeidbare Katastrophe? *Spektrum der Wissenschaft*, August 2006.
- [9] Klaus Böning et al. Conversion of the FRM II. In *Proceedings of the 8th International Topical Meeting on Research Reactor Fuel Management (RRFM)*, 2004.
- [10] Winfried Petry. Neutron research and application at the FRM II. In *Proceedings of the 8th International Topical Meeting on Research Reactor Fuel Management (RRFM)*, München, 2004.
- [11] A. Röhrmoser et al. Reduced enrichment program for the FRM II. In *Proceedings of the 26th International Meeting on Reduced Enrichment for Research and Test Reactors (RERTR)*, Vienna, 2004.
- [12] J.P. Durand et al. LEU fuel development at CERCA: status as of October 1993. In *Proceedings of the 16th International Topical Meeting on Reduced Enrichment for Research and Test Reactors (RERTR)*, Oarai, 1993.

- [13] J.L. Snelgrove et al. Development of very-high-density fuels by the RERTR program. In *Proceedings of the 19. International Meeting on Reduced Enrichment for Research and Test Reactors (RERTR)*, Seoul, 1996.
- [14] Brian Frost. *Material Science and Technology Volume 10A, Nuclear Materials*. VCH Verlagsgesellschaft mbH, Weinheim, Deutschland, 1. edition, 1994.
- [15] G.L. Hofman L.C. Walters. Metallic fast reactor fuels. In Brian Frost, editor, *Material Science and Technology Volume 10A, Nuclear Materials*. VCH Verlagsgesellschaft mbH, Weinheim, Deutschland, 1. edition, 1994.
- [16] S.H. Paine J.H. Kittel. Irradiation effects in uranium and its alloys. In *Proceedings of the international conference on the peaceful uses of atomic energy/7*, New York, 1956. United Nations.
- [17] J. Rest et al. Experimental and calculated swelling behavior of U-10Mo under low irradiation temperatures. In *Proceedings of the 21st International Topical Meeting on Reduced Enrichment for Research and Test Reactors (RERTR)*, Sao Paulo, 1998.
- [18] M.K. Meyer et al. Irradiation behavior of U₆Mn-Al dispersion fuel elements. *Journal of nuclear materials*, 278:358–363, 2000.
- [19] G.L. Hofman. Irradiation behavior of low enriched U₆Fe-Al dispersion fuel elements. *Journal of nuclear materials*, 150:238–243, 1987.
- [20] M.K. Meyer et al. Low-temperature irradiation behavior of uranium-molybdenum alloy dispersion fuel. *Journal of nuclear materials*, 304:221–236, 2002.
- [21] S.L. Fawcett et al. A study of core fuel systems for a fast breeder power reactor. Technical Report BMI-APDA-636, Batelle Memorial Institute, 1957.
- [22] P.C.L. Pfeil. The constitution of Uranium-Molybdenum alloys. *Journal of Institute of Metals*, 77:553–570, 1950.
- [23] M.A. Leiser et al. Radiation stability of fuel elements for the Enrico Fermi power reactor. In *Proceedings of the second international conference on the peaceful uses of atomic energy/5*, page 587, New York, 1958. United Nations.
- [24] A.A. Shoudy et al. The effect of irradiation temperature and fission rate on the radiation stability of the uranium-10wt%molybdenum alloy. In *Radiation Damage in Reactor materials*, Venice, 1962. IAEA.
- [25] M.P. Johnson W.A. Holland. Irradiation of U-Mo base alloys. Technical Report NAA-SR-6262, Atomics International, 1964.
- [26] G.L. Hofman et al. Design of high density γ -phase Uranium alloys for LEU dispersion fuel applications. In *Proceedings of the 21st International Meeting on Reduced Enrichment for Research and Test Reactors (RERTR)*, Sao Paulo, 1998.
- [27] A.N. Holden. *Physical metallurgy of uranium*. Addison-Wesley publishing company, Massachusetts, 1958.

- [28] S. van den Berghe et al. Transmission electron microscopy investigation of irradiated U7wt%Mo dispersion fuel. *Journal of Nuclear Materials*, 375:340–346, 2008.
- [29] K. Colon D. Sears. Neutron powder diffraction of UMo fuel irradiated to 60% burn-up. In *Proceedings of the International Topical Meeting on Research Reactor Fuel Management (RRFM)*, Lyons, 2007.
- [30] S.L. Hayes et al. Modelling RERTR experimental fuel plates using the palte code. In *Proceedings of the 25. International Meeting on Reduced Enrichment for Research and Test Reactors (RERTR)*, Chicago, 2002.
- [31] J.M. Park et al. Phase stability and diffusion characteristics of U-Mo-X (X=Si, Al, Zr or Ti) alloys. In *Proceedings of the 27th International Topical Meeting on Reduced Enrichment for Research and Test Reactors (RERTR)*, Boston, 2005.
- [32] C.D. Cagle L.B. Emlet. Slug ruptures in the Oak Ridge National Laboratory pile. Technical Report ORNL-170, Oak Ridge National Laboratory, 1948.
- [33] G.L. Hofman et al. Post irradiation analysis of low enriched U-Mo/Al dispersion fuel miniplate tests, RERTR 4&5. In *Proceedings of the 26. International Meeting on Reduced Enrichment for Research and Test Reactors (RERTR)*, 2004.
- [34] P. Lemoine et al. UMo dispersion fuel results and status of qualification programs. In *Proceedings of the 8th International Topical Meeting on Research Reactor Fuel Management (RRFM)*, Munich, 2004.
- [35] R.O. Williams. Terminal report on ORNL slug problem - causes and prevention. Technical Report CF-50-7-160, Oak Ridge National Laboratory, 1950.
- [36] L.S. DeLuca et al. Rate of growth of diffusion layers in U-Al and U-AlSi couples. Technical Report KAPL-1747, Knolls Atomic Power Laboratory, 1957.
- [37] G. Hofman et al. Results of Low-Enriched U-Mo Miniplates from RERTR-6 and -7A Irradiation. In *Proceedings of the 28th International Meeting on Reduced Enrichment for Research and Test Reactors (RERTR)*, Cape Town, 2006.
- [38] M. Cornen et al. Physico-chemical aspects of modified UMo/Al interaction. In *Proceedings of the 11th International Topical Meeting on Research Reactor Fuel Management (RRFM)*, Lyons, 2007.
- [39] A. Izhutov et al. The status of LEU U-Mo fuel investigation in the MIR reactor. In *Proceedings of the 31th International Meeting on Reduced Enrichment for Research and Test Reactors (RERTR)*, Beijing, 2009.
- [40] G.A. Birzhevoy et al. Results of post-irradiation examination of the (U-Mo)-Aluminum matrix interaction rate. In *Proceedings of the 11th International Topical Meeting on Research Reactor Fuel Management (RRFM)*, Lyons, 2007.
- [41] H.A. Saller. Uranium alloy newsletter No.13. Technical Report WASH-295, Battelle Memorial Institute, 1955.

- [42] D.D. Keiser et al. Characterization and testing of monolithic RERTR fuel plates. In *Proceedings of the 11th International Topical Meeting on Research Reactor Fuel Management (RRFM)*, Lyons, 2007.
- [43] W.C. Thurber R.J. Beaver. Development of Silicon modified 48wt%U-Al alloys for aluminum plate type fuel elements. Technical Report ORNL-2602, Oak Ridge National Laboratory, 1959.
- [44] R.J. Van Thyne et al. Transformation kinetics of Uranium-Niobium and ternary Uranium-Molybdenum base alloys. *Transactions American Society for Metals*, 49:576–597, 1957.
- [45] M. Rodier et al. Effects of Ti in the UMo/Al system: preliminary results. In *Proceedings of the 11th International Topical Meeting on Research Reactor Fuel Management (RRFM)*, Lyons, 2007.
- [46] Nico Wieschalla. *Heavy ion irradiation of UMo/Al dispersion fuel*. Dissertation, TUM, 2006.
- [47] N. Wieschalla et al. Heavy ion irradiation of UMo-Al dispersion fuel. *Journal of nuclear materials*, 357:191–197, 2006.
- [48] H. Palancher et al. Uranium-Molybdenum nuclear fuel plates behavior under heavy ion irradiation an X-ray diffraction analysis. *Journal of nuclear materials*, 385:449–455, 2009.
- [49] J. Rest et al. U-Mo fuels handbook. Technical Report ANL-09/31, Argonne National Laboratory, 2009.
- [50] D.S. Billington J.H. Crawford. *Radiation damage in solids*. Princeton University Press, New Jersey, 1961.
- [51] W. Schilling H. Ullmaier. Physics of radiation damage. In Brian Frost, editor, *Material Science and Technology Volume 10B, Nuclear Materials*. VCH Verlagsgesellschaft mbH, Weinheim, Deutschland, 1. edition, 1994.
- [52] F. Seitz J.S. Koehler. Displacement of atoms during irradiation. In *Solid state physics 2*. Acadaemic Press, 1956.
- [53] F. Seitz J.S. Koehler. The theory of lattice displacements produced during irradiation. In *Proceedings of the first international conference on the peaceful uses of atomic energy/7*, pages 615–633, New York, 1955. United Nations.
- [54] F. Seitz. The influence of pile radiations on solid materials. In *Nuclear science and technology*. Oak Ridge technical information service, 1951.
- [55] R.S. Averback T. Diaz de la Rubia. Displacement damage in irradiated metals and semiconductors. In *Solid state physics 51*. Acadaemic Press, 1998.
- [56] C. Trautmann. Micro- and nanoengineering with ion tracks. In R. Hellborg et al., editors, *Ion beams in nanoscience and technology*. Springer Verlag, 2009.

- [57] R.L. Fleischer et al. Ion Explosion Spike Mechanism for Formation of Charged-Particle Tracks in Solids. *Journal of Applied physics*, 36:3645, 1965.
- [58] Hyperphysics. <http://hyperphysics.phy-astr.gsu.edu/hbase/nucene/fisfrag.html>.
- [59] J.A. Brinkman. On the nature of radiation damage in metals. *Journal of applied physics*, 25(8):961–970, 1954.
- [60] M.L. Bleiberg L.J. Jones B. Lustman. Phase changes in pile-irradiated uranium-base alloys. *Journal of Applied Physics*, 27(11):1270–1283, 1956.
- [61] A. Meftah et al. Track Formation in SiO₂ quartz and the thermal spike mechanism. *Physical Review B*, 49:12457–12463, 1994.
- [62] C. Trautmann et al. Effect of Stress on Track Formation in amorphous iron boron alloy: Ion Tracks as elastic inclusions. *Physical Review Letters*, 85:3648–3651, 2000.
- [63] J. Ziegler. SRIM. <http://www.srim.org>, 2010.
- [64] E.M. Bringa R.E. Johnson. Coulomb Explosion and Thermal Spikes. *Physical Review Letters*, 88:165501, 2002.
- [65] Misc authors. *DOE Fundamentals Handbook, Material science*, volume 2. U.S. Department of Energy, 1993. DOE-HDBK-1017/2-93.
- [66] S.T. Konobeevskii. On the question of the nature of radiation damage in fissionable materials. *Atomic Energy*, 1:209–216, 1956.
- [67] D.G. Walker. The simulation of fission damage in U₃Si. *Journal of nuclear materials*, 37:48–58, 1970.
- [68] D.G. Walker P.A. Morel. X-ray diffraction studies of ion bombarded U₃Si. *Journal of nuclear materials*, 39:49–58, 1971.
- [69] B. Bethune. Structural transformations in U₃Si. *Journal of nuclear materials*, 31:197–202, 1968.
- [70] W. van Renterghem et al. TEM investigation of irradiated atomised and ground UMo dispersion fuel, with or without Si added to the matrix. In *Proceedings of the 31st International Meeting on Reduced Enrichment for Research and Test Reactors (RERTR)*, Beijing, 2009.
- [71] J.F. Ziegler J.M. Manoyan. The stopping of ions in compounds. *Nuclear Instruments and Methods in Physics Research*, 35:215–228, 1988.
- [72] J. Lehmann R.F. Hills. Proposed nomenclature for phases of uranium alloys. *Journal of nuclear materials*, 2:261–268, 1960.
- [73] H.L. Yakel. A review of X-ray diffraction studies in Uranium alloys. In J.J. Burke et al., editors, *Physical Metallurgy of Uranium alloys*. Brook hill publishing company, 1976.

- [74] D. Blake R.F. Hehemann. Transformation in Uranium base alloys. In J.J. Burke et al., editors, *Physical Metallurgy of Uranium alloys*. Brook hill publishing company, 1976.
- [75] C.W. Jacob et al. The crystalline structure of Uranium. *Journal of the American chemical society*, 59:2588–2591, 1937.
- [76] B. Blumenthal. The transformation temperature of high-purity Uranium. *Journal of nuclear materials*, 2:23–30, 1960.
- [77] P. Chiotti et al. Lattice parameters of uranium from 25 to 1132°C. *Transactions of the American society for metals*, 51:772–786, 1959.
- [78] J.R. Bridge et al. X-ray diffraction determination of the coefficients of expansion of alpha Uranium. *Journal of Metals*, 8:1282–1285, 1956.
- [79] J. Donohue. *The structure of the elements*. John Wiley & Sons, New York, 1974.
- [80] C.W. Tucker. The crystal structure of the β -phase of Uranium. *Acta crystallographica*, 4:425–431, 1951.
- [81] C.W. Tucker P. Senio. An improved determination of the crystal structure of β -Uranium. *Acta crystallographica*, 6:753–760, 1953.
- [82] H. Steeple T. Ashworth. The minimum residual refinement of β -Uranium from polycrystalline data. *Acta crystallographica*, 21:995–998, 1966.
- [83] J. Donohue H. Einsphar. The structure of β -Uranium. *Acta crystallographica B*, 27:1740–1743, 1971.
- [84] A.C. Lawson et al. Structure of β -uranium. *Acta crystallographica B*, 44:89–96, 1988.
- [85] A.S. Wilson R.E. Rundle. The structure of uranium metal. *Acta crystallographica*, 2:126–127, 1949.
- [86] J. Besson et al. Sur l'existence d'une transformation directe $\alpha \rightarrow \gamma$ dans l'uranium disperse dans un milieu inerte. *Journal of nuclear materials*, 16:74–75, 1965.
- [87] H.G. Smith G.H. Lander. Neutron scattering investigations of α -uranium in the charge-density-wave state. *Physical Review B*, 30:5407–5415, 1984.
- [88] Fachinformationszentrum Karlsruhe. Findit, Version 1.4.6, 2009.
- [89] F.G. Foote. Physical metallurgy of Uranium and its alloys. In *Proceedings of the first international conference on the peaceful uses of atomic energy/9*, pages 33–67, New York, 1955. United Nations.
- [90] W.D. Wilkinson. *Uranium Metallurgy Vol. 2*. Interscience Publishers, New York, 1962.

- [91] D.E. Thomas et al. Properties of Gamma-phase alloys of Uranium. In *Proceedings of the second international conference on the peaceful uses of atomic energy/5*, page 610, New York, 1958. United Nations.
- [92] R.W. Dayton. The metallurgy and fabrication of uranium alloy fuel elements. In *Fuel element conference*, Paris, 1957.
- [93] R.A. Vandermeer. Recent observations of phase transformations in a U-Nb-Zr alloy. In J.J. Burke et al., editors, *Physical Metallurgy of Uranium alloys*. Brook hill publishing company, 1976.
- [94] W.D. Wilkinson. *Uranium Metallurgy Vol. 1*. Interscience Publishers, New York, 1962.
- [95] K. Tangri et al. Metastable phases in uranium alloys with high solute solubility in the BCC gamma phase. Part I: the system U-Nb. *Journal of nuclear materials*, 15:278–287, 1965.
- [96] K. Tangri et al. Metastable phases in uranium alloys with high solute solubility in the BCC gamma phase. Part II: the system U-Ru. *Journal of nuclear materials*, 15:278–287, 1965.
- [97] R.J. Jackson W.L. Larsen. Transformations and structures in the uranium-rhenium system I. Metastable α' , α'' and γ^0 structures. *Journal of Nuclear Materials*, 21:263–276, 1967.
- [98] R.J. Jackson W.L. Larsen. Transformations and structures in the uranium-rhenium system II. The β to α transformation. *Journal of Nuclear Materials*, 21:277–281, 1967.
- [99] R.J. Jackson W.L. Larsen. Transformations and structures in the uranium-rhenium system III. Formation and structure of $\delta(\text{U}_2\text{Re})$. *Journal of Nuclear Materials*, 21:282–286, 1967.
- [100] V.K. Orlov et al. Structural features of martensite α -phases in alloys of uranium with transition metals. *Atomic energy*, 86:118–125, 1999.
- [101] K. Tangri G.I. Williams. Metastable phases in the uranium-molybdenum system and their origin. *Journal of nuclear materials*, 4:226–233, 1961.
- [102] B.W. Howlett. A study of shear transformations from the gamma-phase in Uranium-Molybdenum alloys containing 6.0-12.5 at% molybdenum. *Journal of nuclear materials*, 35:278–292, 1970.
- [103] D. Stewart G.I. Williams. The structure and origin of the metastable monoclinic phase, α''_b , in uranium-molybdenum alloys. *Journal of nuclear materials*, 20:262–268, 1966.
- [104] R. Hengstler et al. Physical Properties of Monolithic U8wt.-%Mo. *Journal of nuclear materials*, 2010.

- [105] K. Tangri. Les phases gamma metastables dans le alliages d'uranium contenant du molybdene. *Memoires Scientifiques de la Revue de Metallurgie*, 58:469–477, 1961.
- [106] W.A. Bostrom E.K. Haltemann. The metastable gamma phase in Uranium base Molybdenum alloys. In J.R. Dunning, editor, *Advances in nuclear engineering*. Pergamon Press, 1957.
- [107] B.W. Howlett et al. Uranium-Titanium, Uranium-Zirconium and Uranium-Zirconium alloy systems. In *Proceedings of the second international conference on the peaceful uses of atomic energy/6*, pages 104–110, New York, 1958. United Nations.
- [108] A.G. Knapton. The crystal structure of TiU₂. *Acta Crystallographica*, 7:457–458, 1954.
- [109] A.A. Bauer et al. Physical metallurgy and properties of Zirconium-Uranium alloys. In *Proceedings of the second international conference on the peaceful uses of atomic energy/5*, pages 602–609, New York, 1958. United Nations.
- [110] A.F. Berndt. The unit cell of U₂Ru. *Acta Crystallographica*, 14:1303–1303, 1961.
- [111] E.K. Haltemann. The crystal structure of U₂Mo. *Acta Crystallographica*, 10:166–169, 1957.
- [112] A.E. Dwight et al. The Uranium Molybdenum equilibrium diagram below 900°C. *Journal of nuclear materials*, 2:81–87, 1960.
- [113] H.A. Saller F.A. Rough. The alloys of Uranium. In *Proceedings of the first international conference on the peaceful uses of atomic energy/9*, pages 107–116, New York, 1955. United Nations.
- [114] J. Bloch. Changement de phase et mise en desordre par irradiation du compose U₂Mo. *Journal of nuclear materials*, 1:90–91, 1960.
- [115] O.S. Ivanov Yu.S. Virgiliev. The decomposition of the γ -Uranium solid solutions as revealed by X-ray investigations. *Journal of nuclear materials*, 6:199–202, 1962.
- [116] Thaddeus Massalski, editor. *Binary alloy phase diagrams Vol. 3*. ASM International, Ohio, 2. edition, 1996.
- [117] J. Lehmann. Phases monocliniques dans les alliages uranium-molybdenum. *Journal of nuclear materials*, 4:218–225, 1961.
- [118] X. Iltis, 2010. Private communication.
- [119] S.T. Konobeevsky et al. Some physical properties of Uranium, Plutonium and their alloys. In *Proceedings of the 2nd international conference on the peaceful uses of atomic energy/6*, New York, 1958. United Nations.

- [120] Thaddeus Massalski, editor. *Binary alloy phase diagrams Vol. 2*. ASM International, Ohio, 2. edition, 1996.
- [121] H. Mikailoff. Study of transformation by annealing of the body-centered cubic γ -phase of Uranium-Molybdenum alloys. Technical Report CEA-1270, Commissariat à l'énergie atomique, Paris, 1959.
- [122] D. de Fontain. Mechanical instabilities in the b.c.c. lattice and the beta to omega phase transformation. *Acta Metallurgica*, 18:275–279, 1970.
- [123] R.J. Van Thyne et al. Transformation kinetics of Uranium-Molybdenum alloys. *Transactions American Society for Metals*, 49:588–619, 1957.
- [124] S.T. Konobeevsky et al. Effects of irradiation on structure materials and properties of fissionable materials. In *Proceedings of the international conference on the peaceful uses of atomic energy/7*, New York, 1956. United Nations.
- [125] V.D. Dmitriev et al. Effects of neutron irradiation on the structure and properties of uranium alloys containing 0.6-9% by weight molybdenum. *Atomic Energy*, 22:574–579, 1967.
- [126] S.T. Konobeevskii et al. Effects of reactor radiation on the phase composition of low-alloyed uranium alloys. *Atomic Energy*, 22:565–573, 1967.
- [127] S.T. Konobeevskii et al. Investigation of the structural changes taking place in a uranium-molybdenum alloy under the action of neutron irradiation. *Atomic Energy*, 4:33–45, 1958.
- [128] M.L. Bleiberg. Effect of fission rate and lamella spacing upon the irradiation-induced phase transformation of U-9wt%Mo alloy. *Journal of nuclear materials*, 2:182–190, 1959.
- [129] R.W. Buzzard H.E. Cleaves. The binary alloys of Uranium. In *Nuclear science and technology*. Oak Ridge technical information service, 1951.
- [130] K. Böning W. Petry. Test irradiations of full-sized U_3Si_2 -Al fuel plates up to very high fission densities. *Journal of nuclear materials*, 383:254–263, 2009.
- [131] Donald R. Olander. *Fundamental Aspects of Nuclear Reactor Fuel Elements*. ERDA Technical Information Center, Oak Ridge, Tennessee, 1. edition, 1976.
- [132] H. Palancher et al. Evidence for the presence of U-Mo-Al ternary compounds in the U-Mo/Al interaction layer grown by thermal annealing: a coupled micro X-ray diffraction and micro X-ray absorption spectroscopy study. *Journal of applied crystallography*, 40:1064–1075, 2007.
- [133] M.I. Mirandou et al. Characterization of the interaction layer in diffusion couples U–7 wt.%Mo/Al 6061 alloy at 550°C and 340°C: Effect of the γ -U(Mo) cellular decomposition. *Materials characterization*, 60:888–893, 2009.

- [134] D.D. Keiser et al. SEM and TEM characterization of as fabricated U-Mo dispersion fuel plates. In *Proceedings of the 31st International Meeting on Reduced Enrichment for Research and Test Reactors (RERTR)*, Beijing, 2009.
- [135] S. Klaumüntzer. private communication, 2011.
- [136] H. Palancher R. Jungwirth. Influence of the irradiation temperature on the formation of the IDL during heavy ion irradiation. to be published, 2010.
- [137] G.L. Hofman. recent observations at the postirradiation examination of low-enriched u-mo miniplates irradiated to high burnup. In *Proceedings of the 25. International Meeting on Reduced Enrichment for Research and Test Reactors (RERTR)*, 2003.
- [138] D.L. Porter A. Ewh. Interaction Layer Characteristics in U-xMo Dispersion/Monolithic Fuels. Technical Report INL/EXT-10-17972, INL, Idaho Falls, 2010.
- [139] R. Hengstler. Thermal and Electric Conductivity of a Monolithic Uranium-Molybdenum Alloy for Research Reactor Fuels. Diplomarbeit, Technische Universität München, 2008.
- [140] R. Jungwirth. Thermische und elektrische Leitfähigkeit von hochdichten Uran-Molybdän Kernbrennstoffen. Diplomarbeit, Technische Universität München, 2007.
- [141] S.H. Lee. Thermophysical properties of U-Mo/Al alloy dispersion fuel meats. *International journal of thermophysics*, pages 1578–1594, 2007.
- [142] S.H. Lee. Effect of heat treatment on thermal conductivity of U-Mo/Al dispersion fuel. *International journal of thermophysics*, pages 1355–1371, 2003.
- [143] A. Leenaers et al. EPMA of ground UMo fuel with and without Si added to the matrix, irradiated to high burn-up. In *Proceedings of the International Topical Meeting on Research Reactor Fuel Management (RRFM)*, Marrakesh, 2010.
- [144] M. Ripert et al. Results of the IRIS-4 irradiation in OSIRIS reactor: oxidized U-Mo particles dispersed in Al (with 0 or 2.1%Si). In *Proceedings of the 31st International Meeting on Reduced Enrichment for Research and Test Reactors (RERTR)*, Beijing, 2009.
- [145] W. Petry et al. UMo full size plate irradiation experiment IRIS–TUM – a progress report. In *Proceedings of the International Topical Meeting on Research Reactor Fuel Management (RRFM)*, 2008.
- [146] F. Huet et al. Full-Sized Plates Irradiation with High UMo Fuel Loading: Final Results of IRIS-1 Experiment. In *Proceedings of the International Meeting on Reduced Enrichment for Research and Test Reactors (RERTR)*, 2003.

- [147] J.H. Yang et al. Effect of Si in Al and third elements in UMo on interaction layer growth during irradiation -KOMO 4 irradiation test results . In *Proceedings of the International Meeting on Reduced Enrichment for Research and Test Reactors (RERTR)*, Lisbon, 2010.
- [148] W. van Renterghem et al. TEM investigations of irradiated atomized and ground U(Mo) dispersion fuel, with or without Si added to the matrix. In *Proceedings of the International Meeting on Reduced Enrichment for Research and Test Reactors (RERTR)*, Beijing, 2009.
- [149] A. Leenaers et al. Irradiation behavior of atomized and ground U(Mo) dispersion fuel. In *Proceedings of the International Meeting on Reduced Enrichment for Research and Test Reactors (RERTR)*, Washington, 2008.
- [150] A. Leenaers et al. Microstructural analysis of ground U(Mo) fuel with and without Si in the matrix, irradiated to high burn-up. In *Proceedings of the International Meeting on Reduced Enrichment for Research and Test Reactors (RERTR)*, Beijing, 2009.
- [151] A. Leenaers et al. Irradiation behavior of ground U(Mo) fuel with and without Si added to the matrix. *Journal of nuclear materials*, 412:41–52, 2011.
- [152] W. Schmid. *Sputtering of large scale UMo foils*. PhD thesis, Technische Universität München, 2010.
- [153] T.K. Bierlein et al. The diffusion of Uranium into Aluminum. Technical Report HW-38982, Hanford Atomic Products Operation, 1955.
- [154] D.R. Green et al. Diffusion of uranium an aluminum-silicon eutectic alloy. Technical Report HW-49697, Hanford Atomic Products Operation, 1957.
- [155] M. Ripert et al. Iris-3 experiment Status and result of thickness increase. In *Proceedings of the 10th International Topical Meeting on Research Reactor Fuel Management (RRFM)*, Sofia, 2006.
- [156] J.E. Cunningham R.E. Adams. Techniques for canning and bonding metallic Uranium with Aluminum. In *Fuel element conference*, Paris, 1957.
- [157] A. Leenaers et al. The effect of silicon on the interaction between metallic uranium and aluminum: A 50 year long diffusion experiment. *Journal of nuclear materials*, 381:242–248, 2008.
- [158] A. Leenaers et al. Microstructure of 50 year old SCK-CEN BR1 research reactor fuel. In *Proceedings of the 31. International Meeting on Reduced Enrichment for Research and Test Reactors (RERTR)*, Prague, 2008.
- [159] S. Van den Berghe et al. SELENIUM fuel : Surface engineering of U(Mo) particles to optimise fuel performance. In *Proceedings of the International Topical Meeting on Research Reactor Fuel Management (RRFM)*, Marrakesh, 2010.
- [160] D. Kramer. Finely dispersed phases in Uranium-Molybdenum ternary alloys. *Journal of nuclear materials*, 4:281–286, 1961.

- [161] S. Dubois et al. Development of dispersed UMo fuel : An oxide layer as a protective barrier of the UMo particles. In *Proceedings of the 28th International Meeting on Reduced Enrichment for Research and Test Reactors (RERTR)*, Cape Town, 2006.
- [162] A. Ewh D.D. Keiser et al. Microstructural characterization of U–Nb–Zr, U–Mo–Nb and U–Mo–Ti alloys via electron microscopy. *Journal of phase equilibria and diffusion*, 32:216–222, 2010.
- [163] S. Dirndorfer et al. Characterization of bond strength of monolithic two metal layer systems. In *Proceedings of the International Topical Meeting on Research Reactor Fuel Management (RRFM)*, Marrakesh, 2010.
- [164] G. Cabane. Stabilisation de la phase γ dans les alliages ternaires a base de uranium-molybdenum. *Journal of nuclear materials*, 4:364–373, 1959.
- [165] KAERI. U-Mo powder coating. IFDWG meeting autumn 2010 in Lisbon, 2010.
- [166] T.C. Wiencek et al. Development and compatibility of magnesium-matrix fuel plates clad with 6061-aluminum alloy. In *Proceedings of the 21st International Meeting on Reduced Enrichment for Research and Test Reactors (RERTR)*, Sao Paulo, 1998.
- [167] H.A. Saller J.T. Stacy. Jacketing of Uranium for high temperature service: Part II Barrier coat materials. Technical Report BMI-69, Battelle Memorial Institute, 1951.
- [168] K.H. Kim et al. Development of high-loading U-Mo alloy fuel by centrifugal atomization. In *Proceedings of the 19th International Meeting on Reduced Enrichment for Research and Test Reactors (RERTR)*, Seoul, 1996.
- [169] F. Mazaudier et al. Thermodynamic and Kinetic Features of the Oxidation Treatment of U7Mo Particles. In *Proceedings of the 28th International Meeting on Reduced Enrichment for Research and Test Reactors (RERTR)*, Cape Town, 2006.
- [170] G. Hofman Y.S. Kim. Performance comparison between various U-Mo powders. IFDWG meeting spring 2010 in Marrakesh, 2010.
- [171] Alfa Aesar Homepage. <http://www.alfa.com>.
- [172] H. Juranowitsch. Cross Section Examination of Sputtered Uranium-Molybdenum Nuclear Fuels. Diplomarbeit, Hochschule für angewandte Wissenschaften - FH München, 2010.
- [173] Homepage des Maier-Leibnitz-Laboratoriums München. <http://www.bl.physik.tu-muenchen.de>.
- [174] J. Goldstein et al. *Scanning Electron Microscopy and X-Ray Microanalysis*. Springer, The Netherlands, 2002.

- [175] J. Orloff. *Handbook of Charged Particle Optics*. CRS Press inc., Florida, USA, 1997.
- [176] Zeis - EVO MA 25 Homepage. <http://www.zeiss.de/C1256E4600305472/Contents-Frame/84E6E310B4773CB3C1256E54003A31FE>.
- [177] R.A. Young, editor. *The Rietveld Method*. Oxford Science Publication, Oxford, UK, 2000.
- [178] Fullprof Software Suite. <http://www.ill.eu/sites/fullprof/>.
- [179] Webpage of the μ -XAS beamline at the SLS, PSI. <http://www.psi.ch/sls/microxas/micro-xas>.
- [180] Webpage of the ID22 beamline at the ESRF, Grenoble. <http://www.esrf.eu/UsersAndScience/Experiments/Imaging/ID22>.
- [181] Webpage of the ID18F beamline at the ESRF, Grenoble. Beamline now closed. <http://www.esrf.eu/UsersAndScience/Experiments/Imaging/ID18F>.
- [182] H. Palancher et al. Advances in the Characterization of Annealed Atomized UMo/Al Particles Using Synchrotron Radiation. In *Proceedings of the 30th International Meeting on Reduced Enrichment for Research and Test Reactors (RERTR)*, Washington, 2009.
- [183] H. Palancher et al. Characterization of the Interaction Layer Between Decomposed UMO7 and Aluminum Using Micro-Focused XRD on a Single Particle. In *Proceedings of the 30th International Meeting on Reduced Enrichment for Research and Test Reactors (RERTR)*, Washington, 2009.
- [184] E. Welcomme H. Palancher R. Jungwirth et al. Heavy ion irradiation of UMo7/Al fuel: methodological approach. In *Proceedings of the International Topical Meeting on Research Reactor Fuel Management (RRFM)*, Vienna, 2009.
- [185] R. Jungwirth et al. Progress in heavy-ion bombardment of U-Mo/Al dispersion fuel. In *Proceedings of the International Topical Meeting on Research Reactor Fuel Management (RRFM)*, Hambourg, 2008.
- [186] H. Palancher et al. Heavy ion irradiation as a method to discriminate research reactor fuels. In *Proceedings of the International Topical Meeting on Research Reactor Fuel Management (RRFM)*, Sofia, 2006.
- [187] K. Colon et al. Neutron powder diffraction of UMo fuel irradiated to 60at% burnup. In *Proceedings of the International Topical Meeting on Research Reactor Fuel Management (RRFM)*, Lyons, 2007.
- [188] H. Palancher. Influence of the irradiation temperature on the IDL formation during heavy ion irradiation, 2010. private communication.
- [189] T. Zweifel H. Palancher et al. Heavy ion irradiation on UMo/Al systems: Temperature influence. In *Proceedings of the International Topical Meeting on Research Reactor Fuel Management (RRFM)*, Rome, 2011.

- [190] A. Leenaers et al. Microstructural analysis of irradiated atomized UMo dispersion fuel in an Al matrix with Si addition. In *Proceedings of the International Topical Meeting on Research Reactor Fuel Management (RRFM)*, Hambourg, 2008.
- [191] D.D. Keiser et al. Microstructural development in irradiated U-7Mo/6061 Al alloy matrix dispersion fuel. *Journal of nuclear materials*, 393:311–320, 2009.
- [192] D.D. Keiser et al. Results of recent microstructural characterization of irradiated U-Mo dispersion fuels with Al alloy matrices that contain Si. In *Proceedings of the International Topical Meeting on Research Reactor Fuel Management (RRFM)*, Hambourg, 2008.
- [193] R. Jungwirth H. Palancher et al. Optimization of the Si content in UMo/AlSi fuel plates. In *Proceedings of the 31th International Meeting on Reduced Enrichment for Research and Test Reactors (RERTR)*, Beijing, 2009.
- [194] R. Jungwirth H. Palancher et al. Study of heavy ion irradiated UMo/Al mini-plates: Si and Bi additions into AL and UMo ground powders. In *Proceedings of the International Topical Meeting on Research Reactor Fuel Management (RRFM)*, Marrakesh, 2010.
- [195] X. Iltis et al. Characterization of IRIS-3 as-fabricated Plates (Before Irradiation), 2010. Appendix to technical report INL/EXT-10-17972 by Porter.
- [196] J. Allenou H. Plancher et al. IRIS-3 reception state of the U-Mo7/Al-Si2 plate. IFDWG meeting spring 2010 in Marrakesh, 2010.
- [197] A. Brown et al. Beta-Polymorphs of Uranium and Thorium Disilicides. *Nature*, 183:673, 1959.
- [198] A. Brown et al. Uranium Disilicide. *Nature*, 191:61–62, 1961.
- [199] A.E. Dwight. A study of the Uranium-Aluminum-Silicon system. Technical Report ANL-82-14, Argonne National Laboratory, 1982.
- [200] W.H. Zachariasen et al. Crystal structure studies of Uranium silicides. *Acta Crystallographica*, 2:94–99, 1949.
- [201] Y. Sasa et al. Structure of stoichiometric USi₂. *Journal of solid state chemistry*, 18:63–68, 1976.
- [202] P. Rogl et al. Magnetic structures of U₃M₂M₃', M=Al, Ga; M'=Si, Ge: a neutron powder diffraction study. *Journal of Magnetism and Magnetic Materials*, 191:291–300, 1999.
- [203] H. Palancher. Phase composition of unirradiated IRIS-3 plates. to be published, 2010.
- [204] J. Allenou et al. UMo-AlSi interaction: influence of Si concentration. *Journal of nuclear materials*, 399:189–199, 2010.

- [205] F. Charollais et al. IRIS program: IRIS-4 first results. In *Proceedings of the International Topical Meeting on Research Reactor Fuel Management (RRFM)*, Vienna, 2009.
- [206] F. Huet et al. Post irradiation examinations on UMo full sized plates - IRIS-2 experiment. In *Proceedings of the International Topical Meeting on Research Reactor Fuel Management (RRFM)*, Budapest, 2005.
- [207] KAERI ENDFPLOT. <http://atom.kaeri.re.kr/endfplot.shtml>.
- [208] Thaddeus Massalski, editor. *Binary alloy phase diagrams Vol. 1*. ASM International, Ohio, 2. edition, 1996.
- [209] T. Scott M. Eagleson. *Concise encyclopedia chemistry*. Walter de Gruyter, 1994.
- [210] S. Dirndorfer. Tensile Tests on Monolithic Two Metal Layer Systems for Research Reactor Fuels. Diplomarbeit, Technische Universität München, 2010.
- [211] C.R. Clark et al. Update on Monolithic Fuel Fabrication Methods. In *Proceedings of the International Meeting on Reduced Enrichment for Research and Test Reactors (RERTR)*, Cape Town, 2009.
- [212] R. Jungwirth et al. IRIS-TUM: Microstructure of the Non-Irradiated plates. In *Proceedings of the International Meeting on Reduced Enrichment for Research and Test Reactors (RERTR)*, Lisbon, 2010.
- [213] G. Hofman et al. Recent Observations at the Post Irradiation Examination of low Enriched UMo Miniplates Irradiated to High Burnup. In *Proceedings of the 8th International Topical Meeting on Research Reactor Fuel Management (RRFM)*, Munich, 2004.
- [214] M. Ripert et al. Overview on High Density UMo Fuel In-Pile Experiments in OSIRIS. In *Proceedings of the International Topical Meeting on Research Reactor Fuel Management (RRFM)*, Hambourg, 2008.
- [215] A. Röhrmoser et al. Reduced Enrichment Program for the FRM-II, Status 2004/05. In *Proceedings of the International Topical Meeting on Research Reactor Fuel Management (RRFM)*, Budapest, 2005.
- [216] X. Iltis. Initial state of the IRIS-TUM plates: XRD analysis. Private communication., 2010.
- [217] H. Palancher et al. Quantitative crystallographic analysis of as-fabricated full sized UMo/Al(Si) nuclear fuel plates. *Journal of nuclear materials*, 2011. in preparation.
- [218] A.S. Cooper. Precise lattice constants of Ge, Al, La-As, U, S, Quartz and Sapphire. *Acta Crystallographica*, 15:578–583, 1962.
- [219] F.A. Rough A.A. Bauer. Constitution of uranium and thorium alloys. Technical Report BMI-1300, Battelle Memorial Institute, Columbus, Ohio, 1958.

- [220] Struers Homepage. <http://www.struers.com>.
- [221] H.A. Saller et al. The constitution diagram of U-Mo alloys. Technical Report BMI-730, Battelle Memorial Institute, 1952.